

## ABSTRACT

Past several decades have driven modernization of technology and machinery. This modernization has pushed the limits of our technology and increased our dependence on the energy. Additional side-effect of this rapid growth has been an exponential increase in the generated heat of the modern machinery.

In most cases this waste heat is simply released into the environment. Numerous research groups have pursued an idea of capturing and converting the waste heat. Thermoelectric, pyroelectrics, organic Rankine cycle (ORC), and several other methods have been proposed to capture and convert the waste heat into electricity. Presently, all methods, however, have low conversion efficiency and are not economically feasible.

In this work we focused on a practical approach to convert mid-IR electromagnetic waves to electricity. It is based on inexpensive thin film technology utilizing a junction between a narrow bandgap lead salt and wide bandgap chalcogenide film.

Lead sulfide (PbS) was chosen as the narrow band semiconductors for the IR energy conversion. Lead salt photodetectors uniquely demonstrate high room temperature sensitivity to black-body sources in low temperatures and high internal quantum efficiency (QE). Further, the peculiar band structure of the lead salt allows for small Auger recombination and minimized losses.

Due to its favorable opto-electrical properties and band compatibility with PbS, cadmium sulfide (CdS) was chosen as the wide bandgap semiconductor for this work.

This work has shown that high quality nanocrystalline thin films of lead sulfide (PbS) and cadmium sulfide (CdS) can be grown cost efficiently using chemical bath deposition (CBD) method. Chemical bath seeding procedure was also developed in order to achieve reproducibility in the transport phenomena of the advanced materials. Seeding also allows these films to be deposited on any surface, including smooth flexible materials. Seeded kernels have shown to become the crystallization centers for both nanocrystalline films.

Opto-electrical properties of the films were tuned in such a way to make the materials useful in a broad-band of the IR spectrum. We have shown that altering the parameters of the chemical bath deposition alters the grains hence changing the transport characteristics of the materials. We have shown that parameters of the chemical bath deposition can be optimized to produce highly sensitive thin films tuned to a specific range of the electromagnetic spectra.

Novel transparent conducting oxide, Iridium (Ir) doped Titanium Oxide ( $\text{TiO}_2$ ) was developed in this work for the use in the optoelectronic device. Ir has been shown to be one of the most efficient dopants in thin films. Ir doped  $\text{TiO}_2$  has shown to have transport characteristics similar

to those of the commonly used TCOs, with much higher optical transmittance in the infra-red range.

Lastly devices were manufactured from the developed materials.  $\text{TiO}_2/\text{CdS}/\text{PbS}/\text{Au}$  heterojunctions were manufactured and showed photoresponsivity. Device efficiencies were shown to depend on the doping concentrations of all materials, TCO thicknesses, and electrode selection. Conversion rates of 3% were shown in the devices.

Two secondary contributions to the scientific body of knowledge were also achieved. First, crystalline structure has a profound effect on the opto-electrical properties of the film. Phase transitions from cubic to hexagonal crystals in CdS during heat treatment were observed. Hexagonal phase showed much more favorable opto-electrical properties. Additionally, film's stored energy due to the developed stresses and strains was studied. When the stored energy is larger than the adhesive energy, the deposited film would peel off from the substrate. Low adhesion was observed in films with high stresses. Some of the stresses can be alleviated using heat treatment, hence allowing for higher adhesion.

The result of this work show that a cost efficient method for the conversion of thermal energy into electricity is possible using advanced thin film materials. Conversion efficiencies and cost efficiency make this technology feasible for use in large scale applications.

## ACKNOWLEDGEMENTS

Over the course of graduate studies, I realized that pursuing a Ph.D. was as much an intellectual as a social quest. This thesis was made possible by the guidance, assistance, and contributions of an entire social network of people who selflessly contributed their expertise, collaboration, and valuable assistance. It is the effort of these individuals that ensured successful completion of this work. I am grateful to everyone who has made this work attainable. It is impossible to list everyone by name, and to give everyone a due homage. It is my pleasure, however, to acknowledge the cordial assistance of friends and scholars who have made this monograph possible. This work would not be possible without your guidance, insight, and support.

I would like to extend my greatest appreciation to my advisor Pamela Norris for her assistance, direction, guidance, patience, and support. Dean Norris is one of the busiest and best recognized names on the university grounds. Yet despite the numerous projects she is currently involved with, she always found the time to provide insightful and meaningful feedback and guidance.

I also would like to thank my co-advisor Tatiana Globus for all of her patience, technical guidance, and support. She spent countless hours slowly teaching and walking me through the topics of solid state physics. I know at times it was not easy, and the countless hours we spent writing papers and proposals can never be summed up in a short acknowledgement section. I want to thank you for your time and patience on all topics.

I would also like to extend deep gratitude to Alex Lobo for his patience in explaining and finding the right components for the numerous circuits and testing equipment that was used in the course of this work. Your guidance and expertise ensured my success.

I am infinitely indebted to my collaborators. I would like to especially thank Christopher Saltonstoll for his guidance and work in Raman spectroscopy crystal characterization, Naser Alijabbari for guiding me through the initial phases of chemical process and crystal growth, Michael Melia for help with pulsed laser deposition methods, Marcel Mibus for his guidance on dielectric constant measurements, Keye Sun for never ending help with SEMs and numerous equipment, Zeming Sun for countless hours on XRD, Kai Xie for the vacuum work, Herbert Ryan for NMR studies of crystalline structures, prof. Joe Campbell's research group, and everyone else who was involved over the course of the project. I wish to extend special gratitude to prof. James Fitz-Gerald for his guidance in crystal growth in open vacuum.

Additionally, I express my deepest appreciation to all of the staff, students, and faculty of the School of Engineering and Applied Science, and the University of Virginia. I would like to thank the community of this university for all of the given amazing opportunities.

I feel fortunate and blessed to have an amazing wife, Liliya, who supported me in the busiest of times through all of the ups and downs of this research. I wish to express my gratitude for allowing me to work in the times when our toddlers were demanding most attention.

But most of all my indebtedness is to the One above us all. It is the wisdom and power of the omnipotent God that gave me strength and wisdom to continue in the most difficult of times when my deepest desires were to stop. I thank you Lord for making this work possible.

## Contents

ABSTRACT.....	i
ACKNOWLEDGEMENTS.....	iii
LIST OF FIGURES .....	ix
LIST OF TABLES.....	xiii
LIST OF SYMBOLS AND ABBREVIATIONS.....	xiv
Chapter 1. Introduction .....	1
1.1 Motivation.....	1
1.2 Objectives .....	2
1.3 Semiconductor and electromagnetic radiation physics .....	3
1.3.1 Modeling blackbody radiation .....	3
1.3.2 Energy band structure in semiconductors .....	5
1.3.3 Photovoltaic effect in semiconductors .....	7
1.3.4 Doping concentrations and Fermi energy level .....	9
1.4 Semiconductor carrier transport phenomena .....	11
1.4.1 Drift and mobility.....	12
1.4.2 Resistivity .....	13
1.4.3 Carrier generation and recombination.....	13
1.4.4 Carrier lifetime .....	15
1.4.5 Diffusion .....	15
1.4.6 Tunneling .....	17
1.5 Statistical analysis and experimental error.....	18
1.6 Dissertation goals and organization .....	19
Chapter 2. Heterojunctions .....	21
2.1 Anisotype heterojunction .....	21
2.2 Depletion layer.....	22
2.2.1 Built-in potential and the depletion layer width.....	23
2.2.2 Depletion layer capacitance .....	26
2.3 Lattice matching.....	28
2.4 Current-voltage analysis .....	30
2.5 Semiconductor-metal contacts .....	33

2.5.1 Metal – semiconductor depletion layer .....	36
2.5.2 Practical factors.....	37
2.5.3 Barrier height measurements .....	39
Chapter 3. Chemical bath deposition (CBD) of thin films.....	42
3.1 Fundamentals .....	42
3.1.1 Metal hydrolysis.....	43
3.1.2 Solubility product.....	44
3.1.3 Complexing agents.....	45
3.1.4 Sulphide .....	46
3.2 Nucleation.....	46
3.2.1 Homogenous nucleation.....	47
3.2.2 Heterogeneous nucleation .....	47
3.3 Film growth.....	48
3.4 Growth mechanics .....	49
3.5 Deposition kinetics.....	52
3.6 Effects of substrates and stirring.....	54
3.7 Film characterization .....	56
3.7.1 X-Ray diffractometry (XRD).....	57
3.7.2 X-Ray photoelectron spectroscopy (XPS) .....	57
3.7.3 Optical spectroscopy .....	58
3.7.4 Spectroscopic ellipsometry .....	59
3.7.5 Hall effect electrical analysis .....	60
Chapter 4. Lead (II) Sulfide .....	63
4.1 Introduction.....	63
4.2 Chemical bath deposition of PbS .....	64
4.2.1 Seeding.....	64
4.2.2 Film deposition .....	65
4.3 Material characterization.....	66
4.3.1 Interference spectroscopy .....	66
4.3.2 Hall effect measurements.....	67
4.3.3 Responsivity.....	68
4.3.4 Scanning electron microscopy (SEM) .....	68

4.3.5 Scratch adhesion test.....	68
4.3.6 Raman spectroscopy .....	68
4.3.7 X-Ray photoelectron spectroscopy (XPS) .....	68
4.4 Results.....	69
4.4.1 Seeding.....	69
4.4.2 Deposition temperature variation.....	73
4.4.3 Deposition time variation.....	74
4.4.4 NaOH variation.....	75
4.4.5 Carrier lifetime measurements .....	77
4.4.6 Nanocrystalline structure .....	79
4.5 Conclusion .....	84
Chapter 5. Cadmium Sulfide.....	85
5.1 Introduction.....	85
5.2 Experimental .....	86
5.2.1 Synthesis .....	86
5.2.2 Solid state nuclear magnetic resonance spectroscopy (NMR) .....	87
5.2.3 Temperature dependent Hall effect (TDH).....	87
5.2.4 Optical spectroscopy .....	87
5.2.5 Photo-responsivity .....	88
5.3 Results.....	88
5.3.1 Physical and structural properties .....	88
5.3.2 Optical properties.....	94
5.3.3 Electrical properties .....	100
5.4 Conclusions.....	104
Chapter 6. Transparent conducting oxide –Ti <sub>1-x</sub> Ir <sub>x</sub> O <sub>2</sub> .....	105
6.1 Introduction.....	105
6.2 Experimental .....	106
6.2.1 Materials and methods .....	106
6.2.2 Pulsed laser deposition.....	108
6.3 Results.....	108
6.3.1 PLD target structural properties .....	108
6.3.2 Thin films structural properties.....	109

6.3.3 Thin film electrical properties.....	111
6.3.4 Thin film optical properties.....	114
6.3.5 Iridium doping efficiency.....	117
6.4 Conclusion .....	117
Chapter 7. Glass/Ti <sub>1-x</sub> Ir <sub>x</sub> O <sub>2</sub> /CdS/PbS/Au heterojunction .....	119
7.1 Introduction.....	119
7.2 Experimental procedures .....	120
7.2.1 Junction manufacturing.....	120
7.2.2 Band structure .....	122
7.3 Results.....	124
7.3.1 CdS/PbS structural analysis .....	124
7.3.2 Glass/AuGrid/CdS/PbS/Au device electrical performance.....	125
7.3.3 Glass/Ti <sub>1-x</sub> Ir <sub>x</sub> O <sub>2</sub> /CdS/PbS/Au device electrical performance.....	128
7.3.4 External and internal quantum efficiency of the Glass/Ti <sub>1-x</sub> Ir <sub>x</sub> O <sub>2</sub> /CdS/PbS/Au device .....	133
7.4 Conclusion .....	134
Chapter 8. Conclusions, summary, and future work.....	136
References.....	139

## LIST OF FIGURES

Figure 1.1 Blackbody radiation for light wavelength and blackbody temperatures

Figure 1.2 Graphic representation for the formation of the new quantum states and energy band

Figure 1.3. Computed band structure of TiO<sub>2</sub>

Figure 1.4 Optical absorption coefficients for various semiconducting materials

Figure 1.5 Schematic of the non-degenerate/degenerate semiconductor

Figure 1.6 Schematic of the carrier drift under the applied electric field

Figure 1.7 Radiative, Shockley-Read-Hall, and Auger recombination process schematic

Figure 1.8 Photoconductive decay method

Figure 2.1 Energy band diagram for anisotype heterojunctions.

Figure 2.2 Construction of the band diagram of the heterojunction

Figure 2.3 Mott-Schottky plot of a typical semiconductor

Figure 2.4 Energy gap (eV) and wavelength ( $\mu\text{m}$ ) versus lattice constants ( $\text{\AA}$ ) of common semiconductors

Figure 2.5 Critical thickness versus lattice mismatch

Figure 2.6 Overall view of carrier activity inside a p-n junction structure

Figure 2.7 Diode current-voltage (I-V) characteristics

Figure 2.8 Metal-semiconductor contact energy diagram

Figure 2.9 Metal work functions to the periodic table of elements

Figure 2.10. Band diagram of the low, moderate, and heavy surface doping

Figure 2.11 Schematic and band diagram of the photoelectric measurement of the Schottky barrier

Figure 3.1 Removal of the electron from the O – H bond, and oxidation of the metal

Figure 3.2 Homogeneous and heterogeneous nucleation processes

Figure 3.3 Crystal growth mechanisms

Figure 3.4 Schematic of the ion-by-ion growth mechanism

Figure 3.5 Schematic of the ion-by-ion growth mechanism on the seeded substrate

Figure 3.6 Stability region for the Cd-ammonia system for 0.1 M total Cd concentration at room temperature

Figure 3.7 Typical growth curve shape as a function of time

Figure 3.8 Ellipsometric optical model of air/thin film/substrate structure

Figure 3.9 Hall Effect in a plate

Figure 4.1 Transmittance and reflectance of a 547 nm CBD deposited PbS film

Figure 4.2 SEM image of the seeded sample

Figure 4.3: SEM of PbS seed on rough side of bulk Si wafer

Figure 4.4 Raman spectra of PbS seeds and film.

Figure 4.5 EDS spectrum of PbS seeds showing the composition being primarily composed of Pb and S and the Si substrate.

Figure 4.6 PbS change in film parameters as a function of deposition temperature

Figure 4.7 PbS film parameters as a function of deposition time over the range of 30 to 120 minutes

Figure 4.8 PbS film parameters as a function of NaOH concentration

Figure 4.9. PbS film carrier lifetimes measured by 980 nm laser, and blackbody

Figure 4.10: Scanning electron microscope images of PbS tight crystalline structure

Figure 4.11: Scanning electron microscope images from the stir rate experiments.

Figure 4.12: XPS analysis reveals oxidation at surface

Figure 5.1 Scanning electron microscope images of CdS deposited at various temperatures

Figure 5.2 XRD spectra of thin film CdS deposited at various bath temperatures, after thermal annealing

Figure 5.3  $^{113}\text{Cd}$  spectra acquired using a 1024 scans spin-echo experiment with a recycle time of 150s

Figure 5.4 Grain sizes and lattice parameters for cubic and hexagonal crystalline structures as a function of deposition temperature

Figure 5.5 Number of crystallites per  $\text{m}^{-2}$  ( $N$ ), dislocation density ( $\delta$ ), and microstrain ( $\epsilon$ ) as a function of deposition temperature

Figure 5.6 Film thicknesses as a function of grain size

Figure 5.7 Ellipsometric  $\Psi$  and  $\Delta$  spectra for the CdS films at various deposition temperatures measured at  $70^\circ$  incidence angle

Figure 5.8 Ellipsometric  $\Psi$  and  $\Delta$  for  $95^\circ\text{C}$  samples analyzed at various deposition times

Figure 5.9 Film, layer thickness, and film roughness of  $95^\circ\text{C}$  samples at various stages of film deposition

Figure 5.10 Refractive index ( $n$ ) and extinction coefficient ( $k$ ) as a function of deposition temperature

Figure 5.11 Tauc plot for CdS films grown at various deposition temperatures

Figure 5.12 Optical bandgap and Urbach tail as a function of grain size

Figure 5.13 Hall Effect measurements as function of grain size

Figure 5.14 Hall Effect mobility and carrier concentration as a function of temperature

Figure 5.15 Carrier lifetime as a function of grain size

Figure 6.1 Spark plasma sintering (SPS) setup

Figure 6.2 SPS graphite chamber and die setup schematic

Figure 6.3 PLD targets

Figure 6.4 Cross sectional SEM of the PLD target

Figure 6.5 EDS Phase mapping 1% Iridium doped PLD target

Figure 6.6  $\text{Ti}_{1-x}\text{Ir}_x\text{O}_2$  thin films on glass substrates

Figure 6.7 SEM images of the  $\text{Ti}_{1-x}\text{Ir}_x\text{O}_2$  thin films on glass substrates

Figure 6.8 X-ray diffraction spectra of the target and thin film on the Si substrate

Figure 6.9 Transport properties of  $\text{Ti}_{1-x}\text{Ir}_x\text{O}_2$  films with  $x = 0 - 0.15$  as a function of temperature

Figure 6.10 Spectra for  $\text{Ti}_{1-x}\text{Ir}_x\text{O}_2$  films with various  $x$

Figure 6.11 Optical bandgap as a function of  $n^{2/3}$  in Ir doped  $\text{TiO}_2$  and the dual-band overlap from the defect states

Figure 7.1 Device schematic

Figure 7.2 Device energy band diagram

Figure 7.3 Device equivalent circuit

Figure 7.4 XRD data for the CdS/PbS thin films in heterojunction

Figure 7.5 Mott-Schottky plot and I-V curves as a function of blackbody temperature for a Glass/AuGrid/CdS/PbS/Au structure

Figure 7.6 I-V data for device with variable gold finger spacing

Figure 7.7 %T for various TCO thicknesses

Figure 7.8 Visual observation of the opaqueness of thicker TCOs

Figure 7.9 I-V data at various TCO thicknesses

Figure 7.10 Mott-Schottky diagrams for the Glass/ $\text{Ti}_{1-x}\text{Ir}_x\text{O}_2$ /CdS/PbS/Au structure

Figure 7.11 EQE and IQE of the Glass/ $\text{Ti}_{1-x}\text{Ir}_x\text{O}_2$ /CdS/PbS/Au structure

## LIST OF TABLES

Table 2.1 Electrical nature of metal-semiconductor contacts

Table 2.2 Measured Schottky barrier heights (V) for CdS at 300 K

Table 3.1 Solubility product for PbS and CdS at 300 K

Table 4.1 Characteristics of multiple deposited layers

Table 4.2 Re-characterized PbS Film Parameters

Table 5.1 Re-characterized CdS Film Parameters

Table 6.1 Opto-electrical Properties of  $Ti_{1-x}Ir_xO_2$  at  $T = 300K$

Table 7.1 Glass/AuGrid/CdS/PbS/Au photovoltaic parameters under 1 Sun

Table 7.2 Glass/  $Ti_{1-x}Ir_xO_2$ /CdS/PbS/Au photovoltaic parameters under 1 Sun

Table 7.3 Parameters from the Mott-Schottky analysis

Table 7.4 Base layer thickness (PbS) device performance

## LIST OF SYMBOLS AND ABBREVIATIONS

$a_e$	Epitaxial layer lattice constant [ $\text{\AA}$ ]
$a_s$	Substrate lattice constant [ $\text{\AA}$ ]
$B$	Magnetic field [T]
$C$	Capacitance [F]
$c$	Speed of light in vacuum [m/s]
$D_n$	Coefficient of diffusivity
$D_N$	Coefficient of diffusivity of electrons
$D_P$	Coefficient of diffusivity of holes
$e_B$	Electron binding energy [eV]
$E_C$	Conduction band
$E_F$	Fermi energy level
$E_V$	Valence band
$F(E)$	Fermi-Dirac distribution function
$I$	Current [A]
$K_{eq}$	Equilibrium constant
$K_{sp}$	Solubility product [mol/L]
$k$	Boltzmann constant [ $\text{m}^2 \text{kg s}^{-2} \text{K}^{-1}$ ]
$L_d$	Diffusion length [m]
$L_N$	Diffusion length of electrons [m]
$L_P$	Diffusion length of holes [m]
$M_C$	Number of equivalent minima in the conduction band
$m^*$	Electron effective mass

$m_{ds}$	Density of state effective mass of electrons
$N$	Complex refractive index
$n$	Electron concentration [ $\text{cm}^{-3}$ ]
$n$	refractive index of the material
$n_i$	Intrinsic carrier concentration [ $\text{cm}^{-3}$ ]
$\Delta n$	Excess carriers generated through photons
$N(E)$	Number of states
$N_A$	Acceptor doping concentration [ $\text{cm}^{-3}$ ]
$N_D$	Donor doping concentration [ $\text{cm}^{-3}$ ]
$p$	Hole concentration [ $\text{cm}^{-3}$ ]
$q$	Elementary charge [C]
$R$	Photoresponse
$T_b$	Blackbody temperature [K]
$t_c$	Critical film thickness [ $\text{\AA}$ ]
$U_0$	Strain energy density
$V$	Voltage [V]
$V_A$	Applied voltage [V]
$V_{bi}$	Built in voltage [V]
$v_d$	Drift velocity [m/s]
$V_H$	Hall voltage [V]
$W$	Potential barrier width
$W_D$	Width of the depletion layer [m]
$q$	Elementary charge [eV]

$\alpha$	Absorption coefficient [ $\text{cm}^{-1}$ ]
$\Delta(2\theta)$	Peak full width at half maximum (FWHM) [rad]
$\mathcal{E}$	Electric field [V/m]
$\varepsilon$	Lattice strain
$\varepsilon_0$	Permittivity of free space [C/V-cm]
$\varepsilon_s$	Permittivity of the semiconductor [C/V-cm]
$\Delta_{lattice}$	Lattice mismatch
$\Delta$	Polarized light phase difference
$\emptyset$	Crystal diameter Scherrer's relation [nm]
$\theta$	High frequency cut-off factor
$\rho(x)$	Space charge density [ $\text{cm}^{-3}$ ]
$\lambda$	Wavelength of the X-ray
$\sigma$	Lattice stress [ $\text{N/m}^2$ ]
$\nu$	Frequency of light
$\sigma$	Stefan-Boltzmann constant, [ $\text{W}^{-1} \text{m}^{-2} \text{K}^{-4}$ ]
$\Phi$	Work function [V]
$\Psi$	Polarized light amplitude ratio
$\chi$	Electron affinity [V]

## Chapter 1. Introduction

### 1.1 Motivation

The past two decades have seen an explosion in energy demand by both developed and emerging world markets. World power demand has been growing exponentially with no plateau for energy demand in sight. Current energy demands are ~ 13 TWatts per year and are expected to reach annual demands of ~30 TWatts by 2050 [1]. Part of the reason for this explosion in energy demand is the mass manufacturing of modern machinery, electronic systems, and high tech devices each using excessive amounts of energy and becoming largely accessible to the masses [2]. As accessibility to electronics, machinery, automobiles, and electronic devices increases further, energy demand is expected to grow excessively putting additional stresses on energy resources especially the non-renewables [3]. Presently, roughly 87% of world's power is generated from non-renewable sources, including nuclear and fossil fuels [4]. Further, it has become apparent that these nonrenewable sources generate voluminous amounts of heat and excess CO<sub>2</sub> emissions, which over the years had a profound effect on the overall world climate [5]. There is a large scientific need to combat the grand challenge of ever growing energy demand and the environmental impact of the energy consuming society. Our future success depends largely on our ability to address the current energy demand issues in a cost-effective and methodical manner.

Efficient conversion of the thermal energy produced by modern internal combustion engine, typical of transportation machinery, will play a critical role in the overall success of meeting our energy demands. At the present time only ~25% of the energy stored in fuel is used to propel the vehicle whereas ~75% is released into the environment as waste heat [6]. This percentage is slightly better in diesel engines with ~64% lost to waste heat. Similar loss percentages are observed in fossil and nuclear fuel powered plants, with ~60% of the fuel's energy released into the atmosphere [7]. Further, it has been estimated that more than 80% of the primary energy used in the United States involved thermal transport of energy in the form of cooling, waste heat, etc. [8]. With ~87% of the generated power coming from fossil and nuclear fuels, ~60% released as waste heat, and estimated ~80% of the energy used for cooling and waste heat emissions, the potential for waste heat energy recapturing and conversion is immense.

Further it has been shown that thermal management in electronics plays a key role in the performance and reliability of devices [9]. The recently published International Technology Roadmap for Semiconductors by 2015 demands requirements for 10 nm feature size on chips, with 20 million gates per chip, operating at MHz frequencies, nF capacitances, located on 200-400 mm wafers [10]. The large chips with ultra-fast and-high operating regimes will significantly increase generated heat and requirements for heat dissipation. The voluminous amounts of generated heat will significantly decrease the overall efficiency of the devices, and

will require means of waste heat recapturing in order to improve the overall performance of the device.

The waste heat in the machinery and electronic systems emits photons in the infrared region of the electromagnetic spectrum. The infra-red range constitutes a large portion of the electromagnetic spectrum. This resource is a free, relatively untapped source for energy generation, as most of it is left in the environment without extensive consideration. Recycling of the waste heat will improve overall efficiency and performance of devices, while reducing ozone depletion, greenhouse emissions, and fossil fuel usage. Hence the goal of waste heat recycling has become a focus of intensive research for numerous research groups around the world.

Infrared electromagnetic spectrum recovery has been proposed through thermoelectric devices [11], pyroelectrics [12], organic Rankine cycles (ORC) [13], and CO<sub>2</sub> trans-critical power cycles, [14] but a dense, inexpensive form of recovery and conversion has yet to be developed. Current low-grade IR recovery systems have been shown to be expensive, with costs per kilowatt well above the threshold to become economically feasible.

This dissertation focuses on converting IR photons to usable electricity using a heterojunction between a narrow bandgap lead salt and a wide bandgap chalcogenide thin film. The IR spectrum can be naturally modeled as radiation of low temperature blackbody sources with rather broad spectra. The IR energy photons from these spectra are effectively absorbed by narrow bandgap semiconductor materials, whereas the high energy photons are absorbed by the wide bandgap chalcogenide for effective temperature control in the device. Generated carriers are swept away by the electric field in the device and carried to the electrodes to complete the circuit.

This work focuses on growing narrow bandgap thin film lead sulfide, wide bandgap thin film cadmium sulfide, transparent conducting oxide iridium doped TiO<sub>2</sub>, and a working heterojunction between these elements. In an effort to improve the efficiency of the device, transparent conducting oxide (TCO) thicknesses, doping density, and optimal electrodes are also studied.

## 1.2 Objectives

The overall aim of this work was to create a cost efficient device which would efficiently convert waste heat radiation into usable electricity. There are several objectives that were pursued in an effort to attain this goal:

- A p-type semiconducting thin film to act as a base of the device has to be developed and analyzed. In this work PbS was selected due to the favorable optical and electrical properties and high sensitivity in the IR range.
- A cost efficient method of depositing nanocrystalline PbS needs to be developed. The deposited film needs to possess good adhesion to the substrate, resistance to oxidation, robustness, and controllable opto-electrical properties.

- Optical, electrical, and structural properties of the PbS deposited under various conditions needs to be studied meticulously in order to understand the effects of the deposition parameters on the performance of the film.
- An n-type wide bandgap semiconductor needs to be developed for the device. The wide bandgap material is to act as a high energy photon absorber. The structural properties of the n-type material need to be compatible with the structural properties of the PbS. CdS is chosen due to its cubic structure, ease of deposition, and no post deposition treatment.
- A successful heterojunction between the materials is to be demonstrated. The heterojunction needs to be evaluated under infrared radiation in order to grasp the device's ability to convert thermal radiation into electricity.
- Transparent conducting oxide (TCO) for the use in the device is to be developed. The transparent conducting oxide needs to possess highly transparent properties in the visible and infrared spectral regions. Preferred transmission needs to be above 80% across the Vis-IR range. In order to maintain low parasitic resistance the resistivity of the material needs to be on the order of  $10^{-4} \Omega \text{ cm}$ .  $\text{TiO}_2$  is a suitable candidate for the device.  $\text{TiO}_2$  needs to be doped with a highly efficient dopant for optimal electrical performance.
- Heterojunction efficiency needs to be improved. Several routes of efficiency improvements are to be pursued. First, minimization of parasitic resistance through TCO thickness variation. Second, absorption of all photons by creation of optimal base thickness. Third, study of the performance under different doping profiles, and grid spacing. Theoretical efficiency of the devices is expected to be ~5% under 1 sun, and 30% Quantum Efficiency (QE) across the infrared region.

### 1.3 Semiconductor and electromagnetic radiation physics

The physics of semiconductor devices is inextricably dependent on the physics of the semiconducting materials as well as the properties of the electromagnetic spectrum. Our ability to understand both the phenomena of light and the physics behind the properties of the semiconductors will ensure success with architecting efficient photovoltaic devices. Hence it is paramount to give a brief explanation of the workings of the semiconducting devices and electromagnetic spectra.

#### 1.3.1 Modeling blackbody radiation

A blackbody is a theoretical idealized object absorbing all incident radiation [15]. Although Planck described a blackbody as a cavity or an empty bottle or a box inside which waves and photons bounce at a certain rate depending on the temperature, in reality this was Planck's attempt to model his law, and an analogy used to show the real aspect of the blackbody. In Planck's blackbody cavity a small hole was present through which escaping radiation could be observed. The real blackbody is an infinitude of infinitesimal peep holes signifying the ever escaping photons of certain wavelengths escaping at all times. This infinitude of escaping radiation in a lump summation gives a visible glow varying in intensity based on the temperature of the blackbody.

Photons are the particles of light oscillating at a certain natural frequency  $\nu$ . The total energy of these particles equals  $h\nu$  derived from Einstein's model of the photovoltaic effect [16]. The concept that the oscillating particles of light will possess a certain amount of energy was introduced by Planck and further expanded by Einstein as an effort to explain the radiation energy  $R_\nu(T)$ , which was observed to be emitted from the blackbody. This blackbody radiation was observed to be a function of  $\nu$  and  $T$ . Based on the frequency, solid angle, and surface area the radiation of the blackbody is modeled to be

$$R_\nu(T) = \frac{2k}{c^2} T \nu^2 \theta(\nu, T) \quad (1.1)$$

Cut-off factor,  $\theta(\nu, T) \approx 0$  for  $\frac{h\nu}{kT} \geq 10$ , and  $\theta(\nu, T) \approx 1$  for  $\frac{h\nu}{kT} \leq 1$ . The ratio between the Planck and the Boltzmann constant,  $h/k \approx 10^{-10}$ , is the causation behind the cut-off ratios. Physically, this means that only frequencies below  $\sim 10^{11}$  are emitted. This mathematical derivation is validated by experimental work. A black surface heated by the blackbody will not shine like the blackbody, but will radiate only at lower frequencies. Cut-off frequency can be reduced to  $\frac{kT}{h}$ , since frequencies above that range will be strongly damped out. This result shows that the cut off frequencies are also temperature dependent, this is known as Wien's Displacement Law, shown in Figure 1.

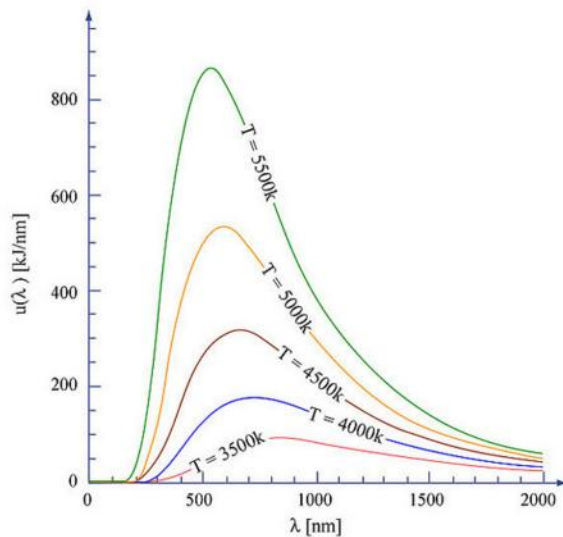


Figure 1.1 Blackbody radiation for light wavelength and blackbody temperatures.

Assuming no cut-off frequency results in ultraviolet catastrophe. In this case the total radiative energy becomes infinite above blue light frequencies as  $R_\nu(T) \approx T\nu^2$ . Ultraviolet catastrophe was deduced using classical methods in Rayleigh-Jeans Radiation Law, however, was contrary to the observation, since no ultraviolet catastrophe was ever observed.

The Stefan-Boltzmann Law states that the total radiated energy  $R(T)$  per unit surface area emitted by a black-body is proportional to  $T^4$ , and is computed from the integration of Planck's Law over the range of the frequencies, giving:

$$R(T) = \sigma T^4 \quad (1.2)$$

The Stefan-Boltzmann Law gives a very good fit to the observed data, Figure 1.1 [17].

Using Planck's and Stefan-Boltzmann's Laws, in addition to Wien's Displacement Law, it is possible to architect a device in such a way to collect the majority of the photons generated by a blackbody, and convert these photons into electricity in a photovoltaic effect.

### 1.3.2 Energy band structure in semiconductors

By the end of the nineteenth century the concept of a negatively charged electron orbiting a heavier positively charged nucleus was a well established fact, observed in hydrogen atoms. The dilemma however, consisted in the nature of light emitted from the system when the hydrogen atom was heated to an elevated temperature. More specifically, the emitted light was observed only at discrete wavelengths. Bohr assumed that the hydrogen atom electrons were restricted to well-defined orbits, and only certain angular momentums could be contained in the orbits, hence offering a solution to the conundrum. This novel concept, termed "quantization of the angular momentum", was directly related to the energy required to push the electron into higher orbits [18]. Assuming an electron's angular momentum to be equal to  $\frac{nh}{2\pi}$  from the conservation of angular momentum, electron binding energy can be deduced to be:

$$e_B = -\frac{m^* q^4}{2(2\varepsilon_0 h n)^2} \quad (1.3)$$

where  $e_B$  is the electron binding energy,  $m^*$  electron effective mass,  $q$  the elementary charge,  $\varepsilon_0$  the permittivity of free space, and  $n$  the orbital quantum number. From the Bohr model, it is apparent that the energy of electrons in atomic systems can hold a limited set of values, and electrons within this model cannot share the same quantum number.

Building upon this knowledge and assuming two atoms drawn closer to one another with no two electrons that can occupy the same state (Pauli Exclusion Principle), the interatomic forces lead to a progressive spread in the allowed energies. The dislocation of the energy bands gives rise to the newly formed spaced sets of allowed quantum states, commonly referred to as the energy bands. This concept is conceptually shown in Figure 1.2.

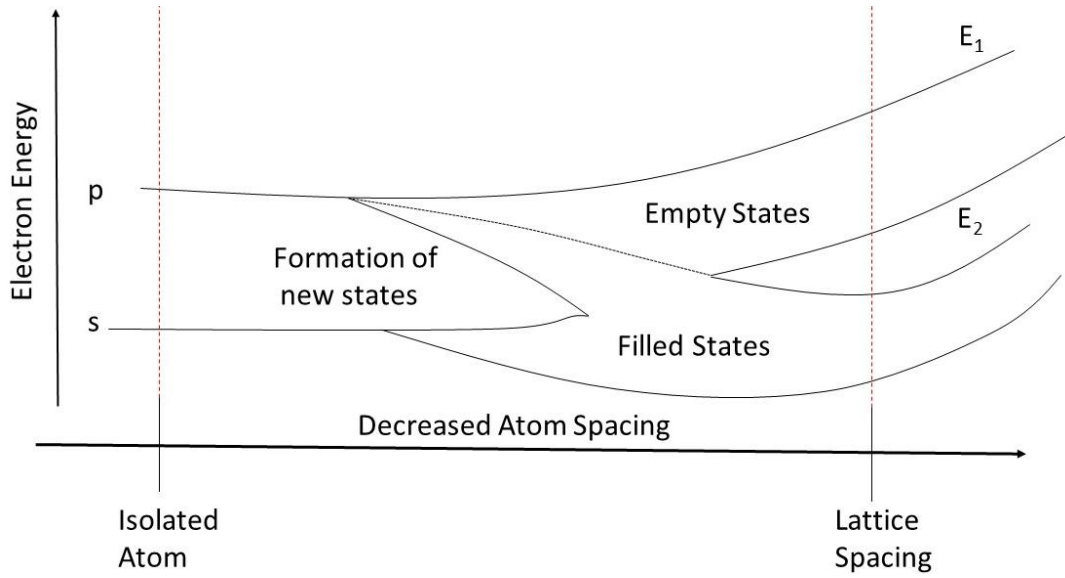


Figure 1.2. Schematic representation of the development of the new quantum states and energy band.

In the newly formed allowed states the upper ones are referred to as the conduction band, and the lower as the valence band. The intervening energy gap is the forbidden gap, commonly called the semiconductor bandgap.

Electrons tend to occupy the lowest possible energy states, and noting that no two electrons can occupy the same state, hence commonly the valence band is filled with electrons, and the conduction band is typically completely devoid of the electrons.

In the crystal structure, contrary to the isolated atom case, electrons do not become tied to any one particular atom. In this non-tied configuration electrons become mobile, traversing from one point in the crystal to another. Hence the allowed electron states no longer belong to a single atom, but are associated with the crystal as a whole. In a perfect crystal, the configuration of the allowed states is the same regardless of the examined point. In reality the band structure of the crystal is not uniform and is more complex.

The band structure of the crystal lattice is obtained by making an approximated solution of the one-electron function to solve the Schrodinger equation [19]. Schrodinger's equation ,

$$\left[ \frac{\hbar^2}{4m^*} \nabla^2 + V(r) \right] \psi(r, k) = E(k) \psi(r, k) \quad (1.4)$$

where  $V(r)$  is potential energy,  $\psi(r, k)$  the wavefunction,  $k$  momentum, and  $E(k)$  the energy as a function of electrons momentum, is solved using Bloch's function:

$$\psi(r, k) = e^{(jk \cdot r)} U_b(r, k) \quad (1.5)$$

From Bloch's theorem it is also apparent that the  $E-k$ , energy-momentum, relationship is periodic in the reciprocal lattice. Using iterative numerical computation, band structures for the lattice structure can be computed. The computed bandgap of  $\text{TiO}_2$  is shown in Figure 1.3 [20].

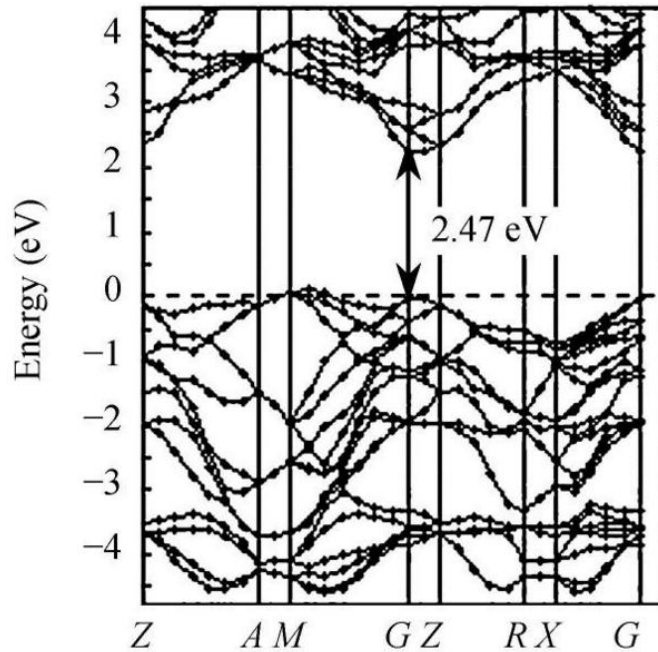


Figure 1.3. Computed band structure of  $\text{TiO}_2$ .

There are several important results from the Schrodinger's computation. First, the forbidden bandgap can be direct or indirect. In a direct bandgap, an electron simply moves from one band edge to the other, whereas in an indirect bandgap there is lateral motion of the electron as well as the traversing of the bandgap. Additionally, besides the bands there are a series of smaller sub-bands in the lattice. Sub-bands play a crucial role in the efficiency of the semiconductor, most notably Auger losses and recombinations [21].

### 1.3.3 Photovoltaic effect in semiconductors

One of the greatest scientific achievements by the end of nineteenth century was the development of classical electromagnetic theory. Deviating from classical mechanics, electromagnetic theory was able to explain a variety of experimental observations. The phenomenon of electron emission by certain metals when shined upon by light, however, caused a bit of a dilemma in classical electromagnetic theory and led to its further refinement.

This phenomenon was discovered by Hertz in 1887, while observing that metals emit negative electricity while illuminated by ultra-violet light [22]. This observation opened a new field of research in photovoltaics and provided experimental proof for the Einstein-Richardson equations as a law which governs this effect [23]:

$$V_o = h(\nu - \nu_o) = h\nu \quad (1.6)$$

Where  $V_o$  is the voltage required to stop the electron emission at the frequency of the incident light  $\nu$ , and  $h$  is Planck's constant. With the experimental validation, this equation shows that the frequency of the incident light will cause an emission of an electron with the velocity or the kinetic energy equaling zero.

Absorption of the particle of light and emission of the electron is referred to as the photovoltaic (sometimes photoelectric) effect. Numerous devices have been developed to use this effect for electronic purposes. Such optoelectronic devices operate on the principle of the quantum photoelectric effect, where a photon excites an electron within the semiconductor, which contributes to the overall photocurrent.

The photoelectric effect is based on photon energy,  $h\nu$ . The wavelength associated with this energy of the photon is related through Planck's relationship,

$$\lambda = \frac{hc}{\Delta E} \quad (1.7)$$

Typically  $\Delta E$  is the energy gap of the semiconductor, in some cases depending on work function of the semiconductor and metal it can be the barrier height in a metal-semiconductor photodiode, or in the case of an extrinsic semiconductor, a transition energy between an impurity level and one of the band edges. Thus, the semiconductor materials need to be chosen for the wavelength of interest in order to optimize performance.

Optical absorption is another parameter that needs to be carefully considered in the semiconductor selection process. It is important to know not only whether the light will generate an electron from the photon, but also where the light is absorbed. Optical absorption coefficients for various photodetector materials in various spectral regions are shown in Figure 1.4 [24]. Light is absorbed near the surface at high absorption coefficients. Low absorption coefficients will allow the light to pass through the material without absorption. In some cases light can pass through the material without carrier generation. Thus, the efficiency of the devices is largely dependent on the absorption coefficient of the material. Optoelectronic devices have to be architected accordingly to optimize their use in the desired spectral region.

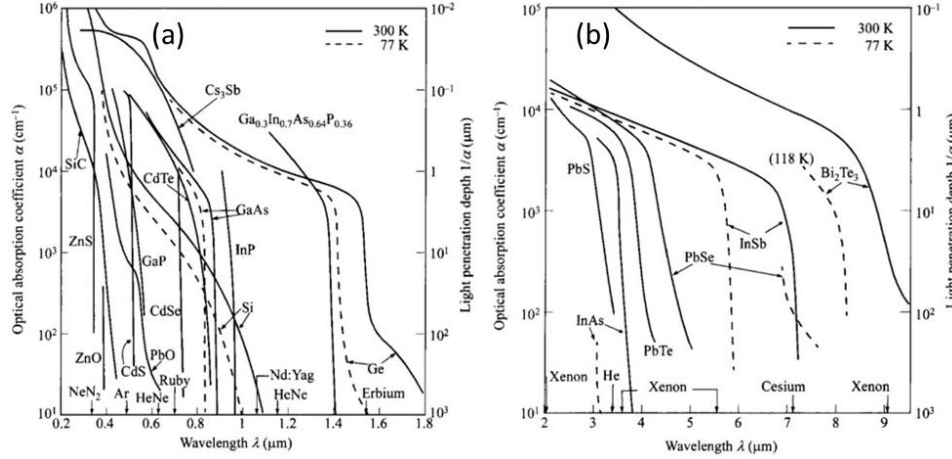


Figure 1.4 Optical absorption coefficients for various semiconducting materials in (a) near optical (b) infrared spectral regions.

When the energy of the photon is larger than the bandgap of the material, and the photon is absorbed by the semiconducting material, then through a photoelectric effect a free carrier will be generated which will effect the photocurrent of the device.

### 1.3.4 Doping concentrations and Fermi energy level

In the case of an intrinsic semiconductor, the material with no added impurities, the number of electrons in the conduction band is given by the total possible number of states,  $N(E)$ , multiplied by the Fermi-Dirac distribution function,  $F(E)$ , integrated over the entire conduction band [25]:

$$n = \int_{E_C}^{\infty} N(E) F(E) dE \quad (1.8)$$

Assuming low carrier densities at low temperatures the density of states can be approximated to be [26]:

$$N(E) = M_C \frac{\sqrt{2} m_{ds}^{3/2} (\Delta E - E_C)^{1/2}}{\pi^2 \hbar^3} \quad (1.9)$$

where  $M_C$  is the number of equivalent minima in the conduction band,  $m_{ds}$  is the density of state effective mass for electrons, and  $\hbar$  is the reduced Planck's constant. Density of state effective mass of electrons can be computed from the effective masses of electrons,  $m_1^*$ ,  $m_2^*$ , etc., along the principal axis of the ellipsoidal energy surface [26]:

$$m_{ds} = (m_1^* m_2^* m_3^*)^{1/3} \quad (1.10)$$

The Fermi-Dirac distribution function is a strong function of energy as well as temperature and is given by [27]:

$$F(E) = \frac{1}{1 + e^{(E-E_F)/kT}} \quad (1.11)$$

where  $E_F$  is the Fermi energy level, which can be computed from the donor acceptor concentrations.

In an ideal intrinsic case, since neither the electron donors nor acceptor impurities are present, the Fermi energy lies in the middle of the forbidden gap. A purely intrinsic semiconductor is impossible, however, an extremely pure semiconductor contains an insignificant amount of impurity atoms, with negligible changes in the Fermi energy position. In such a case, the properties of the semiconductors are native to the material. Additionally, carrier generation and recombination is balanced in the conduction and valence bands for electrons and holes respectively, with the net result of electrons and holes equal to one another.

The addition of dopants, however, alters the intrinsic nature of semiconductors. An acceptor impurity has a valence electron which becomes neutral if empty and negative if filled by an electron. Conversely, a donor impurity has a donor level which is neutral if filled by an electron and positive in its absence.

Addition of either the donor or acceptor impurity introduces an impurity energy level. Addition of the acceptors pushes the Fermi level closer to the valence band, whereas addition of the donors will push the Fermi levels closer to the conduction band. As long as the Fermi energy level lies more than  $3kT$  below and above  $E_C$  and  $E_V$  respectively, such a semiconductor is considered non-degenerately doped. This is shown schematically in Figure 1.5.

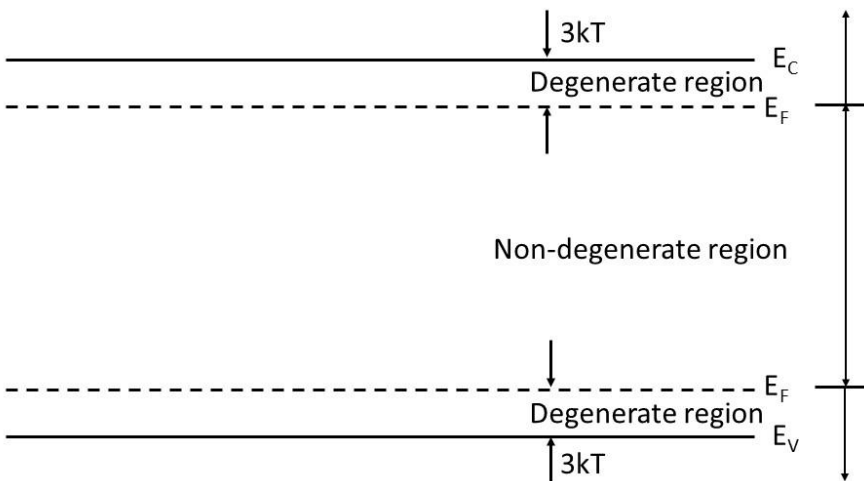


Figure 1.5 Schematic of the non-degenerate/degenerate semiconductor.

Carrier concentrations in extrinsic non-degenerate semiconductors are no longer in equilibrium with one another. In the acceptor doped semiconductor the number of positively charged carriers,  $p$ , is greater than that of the negatively charged carriers,  $n$ . In the donor doped case, negatively

charged carrier concentrations are larger than that of the positively charged ones. The location of the Fermi level can be computed from the doping carrier concentrations using:

$$E_F - E_i = kT \ln \left( \frac{N_D}{n_i} \right) \quad (1.12)$$

$$E_i - E_f = kT \ln \left( \frac{N_A}{n_i} \right) \quad (1.13)$$

where  $N_A$  and  $N_D$  represent the doping concentrations of acceptors and donors respectively. In both cases dopant concentrations are larger than the intrinsic carrier concentrations,  $N_A \gg n_i$ , and  $N_D \gg n_i$ .

In the case of the degenerately doped semiconductor, where  $n$ - or  $p$ -concentrations are above  $3kT$  or beyond the effective density of states ( $N_C$  or  $N_V$ ), the Boltzmann approximation will no longer hold true, and the Fermi-Dirac function needs to be integrated. It is also necessary to note that at times the Fermi level may lie outside of the energy gap. In the degenerate case a filling of the empty states may take place and an increase of the bandgap may be observed, called a Burstein-Moss shift [28]. Thus the location of the Fermi level can only be approximated for  $n$ -type semiconductors [29]:

$$E_F - E_C \approx kT \left[ \ln \left( \frac{n}{N_C} \right) + 2^{-3/2} \left( \frac{n}{N_C} \right) \right] \quad (1.14)$$

and for  $p$ -type semiconductors

$$E_V - E_F \approx kT \left[ \ln \left( \frac{p}{N_V} \right) + 2^{-3/2} \left( \frac{p}{N_V} \right) \right] \quad (1.15)$$

The Fermi energy becomes a pivotal parameter in the creation of the  $p$ - $n$  junction, heterojunction device.

#### 1.4 Semiconductor carrier transport phenomena

Carrier generation, in both doped and undoped semiconductors, in conditions of equilibrium is important since this becomes a baseline for further discussion. From the device standpoint, however, equilibrium zero current conditions are not realistic and neither are they of any special interest. Systems perturbed out of equilibrium give rise by generating novel carriers as well as net carrier response, giving rise to current flow inside and outside of the semiconductor device. Carrier transport phenomena requires brief discussion.

Drift, mobility, resistivity, carrier generation, recombination, lifetimes, diffusion, and tunneling effects are of greatest interest in the heterojunction and are briefly analyzed.

### 1.4.1 Drift and mobility

Motion of a charged particle as a response to an electric field is known as *drift*. Whenever an applied electric field ( $\mathcal{E}$ ) is applied across a semiconducting material, negatively and positively charged carriers accelerate across the semiconductor lattice opposite and in the direction of the applied electric field, respectively. Due to lattice imperfections, grain boundaries, and collisions within the lattice the acceleration of the charged particles is often halted. This is shown schematically in Figure 1.6. Vibrations of the crystal also play a crucial role in the drift of the charged particles. At high temperatures scattering of the carriers from the vibrations of the atoms, phonon scattering, becomes significant in altering the drift and mobility of carriers.

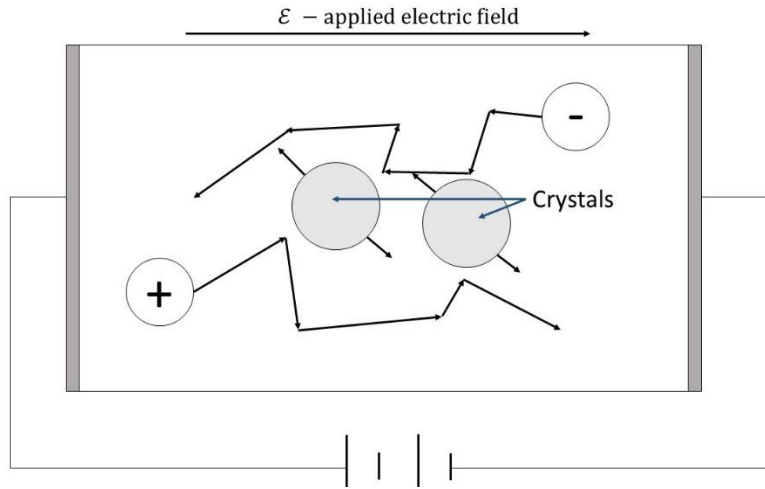


Figure 1.6 Schematic of the carrier drift under the applied electric field.

At low electric fields, the drift velocity,  $v_d$ , is proportional to the strength of the electric field through a proportionality constant. This constant is defined as carrier mobility,  $\mu$ . The relationship between drift velocity, mobility, and the strength of the electric field is:

$$v_d = \mu \mathcal{E} \quad (1.16)$$

Mobility from the interaction between the carrier and the acoustic atom (phonon) in the lattice has been approximated to be [30]:

$$\mu = \frac{\sqrt{8\pi} q \hbar^4 C_l}{3 E_{ds}^2 m^{*5/2} (kT)^{3/2}} \propto \frac{1}{m^{*5/2} T^{3/2}} \quad (1.17)$$

Where  $C_l$  and  $E_{ds}$  are the semiconductor lattice parameters, average longitudinal elastic constant and the displacement of the band edge per unit dilation respectively. From Equation (1.17) it should be apparent that mobility decreases with an increase in temperature, this is largely due to the increase in the vibrations of the phonons at high temperatures.

In addition to the phonon scattering described above, additional mobility is also effected by intravalley scattering in which an electron is scattered within the atom's electron shell [31], and intervalley scattering in which the electron is scattered between the phonon minima [32].

Carrier mobility is one of the most important parameters in highly efficient photoelectric devices. Success in creating highly efficient devices depends on the ability of increasing mobility of carriers.

#### 1.4.2 Resistivity

Given the flow of electrons under an applied electric field, material will have an inherent resistance to current flow, this important parameter of semiconductors is known as the *resistivity*,  $\rho$ . Resistivity is a normalized parameter of the material that is independent of the physical dimensions of the material. Mathematically it is a proportionality constant between the electric field and the total current per unit area flowing in the material [33]:

$$\mathcal{E} = \rho I \quad (1.18)$$

therefore

$$\rho = \frac{1}{q(\mu_n n + \mu_p p)} \quad (1.19)$$

In a non-degenerately doped semiconductor, contributions from the minority carriers are small and may be disregarded, and Equation (1.19) in such a case can be simplified. From the above equation it can be seen that the addition of dopants will in general decrease the resistivity of the material. The addition of dopants, however, inevitably will increase the number of deficiencies within the crystal as well. At a certain threshold doping level the resistivity of the semiconductor will begin to increase [34]. Presumably this threshold level will be reached beyond the degenerate doping, where the semiconductor will begin exhibiting semiconducting behavior.

#### 1.4.3 Carrier generation and recombination

The perturbation of a semiconducting material from its equilibrium state will unavoidably generate excess carriers inside the material. Recombination is the order restoring mechanism present inside such materials. In general any excess carrier generation will be stabilized reaching some equilibrium if the perturbation is maintained, or gradually eliminated if the perturbation is removed. In general, optoelectronic devices operate in non-equilibrium conditions, hence generation and recombination of carriers plays a crucial role in the device performance and characteristics.

Carriers can be generated and recombine through several processes. In the case of a photoelectric device, the majority of the carriers are generated by absorbing photons of light, which generate electron hole pairs inside the heterojunction.

Recombination in photovoltaic devices can be either due to a) radiative, b) defect driven (Shockley-Read-Hall), or c) Auger recombination, or by a combination of each. Each process is complex, schematically shown in Figure 1.7, and needs to be addressed individually.

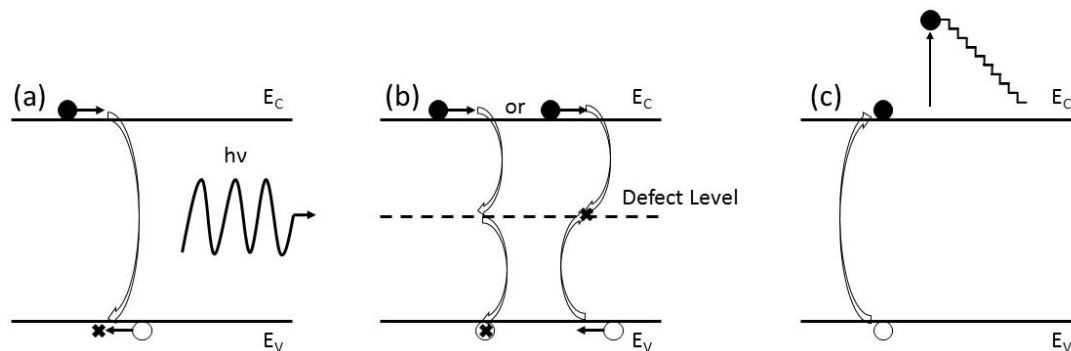


*Figure 1.7 Recombination processes: (a) radiative, (b) Shockley\_Read-Hall recombination (c) Auger recombination process schematics.*

The radiative recombination mechanism is prevalent in direct bandgap semiconductors. In this case the generated electron in the conduction band falls directly into the hole in the valence band. Such recombination releases a photon of energy equal to the energy of the bandgap. Due to this similarity, this photon is not readily absorbed by the material, and generally exits the semiconductor.

Shockley-Read-Hall recombination, better known as defect recombination, is typical in heavily doped semiconductors. A carrier is trapped in the forbidden gap by a defect. This trapped carrier recombines with opposite carriers releasing a photon of lower energy or the energy is absorbed by the phonons.

Auger recombination involves 3 particles. In this case, an electron from the conduction band recombines with a hole in the valence band, but in lieu of releasing a photon, the excess energy is absorbed by the third particle which then is pushed into higher sub-bands, before thermalizing back down to lower band. “Thermalization” typically takes places in small steps through heat producing collisions with the semiconductor lattice. Lead salts possess a unique bandstructure which fills higher bands with the thermalized carrier [35]. This unique structure minimizes the Auger losses by as much as two orders of magnitude as compared to other semiconductors. Carrier lifetimes are increased by minimizing recombination rates in the semiconductors, hence improving the overall performance of the photovoltaic devices.

### 1.4.4 Carrier lifetime

Excess carriers generated inside of photoelectric devices do not disappear instantaneously all at once, rather the carriers systematically recombine to be eliminated. Hence some of the generated carriers have short lifetimes, whereas others may exist for prolonged periods of time. Physically, the average time an excess carrier will live is called the carrier lifetime,  $\tau$ . Like the mobility and resistivity, the carrier lifetime is an important parameter in the performance of an optoelectric device.

Carrier lifetimes can be easily deduced using a photoconductive decay method [36], schematically shown in Figure 1.8 [37].

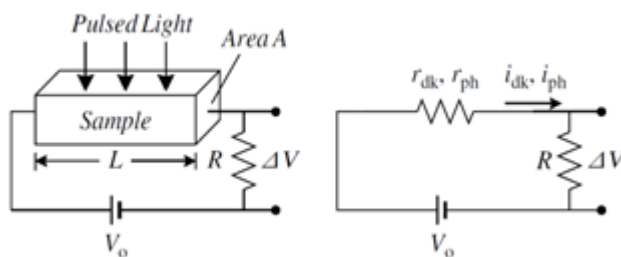


Figure 1.8 Photoconductive decay method.

Pulsating light will generate excess carriers, hence generating a photocurrent. This additional current is then forced through a resistor which will cause a voltage change in the resistor of known resistance. Capturing the voltage change across the resistor versus the time with an oscilloscope will provide a graph of the decay for carriers.

Excess carrier concentrations ( $\Delta n$ ) can be derived using:

$$\Delta n = \Delta n_0 e^{-t/\tau} \quad (1.20)$$

where  $\Delta n_0$  is the carrier concentration at  $t=0$ , or when the light is off. Carrier lifetime,  $\tau$ , is derived with the help of the Arrhenius plot, as the slope of the graph.

In general, there is an absence of experimental data on the carrier lifetime of materials in the literature. This is mainly due to the fact that carrier lifetimes vary over orders of magnitude all depending on the electrical and structural properties of the materials. It is imperative, however, to increase the carrier lifetimes of an optoelectronic device. Long lifetimes increase the electron mean free paths, and increase the probability of electron capture by the electrode.

### 1.4.5 Diffusion

The preceding section discussed a case where the carriers were generated in uniform space. In this section a situation where carriers are introduced locally is discussed. Such a situation causes

a condition of non-uniform carriers localized to a specific region of the semiconductor. Examples are local injection of carriers, such as in the case of a junction, or non-uniform illumination of the device. In an attempt to reach equilibrium, any situation where a gradient of carriers is present results in a flow of carriers from the area of high concentration to the area of low concentration. This flux of carriers is governed by Fick's Law [38]:

$$\left. \frac{d\Delta n}{dt} \right|_x = -D_n \frac{d\Delta n}{dx} \quad (1.21)$$

$D_n$  is the proportionality constant, commonly referred to as the coefficient of diffusivity. This flow of carriers will generate additional current, known as the diffusion current,  $I$ :

$$I = qD_n \frac{d\Delta n}{dx} \quad (1.22)$$

In a physical sense diffusion is due to the random thermal motion of carriers as well as scattering.

Since diffusion generates a current, one would expect a relationship between the diffusion coefficient and mobility of the carriers. This relationship is known as the Einstein relation, and has been derived to be [39]:

$$D_n = \frac{kT\mu}{q} \quad (1.23)$$

This equation is valid for non-degenerately doped semiconductors. Contributions from diffusivity of electrons are negligible in degenerately doped semiconductors since such materials exhibit metallic behavior. The importance of the diffusion coefficient should be apparent from the relation, and it is a central parameter in the performance of optoelectrical devices.

It should be briefly mentioned that the location of the band levels will change with the gradient of carriers, while the Fermi level will remain unchanged. This becomes a significant factor in the performance of the heterojunction with non-uniform carrier concentrations.

Another important parameter closely related to the diffusion coefficient is the diffusion length,  $L_d$ , given as:

$$L_d = \sqrt{D_n \tau} \quad (1.24)$$

The diffusion length can be viewed as the distance carriers can diffuse before they are annihilated. Diffusion length can vary by orders of magnitude depending on the carrier lifetimes of the materials.

### 1.4.6 Tunneling

Tunneling is a pure quantum mechanical phenomenon. In classical mechanics particles are completely confined to the barriers of the walls. Only the particles with the potential energy above that of the barrier can escape the confinement. In the quantum mechanical sense, however, an electron will have a particle as well as a wave property. The wave function of the electron is not terminated at the barrier wall, but has a probability of penetrating the barrier.

The probability of quantum tunneling has been derived from Schrodinger's equation, and shown in Figure 1.9. Assuming negligible variation rates of the tunneling barrier the tunneling probability has been shown to be [40]:

$$T_t = \frac{|\Psi_B|^2}{|\Psi_A|^2} \approx \exp\left\{-2 \int_{x_1}^{x_2} |k(x)| dx\right\} \approx \exp\left\{-2 \int_{x_1}^{x_2} \sqrt{\frac{2m^*}{\hbar^2} [U(x) - E]} dx\right\} \quad (1.25)$$

And from the known tunneling probability, tunneling current,  $I_t$ , can be computed from the number of available carriers in Region A (Figure 1.9).

$$I_t = \frac{qm^*}{2\pi^2\hbar^3} \int F_A N_A T_t (1 - F_B) N_B dE \quad (1.26)$$

Where  $F_A$ ,  $F_B$ ,  $N_A$ ,  $N_B$  are Fermi-Dirac and density of states in Regions – A and B accordingly. Equation (1.26) shows that a small amount of current will “leak” through the thin film optoelectronic device due to the tunneling of carriers.

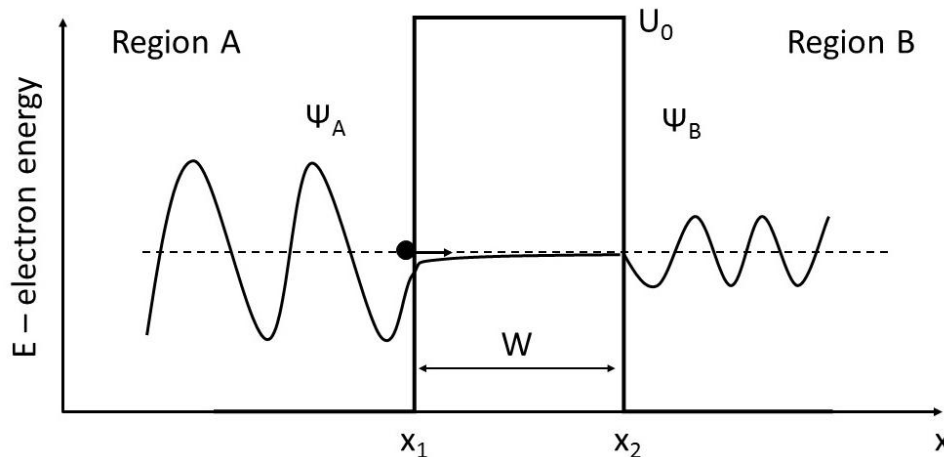


Figure 1.9 Wavefunction of an electron tunneling through a rectangular barrier.

Probability of tunneling is a function of the potential width, and previous work has shown that this current leakage due to tunneling is significant at  $W < \sim 100 \text{ \AA}$  [41]. Modern day thin film devices have thicknesses ranging from  $\sim 300 \text{ nm} - 1 \text{ \mu m}$  and the probability of carrier tunneling is greatly decreased at such thicknesses, nevertheless, tunneling may be significant enough to

effect the overall performance of the device. Devices have to be architected with the tunneling from valence to conduction band, i.e. Zener tunneling, in mind. This is important in order to minimize the losses.

Overall the desire is a device for which the mobility is increased, the resistivity is decreased, and with the highest probability of carrier generation by each photon of light with low regeneration rates and long carrier lifetimes. Reverse saturation current (leakage current), often caused by tunneling phenomena in the thin film devices, and also has to be minimized. All of these factors have to be analyzed and kept in mind when designing highly the proposed efficient thin film optoelectronic device.

### 1.5 Statistical analysis and experimental error

Due to the large number of performed experiments and extensive use of instruments in materials characterization, it is inevitable that a certain degree of experimental variation and error existed.

In order to address possible variability within the experimental results, experiments were repeated a minimum of three times and statistical analysis of the experimental data was conducted. Mean of the experimental values is computed and presented as a point on the graph. Mean is presented along with the error bars. Error bars represent +/- one standard deviation based on three repeated experiments at identical deposition and measurement conditions. When an outlier was perceived, two additional experiments were conducted at identical conditions. The average and standard deviations are based on the results from all five measurements.

Standard deviation was analyzed using the following equation:

$$\sigma = \sqrt{\frac{1}{N} \sum_{i=1}^N (x_i - \mu)^2} \quad (1.27)$$

where  $x_i$  represents the experimental value and  $\mu$  the experimental mean from the repeated experiments.

In the case that the experimental value produced a complete outlier, the distance of the outlier from the standard result was also assessed. If the outlier did not change the results or the trend of the data, or created a significant dissociation, then in some cases such outliers were discharged. In the case that the outlier effected both the result and the outlining assumptions, such outliers were not discharged. In such cases experiments were reproduced to confirm validity of the outlier. The outliers were then considered in the statistical analysis.

Experimental error was also considered in the analysis of the experimental results. Error propagation rules are applied in the analysis of the overall experimental result and error. Only the results where the experimental error was found to be reasonably small are presented, i.e. the presented experimental results are deemed to be true.

## 1.6 Dissertation goals and organization

This dissertation is divided into a total of 8 chapters. Chapter 1 gives a brief introduction of the physics behind electromagnetic radiation as well as semiconducting devices.

Chapter 2 provides the basic workings of the heterojunction, metal-semiconductor contacts, and the electrostatics of such devices. Theoretical background for the characterization and analysis of the heterojunction is introduced. Various crystalline structures and their importance, as well as the effects of the crystalline structures on the overall performance of the device are discussed. Also the effects of altering experimental parameters on the performance of the junction are analyzed. Similarly the band structure of the heterojunction and importance of band bending and Fermi level alignment are examined.

Chapter 3 focuses on the chemical bath deposition fundamentals. There are numerous phenomena taking place during the chemical bath deposition process. Metal hydrolysis, solubility of reagents, and the extraction of the sulfur from the chemical constituents are all pivotal steps in the chemical bath deposition process. Deposition kinetics, film growth mechanisms, and some of the most common characterization techniques are all briefly introduced.

Chapter 4 focuses on the growth and characterization of the narrow bandgap chalcogenide thin film, lead sulfide (PbS). Deposition parameters, seeding, and film proliferation are all discussed. Growth of PbS is a complex process and requires in-depth analysis of the kinetics and mechanisms. Additionally, the analysis of the PbS is discussed. Results of the film growth parameters, and the film characteristics are analyzed in great detail.

The *n*-type semiconductor, CdS, is discussed in detail in Chapter 5. CdS is a widely studied semiconductor. The novel chemical bath deposition method is discussed. This method produces high quality nanocrystalline CdS. Effects of temperature variation in CBD of CdS effects the opto-electrical properties of the film. Electrical, optical, and photo-responsive properties are discussed in detail. Growth mechanisms of the films are also analyzed.

Chapter 6 focuses on the transparent conducting oxide (TCO), TiO<sub>2</sub>, developed for high transmittance in the infrared spectrum. The titanium oxide is transparent across a large portion of the infrared and visible regions. The electrical and optical properties of the TCO are discussed in detail. It has been shown that iridium is an efficient dopant that may be used in such applications as the doping of the titanium oxide. Films exhibit low reflectance, and low absorption in the infrared and visible regions. The films become highly absorptive near the UV region.

Work on putting all of the above discussed components into one functional device is discussed in Chapter 7. First a heterojunction between the CdS and PbS is shown. Also, the TCO is introduced to the device in order to allow for carrier collection with minimal losses. A gold

electrode is used on the PbS side, and the contacts between TCO, Au, and the semiconductors are discussed. Efficiencies of the device at various doping concentrations, TCO thicknesses, profile doping, and interface barrier heights are assessed.

The final chapter summarizes the findings of the dissertation and discusses potential future work. Some of the suggested improvements discuss possible routes to pursue to improve the efficiency of the device. Additional suggestions are made into the applications of the device.

## Chapter 2. Heterojunctions

A junction of two dissimilar semiconductors creates a heterojunction. Typically, one semiconductor is doped with donors, whereas the other one is doped with acceptors. This mismatch creates a non-equilibrium condition and properties of interest for such devices. In semiconductor devices, the difference in bandgaps provides an additional degree of freedom for phenomena of particular interest. Many of the successful devices utilize heterojunctions of doped semiconductors with well-designed bandgaps, Fermi levels, and non-equilibrium conditions.

### 2.1 Anisotype heterojunction

When the two heterojunctions possess same type of conductivity, the heterojunction is called isotype. On the other hand when the conductivity types differ, such a heterojunction is called anisotype. Anisotype heterojunctions possess qualities much more interesting than the counterparts, and are much more useful. Devices developed during the course of this work were anisotype and hence such heterojunctions will be briefly discussed.

The concept of a heterojunction was proposed by Shockley for use as a bi-polar transistor [47]. The same year, however, A. Gubanov published a theoretical paper on the various applications of heterojunctions [49]. Kroemer and numerous others followed with the discussion of several applications for heterojunctions [50]. Discussion of these early pioneers drove the revolution which birthed modern day development and research in the field of semiconductors and heterojunctions.

Only an anisotype heterojunction is considered, since the focus of this research was specifically this type of a device. Figures 2.1 (a) and (b) show a sketch of two semiconductors of opposite types separated from each other. The two semiconductors are assumed to have different bandgaps,  $E_g$ , work functions  $\phi$ , electron affinities  $\chi$ , and permittivities  $\epsilon_s$ . Electron affinity and work function by definition is the amount of energy required to remove an electron from the conduction band and Fermi energy to a vacuum level, respectively. But more precisely these values are indicative of the locations of the conduction energy band and the Fermi level. In Figure 2.1 the difference in energy of the conduction and valence band edges is shown as  $\Delta E_C$  and  $\Delta E_V$  respectively. Electron affinity, measured in eV is hence the elementary charge multiplied by the electron affinity of the material, i.e.  $\Delta E_C = q\chi$ . Electron affinities for various materials have been deduced computationally as well as experimentally. With this foundation in place, Anderson's model is valid.

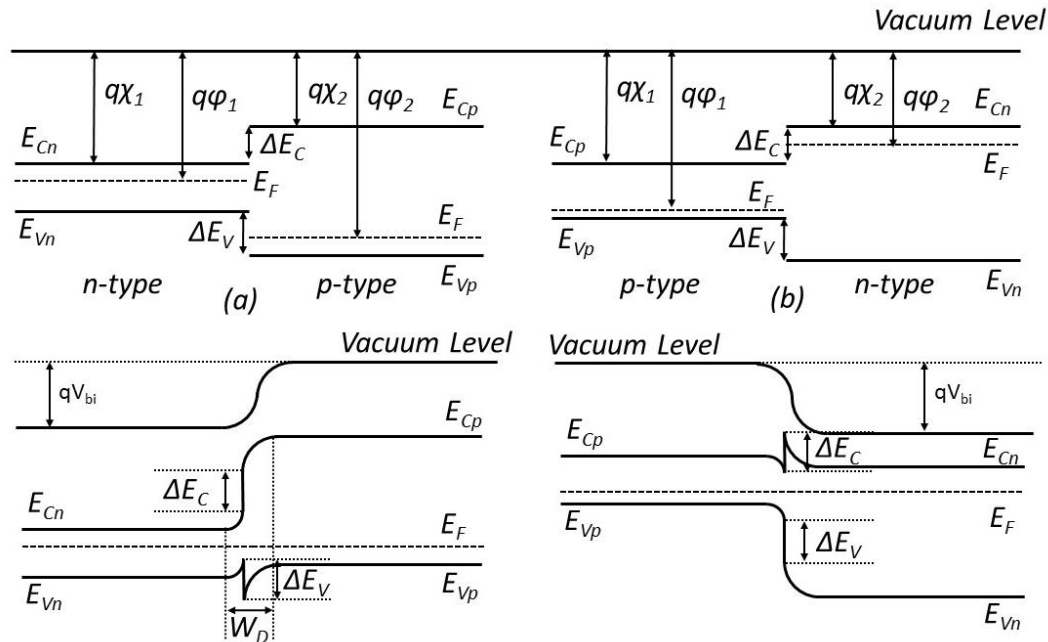


Figure 2.1 Energy band diagram for an anisotype heterojunctions. Case (a) the n type semiconductor is the smaller bandgap, and case (b) the smaller bandgap is the p type semiconductor.

When semiconductors are brought close to one another, the Fermi levels align creating a heterojunction and energy level band bending takes place as shown in Figure 2.1. Since the Fermi level must coincide on both sides and must be continuous and parallel, the discontinuity of band edges will be bridged by the bending of the energy levels. Fermi levels can be controlled by the doping of the semiconductors, as will be discussed later. Hence from the graph it is apparent that band bending can be controlled by the doping of both the  $p$ - and the  $n$ - sides of the device. Additionally, mismatch between the energy levels of the opposite semiconductors will create a built-in potential resulting in the electric field in the middle of the heterojunction. The total built in potential may be simplified to be equal to the difference of the work functions of the two semiconductors, i.e.  $V_{bi} = |\phi_1 - \phi_2|$ . Several other electrostatic coefficients result from the bringing of the two semiconductors close to one another: depletion width, electric field, and depletion layer capacitance.

## 2.2 Depletion layer

Heterojunctions are commonly referred to as p-n junctions. This term comes from the fact that two semiconductors are present in the heterojunction, one is doped with donors,  $n$ -type semiconductor, and one is doped with acceptors,  $p$ -type semiconductor. The theory of such junctions is the foundation for semiconductor devices.

Placing the two mismatched semiconductors together will create certain phenomena which determine the overall performance of the device.

### 2.2.1 Built-in potential and the depletion layer width

The energy band model of an idealized heterojunction without interface traps was proposed by Anderson [48], although much of his work was based on the derivations of Shockley. When a layer with a heavy concentration of acceptors is placed against another layer with a heavy concentration of donors, a junction is formed between these two layers. The condition of zero net electron and hole currents requires that the Fermi level must be constant throughout the sample. This applies only to the non-degenerate case. As previously mentioned, in the case of a degenerate semiconductor, the Fermi level is above one of the energy bands, hence a careful computation must be done to find the location of the Fermi energy level.

Given that the semiconductors are far removed from one another, as shown in Figure 2.2 (a), it is safe to assume that the semiconductors will maintain characteristics independent of the external conditions. Under equilibrium conditions the Fermi level is constant and independent of location. If the semiconductors are brought together closer, as shown in Figure 2.2 (b) the Fermi levels of the materials align. This leads to the connecting of the valence and conduction bands, which are bound to bend in order to reach the new equilibrium, Figure 2.2 (c). Although, the exact band bending needs meticulous calculation near the heterojunction, it is reasonable to assume that the variations are monotonic; however, this is not always the case, especially in heavily doped semiconductors.

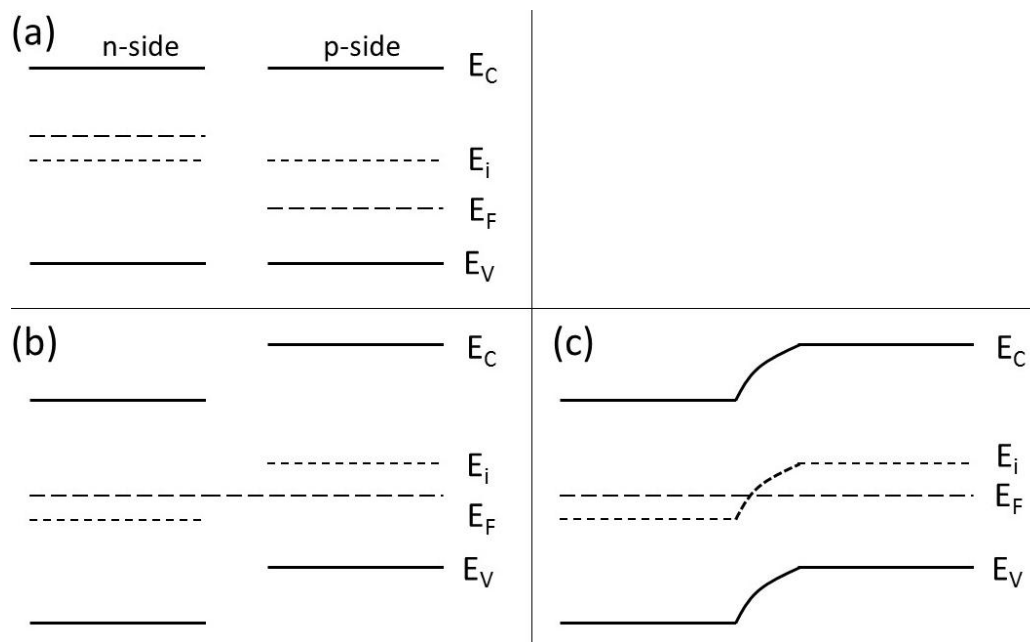


Figure 2.2 Construction of the band diagram of the heterojunction.

The locations of the energy bands in semiconductors can be deduced from band structures of the semiconductors. The location of the energy levels is often represented as the electron affinity multiplied by the basic charge, as previously discussed.

From the above discussion several electrostatic variables can be deduced. From the band bending taking place in the heterojunction, certain potential versus distance  $x$  dependencies will arrive.  $V$  versus  $x$  must have the same functional form as the band bending. In general,  $V$  is set equal to zero on one side and  $V$  is constant on the opposite side. The overall difference between the potentials from the  $n$ - to the  $p$ - sides is known as the built in potential,  $V_{bi}$ .

Built in voltage, sometimes referred to as the voltage drop across the junction, is important enough to merit further discussion. Given that the electric field is equal to the voltage over distance:

$$\mathcal{E} = -\frac{dV}{dx} \quad (2.1)$$

and assuming that the voltage drop takes place only in the depletion layer, the electric field can be integrated over the width of the depletion width to be

$$V_{bi} = -\int_{x_p}^{x_n} \mathcal{E} dx \quad (2.2)$$

Using Einstein's relationship and integrating the equation for the built in voltage in terms of doping concentrations, the following relationship is obtained

$$V_{bi} = \frac{kT}{q} \ln \left[ \frac{N_A N_D}{n_i^2} \right] \quad (2.3)$$

From the equation it should be noted that the doping concentrations will have a profound effect on the built in voltage which in turn will affect the strength of the electric field in the depletion layer. The electric field is the driving force that sweeps away the carriers in the depletion layer, and hence is an important factor in ensuring efficiency of the device.

Mechanism for the charge in the depletion layer should also be briefly discussed. For separated semiconductors, charge neutrality is maintained. As the two semiconductors are moved closer to one another, naturally since a disproportionate concentration of positively and negatively charged carriers exist, the carriers begin to diffuse from one side to another. After the diffusion is complete in the vicinity of the junction, an unbalanced dopant site and a significant non-zero charge exists. This region is known as the space charge region, or the depletion region. Depending on the built in potential of the junction, the electric field within the depletion region will swipe away all carriers to be collected by the electrodes.

The width of the depletion layer will play a crucial role in determining the number of carriers that will be swept away in the region. The width of this depletion layer can be derived from the one dimensional Poisson equation:

$$-\frac{d^2V}{dx^2} = \frac{d\mathcal{E}}{dx} = -\frac{\rho(x)}{\epsilon_s} \quad (2.4)$$

where  $\epsilon_s$  is the permittivity of the semiconductor, and  $\rho(x)$  is the space charge density as a function of length  $x$ . In order to solve the differential equation for  $\mathcal{E}$  and to integrate for  $V$  versus  $x$ , it is necessary to know the carrier concentrations in the space charge region, which unfortunately are not specified prior to solving the Poisson equation. Rather the carrier concentrations are functions of the potential, as is shown in Figure 2.2 (a). However, an approximation can be used assuming that the carrier concentrations are uniform across the semiconductor, and that the space charge density is a function of dopants, acceptors, and intrinsic hole and electron concentrations, then space charge density can be approximated as:

$$\rho(x) = q(N_D - N_A + p - n) \quad (2.5)$$

The resultant Poisson equation for the depletion layer becomes

$$-\frac{d^2V}{dx^2} = \frac{d\mathcal{E}}{dx} = -\frac{q(N_D - N_A + p - n)}{\epsilon_s} \quad (2.6)$$

utilizing the assumption of complete ionization inside the depletion region,  $n(x) \approx p(x) \approx 0$ . The electron and hole concentrations at that region are respectively given by

$$\frac{d^2V}{dx^2} \approx \frac{qN_A}{\epsilon_s} \quad (2.7)$$

and

$$-\frac{d^2V}{dx^2} \approx \frac{qN_D}{\epsilon_s} \quad (2.8)$$

Integrating the Poisson equation over the length of the depletion layer thus gives the strength of the electric field inside the depletion layer as

$$|\mathcal{E}| = \sqrt{\frac{2qNV_{bi}}{\epsilon_s}} \quad (2.9)$$

And the width of the depletion layer becomes

$$W_D = \sqrt{\frac{2\epsilon_s}{qN} \left[ V_{bi} - \frac{2kT}{q} \right]} \quad (2.10)$$

Hence the width and the strength of the electric field inside the depletion layer is a direct function of the doping concentrations, as is expected from the band bending diagram, Figure 2.2 (c). Increasing the doping concentrations pushes the Fermi energy levels closer to the band edges, hence increasing the built in voltage, which is directly related to the strength of the electric field inside of the depletion layer.

The thicknesses of conventional bulk semiconductors are on the order of hundreds of microns, whereas the typical depletion thicknesses are only on the order of ~1-2 microns. Hence in the classical 1<sup>st</sup> generation bulk semiconductor devices the width of the depletion layer played a crucial role in the overall performance of the device. 2<sup>nd</sup> generation semiconducting devices are thin film devices composed of advanced materials of ~1  $\mu\text{m}$  in thickness. The width of the depletion region does not play a crucial role in the performance of 2<sup>nd</sup> generation opto-electric devices. The strength of the built in voltage is nevertheless important and needs to be considered in the design of such devices.

### 2.2.2 Depletion layer capacitance

Under reverse bias conditions a heterojunction becomes functionally equivalent to a capacitor. The main difference between a standard capacitor and a reverse biased heterojunction is the fact that in the diode capacitance decreases logarithmically with an increase in the reverse potential.

This behavior is explained by the fact that under the conditions of alternating current in the positive portion of the cycle, the width of the depletion layer decreases, hence resulting in the decrease of charge on both sides of the depletion region. In the negative portion of the alternating current cycle the depletion width increases, increasing overall charge inside the depletion region. Hence alternating current can be viewed as the increase and decrease of the depletion width and space charge around steady state conditions. In the parallel plate capacitor the capacitance is given by the dielectric permittivity of the material between the plates, times the area of the plates divided by the distance between the plates

$$C = \frac{\epsilon_s \epsilon_0 A}{W_D} \quad (2.11)$$

As can be seen from the above equation, larger oscillations in the depletion layer width caused by higher voltages will inevitably lead to decrease in overall device capacitance.

Knowledge of the capacitance versus potential data of the heterojunction can be used in characterization of the device. Depletion layer capacitance per unit area is defined as  $C_D = dQ_D/dV = \epsilon_s/W_D$  where  $dQ_D$  is the incremental charge inside the depletion layer. Applying the previous discussion and integrating over the length of the depletion layer gives the capacitance per unit area as

$$C_D = \frac{\epsilon_s}{W_D} = \sqrt{\frac{q\epsilon_s N}{2}} \left[ V_{bi} - V - \frac{2kT}{q} \right]^{-1/2} \quad (2.12)$$

where  $V$  is the forward and reverse bias. Rearranging the above equation gives

$$\frac{1}{C_D^2} = \frac{2}{q\epsilon_s N} \left[ V_{bi} - V - \frac{2kT}{q} \right] \quad (2.13)$$

$$\frac{d\left(\frac{1}{C_D^2}\right)}{dV} = -\frac{2}{q\epsilon_s N} \quad (2.14)$$

From Equations (2.13) and (2.14) it is apparent that by plotting  $1/C_D^2$  versus the applied potential a straight line should result for a portion of the results. Slope of this line will provide impurity concentration  $N$ , and the extrapolation of  $1/C_D^2$  will give  $V_{bi} - 2kt/q$ . The plot of  $1/C_D^2$  versus  $V$  is the Mott-Shottky plot and is used regularly for such applications. Figure 2.3 graphically shows a Mott-Schottky diagram and the results. Simple  $V$  and  $C$  measurements will provide important electrostatic information about the device and device performance.

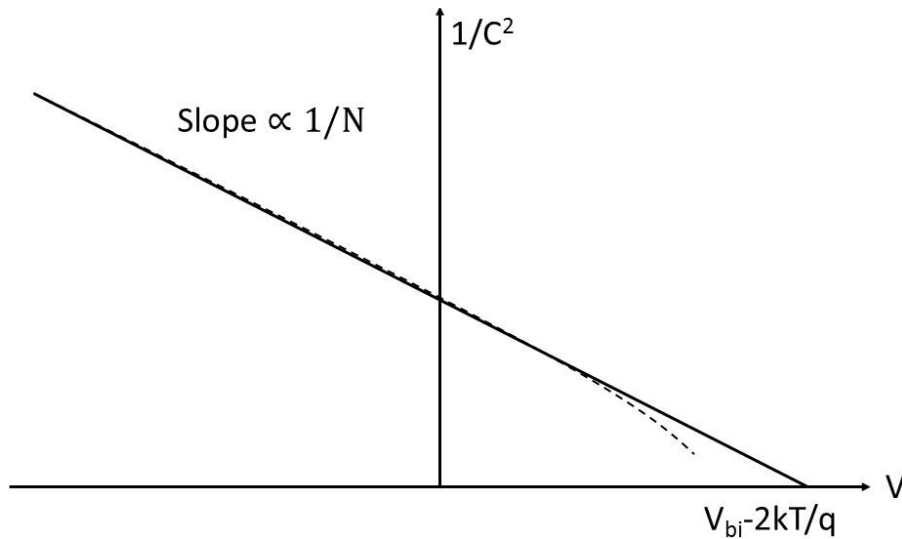


Figure 2.3 Typical Mott-Schottky plot.

It should also be mentioned briefly that capacitance-voltage data are not sensitive to the doping profile alterations taking place at distances below the Debye length [46]. This length gives an approximation to the limit of the potential change in response to doping profile. In other words if the doping profile changes abruptly, on the scale less than the Debye length, the abrupt change has no effect on the overall performance. Additionally, if the depletion width becomes smaller than the Debye length, the Poisson equation can no longer be used for the depletion width and built-in voltage computation, invalidating previous mathematical analysis of the heterojunction.

The depletion width must cover the entire width of the thin film device, but must not be smaller than the Debye length.

### 2.3 Lattice matching

Successful heterojunctions utilized a well-matched lattice prepared on top of one another. This approach limits interface traps, and allows for ease of carrier transport. The underlying physical requirement for the epitaxial heterojunction is matching of the lattice constants. Severe lattice mismatch causes numerous breaks and dislocations along the lateral directions of the heterojunction, which results in inhibited electrical properties and an increase in the number of trap states. Lattice constants for some of the commonly used semiconductors are shown in Figure 2.3 [42]. A successful heterojunction is composed of two materials of similar lattice constants but of different bandgaps.

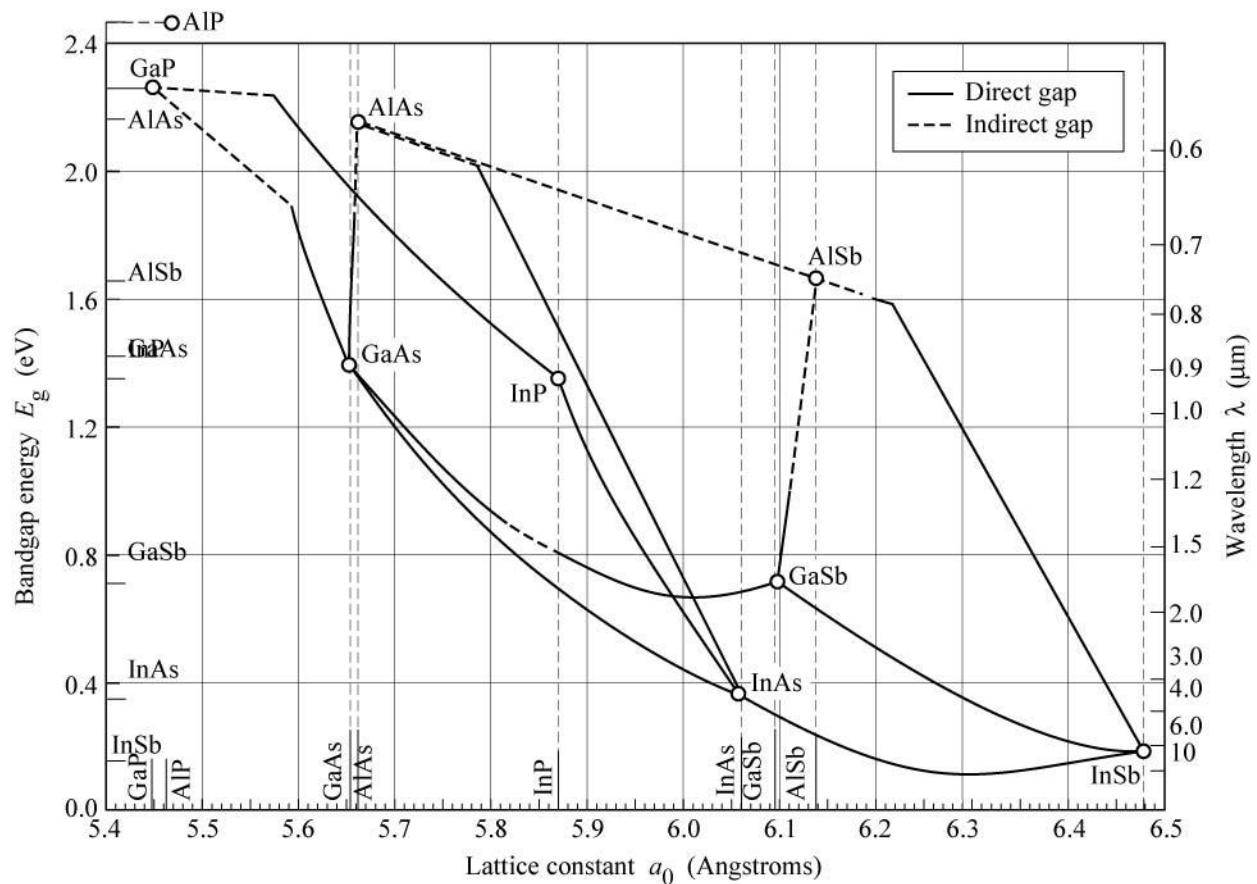


Figure 2.4 Energy gap (eV) and wavelength ( $\mu\text{m}$ ) versus lattice constants ( $\text{\AA}$ ) for commonly used semiconductors.

It has been shown, however, that thin epitaxial layers with small mismatches within the lattice constant nevertheless result in high quality heterojunctions. This is mainly due to the fact that thin films can only resist molding of their structures to an extent. In the case of thin films the

epitaxial structure will compress or extend to match its counterpart, and will acquire a certain amount of strain and stress within its structure. In a case where strain and stress of the epitaxial film occurred, a certain amount of energy will be stored in the crystalline structure. This energy is equivalent to the area under the strain-stress curve and can be computed using:

$$U_o = \int_0^\varepsilon \sigma d\varepsilon \quad (2.15)$$

where  $U_o$  is the strain energy density,  $\sigma$  is the stress, and  $d\varepsilon$  is the increment of strain. In the case where energy contained within the thin film exceeds the adhesion energy of the film, the thin films will peel off the substrate [43]. Hence the lattice mismatch must not be too significant in the crystals if a successful heterojunction is desired.

Estimates for the critical thickness of the strained films have been previously computed. In achieving such computations an assumption of epitaxial film growth is assumed. Initially the atoms fall in to the lattice of the substrate creating a small strain within the structure. As the deposited film becomes thicker the strain energy builds up. If the strain energy is too large to sustain the film, it will go back to the relaxed state, i.e. by going back to its original state or, more commonly, by peeling off the substrate.

The lattice mismatch for various semiconductors has been computed from experimental data, and derived to be [44]:

$$\Delta_{lattice} \equiv \frac{|a_e - a_s|}{a_e} \quad (2.16)$$

where  $a_e$  and  $a_s$  are the lattice constants of the epitaxial film and the substrate respectively. With the above computation the critical thickness can be approximated to be:

$$t_c \approx \frac{a_e}{2\Delta} \approx \frac{a_e^2}{2|a_e - a_s|} \quad (2.17)$$

Typical values for the critical thickness from a percentage of lattice mismatch are shown in Figure 2.4 [45]. From the graph below it can be seen that in order to achieve film thicknesses of ~500 nm, i.e. where tunneling effects become negligible, the lattice mismatch may not be larger than ~3%. This result significantly limits the combination of semiconductors that may be used in a successful heterojunction thin film device.

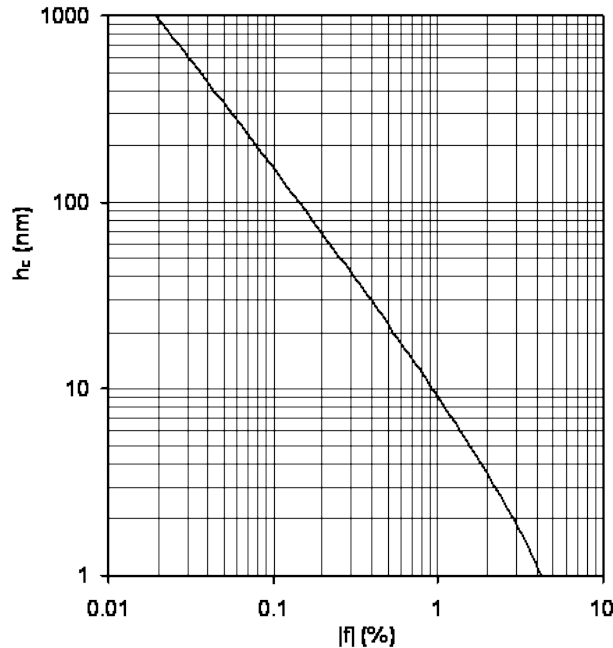


Figure 2.5 Critical thickness versus lattice mismatch.

A large number of semiconducting materials will also undergo a phase transition under certain growth conditions. For example, cadmium sulfide is a well-known semiconductor exhibiting a phase transition from a cubic to a hexagonal structure during heating. Hence manufacturing parameters and methods need to be considered during the growth of thin films for a successful heterojunction.

Further, a typical heterojunction will contain two electrodes for the carrier collection. In the photovoltaic device one electrode will be transparent, such as the transparent conducting oxide (TCO). In each case the electrode lattice constant has to closely match the lattice constants of the films of the device with which the contacts will be made.

#### 2.4 Current-voltage analysis

In order to conduct current-voltage analysis, four preliminary assumptions are made: (1) the Boltzmann statistic relationship is valid, i.e. non-degenerately doped semiconductor, (2) majority carrier concentrations dominate carrier densities in the semiconductor, (3) no additional generation-recombination is taking place inside the depletion region, and (4) depletion layer approximations are valid, i.e. depletion width is larger than the Debye length. Given that these four conditions are met, the heterojunction can be modeled as an ideal diode. Although this is a simplified analysis of the heterojunction, it nevertheless gives good preliminary characteristics of the device. Carrier activity inside a p-n junction is shown schematically in Figure 2.5.

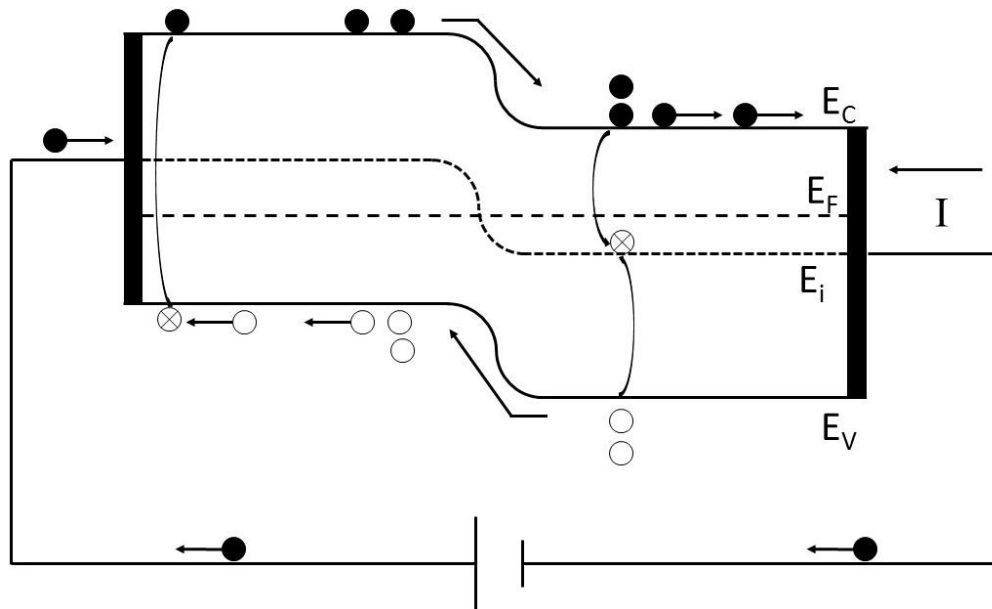


Figure 2.6 Energy band and circuitry diagram, showing overall view of carrier activity inside a  $p$ - $n$  junction structure.

With the understanding of the carrier activity inside of the heterojunction, the current voltage characteristics can be analyzed. With zero applied bias, the  $p$ - $n$  junction will come to an equilibrium state with the Fermi levels aligning in the way described in Figure 2.5. Carriers that can go into the depletion layer will be swept away by the present electric field inside the junction. The addition of a potential in the forward direction, i.e. negative to the  $n$ - side of the junction and positive to the  $p$ - side of the junction, yields a barrier hill that can now be lowered. Hence more electrons and holes can overcome the barrier hill, and more carriers can now travel to the opposite sides of the junction. This gives rise to the additional current resulting from the movement of the additional carriers from the  $n$ - side to the  $p$ - side and vice versa. Further, there is a linear relationship between the height of the barrier hill and the applied bias, but concentration of the carriers increases exponentially in the lower states, hence the number of carriers able to surmount the barrier grows exponentially with the applied voltage,  $V_A$ .

In the case of the reverse applied bias, i.e. negative contact is applied to the  $p$ - side and positive contact is applied to the  $n$ - side of the heterojunction, the barrier hill to be overcome by carriers is increased. Whereas under no applied bias, some carriers could overcome the potential barrier, in the reverse applied bias that number of carriers decreases. It has been shown that a reverse bias above  $\sim 3kT/q$  in magnitude will reduce the number of carriers able to overcome the potential hill to negligible levels. Carriers, however, may still wander into the depletion layer to be swept away to the electrodes at the opposite ends of the junction. This mechanism gives rise to the current flow from the  $n$ - side to the  $p$ - side, produced by the minority carriers, and hence is expected to be extremely low.

From the previous discussion, current on the  $n$ - and  $p$ - sides can be respectively found to be

$$I_n = qD_n \left. \frac{dn}{dx} \right|_{-W_D} \quad (2.18)$$

and

$$I_p = qD_p \left. \frac{dp}{dx} \right|_{-W_D} \quad (2.19)$$

The total current in the device is equal to the summation of the currents on the  $n$ - and the  $p$ -sides, i.e.  $I = I_n + I_p$ . Keeping this in mind, and making use of the Einstein relationship and integrating over the width of the depletion layer gives the current equal to

$$I = I_0 \left[ e^{\left(\frac{qV_A}{kT}\right)} - 1 \right] \quad (2.20)$$

where  $I_0$  is the reverse bias saturation current. Equation (2.20) is known as the Shockley equation, and is an ideal diode law [47]. This equation shows very nicely why the solid state device will allow for large current passage in the forward bias and very small current passage in the reverse bias. Forward biasing lowers the potential barrier hill and exponentially increases the number of carriers allowed to flow in the device, whereas reverse biasing increases the potential barrier, allowing only residual current across the depletion region.

Unfortunately there is no easy way to measure the reverse saturation bias current in Equation (2.20). This current has been studied and empirically deduced to be

$$I_0 \equiv qA \left[ \frac{D_N n_i^2}{L_N N_A} + \frac{D_P n_i^2}{L_P N_D} \right] \quad (2.21)$$

where  $L_N$  and  $L_P$  are the diffusion lengths of the electrons and holes respectively. As can be seen, there is no easy way to deduce some of the variables in the equation. The value of  $I_0$  can be measured experimentally, as shown on the current voltage graph in Figure 2.6. Several important observations need to be stressed regarding the saturation current. From Equation (2.21) it is apparent that saturation current can vary several orders of magnitude depending on the material properties such as the intrinsic carrier concentrations,  $n_i$ . The area of the heterojunction plays an important role in the saturation current as well, increasing the area will increase the saturation current proportionally. Addition of dopants will also change the reverse saturation current. In a photovoltaic device, the reverse saturation current is sometimes referred to as the leakage current. Excessive  $I_0$  will have a detrimental effect on the efficiency of the device.

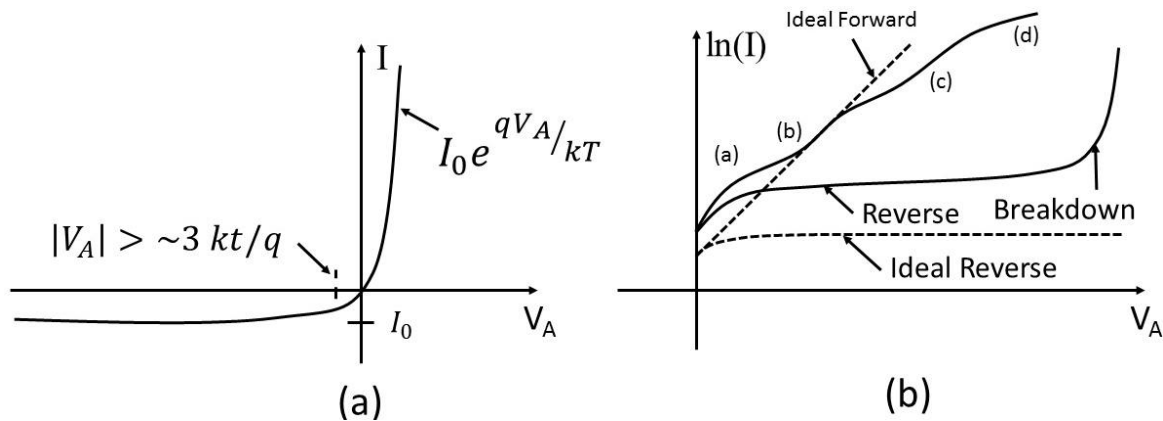


Figure 2.7 Diode current-voltage ( $I$ - $V$ ) characteristic on a (a) linear plot and (b) semi-log plot. In the semi-log plot sections represent: (a) generation-recombination current region, (b) diffusion-current region, (c) high injection region, and (d) series resistance effect.

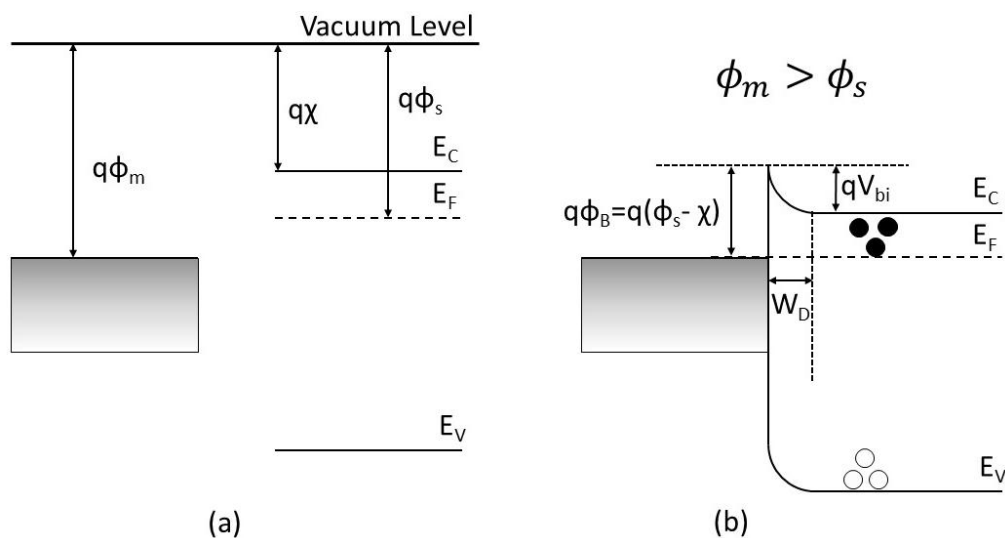
In a more realistic case, there is a point at which a breakdown of the heterojunction will take place, as shown in Figure 2.7(b). Although referred to as the break down, this is a completely reversible process. At this point the applied voltage is high enough to cause the diode to break down allowing for passage of high current in the opposite direction. This current should be limited, however, in order to avoid excessive heating of the device. Beyond the breakdown point the diode begins to act as a resistor rather than a diode, no longer possessing its intrinsic qualities. Additionally, in the real case of a forward sweep the current will not be a linear relationship to the applied voltage, shown in Figure 2.7(b). Since there are several factors effecting current in the forward sweep, the linear graph will have nonlinear regions caused by various factors. Region (a) is effected by the generation-recombination current, region (b) by diffusion current, region (c) is current due to high injection, and region (d) is current from the series resistance. Current behavior of the heterojunction can be controlled by careful selection of the material as well as thoughtful doping concentrations of the  $n$ - and  $p$ - portions of the heterojunction.

## 2.5 Semiconductor-metal contacts

Any carrier generated inside the heterojunction needs to be swiped away in the depletion layer and brought to the opposite side of the heterojunction contact to complete the circuit. Typically the contact is a metal. In the case of optoelectronic devices the contact may be a transparent conducting oxide (TCO), or another transparent contact such as the transparent conductive polymer PEDOT:PSS. Depending on the work function of the semiconductor and metal in relation to each other, such a marriage can either form a barrier, commonly referred to as a Schottky barrier, or possess negligible junction resistance referred to as the Ohmic contact allowing current flow in and out of the device.

When metal makes contact with a semiconductor a junction of sort is formed at the interface of the two materials. This barrier will have an effect on the electrical properties of the device. Additionally, in a more complex case, a rectifying barrier may form allowing for current to pass only in one direction through the device.

It is necessary to first analyze an ideal case condition for the metal-semiconductor contact. Under such conditions the lattice mismatch that may be taking place between the metal and the semiconductor as well as any other surface anomalies are ignored. Each metal will have the work function of itself. Unlike the semiconductor however, there is no energy bandgap in the metal. In such a case the conduction, valence, and Fermi levels all align at the location of the work function of the metal multiplied by the elementary charge, as shown in Figure 2.8. Given that an infinite gap exists between the metal and a semiconductor, no band bending, and no alignment of the Fermi levels will be taking place. Each component will maintain its equilibrium state, Figure 2.8 (a). If the two components are brought together, the Fermi level of the semiconductor will align with the Fermi level of the metal, as shown in Figure 2.8 (b). The Fermi level inside the semiconductor will be lowered proportionally in order to line up with the Fermi level of the metal. In the other case, if the work function of the semiconductor is less than that of the metal, the Fermi levels will align with the band bending taking place in the opposite direction. There is a potential difference between the work functions of the metal and the semiconductor,  $V_{contact} = \phi_m - \chi - \phi_s$ , and is referred to as the contact potential. As the two components are brought together, there is a built up of the negative charge at the surface of the metal contact. An equal positive charge is built at the semiconductor surface brought into contact with the metal. As the materials make contact the carriers may now begin to move from one element to the next as shown in Figure 2.8 (b). It is also apparent that the barrier height in the metal-semiconductor contact is simply the difference between the metal work function and the electron affinity of the semiconductor.



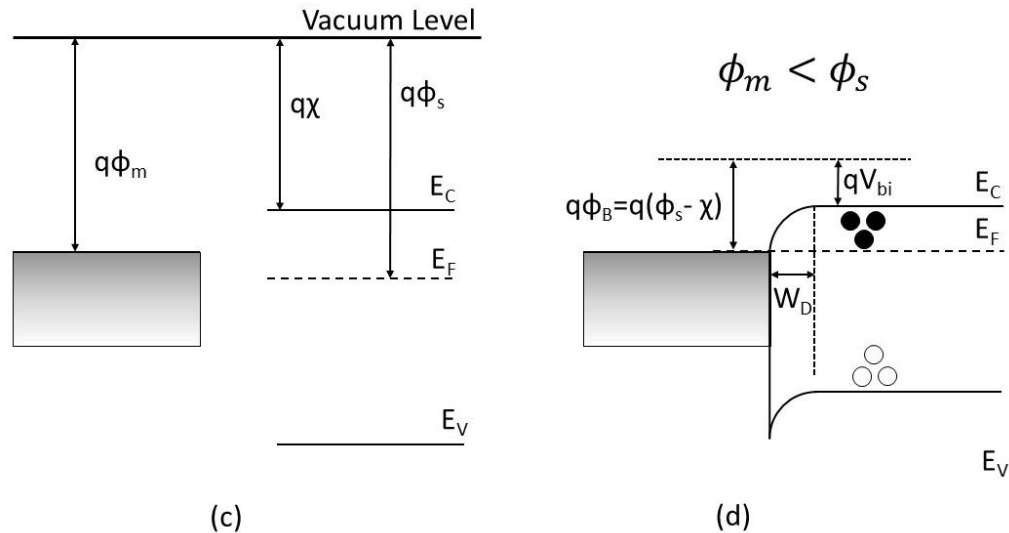


Figure 2.8 Metal-semiconductor contact energy diagrams. (a) and (b) represent the location of the Fermi energy above the work function of the material, thus upward bending of the bands. (c) and (d) show a Fermi level of the material below the work function of the metal and downward bending of the bands. Upward and downward bending causes barriers for the electrons and holes respectively.

Thus the barrier heights between an  $n$ - and  $p$ - type semiconductor and metal are

$$\varphi_{Bn} = \varphi_s - \chi \quad (2.22)$$

and

$$\varphi_{Bp} = \frac{E_g}{q} - (\varphi_s + \chi) \quad (2.23)$$

respectively. It should be apparent that depending on the type of bending that will take place the junction could form a barrier for either the electrons, as in the case of the metal work function greater than semiconductor's work function, or for holes as in the opposite case. In the first case a rectifying contact exists for the  $n$ - type semiconductor, whereas in the latter case a rectifying contact exists for the  $p$ - type semiconductor. These results are summarized in Table 2.1. Hence choosing an electrode with suitable work function is an important part of the device design.

Table 2.1 Electrical Nature of Metal Semiconductor Contacts

	Semiconductor Type	
	$n$ - type	$p$ - type
$\phi_m > \phi_s$	Rectifying	Ohmic

Electron affinities of numerous semiconductors as well as the work functions of numerous metals have been well studied and established. For metals the work functions range from  $\sim 2$  to  $\sim 6$  eV. However, it has been previously reported that the work functions are also extremely sensitive to surface contaminations [51]. Even water contamination from prolonged exposure to damp air changes the work functions of metals. Hence the work function of metals needs to be taken into account to allow for good contact with possible variability in the work function. Extensive studies of suitable metals to semiconductors have been previously carried out [52]. Figure 2.9 lists work functions for some of the commonly used metals.

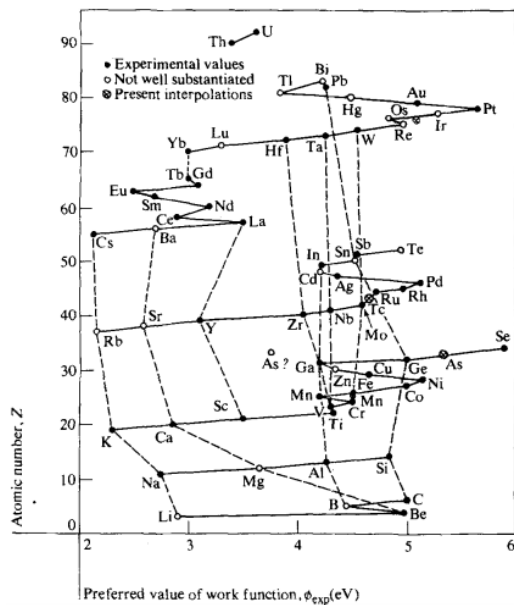


Figure 2.9 Metal work functions to the periodic table of elements. Solid lines correspond to rows in the table of the elements and dashed lines to columns [52].

### 2.5.1 Metal – semiconductor depletion layer

The depletion layer in a contact between a metal and a semiconductor is analogous to the one found between two semiconductors. The above discussion showed that a contact between a metal and a semiconductor forces alignment of the Fermi levels, and a band of the conduction and valence bands accordingly. Electrostatic constants for metal semiconductor junctions can be deduced using the Poisson relationship, similar to the one used for the analysis of the heterojunction.

Solving Poisson's equation for the metal contact with an  $n$ -type semiconductor, the width of the depletion layer is found to be

$$W_D = \sqrt{\frac{2\varepsilon_s(V_{bi}-V_A-kT/q)}{qN_D}} \quad (2.24)$$

and the maximum electric field strength is

$$\mathcal{E}_m = \mathcal{E}(x = 0) = \frac{2[V_{bi}-V_A-kT/q]}{W_D} \quad (2.25)$$

while the location of the conduction band is

$$E_C = qN_D - \frac{q^2N_D}{\varepsilon_s} \left[ x - \frac{x^2}{2} \right] \quad (2.26)$$

and capacitance per unit area is

$$C_D \equiv \frac{\varepsilon_s}{W_D} = \sqrt{\frac{q\varepsilon_sN_D}{2[V_{bi}-V_A-kT/q]}} \quad (2.27)$$

Equation (2.26) can be rewritten for  $1/C_D^2$  and a plot of capacitance versus voltage can be used to determine the doping profile of the metal semiconductor contact. Capacitance-voltage measurements may also be used to study the impurity gradient across the device [53]. If a small alternating current is superimposed on the direct current signal, there will be a frequency dependence on the capacitance. This is due to the ionization of impurities. All shallow donors above the Fermi level will be ionized. However, only the impurities deep in the junction above the Fermi level near the surface will be ionized, giving higher effective doping near the contact interface. In this case the deep impurities can respond to low frequencies, because  $dN_D/dV$  will not be present at high frequencies. Thus an analysis of capacitance versus frequency will show a doping profile between the contact. Doping frequencies will determine the width of the depletion layer, hence the overall position of the conduction energy band. These parameters become important in carrier collection at the electrodes.

### 2.5.2 Practical factors

Initially an ideal case of the metal semiconductor contact was considered. In an ideal case there is no intermixing of the components, no surface impurities, ideal contact between the metal and the semiconductor, and no surface charge on the interface. Unfortunately, every material is prone to oxidation, charge build-up, adsorption of impurities and other non-idealities which are inevitably introduced to the system. Dangling bonds of various metals will inevitably oxidize creating thin oxide layers ( $\sim 5\text{\AA} - 25\text{\AA}$ ) in atmosphere. Lead oxides are known to form on the surfaces of lead salts, cadmium is also known to form tin oxide layers in the atmosphere. Virtually all known materials will exhibit some non-ideality when exposed to the atmosphere. In the cases where atmospheric reactions are extreme, the non-idealities will result in a non-

functioning contact, hence inhibiting overall device operability. A great deal of attention needs to be paid to the non-idealities taking place on both the metal and semiconductor surfaces. With minor oxidations ( $< \sim 50\text{\AA}$ ), and small unwanted impurity diffusion into the semiconductor, only the barrier height is affected. Changes in the electrical properties of the device from minor non-idealities will not significantly alter electrical characteristics of the device.

Previous results have suggested that the impurities introduced from the atmosphere tend to “pin” the equilibrium Fermi level in the forbidden gap [54]. Assuming that the effects of the non-idealities are minor, the pinning effect causes only variations within the barrier height, and even then the changes are minor. Since neither the exact location of the Fermi level in the metal nor the semiconductor can be predicted exactly (due to atmospheric non-idealities) it is necessary to determine the locations of the Fermi levels and barrier height post deposition when supposedly no additional non-idealities will be introduced. This can be achieved experimentally using the capacitance-voltage measurements described above.

Although it is expected that a metal-semiconductor contact where the work function of metal is less than the work function of the semiconductor (for  $n$ - type semiconductor) and the work function of metal is greater than the work function of semiconductor (for  $p$ - type semiconductor) will produce Ohmic contact allowing for current to flow in both directions, from previous discussion it should be apparent that this will not always be the case due to non-ideal conditions of the materials. In some cases the contacts could become rectifying effecting the efficiency of the device.

In an ideal case of the metal-semiconductor contact the barrier height is determined simply from the characteristics of the metal and the semiconductor at the interface. Hence in a typical Schottky barrier for a given semiconductor there exists a limited number of suitable metals that may be used. As previously discussed by introducing a thin layer ( $\sim 10\text{ nm}$ ) of doped surface layer with a controllable number of dopants (e.g. by ion implantation) the effective barrier height can be altered, and an effective barrier height can be varied [55].

In practice it is possible to achieve Ohmic contacts by heavily doping the surface of the semiconductor. In the case of an  $n$ - type semiconductor, donor dopants will push the Fermi level close to the conduction band. In such a case the heavy doping will be less prone to changes from the impurity doping that may be introduced from the atmosphere. In  $p$ - type semiconductors just the opposite would be true, with heavy acceptor doping on the surface prior to metal deposition. Effects of doping are shown schematically in Figure 2.10. In the case of heavy surface doping an additional thin layer of  $n^+$  or even  $n^{++}$  is achieved. This forces the Fermi level of the surface close to the conduction band. When the Fermi levels align during the contact of the metal and the semiconductor, the band bending is “severe” and the depletion width is small. As previously discussed for the case of widths smaller than  $\sim 100\text{ \AA}$ , the effect of tunneling becomes significant.

Thus rather than overcoming the potential barrier, the carriers will tunnel through the existing barrier.

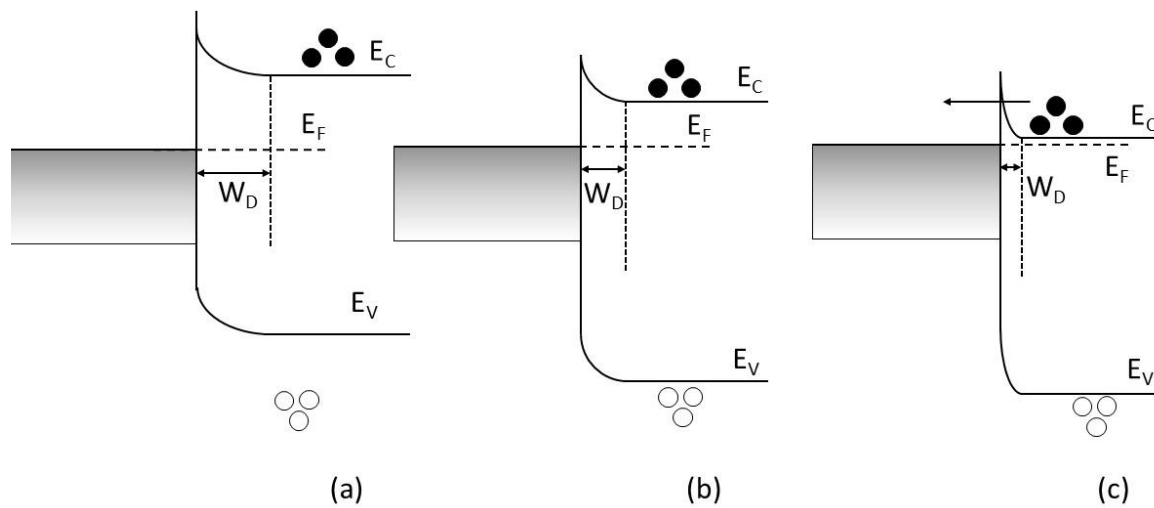


Figure 2.10. Band diagram of the (a) low, (b) moderate, and (c) heavy surface doping.

Doping the surface of the semiconductor is particularly useful if selecting a metal with the most desirable properties (e.g. lowest electrical resistivity, cost, etc.). This approach can be used to essentially make any metal contact with the semiconductor. However, the approach may require specialized machinery for precise doping of the semiconductor.

Stability of the metal-semiconductor contact is another additional factor that needs to be addressed. Numerous deposition methods require post growth annealing and treatment. In such cases the contact may break down. Hence either the manufacturing methods, or the metal oxide contacts need to be selected in such a manner to ensure stable Ohmic contact for the optoelectronic device.

### 2.5.3 Barrier height measurements

Several methods exist to measure the barrier height in a metal-semiconductor junction. Capitalizing on the bandgap of the semiconductor the photoelectric measurement is one of the most prevalent measurements [56]. The basic schematic for the photoelectric measurement is shown in Figure 2.11. Two carrier excitation processes can contribute to the overall photocurrent. First, is the excitation of the carrier over the barrier on the metal side and second, the band to band excitation, Figure 2.11 (b). In measuring the barrier height only the wavelength required to excite the carrier over the barrier is of interest. Additionally, the metal contact should be thin enough to allow light penetration from the back illumination to the interface of the metal-semiconductor surface. The requirement for the front illumination is only that the energy of the photon is less than the bandgap of the semiconductor, in order for the light photons to reach the interface layer.

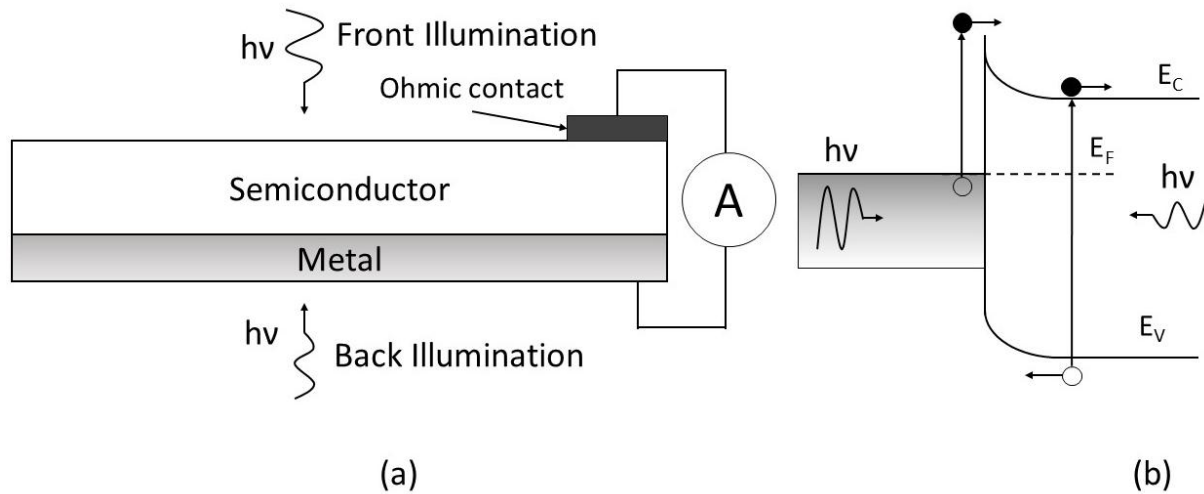


Figure 2.11 Schematic and band diagram of the photoelectric measurement of the Schottky barrier.

Photo-response, photocurrent per absorbed photons,  $R$ , can be determined as a function of the photon energy using Fowler theory [57]. Fowler's equation is

$$R \propto \frac{T^2}{\sqrt{E_s - hv}} \left[ \frac{x^2}{2} + \frac{\pi^2}{6} - \left( e^{-x} - \frac{e^{-2x}}{4} + \frac{e^{-3x}}{9} - \dots \right) \right] \quad (2.28)$$

where  $E_s$  is the sum of  $hv = q\Phi_B$  and the Fermi energy measured from the bottom of the metal conduction band.  $x \equiv h(\nu - \nu_0)/kT$ . With the  $E_s \gg hv$  and  $x > 3$  Fowler's equation simplifies to

$$R \propto (hv - hv_0)^2 \quad (2.29)$$

From the above equation it can be seen that a plot of the photon energy versus the photoresponse will result in a straight line. Extrapolation of the value on the energy axis will give the barrier height. This approach has been shown to provide accurate data on the barrier height even at various temperatures, and can be used to study the temperature dependence of the barrier height variations [58]. Extensive research on the barrier height for various metal-semiconductor contacts has been studied. Results for the CdS are presented in Table 2.2

Table 2.2 Measured Schottky Barrier Heights (V) at 300 K for CdS [59]

	$E_g$	Ag	Au	Cu	Ni	Os	Pb	Pd	Pt	Ti
CdS	2.42	0.56	0.78	0.5	0.45	0.53	0.59	0.62	1.1	0.84

Numerous factors need to be accounted for when designing an opto-electrical device. The inextricable dependence of all parameters on the performance of the device requires a methodological thought process when designing an efficient device.

### Chapter 3. Chemical bath deposition (CBD) of thin films

This chapter of the dissertation introduces one of the most well studied and cost efficient methods of growing thin films, the Chemical Bath Deposition (CBD). This process is sometime sknown as Chemical Solution Deposition (CSD). The method does not require expensive machinery or the use of the clean room, and has been utilized in a variety of semiconductors with favorable opto-electrical properties and nanocrystalline structures.

#### 3.1 Fundamentals

The purpose of this introductory section is to give a qualitative and a semi-quantitative background for the understating of the CBD process. The idea is to give enough theoretical background for the understanding of the future work.

Typically CBD is referred to as the growth of thin nanocrystalline films on a solid substrate from a chemical reaction occurring inside a solution. In general the solution is aqueous. In the chemical bath deposition the skill and the art of film growth is to control the reaction rate in such a way to avoid agglomeration but rather to have the film coalesce unto the substrate or the already formed film. The rate control of the growth can be achieved by controlling the saturation rate of one of the ions of the final film. For example, in lead (II) sulfide (PbS), concentration of the sulfur ion only needs to be controlled in order to control the entire precipitation rate of the PbS. Saturation rates are controlled by the acidity or alkalinity of the deposition solution. In general alkaline solution is preferred in order to release sulfide ions from the complexes.

In order for the CBD method to work the material needs to meet one of the following criteria.

1. The material needs to form from simple precipitation. Hence this method is limited to materials formed by ionic reactions.
2. The compound needs to be insoluble in the used solution. Growth of the thin films is achievable only in the cases where the formed films will not dissolve in the deposition solution.
3. Ion generation should be slow and controllable. In the case the solution is oversaturated with ions, rapid precipitation without film formation will take place.
4. The formed compound should be stable in the deposition solution.

In general CBD works by breaking apart the constituents of the chemical bath into their basic ions and then controlling the recombination of the ions in the bath to achieve high quality films. Dissolution of the constituents typically is achieved through the control of the acidity and basicity,  $pH$ , of the solution.  $pH$  is the negative logarithm of the hydrogen ion concentration inside the solution

$$pH = -\log[H^+] \quad (3.1)$$

In chemistry it is typical to denote concentration of an element in square brackets. In the case of the acidity of the solution the square brackets signify the concentration of the hydrogen,  $H^+$ , ion.

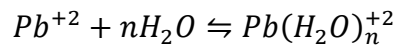
Another constant of interest in the CBD process is the equilibrium constant,  $K_{eq}$ . The equilibrium constant is given by

$$K_{eq} = \frac{[E]^e[F]^f \dots [H]^h}{[A]^a[B]^b \dots [C]^c} \quad (3.2)$$

where the numerator denotes the concentrations of the products, and the denominator denotes the concentrations of the reagents. Given that the reagent concentrations (concentrations of the initial constituents) are known, hence by controlling the  $pH$  of the solution the concentrations of the products can be controlled in such a way to keep the equilibrium constant stable. There is a proportional relationship between the growth rate and the ratio of the experimental equilibrium constant to the material's  $K_{eq}$  [60].

### 3.1.1 Metal hydrolysis

Most positively charged ions, which is typical of many metals, will hydrate, i.e. attract a water molecule, in a chemical bath solution. In the case of the lead, which has a positive charge of two,  $Pb^{+2}$ , there is a strong tendency to attract molecules of water. Chemically this will result in the following reaction



This phenomenon is caused by the tendency of water to become polarized, hence it becomes attracted to the positively charged cations. The greater the positive charge of the cation, the greater is the attraction between the water and the positively charged ions. Hence, the large metal atoms, with high numbers of valence positive charges, in general are less solvated than the less valent ones. Additionally, the positively charged cation will attract the electrons from the O – H bonds of water. As a result the O – H bond will weaken and under strong cation interactions will break, resulting in a covalent bond between the metal and oxygen, hydro-oxidizing or oxidizing the metal. This is shown schematically in Figure 3.1.

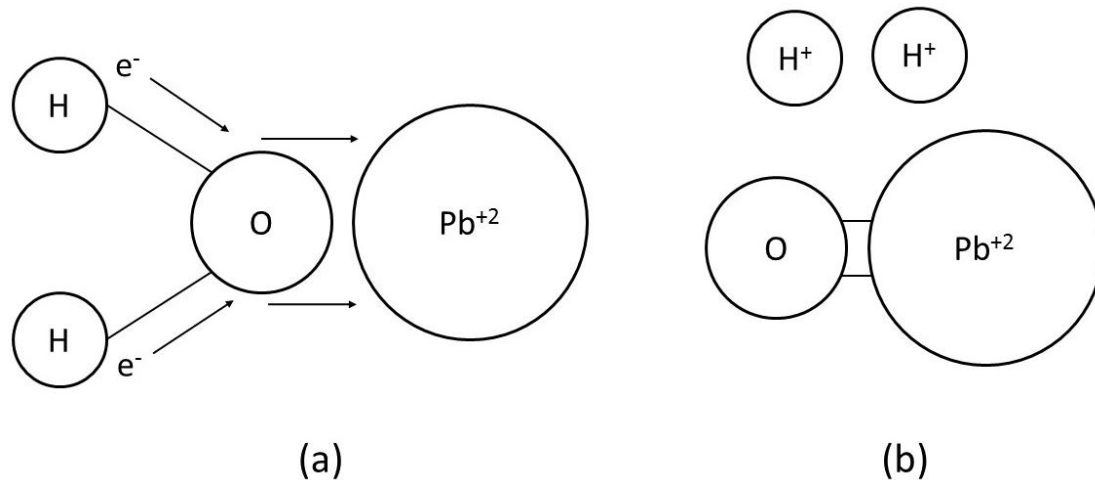


Figure 3.1 Diagrams showing (a) removal of the electron from the O – H bond, hence weakening and breaking the bond resulting in (b) oxidation of the metal.

Oxidized and hydro-oxidized metals become largely insoluble and remain in this state without further reaction. This phenomenon is a significant barrier in achieving controlled precipitation of the materials in the chemical bath.  $pH$  of the solution needs to be significantly high in order to break these bonds. Hence, it is important to avoid the occurrence through mitigation.

### 3.1.2 Solubility product

The solubility product,  $K_{sp}$ , is the pivotal portion of the chemical bath deposition method. Mathematically, the solubility product is the product of the dissolved ions in the solution that are to be precipitated. In general the stoichiometric equilibrium equation and the solubility product can be expressed as



For example for the case of lead (II) sulfide ( $PbS$ ), the stoichiometric equation and the solubility product are equal to



The subscript on the  $PbS$  denotes the solid phase of the material. Constituents from which lead and sulfur are obtained are dissolved in water, to give small amounts of the respective ions. Given that the multiplication of the concentrations of the ions becomes greater than the solubility product of the material, precipitation takes places.

Solubility products of numerous materials have been measured experimentally over the years. Table 3.1 shows the solubility product values for *PbS* and *CdS* [61].

*Table 3.1. Solubility Product for PbS and CdS at 300 K*

Material	PbS	CdS
$K_{sp}$ (mol/L)	$10^{-28}$	$10^{-28}$

It should be also noted that there is some variation in the values of the solubility product for sulfides. This is due to the extraction of sulfur from the secondary dissociation of the  $H_2S$  gas. Hydrogen sulfide is also highly volatile, requiring an additional capturing mechanism. Further, due to the hydrolysis effect some of the metals such as lead oxidize, i.e. bind to the oxygen atoms, rather than precipitating with sulfur.

### 3.1.3 Complexing agents

In order to avoid the oxidation of the metals, many of chemical bath depositions are done in alkaline solutions. Often a complexing agent is added to the solution to act as the electron donor. Additionally, typically such donors will reduce the concentration of free metal ions, which helps with control of the precipitation of the desired product.

For example, addition of NaOH as a complexant to the solution  $CdSO_4$  will be dissolved into  $Na^+$  and  $OH^-$  ions. Similarly  $CdSO_4$  will dissolve into  $Cd^{2+}$  and  $SO_4^{2-}$  ions. The solubility product of cadmium hydroxide allows for precipitation of  $Cd(OH)_2$ . Assuming the *pH* of the solution is kept relatively high in the acidic regime, i.e. above ~11, Equation (3.3) can then be used to compute the required cadmium concentration to be  $\sim 2 \times 10^{-8}$  M.

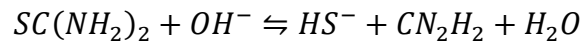
Using ammonia,  $NH_4^+$ , as the dissolving agent and from the equilibrium constant of  $Cd(OH)_2$ , Equation (3.2) may be used to compute the concentration of reagent  $CdSO_4$  required to saturate the solution with  $Cd^{2+}$  ions for successful precipitation. Oversaturation of the solution with one of the ions may shift the reaction towards one side. For example oversaturating the solution with NaOH will produce an excess of  $OH^-$  ions, which may eventually lead to excessive saturation of the  $Cd^{2+}$  ions. The extra cadmium ions will then be caught in the forming lattice as interstitial defects in the film, altering the electrical properties of the film.

It has also been observed that temperature will have a profound effect on the solubility constant of materials [63]. In principle this is analogous to Newton's Third Law of equal and opposite reaction. In chemistry this principle is referred to as the Le Chatelier principle. It states that if there is a change in the reaction parameter, the reaction will proceed in the direction that opposes the change. Addition of heat causes the reaction to shift in the direction of heat absorbance, which results in the dissociation of the complexes into ions.

Hydrolysis, solubility constants and products, as well as equilibrium constants and chemical reaction parameters need all be considered during the chemical bath deposition technique. However, understanding of the chemical bath deposition principles allows for a well-controlled deposition process.

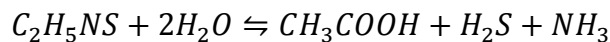
### 3.1.4 Sulphide

The most commonly used sulphur precursor is thiourea ( $SC(NH_2)_2$ ). Thiourea is a stable compound in both ambient air as well as numerous chemical solutions. On the other hand with careful alkalinity control of the solution, thiourea is broken apart to release the sulfur cation. There are several possible decomposition routes for thiourea in the aqueous alkaline solution. One that has been used most commonly and is well elucidated is [64]



which generates hydrogen sulfide ions. The cyanamide complex,  $CN_2H_2$ , hydrolyzes further, however, it does not take part in the rest of the chemical film growth of chalcogenides, hence is ignored in further discussion. Since thiourea is a fairly stable ion, the decomposition of thiourea is driven to the right by the excess hydroxide ions. Hence a reasonably well controlled saturation of hydrogen sulfide in the solution can be achieved through a careful addition of the hydroxide ions.

Sulphide can also be extracted from the thioacetamide (TAA),  $C_2H_5NS$ . The advantage of TAA over thiourea is that it can be used in both alkaline and acidic solutions. An elucidated decomposition of TAA in acidic solution is as follows [65]



In the alkaline solution the only difference will be the formation of  $HS^-$  in lieu of  $H_2S$ .

Another potential source of sulfur is thiosulfate,  $S_2O_3$ , however, it has been disused for its unstable nature. There are some additional less favorable precursors for the sulfur ion as well.

In general the sulfur ion is extracted from the breaking of thiourea or the thioacetamide. It should also be stressed, however, that the breaking of both elements is a two-step process which adds additional lag time in the precipitation reaction.

### 3.2 Nucleation

Nucleation of the ions into crystals can be of different forms, and is only the initial step in crystal growth. There are two main nucleation processes and resulting film growth processes that occur from there.

### 3.2.1 Homogenous nucleation

From the solubility product equation, once the multiplication of the concentration of ions in the solution exceeds the solubility product, nucleation will take place. Homogeneous nucleation is caused by non-equilibrium conditions within the solution. When any sudden changes in concentrations, temperature, or other variables take place, certain non-idealities are introduced causing excessive collisions between ions. Once the ions begin to collide there is an agglomeration of these ions into clusters. Clusters continue to collide with ions in the solution and grow in size, or collide with other clusters to combine into super-clusters. At times these clusters dissolve in the solution before they become a stable crystal. The dissolution of these clusters is caused by the large surface areas, hence high surface energies, giving these clusters thermodynamic instability. There is a certain point when the cluster reaches a certain radius it has a 50:50 chance of becoming a stable crystal. This radius is called the critical radius.

### 3.2.2 Heterogeneous nucleation

Heterogeneous nucleation uses a substrate to collect the formed clusters and ions. In the case that a substrate is present the energy required to form an interface between the cluster and a substrate is typically much smaller than required in homogeneous nucleation. Therefore heterogeneous nucleation tends to produce formed particles even in the cases where homogeneous precipitation did not occur. Heterogeneous and homogeneous nucleation are shown in Figure 3.2

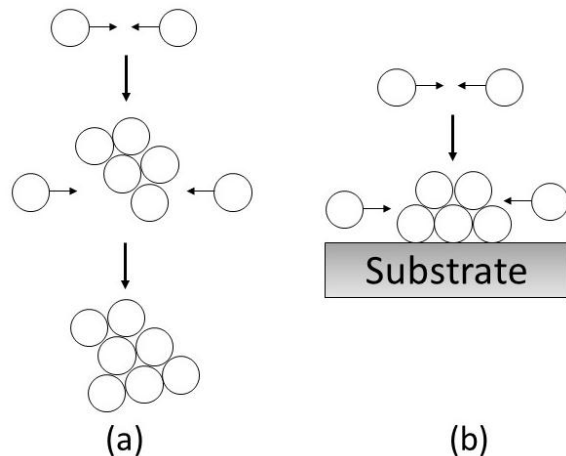


Figure 3.2 Schematics of (a) homogeneous and (b) heterogeneous nucleation.

Due to the lower energy requirements of heterogeneous nucleation, this process can take place close to the equilibrium saturation conditions. Homogeneous nucleation typically requires higher saturation conditions. The nucleation on the substrate can take place by either additional ion collisions from the solution, or surface diffusion as shown in Figure 3.2 (b). Clusters that are below critical radius in the solution enter the supercritical regime once they hit the surface.

Clusters on the surface of the substrate may also become nucleation centers for subsequent film growth.

In general, homogeneous nucleation is uncommon due to the factors discussed above. Additionally, without some solid surface or solid kernels, precipitation of solids become difficult and inefficient. Hence, either a seeding procedure or a solid kernel may be necessary for successful film precipitation.

### 3.3 Film growth

Once stable nucleation is achieved on the substrate surface in order to achieve stability and lowest energy the clusters will crystallize. There are several ways in which these clusters will crystallize and grow in size. One method is the continuation of the cluster growth through the absorption of the ions in the solution. This process is typically referred to as self-assembly. As can be easily imagined this process will generate crystals oriented in various directions, with no particular preference to the crystal orientation. The other method is absorption of another cluster or a crystal. This growth can continue indefinitely as long as the solution has enough ions for the formation of crystals and enough room to grow the forming films. In the case that there is no more room for lateral growth, aggregation in the vertical direction will begin. Additionally, the crystals will be strained from the lack of room. In some cases new clusters will grow on top of the old ones to give rise to the poly-crystallinity. At times the larger crystals can absorb the smaller unstable crystals by the means of crystal disassembly. This is known as Ostwald ripening. Growth mechanisms are shown schematically in Figure 3.3.

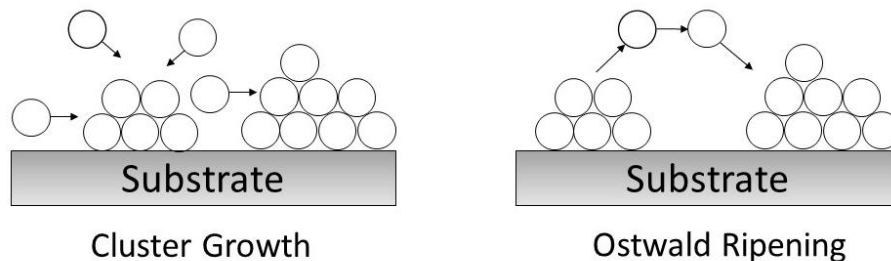


*Figure 3.3 Crystal growth mechanisms.*

If the nucleation takes place over a short period of time, then the distribution of the size of the particles is likely to be small. The opposite is true in the long growth processes. Prolonged growth processes will result in a wide distribution of the times that the clusters form, hence a wide distribution in the particle size. Grain particles and crystallinity of the film play a crucial role in the electrical properties of the films. By careful consideration, high quality films can be achieved for opto-electrical purposes.

### 3.4 Growth mechanics

One of the main requirements for a successful chemical bath deposition of a thin film is the release of the positively charged anion, and a negatively charge cation. Although, the mechanisms of the chemical bath deposition are a bit more complex than that. The two steps in the chemical bath deposition are: 1. the breaking apart of the metal complexes, and 2. the formation of the desired compound by the ionic interactions. Formation of the desired compound can be sub-divided further into: 1. formation of the single molecules, gradually clusters and 2. emergence of the solid phase.

The simplest growth mechanism, and that most often most preferred, is the ion-by-ion. This growth occurs by sequential reactions between the ions to form clusters. In this case one anion and one cation react to form one unit of the desired element. If the reaction is carried out under controlled  $pH$ , temperature, concentration etc. the ion-by-ion growth rate can be controlled. Ideally the final product will form on the substrate to crystallize into a uniform structure, and not in the solution. Adhesion of the films to the substrate is most affected by the van der Waal forces. In the initial growth stage, there is a strong interaction between the desired element and the substrate. In most cases the substrate is either gold,  $Au$ , or a transparent electrode such as  $TiO_2$ . The initial attraction between the element and the substrate promotes good adhesion. Additionally, there are chemical and electrostatic interactions between the surface and the individual crystals. Such interactions can also be induced by an induced charge on the surface. Typically the interaction between the atoms and the substrate is enough to ensure good adhesion. As the film grows, however, suitable orientation of the film in the chemical bath deposition process is very unlikely and thus the random orientation of the crystals as they grow will eventually destroy the film's adhesion. The van der Waal forces between the crystals of the desired film, however, ensure adhesion to one another and the substrate. This concept is apparent from the fact that thin films can be grown even on fairly unreactive surfaces such as plastics and even hydrophobic materials such as Teflon.

In the case that the adhesion is unachievable to the substrate, the substrate may be seeded with kernels to become centers of nucleation [68]. It has also been shown that such cases achieve nano-crystallinity, as compared to the poly-crystallinity often resulting in the non-seeded samples [69].

Step by step of the formation of chalcogenide in the chemical bath deposition is shown in Figure 3.4. It is generally believed that the formation will occur between the reaction of two ions. The reactions will then form a cluster that will set into the substrate, from which further nucleation will take place. As is apparent from the image, the formation may result in the poly-crystalline structure. Such structure will result in additional grain boundaries inhibiting transport phenomena, as well as pores which will degrade the films with time.

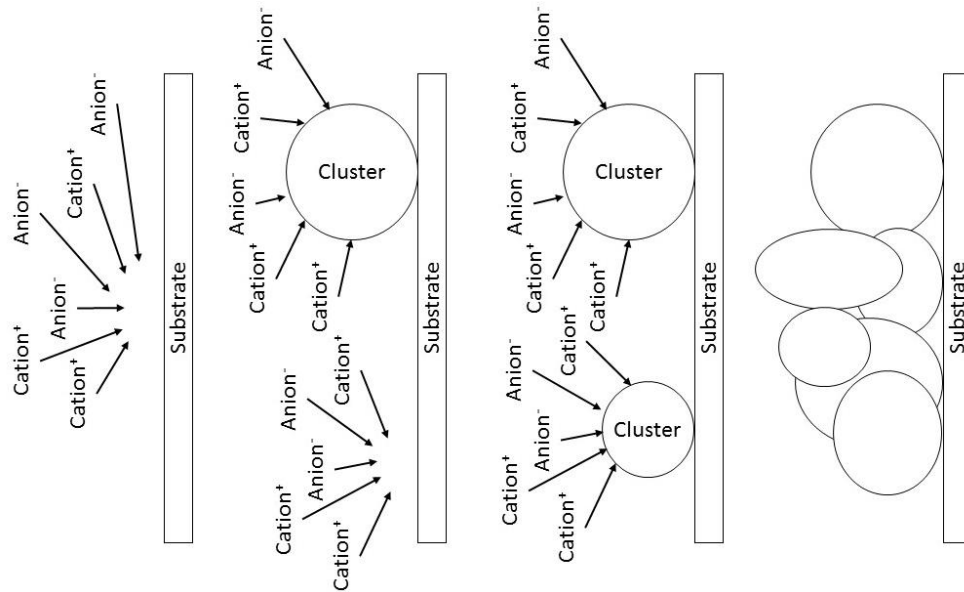


*Figure 3.4 Schematic of the ion-by-ion growth mechanism.*

In the case that the seeded layer is present the kernels will act as the centers of the nucleation. In this case there is a preferential lateral growth as opposed to the vertical deposition. In addition, it is typical for the kernels to grow outward once the free spaces between the kernels have been completely filled. In such a case a high quality adhesion and nano-crystallinity may be reached in thin films. This is shown schematically in Figure 3.5. In the case of the seeded sample, and given that the growth rate is slow, the film begins to coalesce rather than acquiring the agglomerate form such as the one commonly found in the unseeded samples. It should be noted, however, that coalescing of the film may be achieved without seeding as well under proper growth parameters [70].

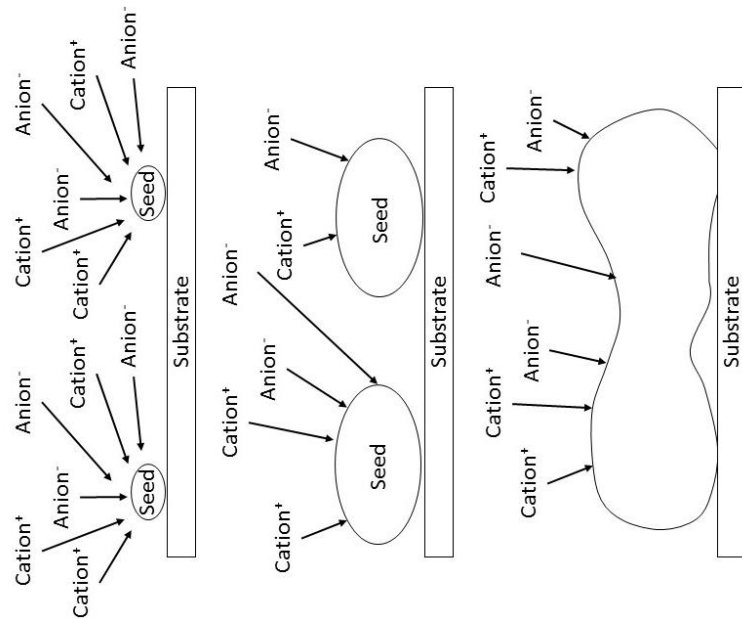


Figure 3.5 Schematic of the ion-by-ion growth mechanism on the seeded substrate.

The less preferred growth mechanism is the cluster-by cluster method. In this case, given that the product of the concentrations of the ions saturating the chemical bath are high above the solubility product of the desired element, a rapid precipitation will occur. In this rapid precipitation, in lieu of ions forming clusters on the substrate and further ion seeding, clusters will form and seed the substrate. Although this mechanism is known to produce thin films, the cluster by cluster growth mechanism often produces rough films (roughness of  $> 40$  nm) as well as porosity of the film. These films will have less favorable optical and electrical properties.

$pH$  deviations from the neutral position will increase the saturation rates of the ions. Saturation rates versus acidity and alkalinity for various elements have been well studied, and in general possess linear relationships.  $pH$  versus the concentrations of the  $Cd^{+2}$  ion is presented in Figure 3.6. Hydroxide complexes will form above the hydroxide line, and ion-by-ion growth mechanism dominates below the hydroxide line. The complex line gives the concentration of  $Cd^{+2}$  at any  $pH$  value, given that the  $pH$  is controlled by the ammonia concentration [71].

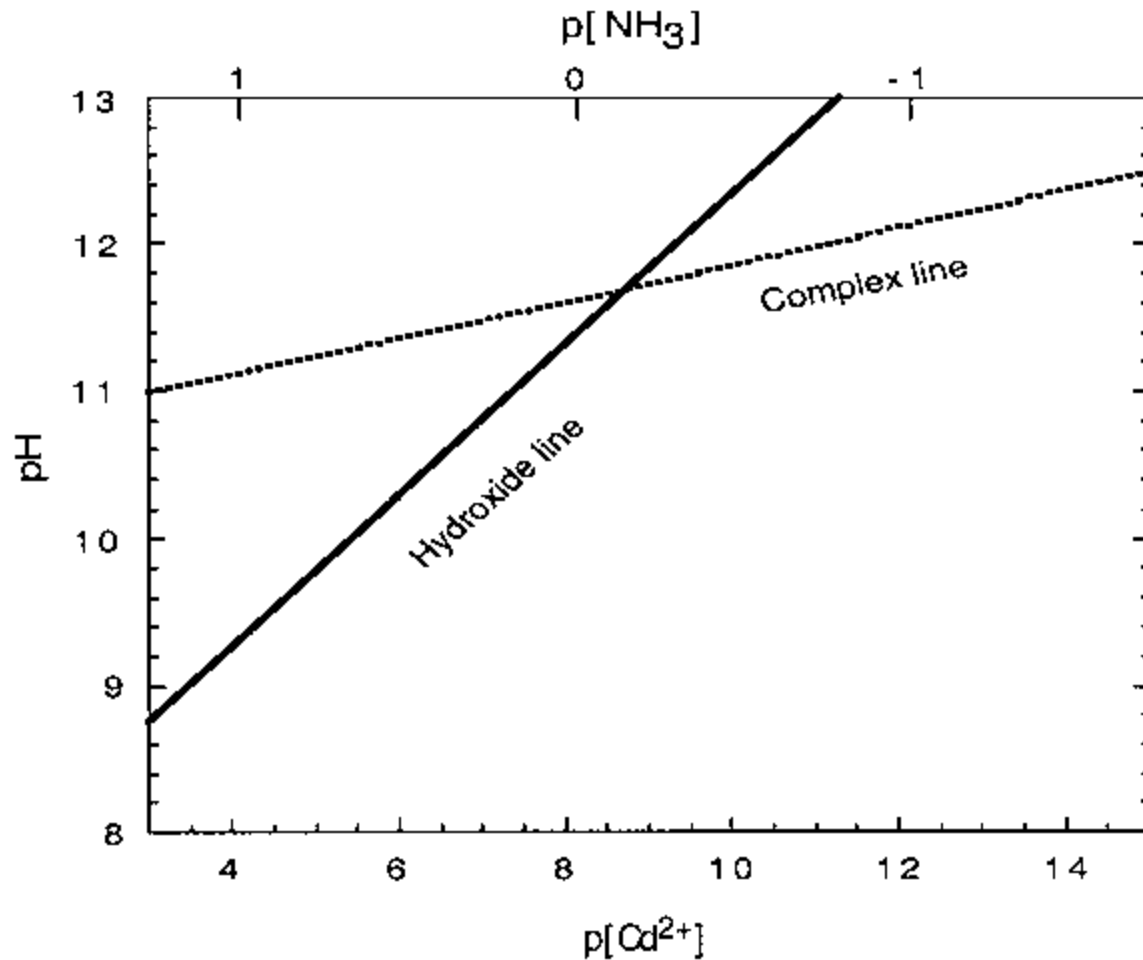


Figure 3.6 Stability region for the Cd-ammonia system for 0.1 M total Cd concentration at room temperature.

### 3.5 Deposition kinetics

The kinetics of the deposition depend on the deposition parameters, and hence can vary greatly. As previously mentioned, the presence of the substrate itself will change the activation energies of the deposition, hence changing the growth kinetics. Due to this variability in the growth kinetics some depositions may take a few minutes to complete, whereas others may take days.

In general, in chemical bath deposition there is a time during which no noticeable growth is taking place. This is known as the induction period at the beginning of the process. This is followed by a region of nearly linear growth, and then gradual slowing down of the growth until no further depositions are made. This is shown schematically in Figure 3.7.

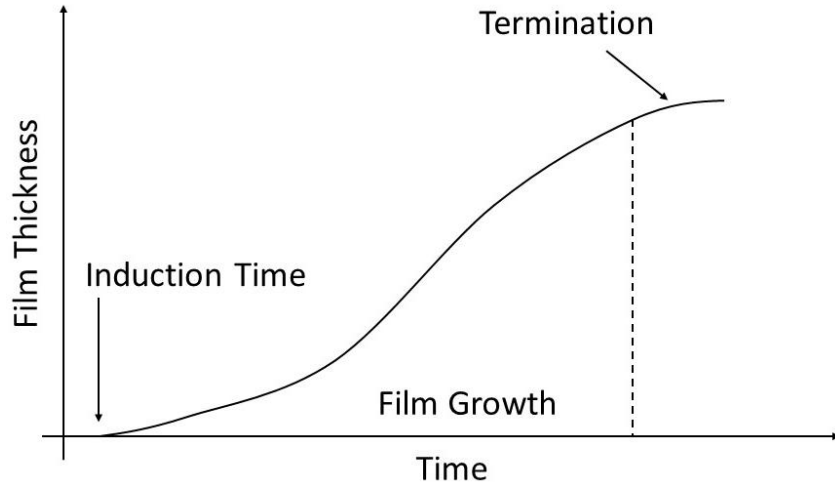


Figure 3.7 Typical growth curve shape as a function of time.

This growth trend is typical of both the ion-by-ion and cluster-by-cluster growth mechanisms. Regardless of the ionic saturation of the chemical bath solution, induction time, followed by a period of film growth and termination are followed. The trend is explained in the following manner. A certain amount of time is required for the saturation of the chemical bath solution with ions. Once the multiplication of the ion concentrations surpasses the solubility product of the material, precipitation will begin to take place. Hence induction time is dependent on the rate at which the concentrations saturate the solution. As long as the saturation rates remain constant the film growth will remain linear. There is a time when the concentration of the initial constituents will decline. In this case ionic saturation is no longer taking place and a gradual halt of the film growth takes place. This is the termination region. Although the film growth region is approximated to be linear, it is rarely a linear relationship. The greater the concentrations of the initial constituents the higher the saturation rates of the ions in the solution. Hence the initial growth rate typically is higher. As the constituents are broken apart, the growth rate gradually slows down to a complete halt.

Given that there are enough constituents in the chemical bath and the deposition is allowed to go indefinitely, film thicknesses can reach on the order of several hundred nanometers. In extreme cases with high cohesive forces in the material, films can be as thick as several micrometers. To a great extent, however, the thickness of the film depends on the deposition parameters. For example in an extreme case, if sulfur is added directly to a solution of Cd, CdS will form on the substrate but not on the walls of the vessel. This signifies that the CdS has a preference of depositing on the substrates, yielding heterogeneous nucleation, in lieu of the homogeneous nucleation. Hence the terminal thickness of the final film is largely dependent on the substrate as well as the parameters of the bath. Of course, films can be made of any thickness by careful planning of the deposition times.

Deposition kinetics have been studied extensively, especially for some commonly used semiconductors, such as CdS. Study of the deposition kinetics revealed the growth mechanisms that deposited the thin films.

Over the years extensive studies into quantum size effects have been carried out. Brus et al. in Bell Labs noticed that the size of the nanocrystals has a profound effect on the optoelectrical performance of the semiconductor [75]. Electrical properties would be expected to improve with the increase in the grain sizes, since in such a case the carrier has less barriers to cross. Additionally, the optical bandgap of the semiconductor is a function of the grain size according to the following relation

$$E_g = \frac{\hbar^2 \pi^2}{2R^2} - \frac{1.79e^2}{\epsilon R} \quad (3.5)$$

The above relationship is an approximation assuming that the crystals are spheres with the radius of  $R$ . Nevertheless it can be seen that an increase in the grain size will generate a decrease in the bandgap with a parabolic relationship. This is a significant effect especially when designing a material for a specific range of the electromagnetic spectrum.

Two main factors that control the size of the crystal in a chemical bath are the deposition mechanisms and the deposition temperature. High temperature allows for more grain growth and longer stabilization times. A similar phenomenon is observed in various other chemical deposition techniques such as Chemical Vapor Deposition [76]. In the baths with high temperatures cluster can grow continuously by collecting a variety of solution species. This process will continue until eventually the cluster is large enough to be thermodynamically stable and will no longer dissolve. There is a direct relationship between the bath temperature and the cluster size. Thus higher temperatures will produce larger grain sizes. It should be noted, however, that large temperatures may accelerate saturation of the ions in the solution as well. This may cause a rapid precipitation. A careful balance is needed between the temperature and desired opto-electrical properties of the film.

### 3.6 Effects of substrates and stirring

One of the great advantages of chemical bath deposition is the fact that CBD can be done on any surface. This is taking into account some very obvious exclusions to the general rule, i.e. any type of the substrate that will react with the chemical bath, or is unstable under the deposition parameters. Another significant impact on the quality of the films is the cleanliness of the substrate. In general minor dust particles are not significant contamination of the macro system, however, the crystalline structures of the films are on the order of ~30 nm in size, orders of magnitude below the size of the minutest particle of dust. Thus even minute dust particles and organic contamination will result in crystalline distortion of the film. It was realized that trace impurities on silicon can lead to detrimental effects on the electrical performance of devices [78].

Meticulous care needs to be taken in the preparation of the substrate. Typically a piranha etch solution (RCA-1) is used to remove any and all contamination from the substrate [77].

A highly effective yet simple and hazard free method for substrate purification is needed for semiconductor thin film growth. Whatever the method may be it should be based on first removing organics by oxidative breakdown, followed by removal of trace metals and chemisorbed ions by solubilization, complexing, and rinsing with high-purity water. In addition, the technique is required to measure the efficiency of cleaning processes and to minimize the time of the procedure [78].

On the basis of reaction chemistry and reagent purity, water-diluted, unstabilized  $H_2O_2$  at 75-85°C and at high pH, attained by adding  $NH_4OH$  solution, appeared to be the ideal reagent for removing organics by oxidative breakdown and heavy metal complexing. Diluted  $H_2O_2$  at low pH with the addition of HCl solution for removing the remaining inorganics in the second step. This step again is completed at 75-85°C. Deionized, distilled, and microfiltered water served as the diluent and rinsing agent. To prevent leaching of alkali and boron from beakers during processing, beakers from fused quartz and wafer holders of Teflon are typically implemented. Concurrently, the origin and concentration of contaminants by adding trace quantities of ions of over one dozen types of radioactive elements to numerous etchant and reagent solutions have been investigated and showed little to insignificant amounts of impurities present upon RCA-1 cleans. Radioactivity measurements, autoradiography, and gamma-ray spectroscopy of semiconductors treated with these tagged solutions allowed quantization of specific impurities initially and after various cleaning steps with the mixtures noted. All of the results from the RCA-1 piranha solution etching and cleansing have shown insignificant traces of impurities. These results allow for optimal use of the substrates in any application. Further the RCA-1 solution is based on organic reagents and does not require use of expensive equipment or the laboratory [Kern1-Kern5].

Nature and cleanliness of the substrate is usually important in order to achieve good adhesion of the films as well. Rough substrates in general are better for film adhesion, since larger area typically will allow for larger contact area, and an increase in anchoring probability initial deposit to the surface.

Oxides, including glass and transparent conducting oxides, have a presence of the hydroxyl surface group, hence making them somewhat reactive in the chemical bath. This has a noticeable effect on the adhesion of the films to the substrate. In general adhesion between oxides and films is less than non-oxide substrates.

Study of the chemical bath deposition of PbS films on various glass substrates found large differences in film formations. Nearly no films would grow on borosilicate glass and silica. Very good film growth was observed on lead flint glasses. The next best substrate for lead sulfide was zinc crown glass, which resulted in the best films [84]. The good film growth of PbS on the latter

substrates was attributed to the ability of the PbO or ZnO in these substrates to combine with sulfur to form insoluble sulphides. This covalent bond between the oxides and the sulfur ensured binding of the film and enhanced growth of the depositing film. Authors also stressed a possibility of ion exchange between metal ions in the glass and those in solution. This is a less likely source of the cohesion and successful film growth, however [84].

Very few studies have been performed on the stirring effect and film deposition to present time. In general the stirring is used as a technique to increase the ionic collisions and to break apart any loose clusters that may be forming. Large agglomerates are destroyed by the disturbances in the solution. This may play a crucial role in ensuring the large agglomerates do not block the substrate and allow for efficient film deposition. Similar effects, however, may be achieved with an inclined substrate in the solution, hence depositions only take place at the undersurface of the substrate. High quality CdS films grown on the undersurface of the substrates have been reported in the literature [85].

Further it was discovered that stirring rates can have an effect on the deposition rates, but the changes were insignificant [86]. In general the most noticeable effect of non-stirring is the loose adherence of the film to the substrate [62]. This can be explained by the non-dissolution of the clusters in the solution. Even in stirred cases, however, no apparent difference between low and fast stirring rates was acknowledged. This implies that even slow stirring is sufficient to dissolve large, loosely adhering particles. Further work by Kaur et al. did discover **that did** affect the quality of the films. This discovery was limited to a very small number of samples with high concentration of ammonia. In the cases with high ammonia and high stir rates, the wurtzite structure of CdS was observed. In the same cases with no stir the more common zinc blende cubic CdS was observed [62]. It is assumed that the stirring prevented formation of clusters hence limited the sticking of the colloidal particles from the solution and limiting the formation of the zinc blende. This resulted in largely wurtzite structure and highly reflective films. Thus to an extent stirring can cause a phase transition in some materials.

Furthermore, in an extreme case experiments were carried out at extremely high stir rates of 1100 rpm. In such cases it was noticed that the extremely high stirring rotations had a profound effect on the deposition rate [87]. The experiments, however, were carried out on silver sulfide, which is a compound with a known low activation energy. Similar results would not be expected on elements with higher activation energies, such as the CdS or Pbs. In the majority of the chemical bath depositions, film growth and film structure are largely independent of the stirring.

### 3.7 Film characterization

As is evident from the above discussion, properties of the advanced materials are often dependent on the structural characteristics of the materials. Hence, the knowledge of the material's structure is just as important as the knowledge of the opto-electrical properties of the

material. Numerous techniques exist in characterizing advanced materials, it is important to discuss several of the more prominent ones.

### 3.7.1 X-Ray diffractometry (XRD)

X-ray diffraction, (XRD) is a characterization technique used to give information on the composition of the film, crystalline phase, and orientation. This method also provides crystal texturing, and can be used in a grazing mode (across the sample) as well as a regular mode looking into the sample for film analysis.

Chemically deposited thin films, due to the growth mechanisms, are typically nanocrystalline. Average crystal diameter can be deduced from the XRD data using Scherrer's equation

$$\phi = \frac{1.3\lambda}{\Delta(2\theta)\cos(\theta)} \quad (3.6)$$

where  $\phi$  is the cluster diameter,  $\lambda$  is the wavelength of the X-ray,  $\Delta(2\theta)$  is the peak full width at half maximum (FWHM) in radians, and  $\theta$  is the peak position.

It should be noted however, that the XRD data will analyze all of the crystals in the film. Hence if the film has a combination of large and small crystals the XRD will retrieve the peaks for all crystals on the plot. The size of the crystal may vary depending on which peak is measured. Also in a mixture of large and small crystals, large crystals tend to dominate the XRD patterns. Even in the case where the number of large crystals is significantly smaller than the number of small crystals, the XRD patterns will be dominated by the peaks of the large crystals. It is important to validate the XRD data with another method.

If the crystals are very small ( $< \sim 10$  nm) the peaks will become very wide and short. In this case the crystalline structure may be classified as amorphous, although in reality it will be crystalline with small crystalline sizes. In such a case it is important to repeat measurements over small scan windows where peaks are expected, and slow scan rates. In general XRD gives a very good analysis technique to assess the crystalline structure of the films.

### 3.7.2 X-Ray photoelectron spectroscopy (XPS)

XPS, also known as the electron spectroscopy, is one of the most common surface analysis techniques. The X-rays used in XPS allow for application to a wide variety of materials, including semiconductors, and metals. Typically the analysis is used to characterize the surface chemistry of materials. Surface characteristics can be important, such as in the case of interface connections between metals and semiconductors. The penetration depth can be adjusted to just a few nm.

In this case the chemical analysis of the surface is conducted by exciting photoelectrons from the surface of the materials. The photoelectric interactions between the electrons and X-rays cause the electrons to be ejected at discrete kinetic energies [66]. The electron energy analyzer then measures the energy of the emitted electrons. The energy required to emit an electron, binding energy, is then plotted against the counts of the emitted carriers. Thus the chemical state and the quantity of the element can be determined.

The power of the X-ray photoelectron method lies in the concept that the quantity of the measured electrons at certain binding energy of an atom is a function of the chemical environment of the atom. From the known binding energies of the electrons, the surface chemical composition of the thin films can be determined. Additionally, modern XPS machines have the ability to etch nanometer thicknesses off the top of the surface for further analysis. Thus a profile of the chemical composition of the thin film can be acquired.

### 3.7.3 Optical spectroscopy

Optical spectroscopy is an important characterization tool to validate the bandgaps of the semiconducting thin films. Shifts in bandgaps are a well-studied phenomena and have been reported by numerous authors [67]. In CBD deposited thin films, crystals can range in size, and the smaller crystal sizes tend to increase the bandgap of the material. Although the bandgap shifts may be minor in some materials, optical spectroscopy is a useful tool in characterizing bandgap and crystalline size variation.

Typically spectrophotometers measure reflectance and or transmittance of a material. However, it is the absorbance property of the material that is used in determining the bandgap of the material. Although, through specialized equipment such as the integrating sphere, absorbance may be measured directly. In general, however, absorbance measurements are done indirectly.

Photons with the energy below the bandgap will be invisible to the material, and will pass through without interaction. Photons above the bandgap will be absorbed by the material. Hence, one would expect a drastic change in the absorbance curve at the location of the bandgap. The absorption coefficient for a material can be derived using a variation of the Beer-Lambert equation  $T = [(1-R)^2 e^{-\alpha d}] / [1 - R^2 e^{-2\alpha d}]$

$$T = \frac{[(1-R)^2 e^{-\alpha d}]}{[1 - R^2 e^{-2\alpha d}]} \quad (3.7)$$

where  $T$  and  $R$  are the transmittance and reflectance percentages respectively,  $\alpha$  is the absorbance coefficient, and  $d$  is the film thickness. The absorbance coefficient can be extracted from the above relationship.

For semiconductors the relationship between the absorption coefficient and the bandgap of the material is derived by the Tauc equation

$$(\alpha h\nu)^n = C(h\nu - E_g) \quad (3.8)$$

where  $n = 2$  for a direct transition semiconductor, and  $C$  is a constant. Plotting  $(\alpha h\nu)^n$  versus  $h\nu$ , is known as the Tauc plot, and should give a straight line over the absorption onset region. Extrapolation of the line to the zero value gives the bandgap of the material.

### 3.7.4 Spectroscopic ellipsometry

Ellipsometry is an optical analysis method that analyzes light reflection and transmission from samples [72]. Spectroscopic ellipsometry operates on the measurement of the changes in polarized light reflection on the sample in the case of reflectance, or transmission in the transmittance case. Ellipsometry is termed from the fact that light becomes “elliptical” after reflection. Two values of light are measured upon reflection. Amplitude ratio,  $\Psi$ , and phase difference,  $\Delta$ , between the  $p$ - and  $s$ - polarized light waves are measured. In spectroscopic ellipsometry wavelengths of light are changed across the spectra of light and the amplitude ratio and phase difference are measured over the range of the spectral region. The incidence angle of the measurement is chosen to give maximum sensitivity to the measurement. In semiconductors this sensitivity is maximized at the incidence angles of  $\sim 70^\circ - 80^\circ$ .

Advantages of spectroscopic ellipsometry are the high precision of the measurements. Sensitivity of  $\sim 0.1 \text{ \AA}$  can be achieved in measurements. Further, the measurements are nondestructive, fast, can be applied to a wide variety of materials and areas, can measure optical constants and thicknesses, and a possible feedback control is possible for the measurement systems. This technique is, however, limited mainly to materials with high absorption coefficients. Materials, and or regions with absorption coefficients  $\alpha < 100 \text{ cm}^{-1}$  generally will not provide solid data [73]. Further this is an indirect measurement technique, requiring a model with defined optical constants and layer thicknesses of a sample.

In ellipsometry the amplitude ratio and phase difference are measured continuously at various wavelengths. The relationship between the two parameters is expressed as follows:

$$\rho_{\text{ellipsometry}} \equiv \tan\Psi e^{i\Delta} \quad (3.9)$$

The optical model for the ellipsometry setup is shown in Figure 3.8

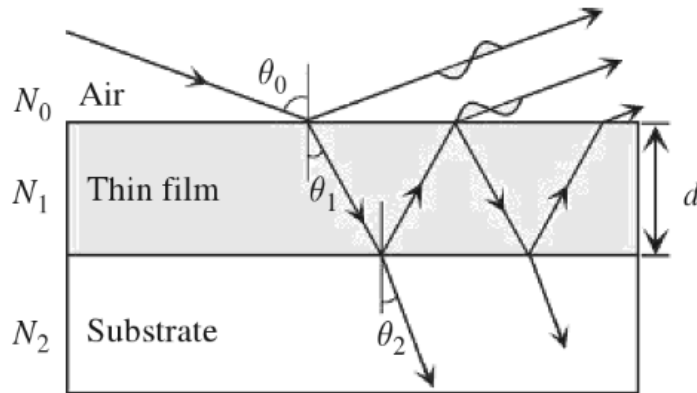


Figure 3.8 Ellipsometric optical model of air/thin film/substrate structure.

In the above model  $\rho$  is expressed as

$$\tan \psi e^{i\Delta} = \rho(N_0, N_1, N_2, d, \theta_0) \quad (3.10)$$

$N$  is the complex refractive index. In the case shown in Figure 3.8,  $N_0$  signifies the complex refractive index of air and is usually taken to be equal to 1.  $N_2$  and  $\theta_0$  are the complex refractive index of the substrate and incident angle respectively. Both values are known before the commencement of the analysis. Given that the thickness of the film,  $d$ , is known, i.e. measured by some mechanical means such as the profilometer, then the complex refractive index of the film,  $N_1$ , can be computed [74].

This technique is not direct, however, it is a powerful nondestructive method to validate film thicknesses, roughness, and optical coefficients. Additionally, this method may be used to analyze the porosity of the film and the most likely growth mechanisms of the films.

### 3.7.5 Hall effect electrical analysis

In 1879 Edwin Hall discovered that application of the magnetic field to a charged plate will produce a small voltage across the plate. Reversal of the magnetic polarity will reverse the induced voltage. This is shown schematically in Figure 3.9. If the magnetic field is perpendicular to the plates, the small voltage across the plates may be measured.

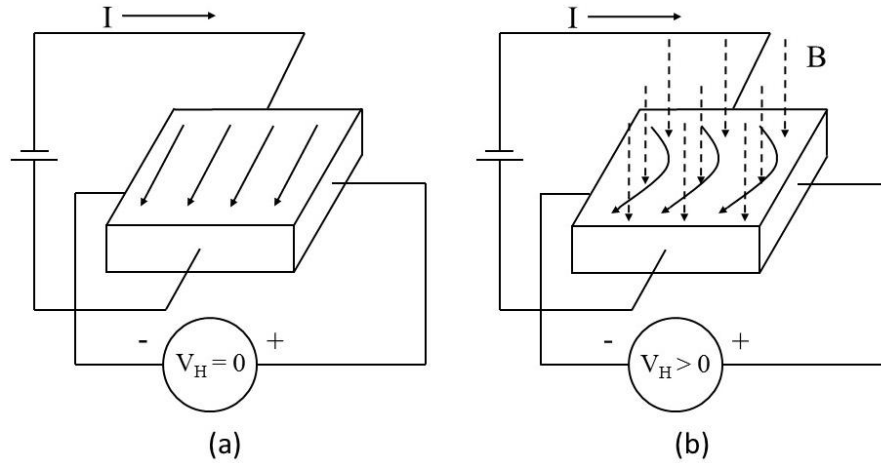


Figure 3.9 Hall Effect in a plate. (a) Hall voltage equal to 0 with no applied magnetic field, and (b) Hall voltage  $> 0$  with the applied magnetic field.

The reason for the bending of the carriers inside the plate under magnetic force is well understood. The force exerted on the carrier, such as the electron by an electromagnetic field is defined Lorentz Force [88]:

$$F_{Lorentz} = q(\mathcal{E} + vB) \quad (3.11)$$

Where  $F_{Lorentz}$  is the exerted Lorentz force, and  $B$  is the magnetic field. In the electric field the charge experiences a force aligning with the direction of the field. The force is proportional to both the magnitude of the charge as well as the strength of the field. This is the effect that causes current flow. When the magnetic field is added, the charged particle will experience force only in the case when it is moving. In motion the force exerted on the charged particle is proportional to the charge, the direction of motion, and the orientation of the magnetic field. The two forces are forcing the particle to move in curved (or helical) path. By applying small voltages in one direction in a perpendicular magnetic field, a Hall voltage will thus be provided. Conductivity and resistivity can both be deduced from the Hall voltage. Carrier concentrations and carrier type (determined from the polarity of the Hall voltage) can be obtained directly from the Hall effect measurements.

Given that the width of the sample, magnetic field and Hall voltage are known, carrier density is found by

$$V_H = \frac{IB}{qnd} \quad (3.12)$$

From the known carrier concentration and resistivity, given that one carrier dominates in the semiconductor, mobility of the carriers is obtained by

$$\rho = \frac{1}{q\mu n} \quad (3.13)$$

As previously discussed resistivity, mobility, and carrier concentrations are crucial parameters in determining the overall performance of the solid state device.

## Chapter 4. Lead (II) Sulfide

Lead sulfide is of great importance in the semiconductor industry. This chapter is dedicated to the growth and development of PbS thin films. Some of the presented material has been copied from the PbS published work by Slonopas et al. in *Electrochimica Acta* [115].

### 4.1 Introduction

Lead (II) sulfide (PbS) is one of the most widely studied semiconductors and also was the first reported semiconductor to be deposited by means of chemical bath deposition in 1869 by C. Puscher [92]. In an effort to find a “cheap process, without using dyes, to coat various metals with splendid lustrous colors” C. Puscher coated several metals with PbS [93]. His deposition method was primitive, and involved depositing lead acetate from thiosulfate solution, and later from Cu and Sb salts.

Over the years PbS has shown to be a very prominent semiconductor with a wide variety of applications. The need for a cost effective method of PbS growth prompted extensive research into the field of chemical bath deposition of PbS. Various precursors for the hydroxide, halides, and sulfur ions have been proposed and well-studied.

Thin films of nano-crystalline chalcogenides (i.e, PbS and PbSe) are attractive semiconductor materials for large-scale applications, because of availability and the low cost of lead, sulfide and selenide compounds [89]. There is a continued and growing interest in lead salt thin films as a result of their potential use as infrared detectors [90] and because of material's high sensitivity to near infrared radiation ( $\lambda = 0.7\text{-}4 \mu\text{m}$ ). Additionally, lead-salt semiconductors are very favorable materials for mid-infrared usage because of their unique energy band structure, and extremely low Auger recombination ( $\sim 2$  orders lower) rate compared to narrow gap III-V or II-VI semiconductors [91].

PbS films with extremely high quality nano-crystalline structure have been manufactured using chemical bath deposition (CBD) technology [90]. PbS (and PbSe) grown in CBD does not require a post deposition treatment (e.g. annealing) in order to achieve optimal parameters. In order to improve semiconducting properties of the film, non-stoichiometric deposition processes can be conducted and oxidants (such as potassium persulfate, hydrogen peroxide or sodium perborate), reducers (such as hydrazinehydrate, hydroxylaminehydrochloride, or others) and surfactants can be included in a chemical bath during the deposition. CBD is a simple and widely used thin film deposition technique due to its low cost and the high quality of the obtained films. In addition, this low temperature technique is most appropriate for deposition on plastic substrates. Structural characteristics of chemically deposited PbS thin films depend strongly on the composition of the deposition bath and the nature of the substrate, and structural properties of PbS in turn influence the photosensitivity.

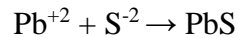
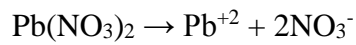
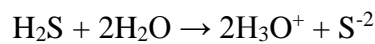
Over the course of this dissertation research an improved chemical bath deposition technique was developed for growing thin film semiconducting nanocrystalline lead sulphide (PbS) for use in photovoltaics. The goal of this work was to produce good quality crystals, with the high mobility of holes and electrons required for effective carrier separation in photovoltaic applications, and to control other electro-physical properties. Tightly attached, densely compacted, nanocrystalline PbS films with tunable electrical, physical, and optical properties were deposited. Adherence to the substrate was attained by establishing firmly attached kernels on the substrate from which crystallization occurred. Nanocrystalline structures were precipitated onto the substrate by controlling the deposition temperatures, time, concentration of the chemical constituents and ionic products. Using this approach nanocrystalline thin film PbS layers with controllable thicknesses were proliferated. SEM images show rigid crystalline structure, and low impurity concentrations in the film. Hall effect and spectroscopy measurements illustrate tunable electrical, physical, and optical properties. Carrier concentrations were achieved between  $6 \times 10^{16} /\text{cm}^3$  -  $8 \times 10^{18}/\text{cm}^3$  and mobility ranged between  $3.4 \text{ cm}^2/\text{Vs}$  –  $33 \text{ cm}^2/\text{Vs}$ . Photoconductivity was measured using a 980 nm laser and blackbodies at temperatures of 450 °C and 800 °C. Results indicate low recombination rates on the surface. Prolonged exposure to air confirms resistance to oxidation, and stability of the optical and electro-physical parameters.

## 4.2 Chemical bath deposition of PbS

### 4.2.1 Seeding

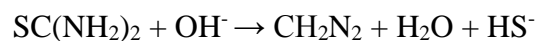
In order to achieve reproducibility in the experimental work a seeding procedure was devised. Seeding was done on glass slide (22 mm X 22 mm X 1 mm) substrates. Substrates were cleaned to remove organic containments from their surfaces, using RCA-1 clean solution [78]. Glass slides boiled in the piranha solution with a chemical composition of 1:1:5 27%  $\text{NH}_4$ :30%  $\text{H}_2\text{O}_2$ : $\text{H}_2\text{O}$  for 15 min, rinsed with deionized water, and dried before use. Seeding solutions had very light chemical constituent concentrations, high enough to create kernels without producing continuous films, and contained 5 mL of polyvinyl alcohol  $[(\text{C}_2\text{H}_4\text{O})_x]$  with concentration of 340 mM, mixed with 5 mL of lead (II) nitrate  $[\text{Pb}(\text{NO}_3)_2]$  with the concentration of 30 mM and 40 mL of thioacetamide (TAA)  $[\text{C}_2\text{H}_5\text{NS}]$  with the concentration of 3.3 mM [94]. Constituents were mixed and 4 mL of nitric acid  $[\text{HNO}_3]$ , as a  $\text{H}^+$  ion controlling agent, molarity of 1 M, was added to the solution. Nitric acid caused the pH of the solution to be reduced from 5 to 3. Acidity of the seeding bath had a profound effect on the seeding procedure. Substrates were kept in the seeding solution with stir set at 50 RPM (required for uniform seeding). A 50 mL beaker containing seeding solution was maintained at 70 °C for 90 minutes and a tight seal was placed over the seeding beaker in order to the prevent escape of  $\text{H}_2\text{S}$  gases. The optimal time, temperature, and constituent concentrations were determined using experimental data obtained from a series of experiments.

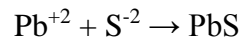
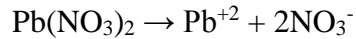
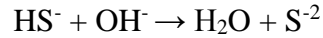
Variations within the seeding procedures resulted in unreproducible, unpredictable and uncontrollable results. Thus seeding was set to a standard and only deposition bath was used to alter the opto-electrical and physical properties of the film. Seeding experiments have elucidated that in an acidic medium TAA decomposes and releases hydrogen sulfide [H<sub>2</sub>S]. It is believed that hydrogen sulfide breaks apart further to release sulfide [S<sup>-2</sup>] ions. Lead (II) nitrate is also broken apart in the acidic medium to release Pb<sup>+2</sup>. The chemical reaction for seeding has not been explicitly elucidated; however, based on the deposition reaction described below. From previous work it is suspected that S<sup>-2</sup> precipitates Pb<sup>+2</sup> ions from the solution by following chemical process:



#### 4.2.2 Film deposition

G. Hodes goes to extreme lengths to explain the chemical deposition process involved in the decomposition of a thiosulphate solution [95]. In this work thiourea [SC(NH<sub>2</sub>)<sub>2</sub>] was used as a source of S<sup>-2</sup> ions. From the onset it must be noted that the mechanism of this deposition is still a topic of debate [96]. The chemical reaction presented below is accepted as reasonable. This method is further supported by the fact that concentrations of the OH<sup>-</sup> ions have a profound effect on the rate of crystal growth of PbS. Initial deposition parameters were taken from Cooperstein to be 18 mL NaOH 2.75 M, 10 mL Pb(NO<sub>3</sub>)<sub>2</sub> 340 mM, 10 mL SC (NH<sub>2</sub>)<sub>2</sub> 990 mM, 240 mg Na<sub>2</sub>SO<sub>3</sub>, and 10 mL C<sub>2</sub>H<sub>6</sub>O [94]. These reagents were mixed in a 50 mL beaker in this order. Chemical reaction among the constituents caused darkening of the fluid. At 25 °C and concentrations stated above, constituent reaction takes place within several minutes, although the rapidity of the reaction was a function of temperature and constituent concentrations. Acidity of the chemical deposition bath was pH ~12. The seeded substrates were placed into the beaker with the chemical components, and the beaker was placed in a warm bath controlled at 25 °C for 30 min, and stirred at 50 RPM for uniform deposition. Literature offers several elucidations for the reaction [96]. The prevailing explanation for the reaction is decomposition of thiourea and release of S<sup>-2</sup> ions, which precipitate Pb<sup>+2</sup> ions from the solution [97]. The initial step in the chemical process consists of breaking apart thiourea [SC(NH<sub>2</sub>)<sub>2</sub>] with OH<sup>-</sup> ions to saturate the solution with HS<sup>-</sup> ions. Once the solution is saturated with hydrogen sulfide, the high concentration of hydroxide ions further breaks apart HS<sup>-</sup> and releases S<sup>-2</sup> ions. The highly alkaline solution also dissolved apart Pb(NO<sub>3</sub>)<sub>2</sub> to release the Pb<sup>+2</sup>





The solubility products equation, states that once the ionic products exceed the solubility product of PbS, precipitation occurs. Solubility product for PbS is found experimentally to be  $10^{-28}$  mol/L and is well studied and cited in the literature [98]. In our work, breaking apart of the constituents was done by controlling the OH concentration in the deposition bath. The alkalinity of the deposition solution was measured to be pH ~12. Excessive addition of NaOH did not have a profound effect on the basicity of the solution raising the pH by 0.4 points at most. However, the concentration of sodium hydroxide had a profound effect on the rate at which ionic products saturated the solution. The rate of precipitation is thus managed by controlling the concentration of NaOH in the emulsion. This gives a finely tunable method to control the growth of nanocrystalline PbS films. Upon the completion of the deposition, samples were removed from the chemical bath, loose precipitation was washed with deionized water, and samples were stored for further analysis. If successive PbS layers were to be deposited on the same glass, then following a rinse with deionized water and through drying, the sample was introduced into a new bath. No new seeding was required due to the already present crystalline structure of the samples.

If successive PbS layers were to be deposited on the same glass substrate, then after the deposition of the first layer the film was washed in DI water to remove any loose particles, dried and introduced in a new bath. When the deposition process was completed, the PbS film from the top layer was removed by wiping with a cotton swab immersed in a 1:3 HCl:H<sub>2</sub>O solution.

### 4.3 Material characterization

#### 4.3.1 Interference spectroscopy

It has been shown that accurate determination of the film thickness can be calculated using interference spectroscopy. Figure 4.1 shows the transmission and reflection spectra of a 547 nm sample measured as obtained using a Cary 5 E spectrophotometer.

$$d = \frac{m\lambda_m}{4n} \quad (4.1)$$

Equation (4.1) is the governing equation for the film thickness computation.  $m$  is an integer number starting from one and corresponding to the order of extremum, including maxima and minima, and  $n$  is the refractive index of the material at the wavelength of  $\lambda_m$  [99]. The order of extremum,  $m$ , is found from the wavelengths of two adjacent extrema in the spectral region, if the refractive index  $n$  does not change appreciably between the  $\lambda_m$  and  $\lambda_{m+1}$  [99],

$$m\lambda_m = (m + 1)\lambda_{m+1} \quad (4.2)$$

In the absence of absorption (i.e. low energy photons) in the film material, reflectance peaks should coincide with the transmission troughs. At low wavelengths (photon energy above the bandgap) the peaks no longer align, indicating that absorption is occurring in the film. In this case the thickness may not be accurately measured, since absorption is unknown in the region where absorption occurs. Location of the trough and peak used for the thickness calculation is identified as 1 and 2 respectively in Figure 4.1. The order of  $m$  was equal to 4. Refractive index,  $n$ , can be reasonably approximated to be a constant equal to 4.2 for the frequency range used in these analyses [100]. Transmittance (or reflectance) are then calculated as ratios of radiation intensity passed through the film (or reflected from the film) to intensity of radiation passed through a holder aperture without the sample material measured in corresponding modes. Measurements have provided an accurate location of the peaks and troughs of the spectra, which were used to calculate the thicknesses of the sample using both Equations (4.1) and (4.2). Due to dispersion of refractive index at energies near the bandgap, the order of extremum determined using Equation (4.2) is not exactly an integer number and has to be corrected. Sample thicknesses were validated using profilometry.

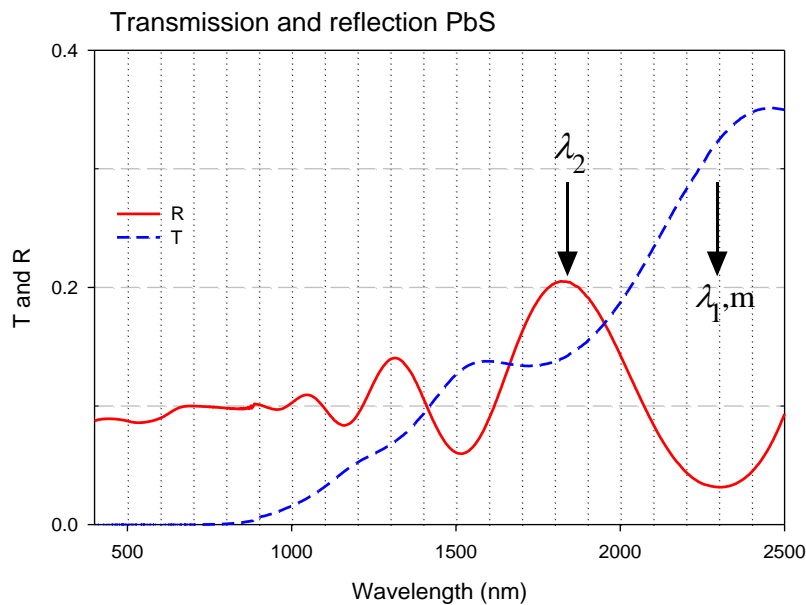


Figure 4.1 Transmittance and reflectance of a 547 nm CBD deposited PbS film.

#### 4.3.2 Hall effect measurements

Substrates were diced into 5 X 5 mm<sup>2</sup> squares. Contacts were added with Ag paint. Hall mobility, resistivity, and carrier concentration were measured in Van der Pauw configuration using an Ecopia HMS-3000 Hall measurement system. The measured mobilities are hole mobilities and the grown PbS film was determined to be a p-type semiconductor.

#### 4.3.3 Responsivity

The photo-responsivity at 25 °C was determined using an IR- 508 (Infrared Systems, Sandcove, CT) cavity blackbody at 800 °C and 450 °C. The diameter of the aperture in front of the blackbody was 0.33 cm, and the distance between the sample and radiator was 4 cm. The radiation beam was modulated using a mechanical chopper with an IR-301 black body source controller. The chopping frequency was selected to be 90 Hz. The AC photoconductive signal was taken from a matched load resistance and measured using a Tektronix MSO/DPO2000B Mixed Signal Oscilloscope, and the circuit was biased at 30 V DC. The radiance of the blackbody is  $0.08 \text{ Wcm}^{-2}\text{sr}^{-1}$ , when the upper limit of the wavelength response of the detector is 3 mm [101]. Carrier lifetime was determined as a function of time using the photoconductance decay method [102].

#### 4.3.4 Scanning electron microscopy (SEM)

A 40VP scanning electron microscope (SEM) operating at 15 keV with an aperture of 50 mm, a working distance of 15 cm, and with the samples angled at 45° relative to the gun was utilized in this work. To improve resolution, the secondary electron regime with low beam current was used.

#### 4.3.5 Scratch adhesion test

Film adhesion was studied by making a 2 mm long scratch on the film surface using a force of 0.25 N. Scratch depth was then measured at various lengths along the indent using a Veeco Dektak 3 ST profilometer.

#### 4.3.6 Raman spectroscopy

Raman spectroscopy was employed to characterize the chemical composition of the seeds and fully deposited film. Raman spectra were collected using a Renishaw InVia Raman microscope. The system utilizes the 488 nm line of an Ar ion laser in 1800 back scattering geometry and a 3000 g/mm grating. The sample was irradiated with 0.1 mW laser power through a 50 X 0.75 NA objective yielding a spot diameter of 900 nm.

#### 4.3.7 X-Ray photoelectron spectroscopy (XPS)

The sample was analyzed with a Thermo VG Scientific Escalab 250 electron spectrometer (10 mA, 15 kV) using monochromatized Al Ka excitation and advanced charge compensation. Sample etching was undertaken in-situ using a Thermo VG Scientific ESCALAB 250 EX05 argon ion etcher with an emission current of 15 mA.

## 4.4 Results

### 4.4.1 Seeding

Experiments have shown that the formation of a PbS film is affected by the initial nucleation at the glass substrate. Thus a seeding procedure was devised in which the initial PbS kernels were grown on the glass substrate without forming a continuous film in order to induce uniform film growth and crystallization during deposition. Seeding was not very dense as shown in the SEM image of a seeded substrate (Figure 4 2).

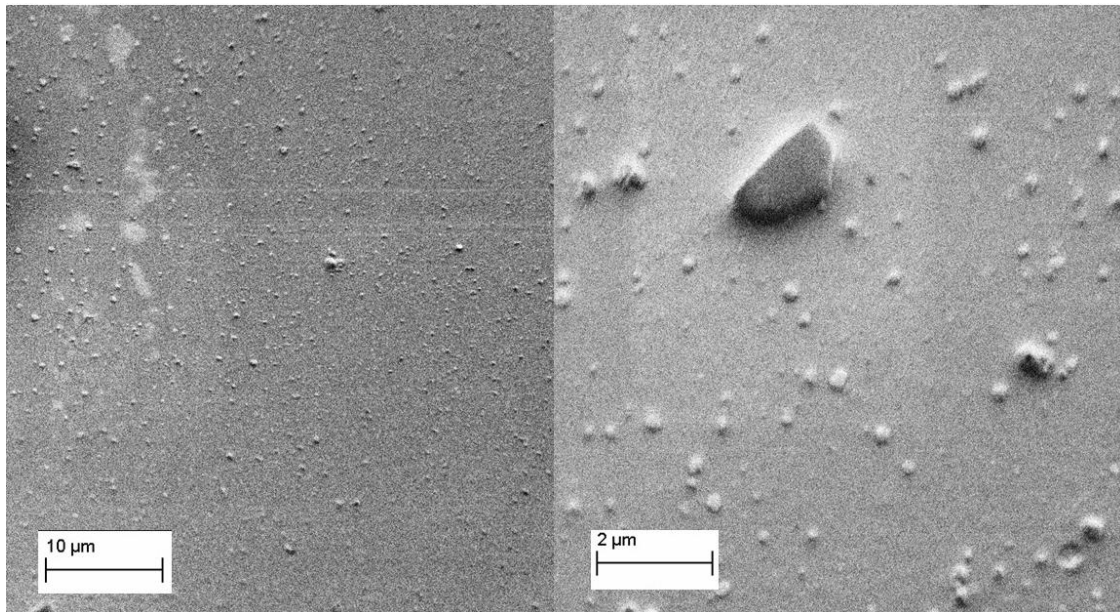


*Figure 4.2 As seen in this SEM image, the seed density of PbS is shown not to be very dense. This density is adequate, however, for the initial film growth.*

The seeding crystals were around 10 nm in diameter, with rare large seeds found to be on the order of a micron, and on average separated by distances ranging from 2 µm to several nm. After the substrates were seeded, the film was deposited and characterized. Results have shown that changing the seeding procedure did not result in a predictable trend in the film parameters.

Seeds were analyzed for the chemical composition using Energy-dispersive X-ray spectroscopy (EDS) and Raman Spectroscopy. A seed larger than the laser spot diameter was grown so that substrate signal subtraction would not be necessary, see SEM Figure 4.3. However, in order to ensure this, seeds and films were grown on bulk Si wafers so that only one peak from the substrate would result at  $520\text{ cm}^{-1}$  rather than a broad spectrum from the glass slide.

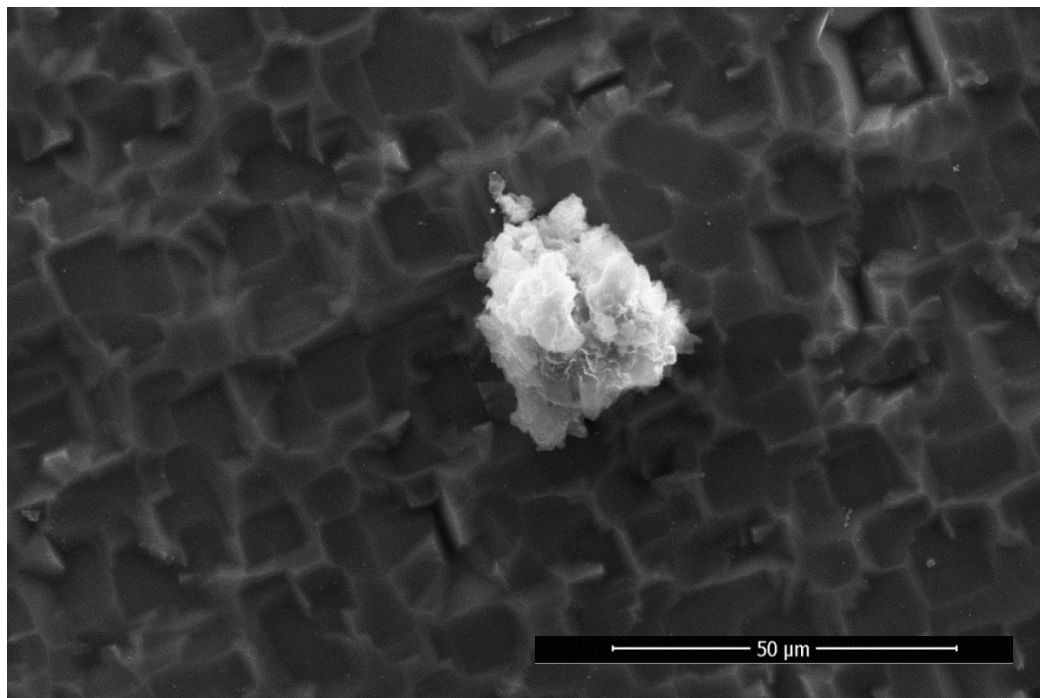


*Figure 4.3 SEM of PbS seed on rough side of bulk Si wafer.*

Figure 4.4 plots the spectra from both the seeds and film. It is clear that both the seeds and film are nearly identical except for a slight broadening of the spectra in the seed, which is likely due to disorder in the crystal structure. Additionally, this spectra matches that of the PbS nano-structures grown by solvothermal synthesis, presented by Zhang *et al.* [103]. Results indicate successful growth of both PbS seeds and films.

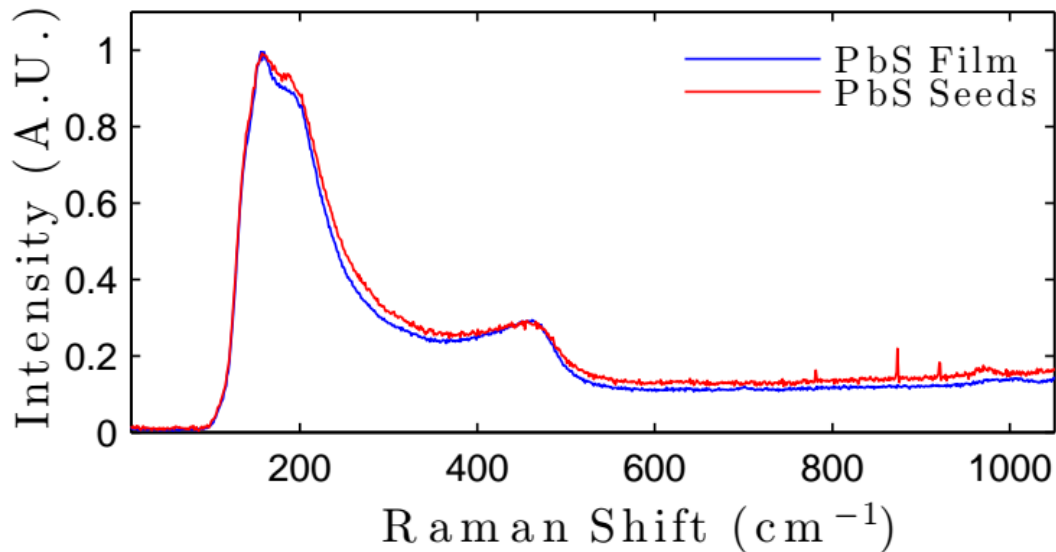


Figure 4.4 Raman spectra of PbS seeds and film. The seed and film spectra match literature for PbS [103].

Finally, to confirm the composition of the film and seeds EDS measurements were taken using a FEI Quanta FEG 250 SEM. Figure 4.5 plots the EDS results of seeds. The main peaks observed were from the Si (substrate), Pb and S again confirming the composition of the seeds. Small C and O signals were also observed which could be from oxidation of the Si surface and the ethanol rinse. The PbS film showed very similar results except the substrate signal was significantly reduced due to the increased thickness and coverage of the film.

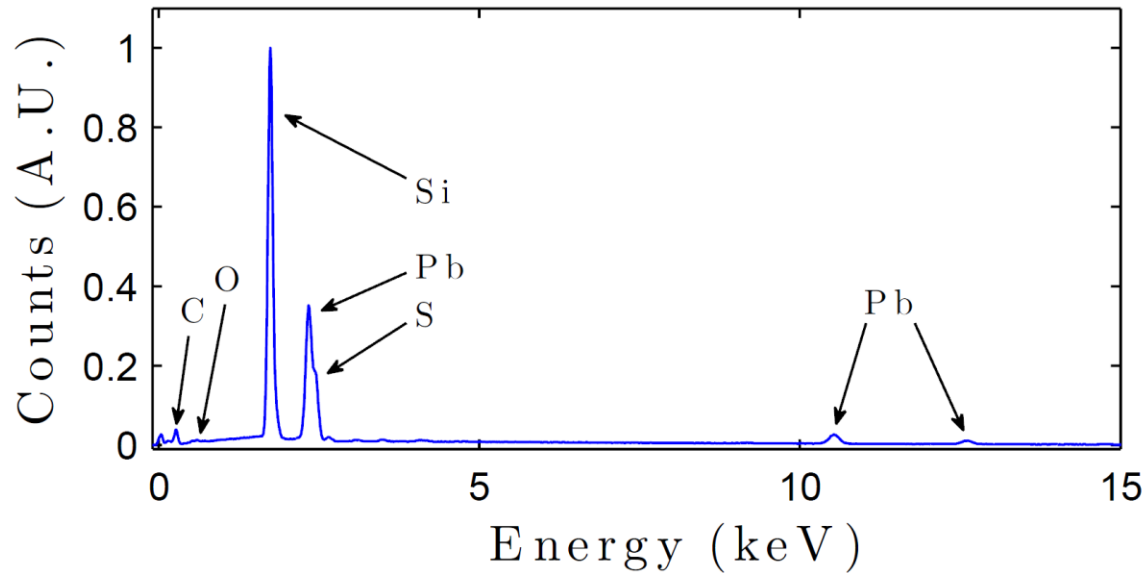


Figure 4.5 EDS spectrum of PbS seeds showing the composition being primarily composed of Pb and S and the Si substrate.

Scratch adhesion tests were performed to test the adhesion of the film. Tests revealed much stronger film adhesion in the seeded samples as compared to the unseeded. An applied force of 0.25 N generated an indent in the film of ~150 nm depth at 200 nm length along the scratch, as compared to ~400 nm depth at the same length in the unseeded samples. The scratch test stylus would penetrate completely through the film to the glass substrate at the length of ~350 nm along the scratch in the unseeded samples. In the seeded sample the stylus perforated the film at lengths over 600 nm. This improvement in adhesion is attributed to the kernels, which became the centers of crystallization during the deposition process. Thus seeding conditions were fixed in order to achieve the same results every time, and only deposition was used as a controlling measure for tuning the film properties.

Film development experiments were designed in such a way to achieve conditions that are easy to implement to produce optimal results (i.e. high mobility, low carrier concentration, and tight crystalline structure) in the shortest deposition times. After the film was deposited the sample was characterized. Deposition at fixed conditions has produced similar physical, electrical, and optical properties.

#### 4.4.2 Deposition temperature variation

For this series of experiments the standard conditions were held constant as discussed in the experimental section, with a deposition time of 1 hour and a stir rate of 50 RPM. Deposition temperature was varied from 30 to 90 °C. Figure 4.6 shows the film parameters, thickness, carrier concentration, and carrier mobility, as a function of deposition temperature over this range. The error bars represent +/- one standard deviation and were achieved through three subsequent experiments at identical deposition conditions. Outliers were verified through two additional experiments under identical conditions and the average and standard deviations are based on the results from all five measurements.

Film thickness decreases steadily from 550 nm to 250 nm with increases in deposition temperature; this is mainly due to the fact that at high temperatures the PbS film gradually decomposes. Carrier concentrations increase significantly before declining gradually with the increase in temperature. The carrier concentrations are roughly two orders above the intrinsic at  $\sim 1.5 \times 10^{18} \text{ cm}^{-3}$ , thus the photoconductive response would not be expected to be high. However, it was possible to obtain lower concentration with a deposition temperature of 25°C by changing deposition time (see below).

An additional experiment was executed at 20 °C. Due to the difficulty of controlling an experiment below room temperature, the experiment did not yield reproducible results. The results of this experiment are not presented on the graph.

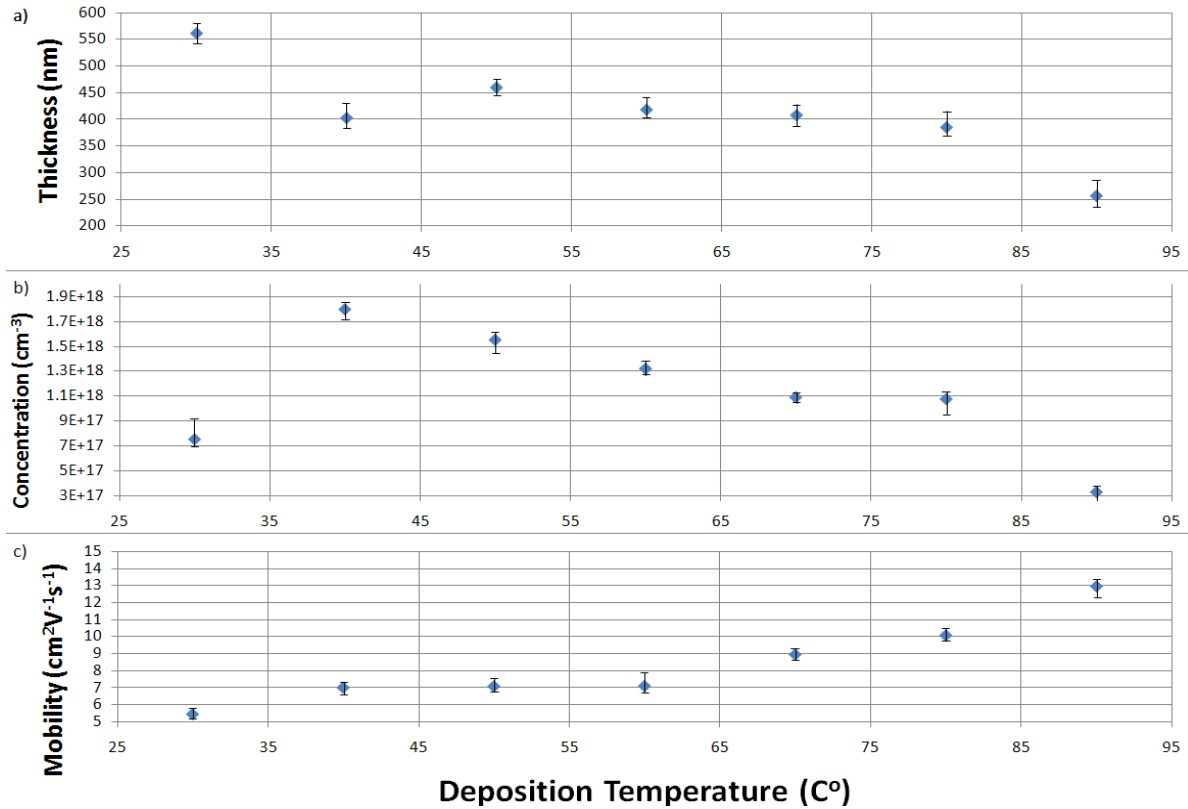


Figure 4.6 Change in film parameters as a function of deposition temperature.

#### 4.4.3 Deposition time variation

For this series of experiments the standard conditions were held constant as discussed in the experimental section. Deposition time was varied from 0.5 to 2 hours. Figure 4.7 shows the film parameters as a function of deposition time over this range.

The optimal deposition time was found to be 0.5 hours (30 min), because at this deposition time carrier concentrations of the film were close to the intrinsic for PbS. While increasing deposition time initially increased the film thickness at deposition times over 1.5 hours (90 minutes), the films progressively eroded, thus decreasing the thickness. This would be expected since the highly acidic solution continues to degrade the film during deposition. As the number of free ions decreases the rate of the film degradation overcomes the rate of film deposition and hence overall diminishment of the film is taking place. Carrier concentrations gradually increased with the increase in deposition times; however, concentrations plateaued at ~50 minutes at a value two orders above the intrinsic at  $\sim 1.3 \times 10^{18} \text{ cm}^{-3}$ . Carrier concentrations show a tendency to gradually rise at deposition times over 100 minutes. Mobility

of the carriers began to decline after 80 minute deposition time, again this is due to the overall film degradation which created an increase in the number of grain boundaries and poor grain compactness, see Figure 4.7. While experiments were conducted with deposition times less than 0.5 hours (30 minutes), SEM imaging showed these films did not have sufficient time to develop good nanocrystalline structure. Overall such films were poor conductors and did not yield good opto-electrical results.

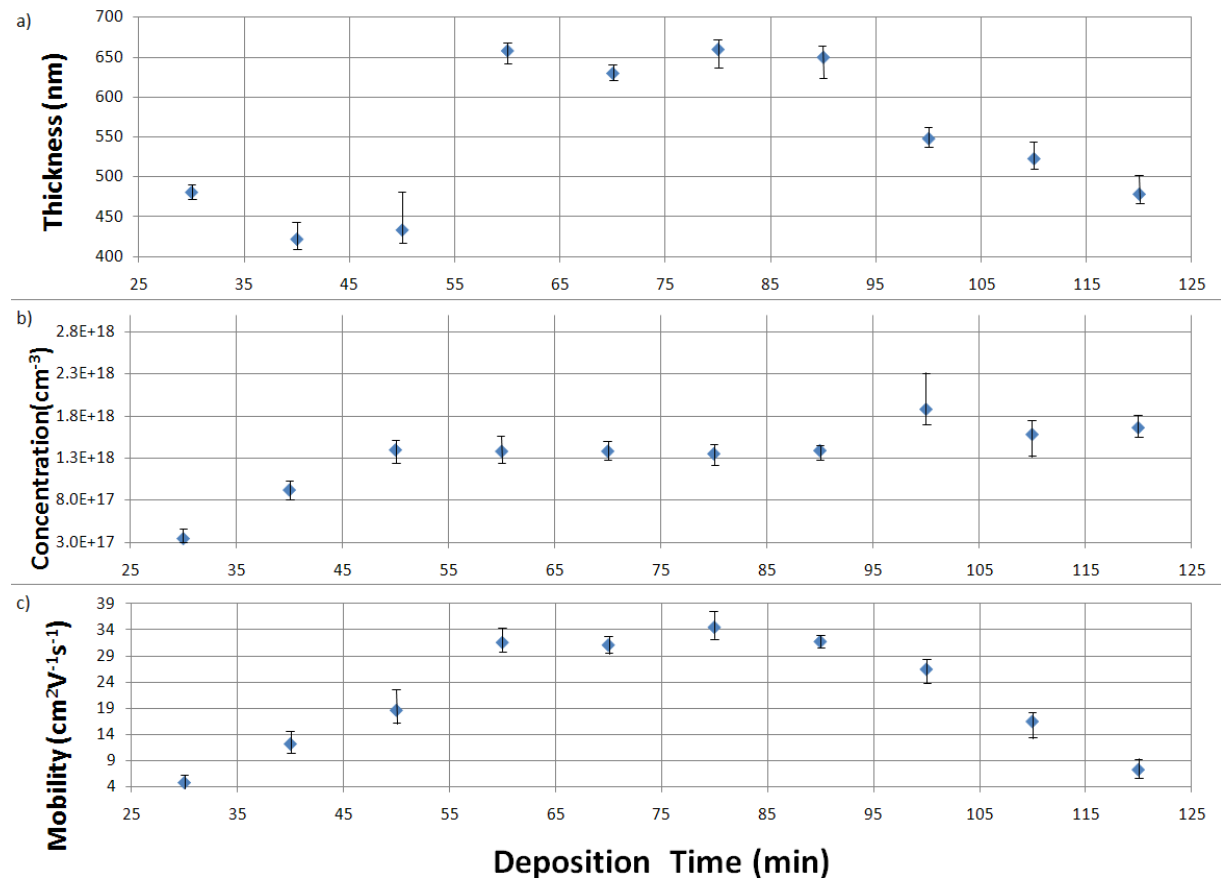


Figure 4.7 Film parameters as a function of deposition time over the range of 30 to 120 minutes.

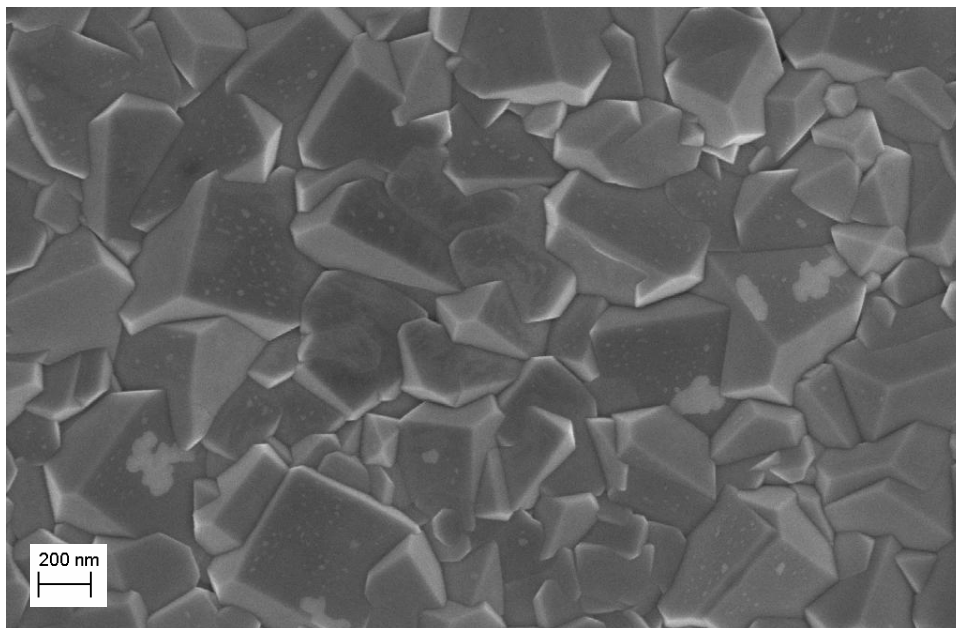
#### 4.4.4 NaOH variation

As previously discussed, control of the acidity/alkalinity of the solution has an overall effect on the growth parameters and overall performance of the films. Hence, hydroxide ion concentrations are expected to effect the concentration of the ionic products ( $\text{Pb}^{+2}$  and  $\text{S}^{-2}$ ) within the chemical bath deposition, and thus growth rate of the film can be controlled by merely controlling the  $\text{OH}^-$  concentrations.

For this series of experiments the standard conditions were held constant as discussed in the experimental section. Deposition temperature was set to 25°C, stir rate at 50 RPM, and deposition time at 30 minutes. NaOH molarity was varied from 0.75 to 3.25 M. The measured film parameters as a function of NaOH concentration are shown in Figure 4.8.

Film thickness varies little around 500 nm as the concentration of NaOH is increased. This can be attributed to the controlled growth of PbS crystals, which resulted in a rather lateral growth of the film, hence having little effect on the thickness of the film. Carrier concentration increases moderately with increasing NaOH molarity; however, it remains close to intrinsic for PbS. Mobility increases significantly as a result of the increase in concentration in NaOH. Such results are expected since the hydroxide ions would gradually saturate the solution with  $\text{Pb}^{+2}$  and  $\text{S}^{-2}$  above the solubility product, resulting in large tightly-compacted crystals and a continuous film.

SEM images reveal a tight crystalline structure achieved from the controlled growth of the crystals. The tight crystalline structure allows for high mobility of the carriers. Images do not reveal a significant increase in the number of crystals with an increase in NaOH concentration. PbS crystals are cubic, however, and do not possess a preferential orientation.



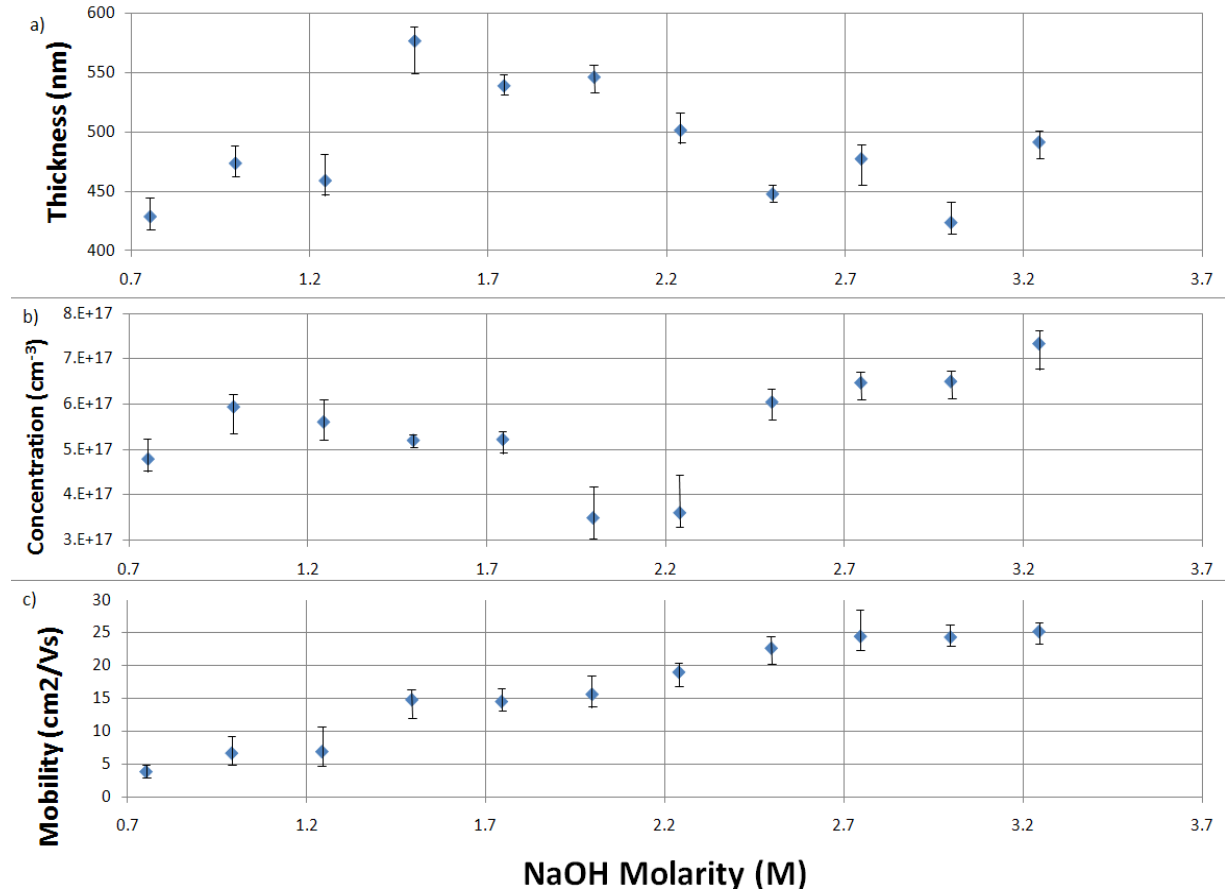


Figure 4.8 SEM image of the film deposited under 2.75 M NaOH (top). Film parameters as a function of NaOH concentration.

Mobility increases steadily with the increase in NaOH molarity. This is mainly due to the controlled and gradual growth of the nanocrystals in the film. Gradual growth of the crystals resulted in large crystals with a tightly packed crystalline structure. Thickness remains nearly constant. While carrier concentration increases gradually, it remains close to the intrinsic.

#### 4.4.5 Carrier lifetime measurements

Carrier lifetimes were measured using the photoconductance decay (PCD) method described by Drummond *et al.* [102]. An excess of carriers was injected through a light source, hence inducing a current. Measurement of the current decay (i.e. photon generated carriers) versus time is the underlying principle in the photoconductive decay method. The radiation of energy (*the absorption of radiation*) increases the conductivity of the semiconductor, which decreases the voltage across the specimen. The specimen voltage change and excess carrier density are

inversely proportional. The time constant of the increase of the specimen voltage when the light is abruptly removed is the photoconductive decay time [104].

Three series of experiments were conducted to measure carrier lifetimes: one with a 980 nm laser, one with an IR-508 (Infrared Systems, Sandcove, CT) cavity blackbody at 800°C, and the final with a cavity blackbody at 450°C. Measurements with the 980 nm laser represent mainly the surface lifetime. The photon energy of a 980 nm laser is  $\sim 1.26\text{eV}$  and the absorption coefficient for the PbS film at such photon energy is  $10^5(\text{cm}^{-1})$  [105]. Computed depth of penetration for such photon energies was found to be around 100 nm, thus ensuring generation mainly of surface carriers. Carrier lifetimes of the nanocrystalline structure measured with the 980 nm laser are shown to be  $\sim 60\ \mu\text{s}$ , while those for crystalline PbS have been extensively studied and shown to be  $\sim 100\ \mu\text{s}$  [106]. The difference in the lifetimes can be attributed to surface generation and recombination.

Measurements with the IR-508 yield information about lifetimes in the bulk material. Measured carrier lifetimes as a function of NaOH concentration are shown in Figure 4.9 where the error bars represent  $\pm$  one standard deviation. Carrier lifetimes increased to  $\sim 70\ \mu\text{s}$  at 800 °C blackbody temperature and  $\sim 95\ \mu\text{s}$  at 450°C. The slight increase in carrier lifetime shows the rate of surface recombination is relatively small. Further, this signifies that most carrier generation occurs in the bulk of the material. Additionally, this is a significant result demonstrating the development of carriers in a broad band of light wavelengths, including far IR wavelengths.

As the temperature of the blackbody was decreased the photo induced signal decayed proportionally. At low blackbody temperatures (i.e. below  $\sim 350\ \text{°C}$ ) the photoconductive decay was no longer visible. Using the oscilloscope in this experimental setup, a signal was visible at blackbody temperatures down to 350°C. However, at such low temperatures the signal was extremely low, a large portion of the signal was lost in the noise, and large error thus resulted in the measured carrier lifetimes. With the enhancement of a low noise amplifier, however, signal at temperatures as low as 350°C could potentially be used for lifetime calculations.

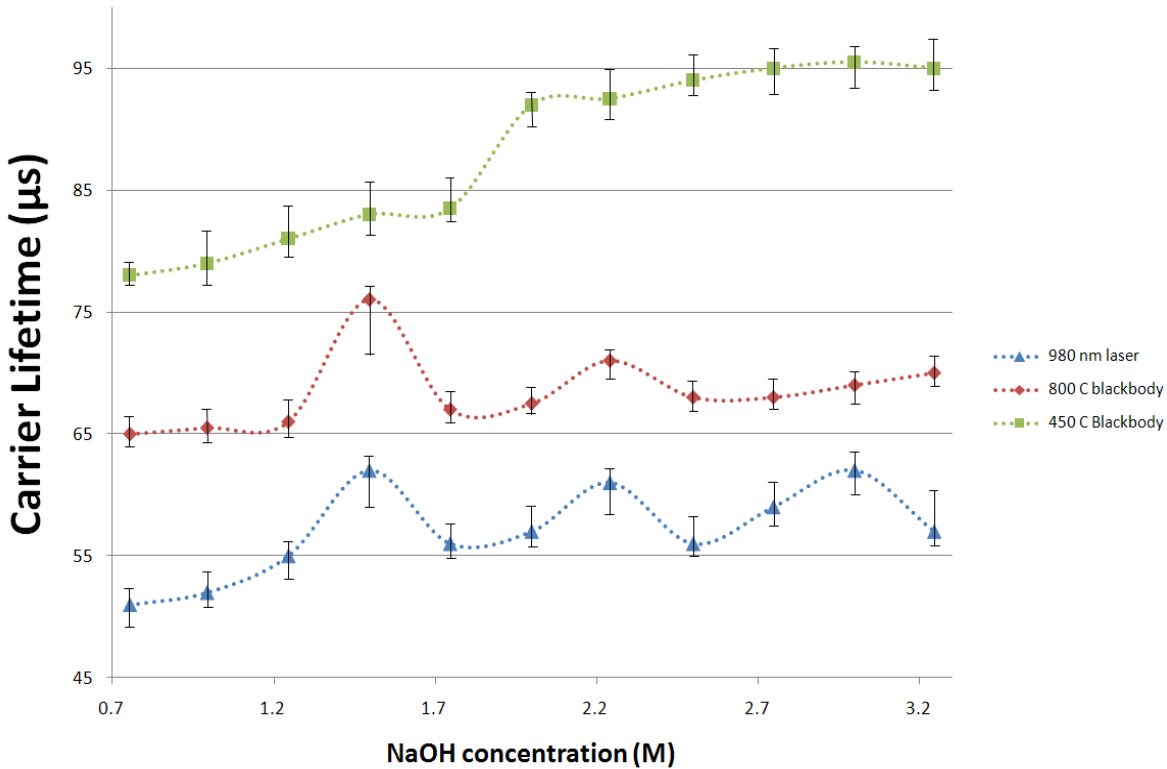


Figure 4.9 Carrier lifetimes increase slightly with the decrease in photon energy, signifying some near surface recombination.

#### 4.4.6 Nanocrystalline structure

Scanning Electron Microscope (SEM) imaging has revealed a tight crystalline structure, as shown in Figure 4.10. This tight crystalline structure allows carriers to easily cross boundaries between the crystals, thus increasing mobility of the carriers; experimentally shown to be up to  $\sim 25 \text{ cm}^2\text{V}^{-1}\text{s}^{-1}$  at standard deposition parameters and NaOH molarity of 2.75. In previous work the highest reported mobility of lead sulfide films was  $\sim 11 \text{ cm}^2\text{V}^{-1}\text{s}^{-1}$  [107].

Additional experiments have been performed to further deposit new layers of PbS on top of previously deposited lead sulfide films. The mobility slowly increases with additional layer deposition; however the carrier concentration remains relatively constant throughout. The resistivity also decreases with additional layer deposition. One possible reason for better film quality with additional depositions can be better crystal quality in the upper layers. As can be seen from Figure 4.10 the first layer is disoriented, but by the third layer cubic crystals about 200 nm wide are visible. This example also

demonstrates that it is possible to deposit relatively thick films with only three depositions. Further, this method demonstrates a possible approach to easy structural alterations in chemical bath through dipping. This could potentially be used as a means to achieve tunable structural, optical, and electrical performance of the device.

The deposition of multiple layers was described earlier, and it involved washing the first layer in DI water to remove any loose particles, drying the film and introducing the substrate into a new bath. Several experiments in which multiple layers were deposited were conducted and Table 4.1 is representative of the results.

Table 4.1 Characteristics of Multiple Deposited Layers

pH	Thickness (nm)	$R_v$ (V/W)	Concentration ( $\text{cm}^{-3}$ )	Mobility ( $\text{cm}^2\text{V}^{-1}\text{s}^{-1}$ )	$\rho$ ( $\Omega \cdot \text{cm}$ )	Molarity (M)
12.86	400	172	$6.9 \times 10^{16}$	3.34	26.92	<b>Deposition Solution:</b> 0.033 M lead acetate 0.133 M thiourea 0.079 M $\text{Na}_2\text{SO}_3$ 0.35 M KOH
12.8	1500	344	$6.6 \times 10^{16}$	4.7	20.4	<b>Seed solution:</b> 0.111 M lead acetate 0.114 M KOH 0.53 M thiourea
12.77	2307	89	$7.4 \times 10^{16}$	15.4	5.6	

As can be seen, the mobility slowly increases with additional layer deposition, however the carrier concentration remains relatively constant throughout. The resistivity also decreases with additional layer deposition. One possible reason for better film equality with additional depositions can be better crystal quality in the upper layers. As can be seen from Figure 4.10, the first layer is disoriented, but by the third layer cubic crystals of about 200 nm wide are visible. This example also demonstrates that it is possible to deposit relatively thick films with only three depositions.

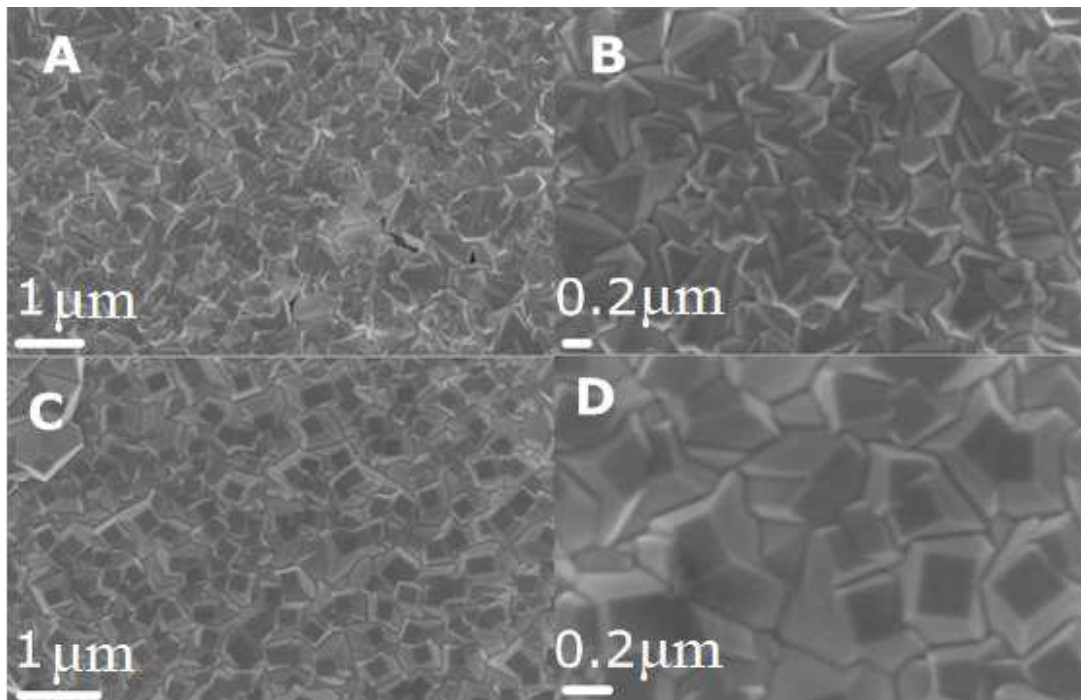


*Figure 4.10 Scanning electron microscope images reveal tight crystalline structure in (a) and (b), additional deposition creates larger and better oriented cubic crystals of about 200 nm (c) and (d).*

A series of experiments was also conducted in which the stir rate of the chemical bath was altered. Although there were noticeable structural changes in the films, the overall opto-electrical performance was insignificant. The opto-electrical characterization is omitted, however, SEM images of the stir rate PbS films are shown in Figure 4.11.

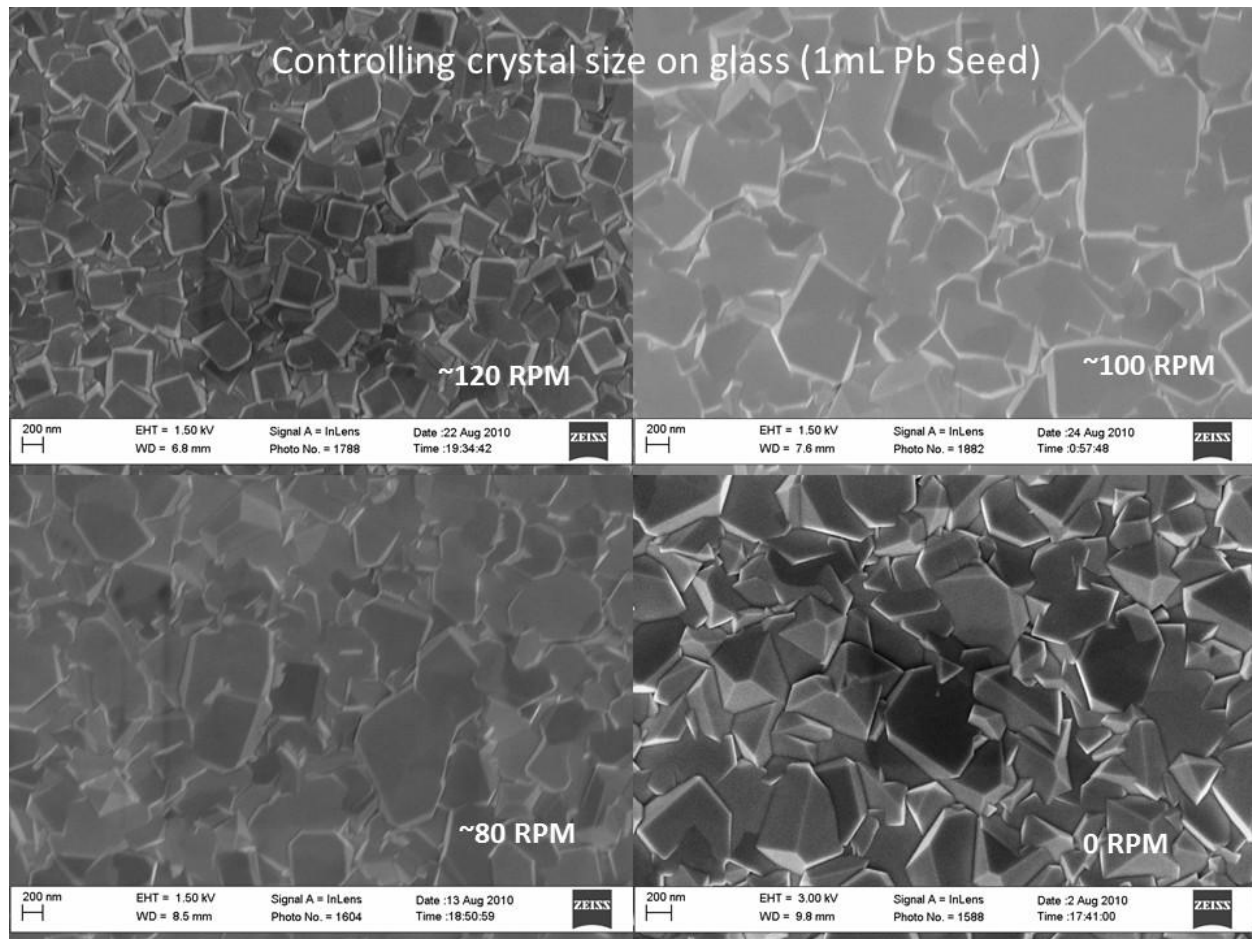


*Figure 4.11 Scanning electron microscope images from the stir rate experiments. Tight crystalline structure is shown with noticeable changes in the crystal sizes.*

XPS analysis was conducted on samples over 30 days old to test the film composition. XPS energy was adjusted to show film composition at a depth of  $\sim 7$  nm. Initial XPS analysis revealed a layer of oxide. Hence the sample was sputter etched with an ion beam for 30 seconds, removing  $\sim 10$  nm of the top layer and reanalyzed for composition. After 90 seconds of sputter etching, or  $\sim 30$  nm of film removal, the film showed a nearly one to one ratio of Pb and S. Amounts of oxide and other contaminants at depths below  $\sim 30$  nm become negligible. The above analysis shows the film is resistant to oxidation even over prolonged periods of time. Results of XPS are shown in Figure 4.12.

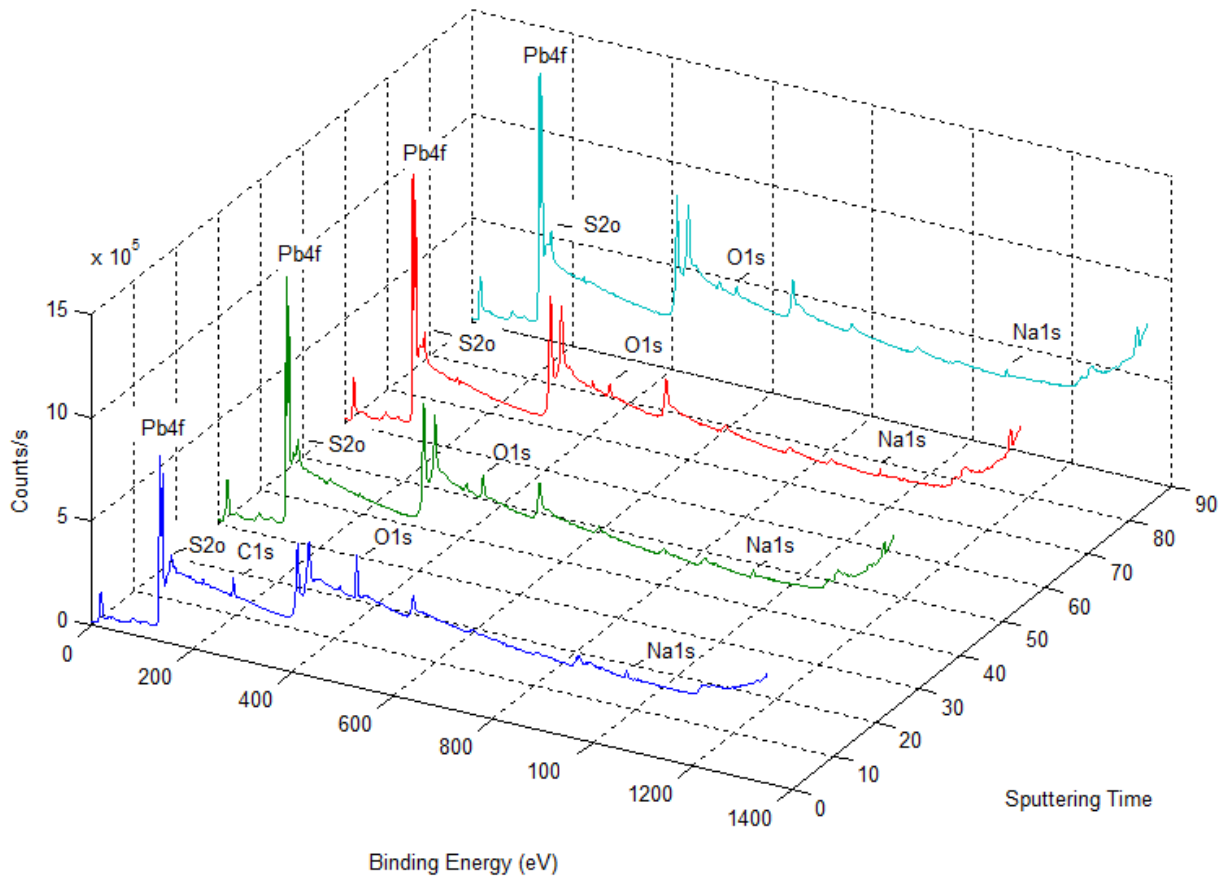


*Figure 4.12: XPS analysis reveals oxidation at surface. Amounts of contaminants decreases with the increase in sputter etching times, and become negligible after 90 s of etching.*

All samples of interest deposited with NaOH variation were re-characterized for the thickness, reflection, transmission, carrier concentration, and mobility 20 and 30 days after the initial characterization. Table 4.1 shows these data for a sub-set of those samples with the highest mobility and lowest carrier concentration. As clearly seen, there was no noticeable change in the above mentioned parameters over this timeframe, despite the fact the samples were simply stored in air and not encapsulated, as would be done in practical applications. This steady performance is a new phenomenon in PbS films. Most likely this is due to the fact that these samples do not develop an oxidation layer and the tight crystalline structure prevents decomposition.

*Table 4.2. Film parameters after a period of time*

Thickness (nm)	Carrier Concentration ( $\times 10^{17} \text{ cm}^{-3}$ )	Mobility ( $\text{cm}^2 \text{V}^{-1} \text{ s}^{-1}$ )
----------------	--	---

NaOH Molarity (M)	Initial	20 days	30 days	Initial	20 days	30 days	Initial	20 days	30 days
2.75	479	478	478	6.47	6.46	6.46	24.5	24.5	24.5
3.0	424	424	424	6.50	6.49	6.49	24.4	24.4	24.3
3.25	493	493	492	7.34	7.33	7.33	25.2	25.2	25.2

#### 4.5 Conclusion

A chemical bath deposition procedure for growing thin film semiconducting nanocrystalline PbS is presented. Growth of PbS nanocrystals is achieved by controlling the reactant ion concentrations in the chemical bath. Chemical bath deposition is a simple technique that avoids the use of expensive equipment or a clean room, with all experiments conducted in a fume hood in a basic laboratory setting, hence reducing the cost of manufacturing such materials. In order to achieve reproducibility, a seeding procedure was devised in which kernels were planted on the substrate. This resulted in a lateral growth of the deposited film and the film was shown to adhere firmly to the substrate and to have a tightly compacted nanocrystalline structure, with high mobility, close adherence to stoichiometry, and low impurity concentrations. The effects of deposition temperature, deposition time, and hydroxide ion concentrations on the resulting electrical, optical and physical properties were examined. A set of conditions yielding desirable film properties for use in photovoltaic applications was identified. It should be noted, however, that each factor was examined independently and any interaction effect of these variables was not considered. A statistically designed experiment would be necessary to completely access these potential interaction effects. Deposited films were also extremely resistive to oxidation and did not decompose over time. In fact, we believe these especially encouraging results are due to the tight crystalline structure, which prevents degradation of the film, and is exceptionally resistive to oxidation. This is a new phenomenon in PbS films.

## Chapter 5. Cadmium Sulfide

### 5.1 Introduction

Cadmium sulfide (CdS) is an important direct wide bandgap semiconductor material, with an energy bandgap of  $\sim 2.42$  eV which falls in the visible spectrum at room temperature [109]. Cadmium sulfide is one of the most important and well-studied semiconductors in the industry. This chapter is dedicated to the growth, development, and characterization of thin film CdS. Some of the presented material is prepared to be published by Slonopas et al. in the Material Science in Semiconductors.

CdS has been the subject of intensive research due to: i) its high absorption coefficient at energies slightly above the forbidden gap; ii) electron affinity compatible to lead sulfide (PbS); iii) the ease of making ohmic contact with Au; and, finally, iv) the cubic and hexagonal crystal structure [110]. Applications for CdS materials are extremely broad. Such materials have been used, integrated, or proposed for use in: photodetector applications [111], solar absorber coatings [112], solar control coatings [113], buffer layers in thin film solar cells [114], mid-IR photovoltaics [115], and numerous other applications [116].

Numerous studies have been used in what is commonly known as the standard deposition bath. In the standard bath cadmium salt, thiourea, and ammonia for the  $pH$  regulation is used. In the standard bath temperatures ranged from  $60 - 90$  °C, and a wide gap of Cd concentrations ranging from 1 mM to 100 mM.

As previously discussed CdS has two predominant structures, hexagonal (wurtzite) and cubic (zincblende). Each crystallographic phase of the material has unique set of electrical and optical properties. Detailed studies have shown that it is possible to form either hexagonal or cubic structures by merely controlling the  $NH_4^+$  concentrations in the solution [62]. Most commonly, however, the standard deposition bath produces a mixed composition of hexagonal and cubic phases [108]. These results are explained by Ortega-Borges et al. by explaining the deposition kinetics of the CdS [86]. Using fractional values of the reaction order they were able to measure the deposition rate of the film. They concluded that there were several rate-determining steps. Given the small energy differences for these steps for both the wurtzite and the zincblende structures, thus both cubic and hexagonal structures were randomly forming on the substrate.

In the course of this research a novel chemical bath deposition technique was developed for growing thin film semiconducting nanocrystalline cadmium sulfide (CdS) for use in photovoltaics. The goal of this work was to produce quality crystals, with a high mobility of holes and electrons required for effective carrier separation in photovoltaic applications, and to control other electro-physical properties. Tightly attached, densely compacted, nanocrystalline CdS films with tunable electrical, physical, and optical properties were deposited. Adherence to the substrate was attained by the ion-by-ion growth mechanism dominating the growth process.

Nanocrystalline structures were precipitated onto the substrate by controlling the deposition temperatures. Using this approach nanocrystalline thin film CdS layers with controllable thicknesses, grain sizes, and lattice parameters were expanded. SEM images show rigid crystalline structure. Ellipsometry analysis shows ion-by-ion as the dominating growth mechanism. Hall Effect and spectroscopy measurements illustrate tunable electrical, physical, and optical properties. Carrier concentrations were achieved between  $1 \times 10^{17} / \text{cm}^3$  -  $8 \times 10^{18} / \text{cm}^3$  and mobility ranged between  $7.8 \text{ cm}^2/\text{Vs}$  -  $33.8 \text{ cm}^2/\text{Vs}$ . Photoconductivity was measured using a 515 nm laser, ensuring carrier generation in the bulk of the material. Prolonged exposure to air confirms resistance to oxidation, and stability of the optical and electro-physical parameters.

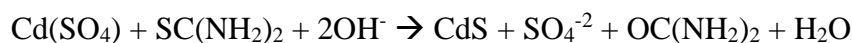
## 5.2 Experimental

### 5.2.1 Synthesis

Film depositions were done on glass slides (25 mm x 75 mm x 1 mm) substrates. Prior to deposition, substrates were cleaned to remove organic contaminants from the surface using RCA-1 cleaning solution [117]. Glass slides were placed in the boiling solution of 1:1:5 27%  $\text{NH}_4$ :30%  $\text{H}_2\text{O}_2$ : $\text{H}_2\text{O}$  for 15 minutes. After the elapsed time, slides were rinsed with deionized water, and dried with compressed nitrogen before use.

Deposition solution contained 30 mL of cadmium sulfate monohydrate [ $\text{CdSO}_4 \cdot \text{H}_2\text{O}$ ] with a concentration of 0.1 M, mixed with 12 mL of 1 M sodium citrate dihydrate [ $\text{HOC}(\text{COONa})(\text{CH}_2\text{COONa})_2 \cdot \text{H}_2\text{O}$ ], 30 mL of 1 M  $\text{NH}_4\text{OH}$ , and 10 mL of 1 M thiourea [ $\text{CH}_4\text{N}_2\text{S}$ ] [118]. All solutions were added in the sequence as described above, and enough deionized water was added to make the deposition bath a total volume of 100 mL. Solutions were mixed in a sealable beaker. The substrates were then placed into the deposition solution with stir rate set to 90 RPM (required for uniform growth). A 100 mL beaker containing the deposition bath was maintained at  $95^\circ \text{C}$  for 15 hours, and a tight seal was placed over the beaker in order to prevent escape of the  $\text{H}_2\text{S}$  gases. Optimal time, temperature, and constituent concentrations were determined using experimental data acquired from a series of experiments. Good quality and high photoconductivity were shown by films deposited from the 1:0.33  $\text{CdSO}_4$  to thiourea ratio, however, equally high quality films were reported using other ratios of the constituents [119]. The solubility product of CdS is very low, i.e.  $\sim 3 \times 10^{-29}$ , suggesting that very low ionic concentrations are sufficient for film deposition in the case of CdS [120].

Literature offers a very well established elucidation for the reaction [121]. Highly alkaline solution decomposes thiourea to release  $\text{S}^{2-}$  ions. Additionally, the deposition solution releases  $\text{Cd}^{+2}$  from the  $\text{CdSO}_4$ .  $\text{Cd}^{+2}$  ions precipitate with the  $\text{S}^{2-}$  ions in the solution [119].



In our work, breaking apart the constituents was done by controlling the  $\text{OH}^-$  concentration in the deposition bath. Alkalinity of the bath was measured to be  $\sim 11$  pH, excessive addition of the  $\text{NH}_4\text{OH}$  did not have a profound effect on the basicity of the solution. Raising the fraction of  $\text{NH}_4\text{OH}$  did however, have an intense effect on the rate at which ionic products saturated the solution. The rate of precipitation was in part controlled by the proportion of  $\text{NH}_4\text{OH}$  in the emulsion. This gave a rather finely tunable method of controlling the growth of CdS.

Once deposition was complete, samples were immediately placed into an open horizontal kiln for annealing. Samples were placed and removed from the kiln heated to the annealing temperature to ensure rapid heating and cooling of the samples. We observed that films have most desirable electrical properties at annealing temperatures of  $450^\circ\text{C}$  and annealing times of 1 hour.

### 5.2.2 Solid state nuclear magnetic resonance spectroscopy (NMR)

A Varian 9.4T VNMRs 400 MHz spectrometer was used to collect nuclear magnetic resonance (NMR) spectra.  $^{113}\text{Cd}$  magic angle spinning (MAS) experiments were performed by rotating a 4 mm zirconia rotor, containing 100-150 mg of sample, at half the tetrahedral bond angle relative to the static magnetic field. A free induction decay was acquired using a spin-echo experiment calibrated on cadmium perchlorate hydrate (Sigma-Aldrich, St. Louis, MO). The interpulse delay (between the  $\pi/2$  and  $\pi$  pulse) was rotor synchronized to  $100\ \mu\text{s}$ , corresponding to a spin rate of 10 kHz. All experiments were recorded at  $20^\circ\text{C}$  using the Varian spectrometer variable temperature controller with a stability of  $0.1^\circ\text{C}$ . Data was Fourier transformed and processed using custom routines written in the Wolfram language.

### 5.2.3 Temperature dependent Hall effect (TDH)

TDH measurements were carried out in the range  $200\text{--}350\ \text{K}$  in a closed-cycle helium cryostat using the van der Pauw geometry according to ASTM F76-86 [122]. An electromagnet provided a magnetic field of 1 T for Hall measurements. In order to improve the accuracy of the measurement three measurements at each temperature were taken, after a holding time of 5 minutes to ensure full thermalization of the sample. Samples were cut to the size of  $9\ \text{mm} \times 9\ \text{mm}$  and placed in the sample holder. Selected samples had very low dislocation densities, in order to avoid any effect attributable to carrier trapping. Ohmic contacts were made using Ag on the corners of the sample.

### 5.2.4 Optical spectroscopy

Optical transmission and reflection spectra were obtained at room temperature between 400 and 800 nm using a Cary 300 UV-VIS spectrophotometer at  $300^\circ\text{K}$  with an integrating sphere for light collection.

The relation between the optical energy gap and absorption can be determined using Tauc's equation:

$$\alpha = \frac{K(h\nu - E_g)^{n/2}}{h\nu} \quad (5.1)$$

where  $K$  is a constant,  $E_g$  is the optical bandgap, and  $n$  is equal to 1 for a direct bandgap material such as CdS [123]. The bandgap  $E_g$  was determined for each film by plotting the Kubelka-Munk function ( $F(R)$ ) versus  $h\nu$  and then extrapolating the straight line portion to the energy axis.

### 5.2.5 Photo-responsivity

The photo-responsivity at 25 °C was determined using a Concepts Research Corporation (CRC) BOREAS G30 laser operating at 515 nm as the excitation source. BOREAS operates at a 20 kHz pulse rate and has a pulse width of about 12 ns full width at half maximum (FWHM), with pulse energy equal to 0.3 mJ. The laser beam was redirected and spliced using a ThorLabs Optical Beamsplitter. One beam was sent to a sensor to be used as reference, and the second beam illuminated the sample. The AC photoconductive signal was taken from a matched load resistance and measured using a Tektronix MSO/DPO2000B Mixed Signal Oscilloscope, and the circuit was biased at 10 V DC. Carrier lifetime was determined from a signal as a function of time using the photoconductance decay method [102]. The photon energy of a 515 nm laser is ~2.4 eV and the absorption coefficient for the CdS film at such photon energy is  $10^5(\text{cm}^{-1})$  [124]. Calculated depth of penetration was found to be ~800 nm, ensuring carrier generation in the bulk of the material.

## 5.3 Results

### 5.3.1 Physical and structural properties

Conditions that are easy to implement and produce optimal results (i.e. high mobility, low carrier concentrations, and tight nano-crystalline structure) in the shortest deposition times were considered prior to film development experiments. Films prepared by chemical bath deposition were found to possess uniform nano-crystalline structure, adhere tightly to the substrate and resist abrasion. After the film was deposited the sample was characterized. Deposition at fixed conditions has produced similar physical, electrical, and optical properties.

Films grown by the CBD method were found to have various advantages over those produced by other techniques (i.e. chemical vapor deposition, epitaxial growth, physical vapor deposition). CdS deposited by the CBD methods were found to be rather insensitive to moisture and oxygen variations. The results were reproducible in physical, structural, and opto-electric properties. In this study un-doped films were studied in order to produce intrinsic or nearly intrinsic properties of the film, which are reported to be  $10^{14} \text{ cm}^{-3}$  [125], for future utility in a p-n junction with narrow bandgap materials.

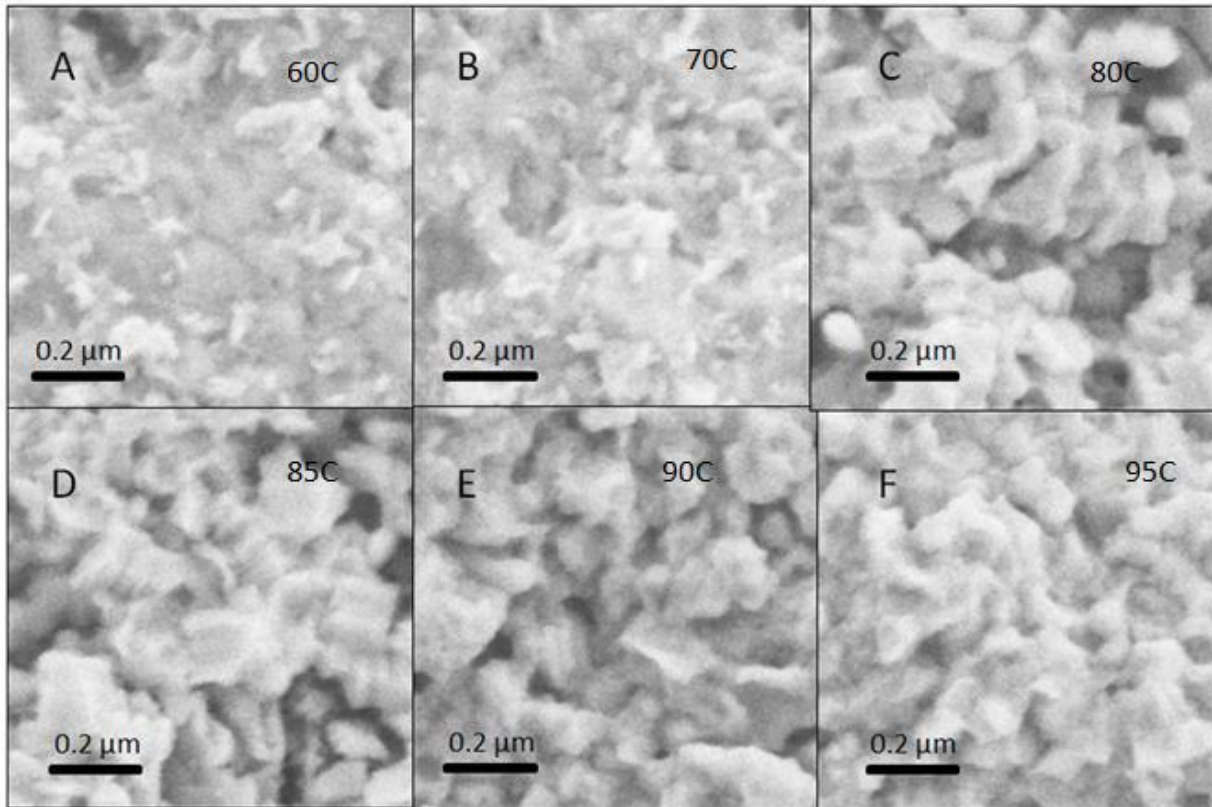


*Figure 5.1 Scanning electron microscope images reveal crystal formation beginning to take shape in low deposition temperature samples in a), b), and c). Tight crystalline structure is visible at higher deposition temperatures d), e), and f).*

Figure 5.1 shows the crystalline structure as a function of deposition temperature. Low deposition temperatures of 60 °C, 70 °C, 80 °C show some crystal formation taking place, whereas higher temperatures show a very well established nano-crystalline matrix. Images also reveal a tight crystalline structure developing at higher deposition temperatures. Additionally, SEM images reveal no oxidation layer (or a virtually unnoticeable oxidation layer) on the film.

The tight crystalline structure and absence of oxidation layer allows carriers to easily cross boundaries between the crystals, thus giving good mobility of the carriers. The crystalline structure is tighter at higher deposition temperatures, hence the highest mobilities of 33.8 cm<sup>2</sup>/Vs at room temperatures were observed at deposition temperatures of 95 °C.

CdS crystalline structure was also studied using XRD analysis. The diffraction spectra for post-deposition thermally annealed samples are shown in Figure 5.2. This figure shows that the diffraction peaks of the samples deposited at low temperatures (i.e. 50 °C, 60 °C) appear weak due to small grain size, and/or the film was too thin to acquire adequate data. Data suggests that at the low temperatures Cd<sup>+2</sup> and S<sup>-2</sup> ions did not saturate the bath at rates high enough to allow for sufficient film growth to take place.

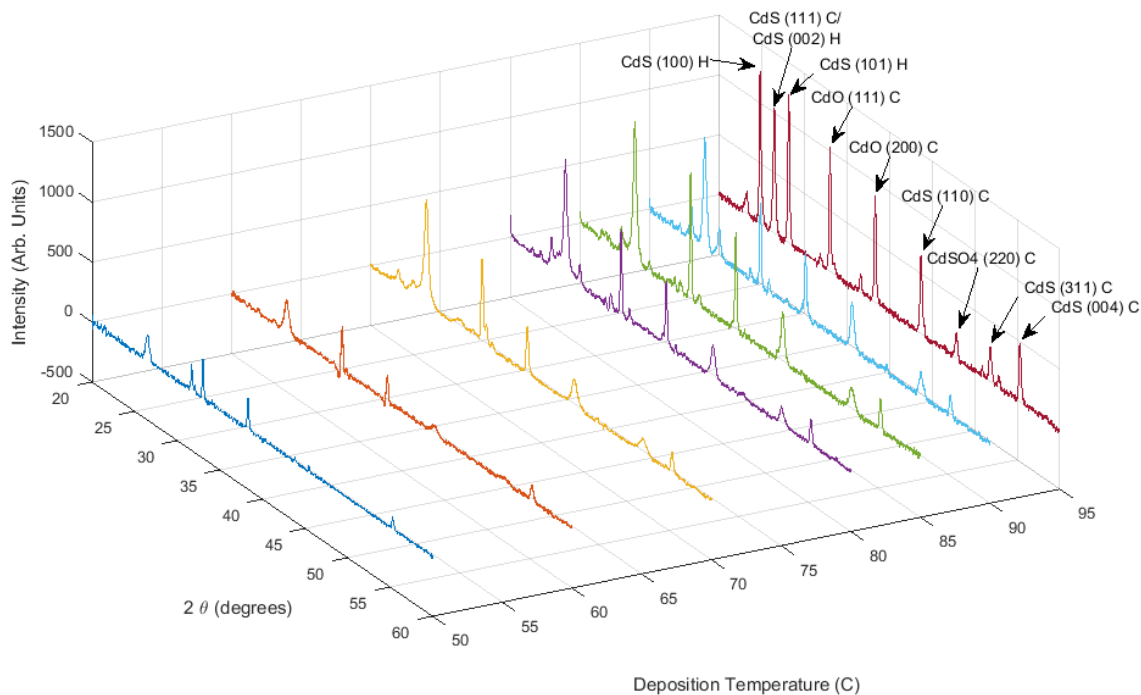


Figure 5.2 XRD spectra of thin film CdS deposited at various bath temperatures, after thermal annealing.

Diffraction patterns show an intense peak located at  $26.6^\circ$ , associated with the (111) plane of the cubic (zincblende) structure, and (002) hexagonal (wurzite) CdS [126]. This peak intensifies with increasing temperature, but is eventually surpassed by the peaks located at  $24.7^\circ$  and  $28.1^\circ$ , which correspond to the hexagonal CdS structure in the (100) and (101) planes, respectively [127]. This observation suggests a phase transition taking place at higher temperatures. Cubic-hexagonal phase transition has been reported in CdS after heat treatment at temperatures ranging from  $300 - 400^\circ\text{C}$  [128]. In the present study only a fraction of the cubic structure transitions to the hexagonal modification, resulting in a fusion of two structures. Additionally, CdO diffraction peaks are observed at  $32.9^\circ$  and  $38.2^\circ$  [129]. Formation of CdO is explained by the transformation of the cubic phase at high temperatures, which is unstable in comparison to the hexagonal CdS, thus yielding CdO [130].

Chemical structure and surface investigations were carried out using solid-state  $^{113}\text{Cd}$  MAS-NMR spectroscopy. A total of 1024 spin-echo transients were acquired to elucidate two lines at 701 and 728 ppm (see Figure 5.3). The peak at 728 ppm has a half height line width of around 25 ppm and is assigned to bulk CdS, which is in agreement with previous reports [131-132]. The zincblende and wurzite conformational states of CdS are indistinguishable from one another using NMR as they occupy the same chemical shift region of the spectra. The isotropic chemical shift anisotropy is determined by the 4s orbital, which is identical for both cubic and hexagonal CdS. The line at 701 ppm can be attributed to unreacted surface Cd atoms present in the sample.

The unreacted Cd line is comparatively narrow with respect to the bulk CdS line, a result stemming from the wide range of  $T_1$  values exhibited by Cd atoms in bulk CdS [131]. At the intersection of the two peaks a noisy flat region can be observed at around 715 ppm. This is caused by spurious short wave radio frequencies only partly suppressed with signal averaging (note that  $^{113}\text{Cd}$  has a frequency of 88.8 MHz at 9.4 T). The  $^{111}\text{Cd}$  nuclei was observed, in a similar spin-echo experiment as described above, to confirm that this interstitial area between the peaks did not contain further information.

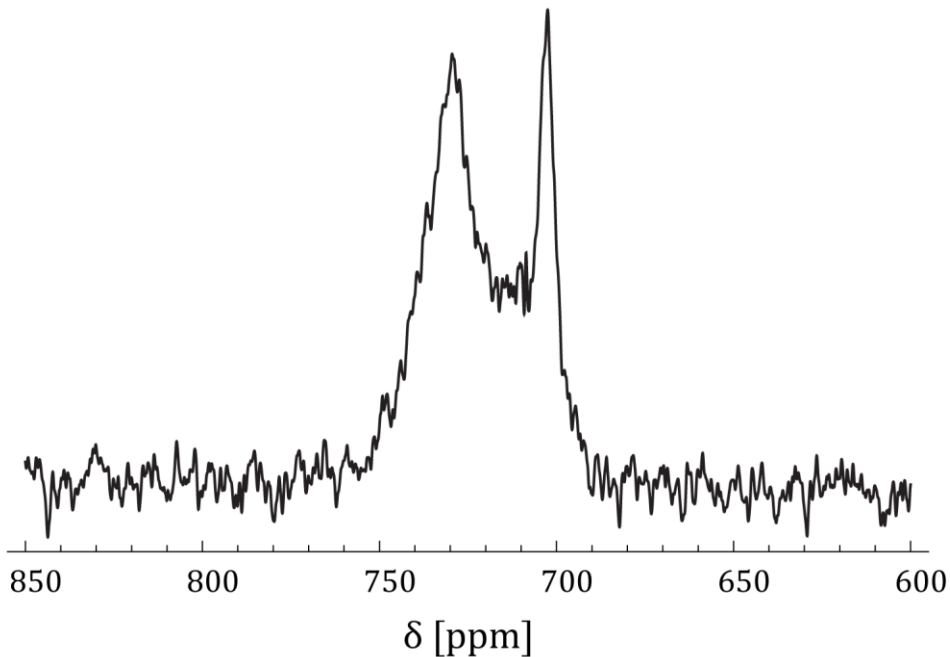
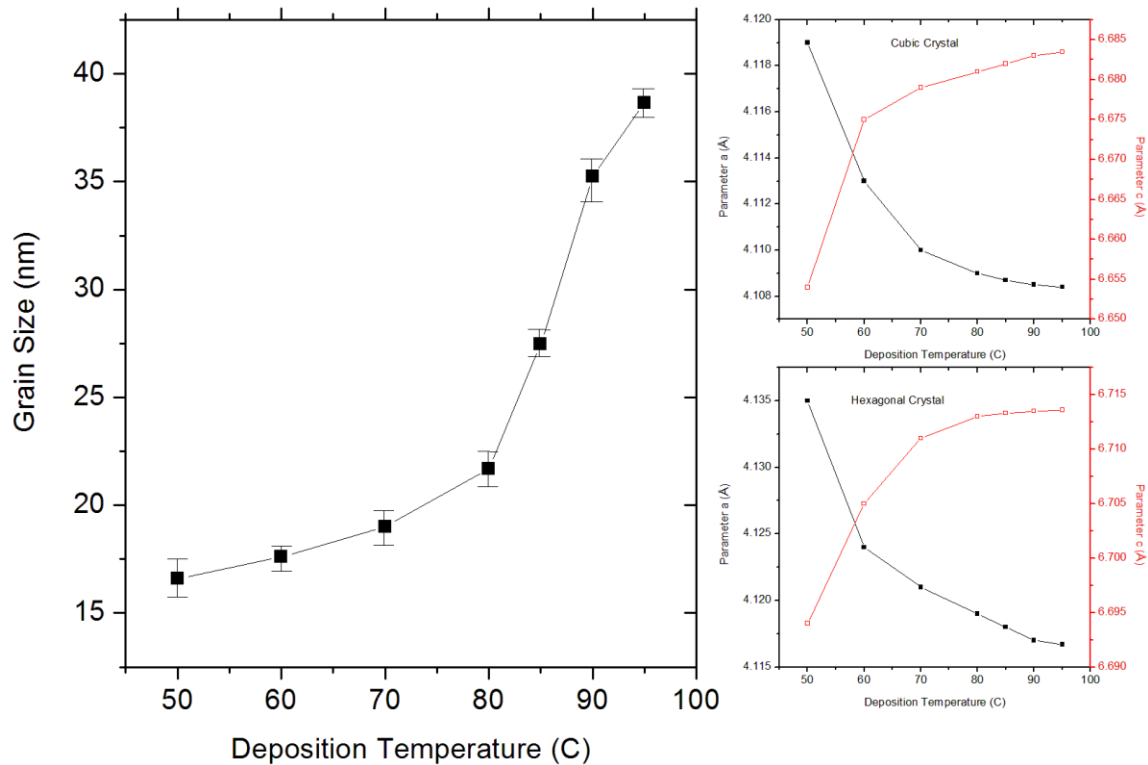


Figure 5.3  $^{113}\text{Cd}$  spectra acquired using a 1024 scans spin-echo experiment with a recycle time of 150s.

Grain sizes and lattice parameters for both the cubic and hexagonal crystalline structure as a function of deposition temperature are shown in Figure 5.4. The error bars represent  $\pm$  one standard deviation based on three repeated experiments at identical deposition and measurement conditions. When an outlier was perceived, two additional experiments were conducted at identical conditions and the average and standard deviations are based on the results from all five measurements.

Grain sizes as well as the lattice parameters are directly controlled by the parameters of the chemical bath. Grain sizes increase exponentially with the increase of the bath temperature reaching a maximum size of 38.6 nm. Such increase can be explained by variation in growth rate. The lattice parameter,  $c$ , in both the cubic and hexagonal crystal increases with an increase in bath temperature. Meanwhile lattice parameter  $a$  in both crystalline structures decreases. This signifies that both the cubic and hexagonal structures are becoming increasingly distorted with

the increase in temperature. Such distortions are believed to have a direct effect on opto-electrical properties of the film.



*Figure 5.4 Grain sizes and lattice parameters for cubic and hexagonal crystalline structures as a function of deposition temperature.*

Figure 5.5 shows microstrain ( $\epsilon$ ), dislocation density ( $\delta$ ), and number of crystallites per  $\text{m}^2$  ( $N$ ) as a function of bath temperature. Strain can either be tensile or compressive, which is caused by non-equilibrium microstructure formations. It was observed that elastic energy is stored in the films due to stresses associated with the strain. When stored energy was larger than the adhesive energy, the deposited film would peel off, hence microstrain is directly related to film adhesion to the substrate [133]. Microstrain is observed to decrease with the increase in deposition temperature, making the film more scratch resistant and more firmly attached to the substrate.

Dislocation densities have been shown to have a direct effect on electrical properties of thin films. It has been shown that minimization of dislocation densities increases overall mobility of thin films [134]. This can be attributed to a decrease in defects in the film. The dislocation density decreases with the increase in deposition temperature, due to the increase in grain boundary size, which results in a more compact structure of the film.

The number of crystallites decreased with increased bath temperature. The observation that the number of crystallites decreased with the number of dislocation densities indicates that the crystallites were becoming larger in size. A conclusion also supported by the observation of larger grain size.

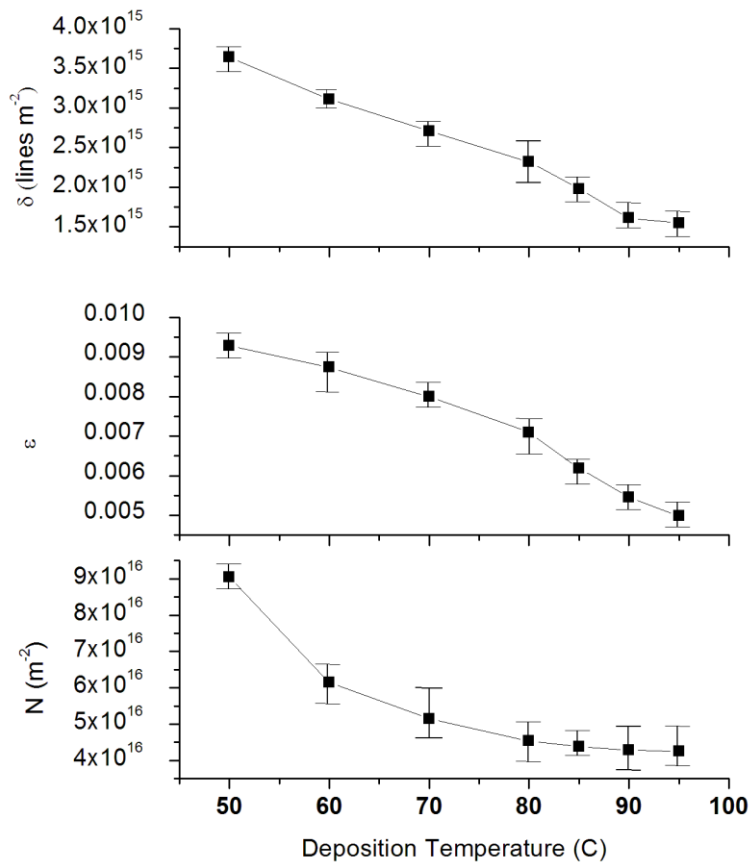


Figure 5.5 Number of crystallites per  $m^2$  ( $N$ ), dislocation density ( $\delta$ ), and microstrain ( $\epsilon$ ) as a function of deposition temperature.

The increase in grain and crystallite size suggests thicker films at higher deposition temperatures. This was in fact observed from interference spectroscopy and further validated by spectroscopic ellipsometry and profilometry. Film thicknesses as a function of grain size are shown in Figure 5.6.

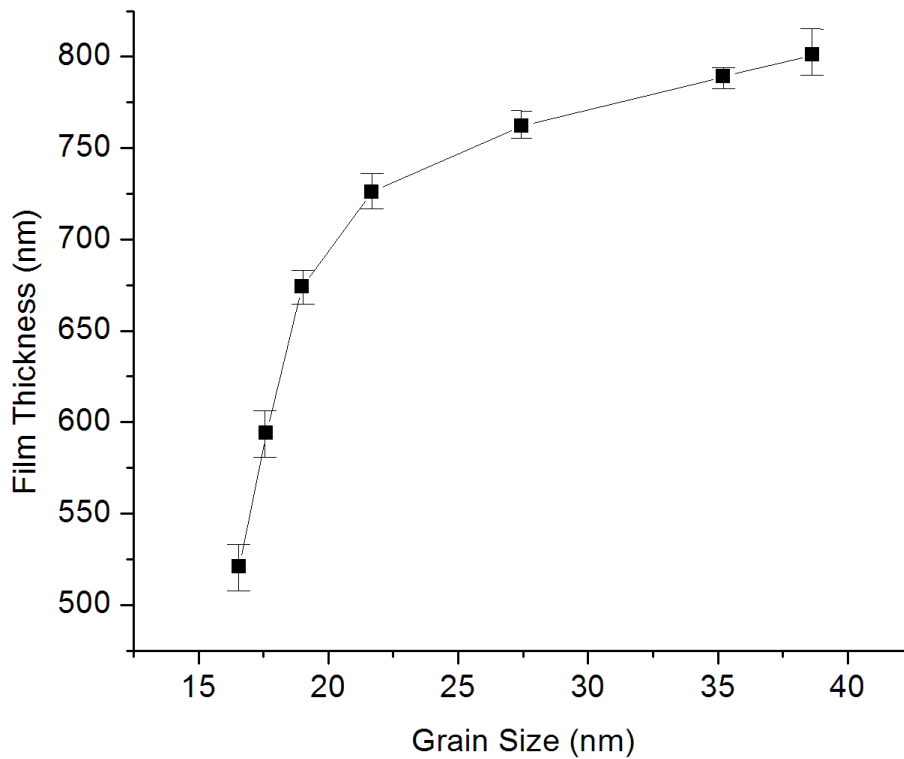


Figure 5.6 Film thicknesses as a function of grain size.

### 5.3.2 Optical properties

Plots of the experimental  $\Psi$  and  $\Delta$  ellipsometric spectra for films deposited at various bath temperatures are shown in Figure 5.7. Points on the graph are the experimental values for the  $\Psi$  and  $\Delta$  as measured by the optical ellipsometry instrument. Solid lines are the best fit curves for the physical model. Physical models were constructed to incorporate film layer thickness for the experimental data analysis. The physical model consisted of quartz glass and the thin CdS film. Films are assumed to have three layers: bottom compact layer grown by the ion-by-ion mechanism, a middle less compact layer of CdS grown by ion-by-ion and cluster-by-cluster mechanisms, and a top roughness layer [135]. Although the depositions were made in an air-tight beaker, the middle porous layer was assumed to have CdS clusters mixed with air. It was noticed that the best curve fits were achieved when the fractions of air were negligibly small, indicating negligible amounts of air and low porosity through the entire thickness of the sample. Further, these results suggest ion-by-ion as the primary growth mechanism for the entire duration of the film growth.

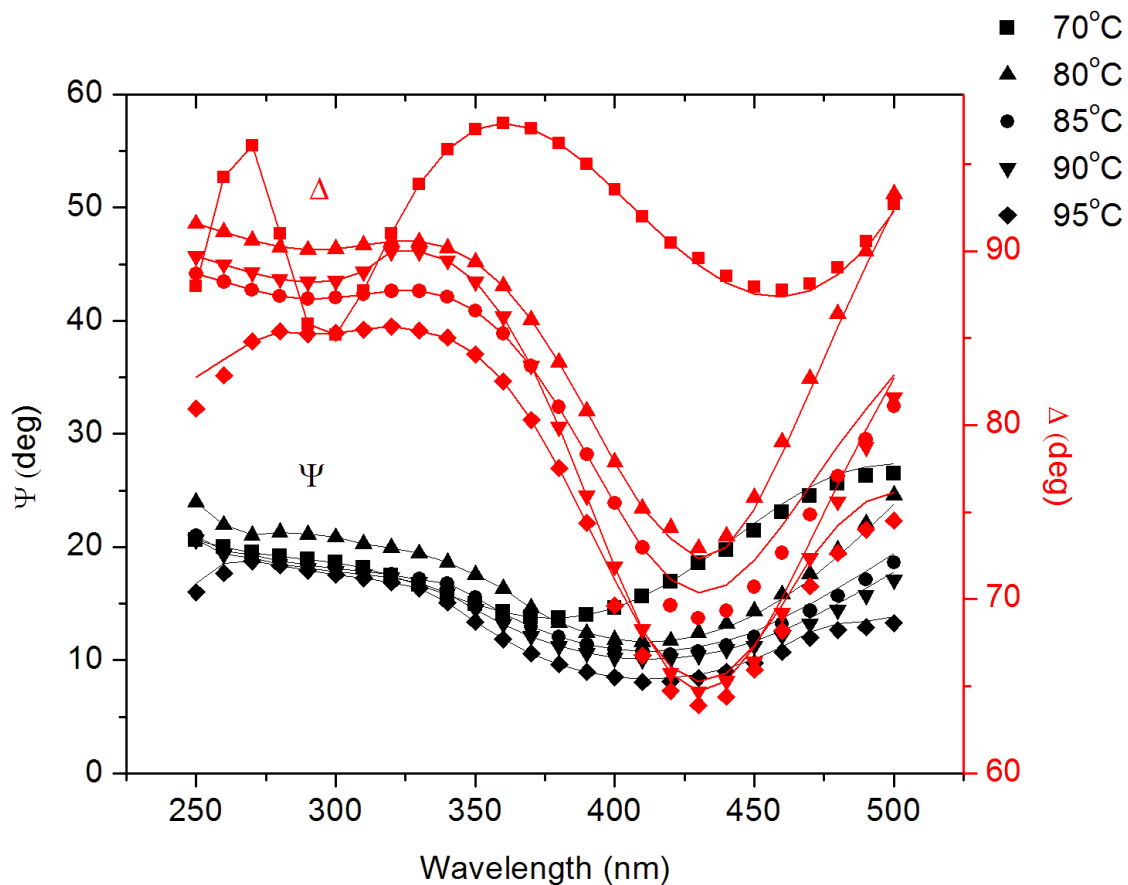


Figure 5.7 Ellipsometric  $\Psi$  and  $\Delta$  spectra for the CdS films at various deposition temperatures measured at  $70^\circ$  incidence angle. Points represent the experimental values, and the solid lines are the best fit curves to the model.

Growth mechanisms were investigated using spectroscopic ellipsometry for  $95^\circ\text{C}$  samples. Substrates were removed from the deposition bath at 3, 6, 9, 12, and 15 hours and analyzed. Film thicknesses for the three layers were investigated where the ellipsometric data gave best fit to the theoretical model. Experimental ellipsometric data is presented in Figure 5.8. Best fit curves at all times were found to be when the fraction of air in the porous (middle) layer was minimal. Growth depositions inside an air tight container are believed to have a profound effect on the lack of porosity within the film.

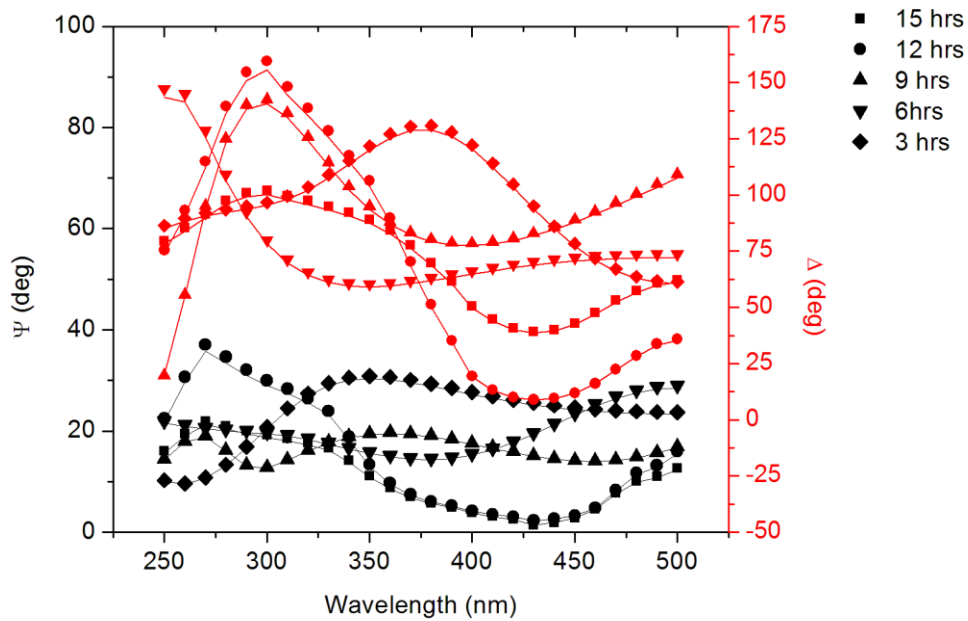


Figure 5.8 Ellipsometric  $\Psi$  and  $\Delta$  for 95 °C samples analyzed at various deposition times.

Figure 5.9 summarizes overall film and layer thicknesses at each stage of the deposition. The bottom layer (ion-by-ion deposition mechanism) dominates the film growth throughout the deposition process, hence ensuring the tight crystalline structure of the films, and tight adherence to the substrate.

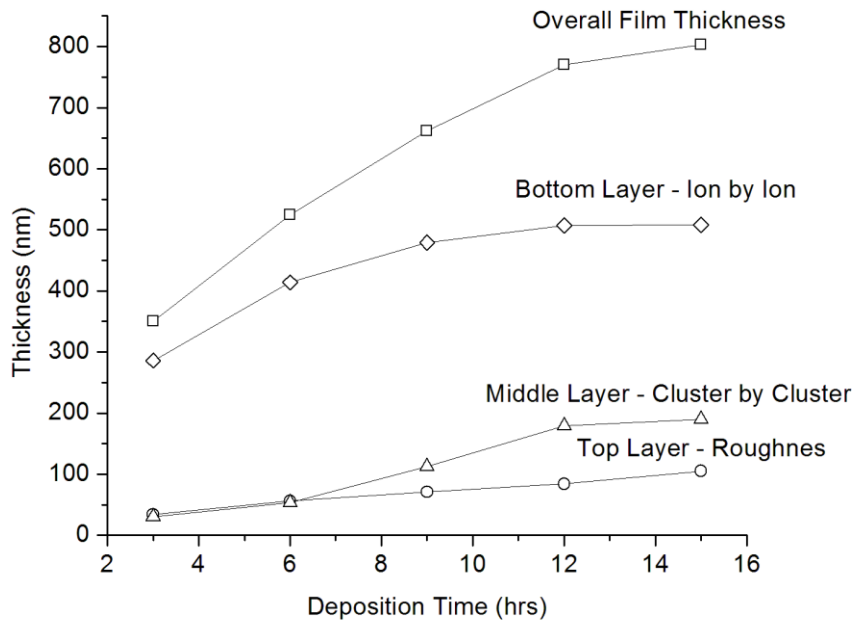


Figure 5.9 Film, layer thickness, and film roughness of 95 °C samples at various stages of film deposition.

At 12 and 15 hour deposition times, the middle layer (cluster – by – cluster deposition mechanism) accounts for ~200 nm of the film, suggesting high precipitation of CdS in the bath in the final stages of the deposition. Nevertheless, air fractions within this layer were found to be negligible, suggesting compact structures. Additionally, the roughness of the film is found to increase with the deposition times as well, again believed to be influenced by the cluster precipitation in the bath in the final stages of deposition.

The refractive index ( $n$ ) and extinction coefficient ( $k$ ) were obtained from the fit of the theoretical models and are shown in Figure 5.10. The refractive index maxima at ~275 nm and ~500 nm have been well studied and are associated with the transition along the  $\Gamma \rightarrow A$  direction of the Brillouin zone (BZ) of the wurzite CdS lattice and fundamental absorption peak, respectively [136]. Refractive index values decrease with the increase in deposition temperatures, signifying higher compactness of the samples deposited at higher temperatures. There is an observed shift in the extinction coefficient as well, implying a shift in the absorption edge of the samples.

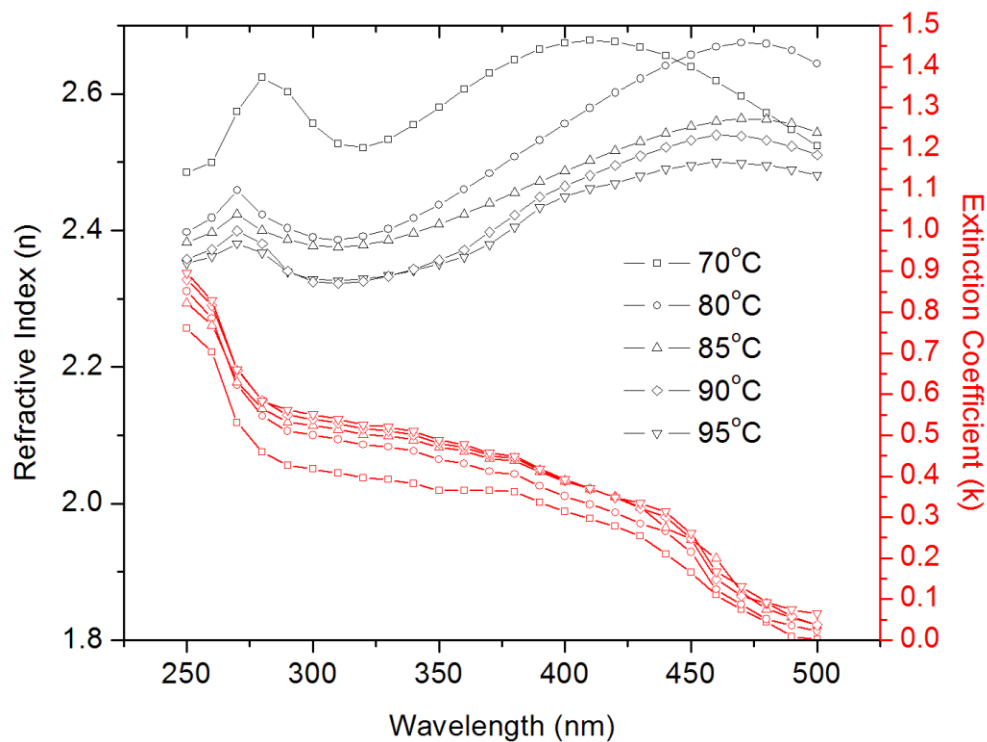


Figure 5.10 Refractive index ( $n$ ) and extinction coefficient ( $k$ ) as a function of deposition temperature.

The shift in the absorption edge was further studied using optical spectroscopy. Tauc plots with the Kubelka-Munk function on the ordinate are shown in Figure 5.11. The inset graph shows the entire measured spectra for the samples.

A red shift is observed in the films deposited at higher temperatures, assumed to be caused by the change in the crystalline structure of the film. Optical bandgaps for purely cubic CdS have been reported to be  $\sim 2.4$  eV [137], and significantly smaller for the hybrids of cubic and hexagonal CdS structures. Additionally the red shift can be attributed to the increase in the grain size.

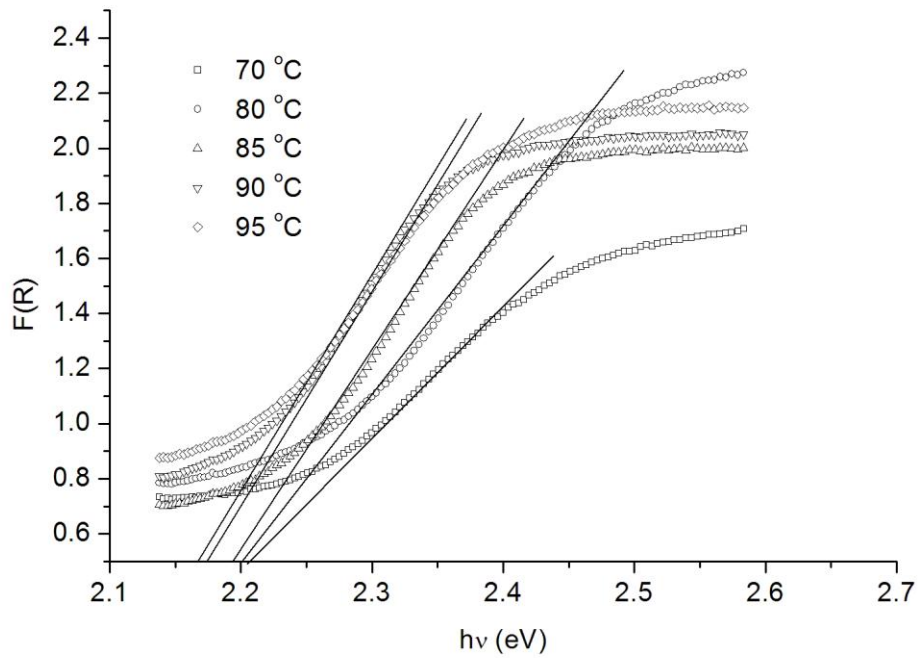


Figure 5.11 Tauc plot for CdS films grown at various deposition temperatures.

The Urbach tail, which is closely related to the disorder of the film matrix, was also computed from the slope of  $\ln(\alpha)$  versus  $h\nu$  (eV). Figure 5.12 shows the optical bandgap and Urbach tail as a function of grain size. Increases in the grain size produced a significant drop in the measured bandgap of the film, however increased overall disorder of the crystals. Increases in the disorder, despite the increase in grain size, further solidifies the claim that the ion-by-ion mechanism is the main contributor to the deposition of the film, hence creating the highly disordered crystalline structure.

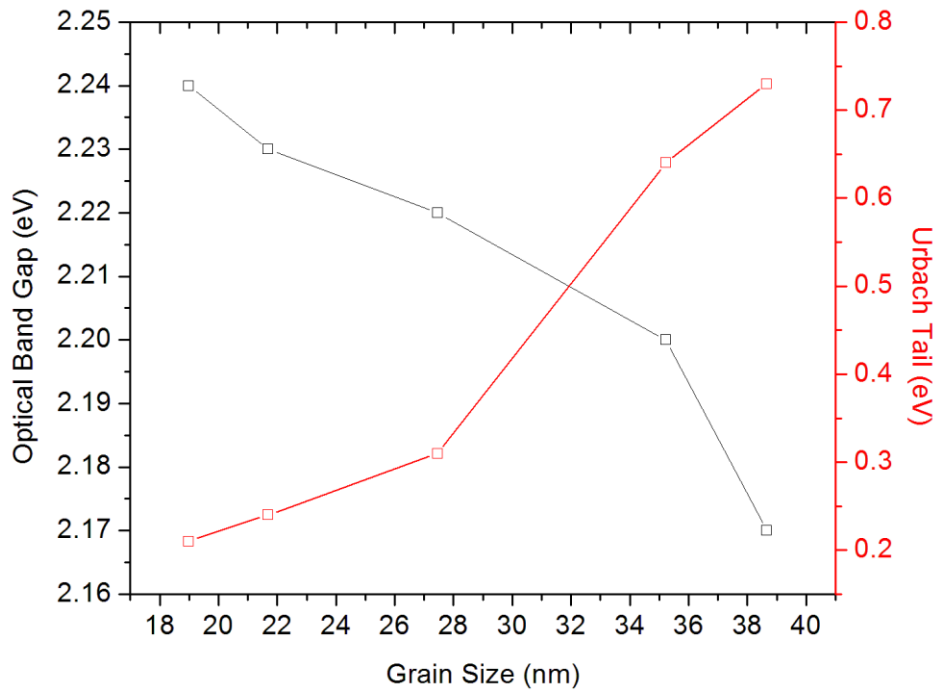
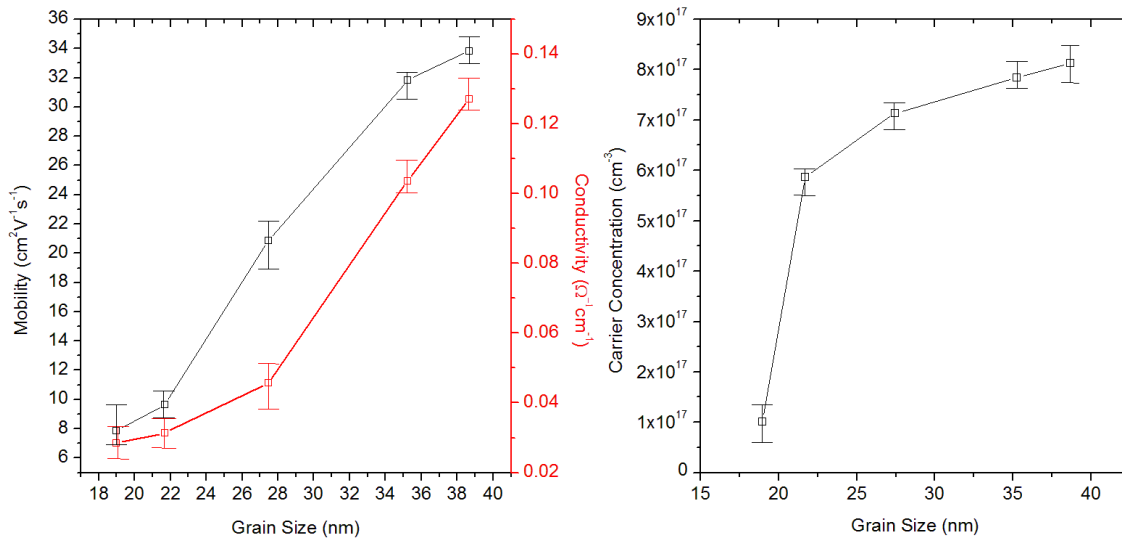


Figure 5.12 Optical bandgap and Urbach tail as a function of grain size.

### 5.3.3 Electrical properties

Mobility, conductivity, and carrier concentration measurements were conducted for films with various grain sizes. Results are summarized in Figure 5.13. Mobility and conductivity increase as a result of the increase in grain size. This is attributed mainly due to the decrease in dislocations per unit area as well the number of grain boundaries the carriers have to cross. Additionally, there is an observed increase in carrier concentrations with the increase in grain size. Such an increase may be explained by the excess of interstitial S ions acting as donors, resulting in an increase in carrier concentration as well as an increase in conductivity [123].



*Figure 5.13 Hall Effect measurements as function of grain size.*

The carrier concentration and mobility in the film are presented in Figure 5.14. The trend in mobility as a function of temperature signifies the presence of defect scattering, i.e. presence of charged impurities. Since no artificial doping has been added, the results suggest that interstitial S<sup>-2</sup> ions are acting as donors in the film. Defect scattering is dominating up to temperatures of ~220 K at which point lattice scattering becomes dominate [139]. We do not have adequate information to make a conclusion about the types of defects present in the film.

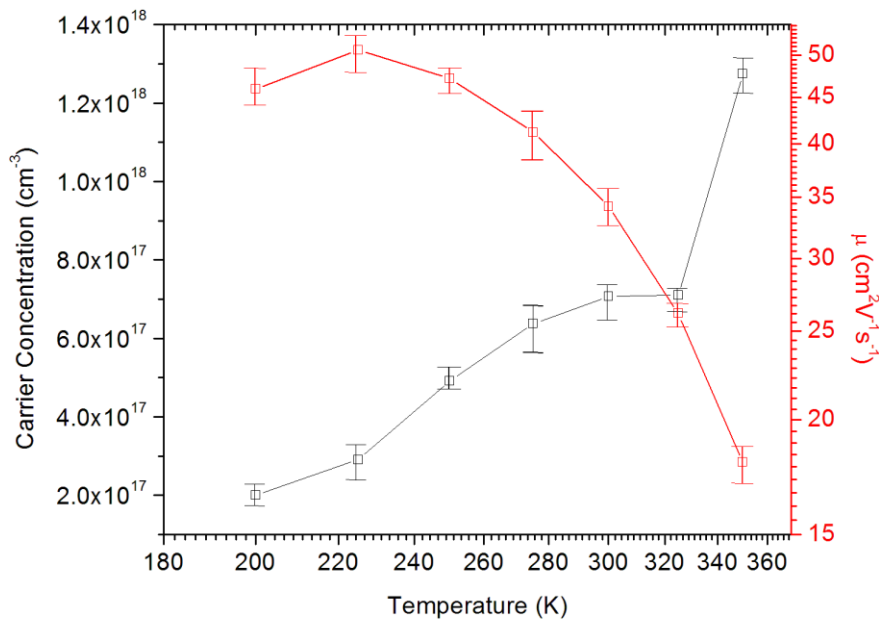


Figure 5.14. Hall Effect mobility and carrier concentration as a function of temperature.

At room temperature the carrier concentrations are found to be  $\sim 6 \times 10^{17} \text{ cm}^{-3}$ , This result further suggests partial entrapment of the interstitial  $\text{S}^{-2}$  ions, which are acting as donors in the film. It is believed that doping by the  $\text{S}^{-2}$  ions can be avoided by close adherence to stoichiometry [140], such results were not however the intent of this study.

Carrier lifetimes were measured using the photoconductance decay (PCD) method described by Drummond et al. [102]. The principle of the photoconductance decay method is based on the analysis of photoconductance decay transients after a very short light pulse from a laser, flash lamp, light-emitting diode (LED) array or laser diode. The effective lifetime is obtained from the slope of the decay curve [141].

Carrier lifetimes measured using photoconductive decay method are shown in Figure 5.15. Lifetime of the nanocrystalline structure deposited at 95 °C measured with the 515 nm laser are shown to be  $\sim 270 \text{ ns}$ , while those for crystalline CdS have been extensively studied and shown to be  $\sim 400 \text{ ns}$  [142]. The difference in the lifetimes can be attributed to surface generation and recombination. Carrier lifetimes increase with the increase in grain size, this signifies improvement in the crystalline structure and the decrease in grain boundaries required to be crossed by the carriers. Measured carrier lifetimes as a function of grain size are shown in Figure 5.15.

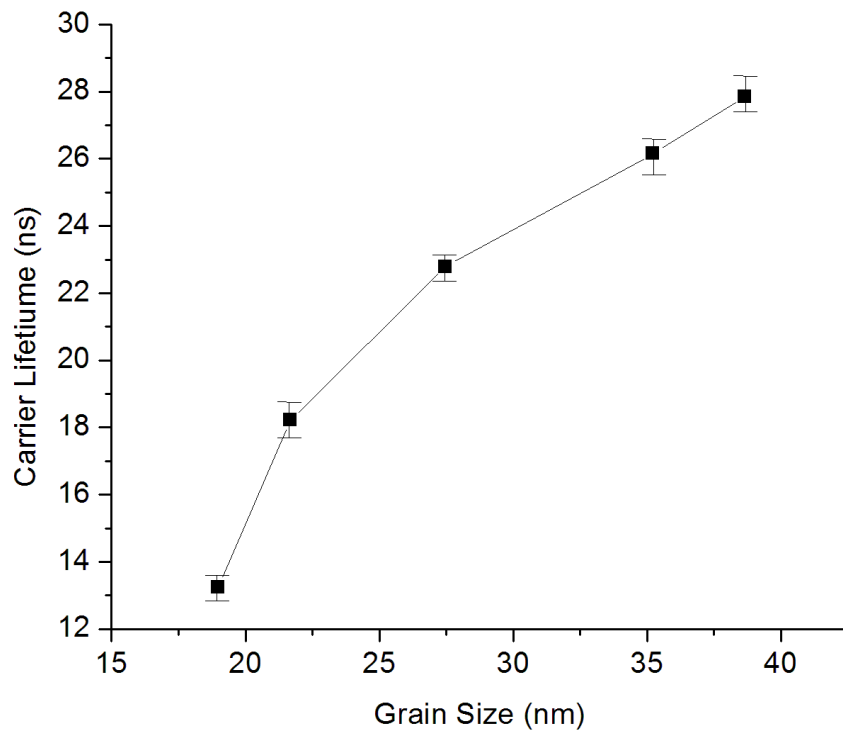


Figure 5.15 Carrier lifetime as a function of grain size.

All samples of interest deposited at 95 °C were re-characterized for thickness, reflection, transmission, carrier concentration, mobility, carrier lifetime and optical bandgap 20 and 30 days after the initial characterization. Table 5.1 shows these data for a sub-set of those samples with the highest mobility and lowest carrier concentration. As clearly seen, there was no noticeable change in the above mentioned parameters over this timeframe, despite the fact the samples were simply stored in air and not encapsulated, as would be done in practical applications. This steady performance is a new phenomenon for CdS films. Most likely this is due to the fact that these samples do not develop an oxidation layer and the tight crystalline structure prevents decomposition.

Table 5.1. Re-characterized CdS Parameters

	Initial	20 days	30 days
Thickness (nm)	812	805	804
Carrier Concentration ( $\times 10^{17} \text{ cm}^{-3}$ )	7.7	8.2	7.9
Mobility ( $\text{cm}^2\text{V}^{-1}\text{s}^{-1}$ )	33.8	32.1	32.3
Carrier Lifetime (ns)	270	265	263
Optical Bandgap (eV)	2.17	2.19	2.20

#### 5.4 Conclusions

A chemical bath deposition procedure for growing thin film semiconducting nano-crystalline CdS is presented. The growth of CdS nanocrystals is achieved by controlling the reaction temperature in the chemical bath. This simple technique avoids the use of expensive equipment or a clean room, with all experiments conducted in a fume hood in a basic laboratory setting. The resulting deposited film was shown to adhere firmly to the substrate and to have a tightly compacted nano-crystalline structure, with high mobility and low impurity concentrations. The effects of deposition temperature on the resulting electrical, optical and physical properties were examined. A set of conditions yielding desirable film properties for use in photovoltaic applications was identified. Deposited films did not show significant changes in electrical properties nor decompose over a time period of 30 days. In fact, we believe these especially encouraging results are due to the tight crystalline structure, which prevents degradation of the film, and is exceptionally resistive to oxidation. This makes the films promising candidates for use in heterojunctions with other materials.

## Chapter 6. Transparent conducting oxide –Ti<sub>1-x</sub>Ir<sub>x</sub>O<sub>2</sub>

### 6.1 Introduction

Transparent conducting oxides (TCOs) are a fundamental component of all optoelectronic devices. TCOs act as an electrode in the optoelectronic device, however, with an added advantage of transparency to certain frequencies of the electromagnetic spectrum. Ideally TCOs should be transparent across a wide range of light wavelengths. Realistically, however, majority of the electrodes are transparent only to a portion of the electromagnetic spectrum. In such cases the operational spectral region of the device is also transparent in the TCO. And as always there is a tradeoff between electrical and optical properties. Improved electrical properties, in general decrease transmittance of the TCO proportionally.

List of TCOs is expansive, and novel materials are discovered regularly. This work focuses on the novel Iridium doped TiO<sub>2</sub>, a promising new TCO with high transmittance in the visible and infrared region.

Further recent increases in the industrial application for optoelectronic devices such as solar cells, lasers, and light emitting diodes (LEDs) have resulted in a high demand for transparent conducting oxides (TCOs) [143]. In general, the material of choice has been ITO due to its low resistivity, ease of fabrication, and high transmittance in the visible spectrum. The radical increase in the cost of In over the last ten years and the need for IR transparent TCOs has increased the demand for high quality films [144-145]. TiO<sub>2</sub> has been shown to have high transmittance in both visible and infrared regions, making it a suitable alternative to the conventional TCOs [146]. However, the resistivity of undoped TiO<sub>2</sub> is  $\sim 10^{-1} \Omega \text{ cm}$ , far above the requirement for optoelectronic devices [147]. Recent work by Furubayashi et al. has shown that the addition of superconducting dopants, such as niobium (Nb) or tantalum (Ta), can decrease the resistivity of the TiO<sub>2</sub> by as much as 3 orders of magnitude [148-149]. Recent studies, however, show a limit in doping efficiency of the commonly used dopants [150]. In other research, Ir, with its nine valence electrons, has been shown to be a highly efficient dopant in optoelectronic devices [151]. During the course of this special focus was given on the electrical properties of TiO<sub>2</sub> thin films doped with Ir grown by pulsed laser deposition. The goal of this research is to decrease electrical resistivity and increase carrier mobility of TiO<sub>2</sub>, while maintaining a high transmittance in the visible and IR spectrums.

High transmittance and low resistivity, make doped TiO<sub>2</sub> films outstanding electrodes for use in optoelectronic devices operating in the infra-red region. Current research showed a limit in doping efficiency of common-dopants. In this work effects of iridium doping on the optoelectrical properties of pulsed laser deposited (PLD) TiO<sub>2</sub> were studied with a goal of finding a suitable material for higher doping efficiency in such films. High quality nanocrystalline Ti<sub>1-x</sub>Ir<sub>x</sub>O<sub>2</sub> thin films  $\sim 60 \text{ nm}$  thick were grown from an Ir doped target with weight % composition ranging from  $x = 0$  to  $0.15$ . Films were deposited on quartz glass and Si substrates at a base

pressure of  $2 \times 10^{-3}$  Pa and a substrate temperature of 780 °K. In terms of electronic properties, the resistivity of the films decreased 3 orders of magnitude when  $x$  increased from 0 to 0.10. The carrier mobility and concentrations nearly tripled from 18 to 46  $\text{cm}^2\text{V}^{-1}\text{s}^{-1}$  at 5% and rose by  $\sim 2$  orders of magnitude from  $10^{19}$  to  $10^{21}$   $\text{cm}^{-3}$  at 15% Ir, respectively. Optimal film properties were found to be at  $x = 0.10$ , where resistivity, mobility, and carrier concentrations were  $5 \times 10^{-4}$   $\Omega$  cm, 32  $\text{cm}^2\text{V}^{-1}\text{s}^{-1}$ , and  $10^{20}$   $\text{cm}^{-3}$  respectively. At the same time film transmittance was found to be above 80% in the visible and infrared regions, suitable for use in both spectral regimes. Highest observed doping efficiency was  $\sim 1.1$ , similar to common dopants. Lower than expected doping efficiency is attributed to the localization of free electrons in polyoxometalate formations, charge trapping from interstitial Ti and O ions.

## 6.2 Experimental

### 6.2.1 Materials and methods

Titanium oxide ( $\text{TiO}_2$ ,  $\geq 99\%$ ) and iridium (Ir, 99.9% trace metals basis) powders purchased from Sigma Aldrich<sup>TM</sup> were used as raw materials.

Previous research has shown that due to the high temperatures and momentum of the ablated species, thin films deposited by PLD retain the stoichiometry of the starting target [152]. Deposition targets were manufactured by Spark Plasma Sintering (SPS) from raw materials according to the mass ratio of  $\text{Ti}_{1-x}\text{Ir}_x\text{O}_2$ , with  $x = 0 - 0.15$ . In an effort to synthesize a target with a uniform composition, the starting powders were dispersed in de-ionized water and stir-dried for 8 hours. Ir distribution and uniformity were checked using energy dispersive spectroscopy (EDS). Samples prepared by the solution dispersion method showed high uniformity and distribution. Ball-milling technique for pellet manufacturing was also analyzed. The ball-milling mixing technique did not result in the uniformity similar to that of the de-ionized water dispersion technique. Mixed powders were then poured into a graphite die (63.5  $\text{mm}^2$  area). In order to prevent reaction of the powder with the die walls, the inner die and punch surfaces were covered with 0.25 mm tantalum foil and placed into the SPS system (GT Advanced Technology SPS). SPS schematic and the die schematic are shown in Figure 6.1 and Figure 6.2 respectively. The SPS chamber was evacuated to  $10^{-2}$  Pa and backfilled with inert gas, Ar.

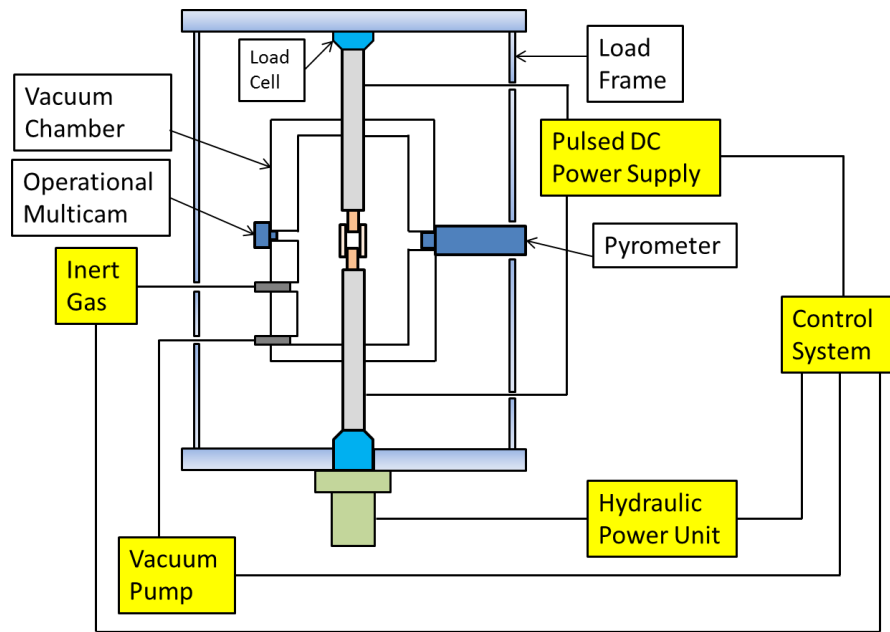


Figure 6.1 Spark plasma sintering setup.

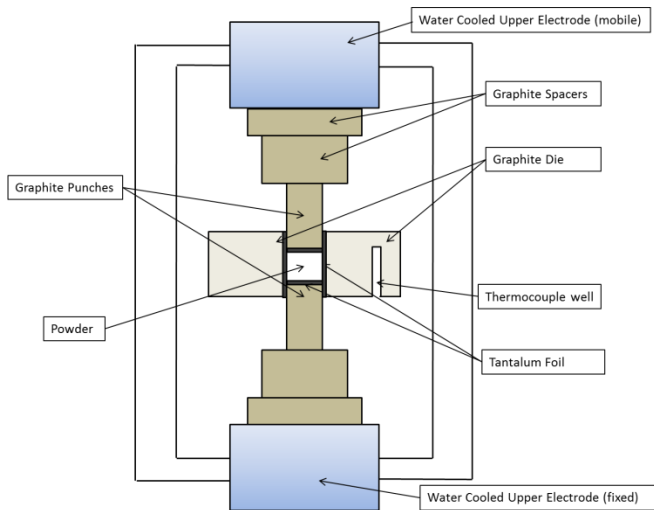


Figure 6.2 SPS graphite chamber and die setup schematic.

The powders were sintered at 1280 °K and 30 MPa for 5 minutes, and cooled at 580 °K/min. Typical sintered target is shown in Figure 6.3 (a). Sintered pellets were polished prior to being used as targets. The SPS material was uniform, planar and dense, which provided the starting target for PLD. Previous literature has shown that the higher substrate temperatures, absence of oxygen, and low laser fluence resulted in the growth of larger grains and more favorable electrical properties [152].

### 6.2.2 Pulsed laser deposition

Once the targets and the substrates were placed in the PLD chamber, laser was aimed at the center of the target and adjusted to hit on the target even when the targets were spinning. PLD chamber was pumped down, and rinsed with nitrogen to ensure minimal amount of present oxygen. Once the substrates reached the deposition temperatures, the PLD laser was activated to begin deposition. Sample target after 13 minutes under the PLD laser is shown in Figure 6.3 (b). Samples were cooled to room temperatures at without any forced cooling. It was found that high quality films were produced at 780 °K substrate temperatures. All films were deposited onto quartz glass and Si substrates at 780 °K at the base vacuum of  $2 \times 10^{-5}$  Torr. Si was used to eliminate additional peaks typically present in the glass substrates. A pulsed KrF excimer (wavelength of 248 nm) with a fluence of  $1.8 \text{ J/cm}^2$  was operated at a repetition rate of 2 Hz for 1560 pulses (13 minutes) resulting in an average growth rate of  $0.384 \text{ \AA/pulse}$ .

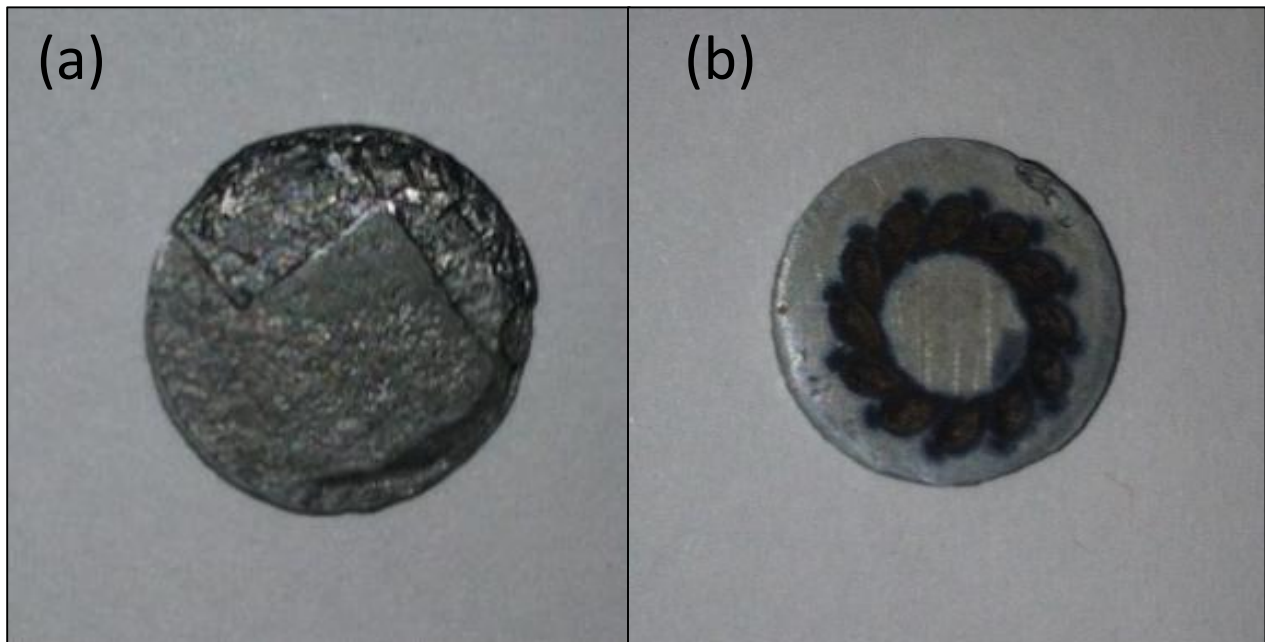


Figure 6.3 PLD targets (a) straight out of the SPS chamber, and (b) after 13 minutes of PLD deposition.

## 6.3 Results

### 6.3.1 PLD target structural properties

Targets were cut in half and analyzed using an SEM and EDS. SEM of the undoped, 1% Ir, and 5% Ir are shown in Figure 6.4 (a), (b), and (c) respectively. Crystals in the undoped target were found to be  $\sim 2$  microns in width average. Crystals appear to be uniform and sintered one to another. Addition of Iridium caused the crystals to become smaller. 1% and 5% pellets show

“amorphous” crystals,  $\sim 100$  nm in size, scattered across the  $\text{TiO}_2$  crystals. Further work is required to analyze the cause of the crystal minimization.

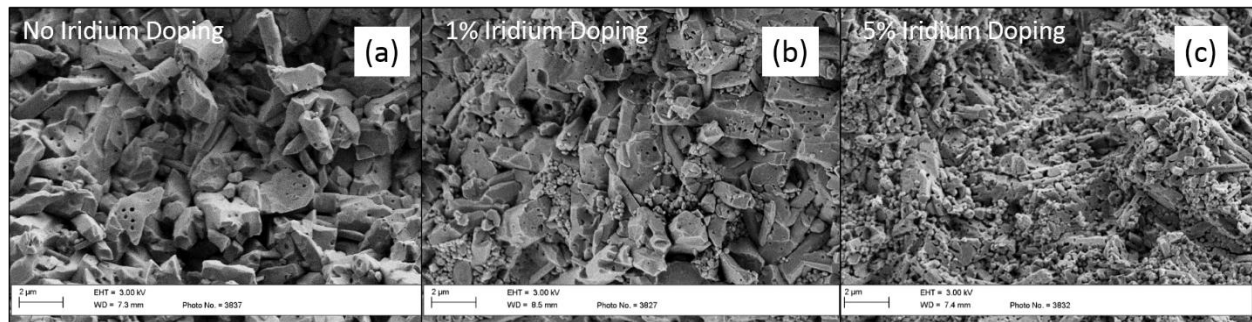


Figure 6.4 Cross sectional SEM of the PLD target. (a) no doping, (b) 1% Ir doping, and (c) 5% Ir doping.

Phase mapping of the energy dispersive spectroscopy (EDS) was used to analyze the locations of the Iridium in the pellet. EDS phase mapping for a 1% Iridium doped target is shown in Figure 6.5. Light areas on the EDS image are the iridium inside the target, whereas the dark areas are the  $\text{TiO}_2$ . Uniform distribution of the iridium across the target is visible. The pulse used in the PLD deposition is  $\sim 1$  cm in diameter. This allows the laser to hit area on the pellet large enough to allow for iridium to be distributed on the deposited film.

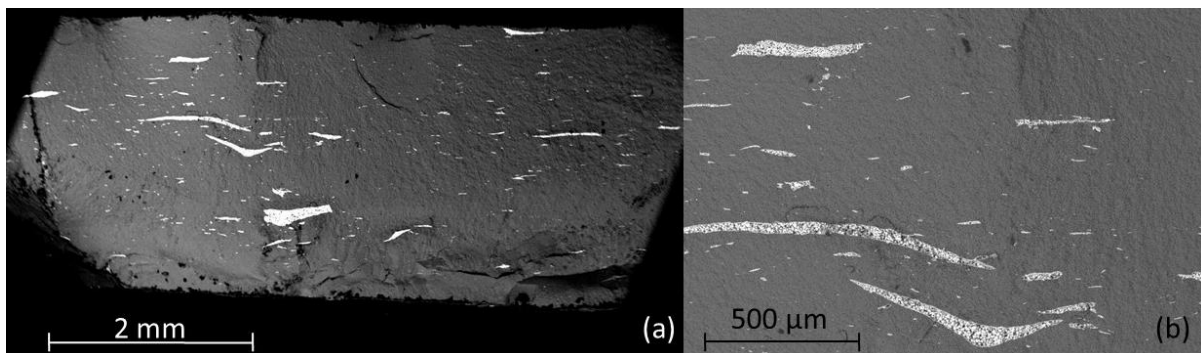


Figure 6.5 EDS Phase mapping 1% Iridium doped PLD target.

### 6.3.2 Thin films structural properties

Optimal film thicknesses were found at 13 minute PLD deposition times. Film thicknesses were found to be  $\sim 60$  nm in thickness and validated using profilometry. Films were extremely smooth, and highly transparent. Figure 6.6 shows typical deposited films. As can be seen the films are highly transparent in the visible range. Silver paste was used in securing the slides during deposition, some of the silver residue is seen on the back side of the glass slides.

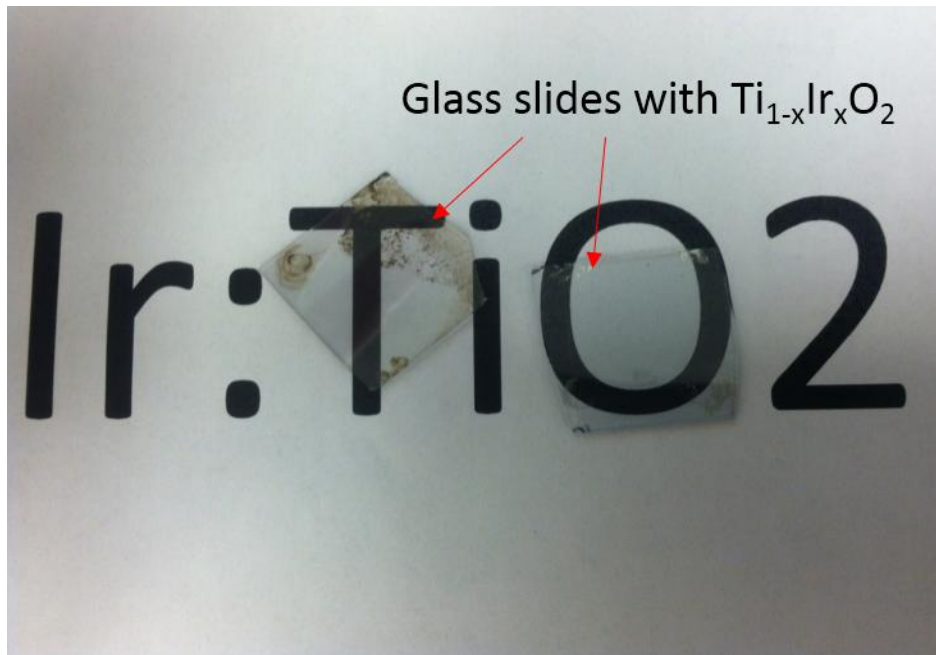


Figure 6.6  $Ti_{1-x}Ir_xO_2$  thin films on glass substrates.

Films were found to be extremely smooth. SEM images of the films were taken at  $45^\circ$  angles of the x-ray gun to the sample due to the high smoothness of the films. Figure 6.7 shows the SEM images of the deposited films. Films are extremely smooth with no obvious or noticeable deficiencies.

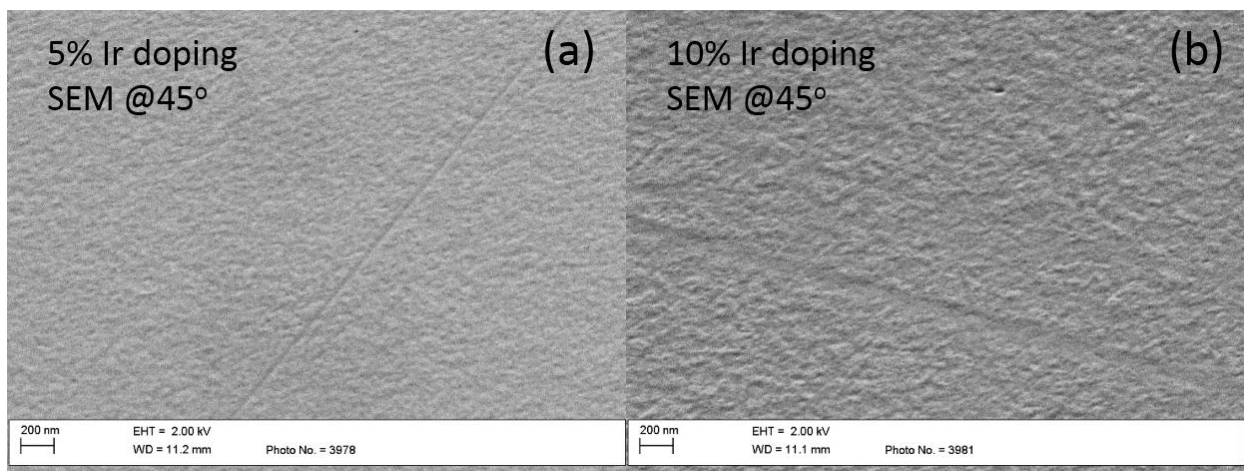


Figure 6.7 SEM images of the  $Ti_{1-x}Ir_xO_2$  thin films on glass substrates.

Diffraction spectra were recorded for both the starting  $Ti_{1-x}Ir_xO_2$  ( $x = 0.15$ ) target and thin films grown on Si substrates as shown in Fig. 1 (a) and (b), respectively. In Figure 6.8, strong peaks of the (110), (101) and (211), as well as weaker peaks at (220) and (204) of the anatase phase of  $TiO_2$  are present [153]. In addition, strong peaks of Ir (111), (200) and (220) were observed

[154]. In comparison, a strong peak of the (301) planes and weaker peaks of the (204) and (211) planes of anatase  $\text{TiO}_2$  were observed in the deposited films. It is important to note that the deposited films exhibited a strong orientation dependence of the (112) and (101) planes for  $\text{IrO}_2$  [153-154]. No  $\text{IrO}_2$  was observed in the XRD patterns of the starting target. These results suggest a substitution of Ir for the Ti takes place during the film deposition. Similar observations have been previously reported in Nb doped  $\text{TiO}_2$  films [155]. Substitution of Ir for Ti introduces charge carriers, profoundly affecting the electrical properties of the films.

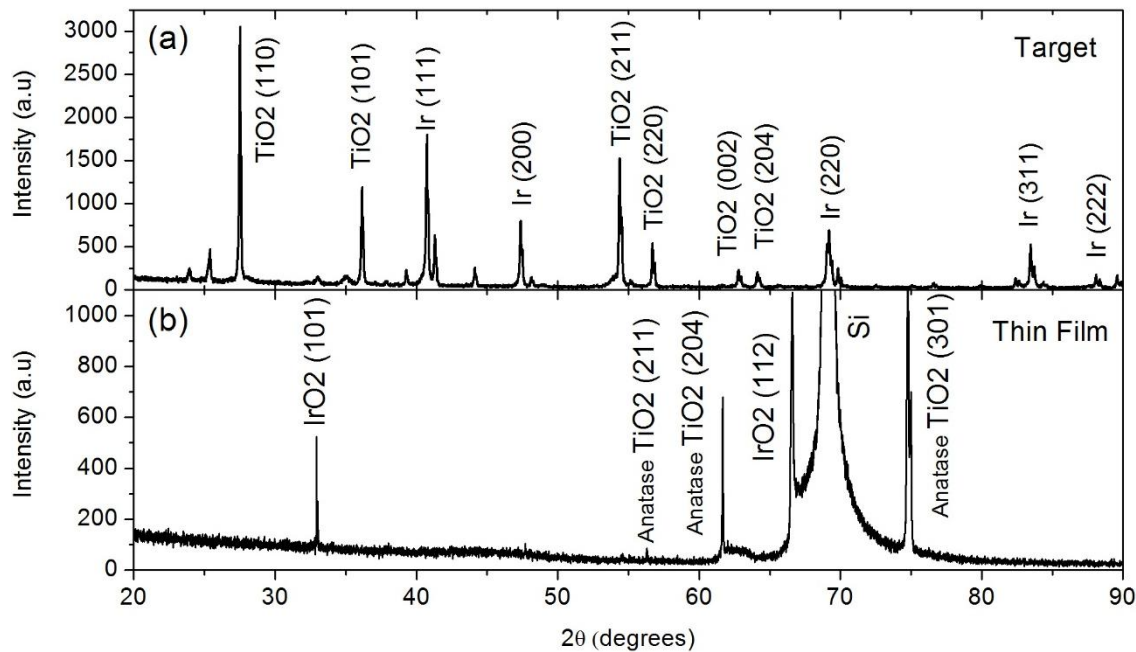


Figure 6.8 X-ray diffraction spectra of: (a)  $\text{Ti}_{1-x}\text{Ir}_x\text{O}_2$  target with  $x = 0.15$ , (b) PLD deposited  $\text{Ti}_{1-x}\text{Ir}_x\text{O}_2$  thin films on Si substrate with  $x = 0.15$ .

### 6.3.3 Thin film electrical properties

Transport properties, namely Hall mobility,  $\mu_H$ , carrier concentration,  $n$ , and resistivity,  $\rho$ , of the anatase  $\text{Ti}_{1-x}\text{Ir}_x\text{O}_2$  films were measured in a Van der Pauw configuration using an Ecopia HMS-5000 Hall measurement system. A summary of the results as a function of temperature,  $T$ , for various concentrations of  $x$  is presented in Figure 6.9.

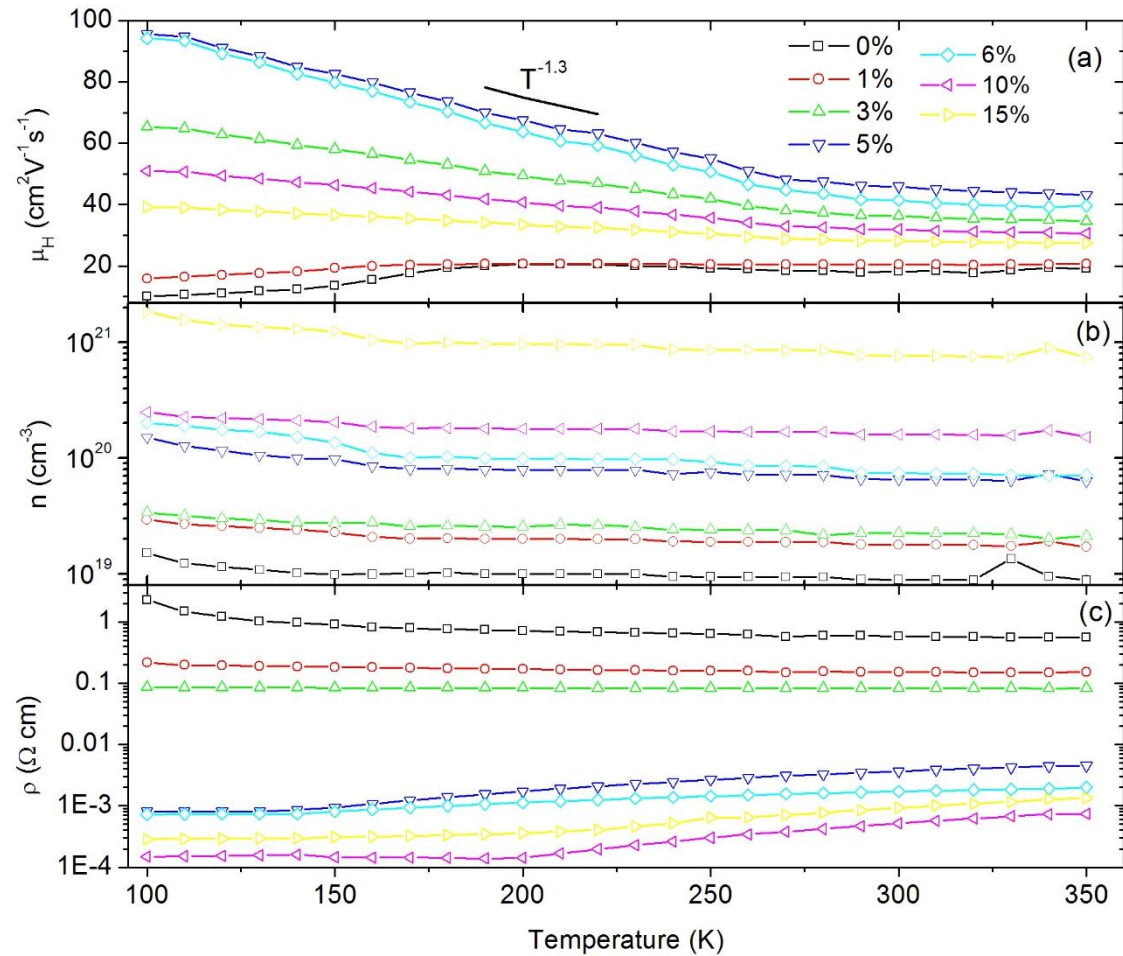


Figure 6.9 Transport properties of  $Ti_{1-x}Ir_xO_2$  films with  $x = 0 - 0.15$  as a function of temperature,  $T$ : (a) Hall mobility  $\mu_H$ , (b) carrier concentration  $n$ , (c) resistivity  $\rho$ .

Mobility was measured to be  $18 \text{ cm}^2 \text{ V}^{-1} \text{ s}^{-1}$  in the undoped films at room temperature, increasing to  $46 \text{ cm}^2 \text{ V}^{-1} \text{ s}^{-1}$  at  $x = 0.05$ . Above this dopant level a decrease in the mobility was observed from  $x = 0.06 - 0.15$ . This phenomenon is explained by the increased density of trap states at higher doping concentrations. Mobility data for  $0.05 \geq x \geq 0.03$  samples are nearly identical and begin to merge at temperatures below 200 K. For these samples there is a near power-law increase in carrier mobility with decreasing temperature,  $\mu_H \propto T^{-1.3}$ . Mobilities still increase with temperature at higher  $x$ , but at systematically lower rates. These results indicate that the mobility of carriers in these films is dominated by phonon scattering [155]. Furthermore, this is typical of behaviors observed in metals, signifying the degenerately doped nature of the films. Using the Arrhenius equation, the activation energy ( $E_a$ ) for  $x = 0.10$  samples was found to be  $\sim 0.06 \text{ eV}$ .  $E_a \geq 0$  has been previously observed and reported in anatase  $TiO_2$  films. This phenomenon suggests that the mobility of the donor-band electrons depends on their energy in relation to the Fermi level. The small energy dependence, however, suggests that most of the current is carried by the donor-band carriers [153].

Carrier concentration increased  $\sim 2$  orders from  $n \sim 10^{19} \text{ cm}^{-3}$  for the undoped films to  $\sim 10^{21} \text{ cm}^{-3}$  for films with  $x = 0.15$ . Carrier concentrations are largely independent of temperature, whereas mobility increased with decreasing temperature. This behavior is indicative of a degenerate  $n$  type semiconductor.

The intrinsic  $\text{TiO}_2$  films had a measured resistivity of  $\sim 10^{-1} \Omega \text{ cm}$  at room temperature, consistent with previously reported results [156]. The resistivity measurements exhibited a temperature independent behavior for  $x \leq 0.03$ . The resistivity decreased gradually with an increase in dopant concentration until  $x = 0.10$ . For films with  $x = 0.10$ , the resistivity is  $\sim 2 \times 10^{-4} \Omega \text{ cm}$  at temperatures below 200 K and  $5 \times 10^{-4} \Omega \text{ cm}$  at room temperature. This is slightly above conventional ITO films reported to have resistivities of  $\sim 1 - 3 \times 10^{-4} \Omega \text{ cm}$  at room temperature [157]. The sheet resistance for the films at  $x = 0.10$  was computed to be  $40 - 90 \Omega/\square$  (in general, the sheet resistance is suitable for use in optoelectronic devices [158]). After reaching a minimum at  $x = 0.10$ , further increases in the dopant concentration results in increasing resistivity to  $7 \times 10^{-4} \Omega \text{ cm}$  at  $x = 0.15$ . This is indicative of an increase in the concentration of traps as a result of excess doping [159]. The ratio of  $\rho(100\text{K})/\rho(300\text{K})$  for 0%, 6%, 15% films is  $\sim 4$ ,  $\sim 0.5$ , and  $\sim 0.3$  respectively. The resistivity ratio found in the undoped samples is typical and signifies largely undoped and defect free nature of the film [158]. The drastic decrease in the  $\rho(100\text{K})/\rho(300\text{K})$  ratio at higher  $x$  indicates highly doped nature of the films, which caused a significant decrease in resistivity,  $\sim 3$  orders of magnitude at  $x = 0.10$ . The nearly flat temperature dependence of resistivity at low temperatures indicates the metallic behavior in films [153]. These results are in contradiction with the reported behaviors in ITOs, and similar to behavior reported for the  $\text{IrO}_2$  conductive oxide, which is well known to exhibit metallic behavior [160]. Flat temperature dependence in resistivity at low temperatures is typical of the heavily doped semiconductors. In such cases the semiconductor tends to acquire metallic behavior. This is also indicative of the metallic donor-band conduction [153]. It should be noted that the resistivity increases in the highly doped samples signifying that the carriers are no longer able to transverse the spatial distances in the semiconductor. Most likely this is cause by the increase in the trap states in the material. As the impurities are caught between the lattices of the semiconductor, these interstitial defect cause recombination traps for the carriers significantly increasing resistivity.

Activation energy can be computed from the resistivity and temperature graph using  $\rho \sim T e^{\epsilon_s/kT}$  [156]. From the computations of the activation energy it can be seen that the activation energy does not drop completely to 0, signifying an activation in Hall mobility. This result indicates that the mobility of the electrons is dependent on their relationship to the Fermi level. Hence the mobility of the electrons can be controlled by the adjustment of the Fermi level.

### 6.3.4 Thin film optical properties

Transmittance and reflectance data for the films were measured in the UV, visible (Vis), and near infrared (NIR) spectral regions (300 nm – 3300 nm) using a Cary-5E UV-Vis-NIR spectrophotometer. Acquired spectra are shown in Figure 6.10 where the transmittance and reflectance of the undoped films was found to be ~95% and ~0.2% in the NIR range respectively. The absorbance was computed from  $\%A = 1 - (\%T + \%R)$ , and found to be ~10% in the Vis-NIR regions in the undoped samples. In the UV range below ~450 nm, the transmittance drops abruptly to nearly 0% and the reflectance rises to ~20% while the absorbance rises to ~80%. The steep drop in transmittance and rise in absorbance in the UV region is caused by the band-gap absorption. In the Vis-NIR range transmittance decreased with the increasing  $x$ , and was found to be ~85% at  $x = 0.10$ . In the same region reflectance and absorbance increased with doping. Reflectance and absorbance reached ~1.0% and ~15%, respectively, at  $x = 0.10$  in the Vis-NIR region. Variations in the optical properties as a function of doping concentration have been widely studied in TCOs. Such behavior is attributed to the increase of free carrier absorption in terms of Drude's theory [162]. Slightly reduced transmittance and increased absorbance of the undoped samples in the Vis-NIR regions is attributed to the presence of impurities in these films [163]. Changes in transmittance and reflectance are mild with the increase of Ir doping concentrations and are sufficient for use in the visible and NIR regions.

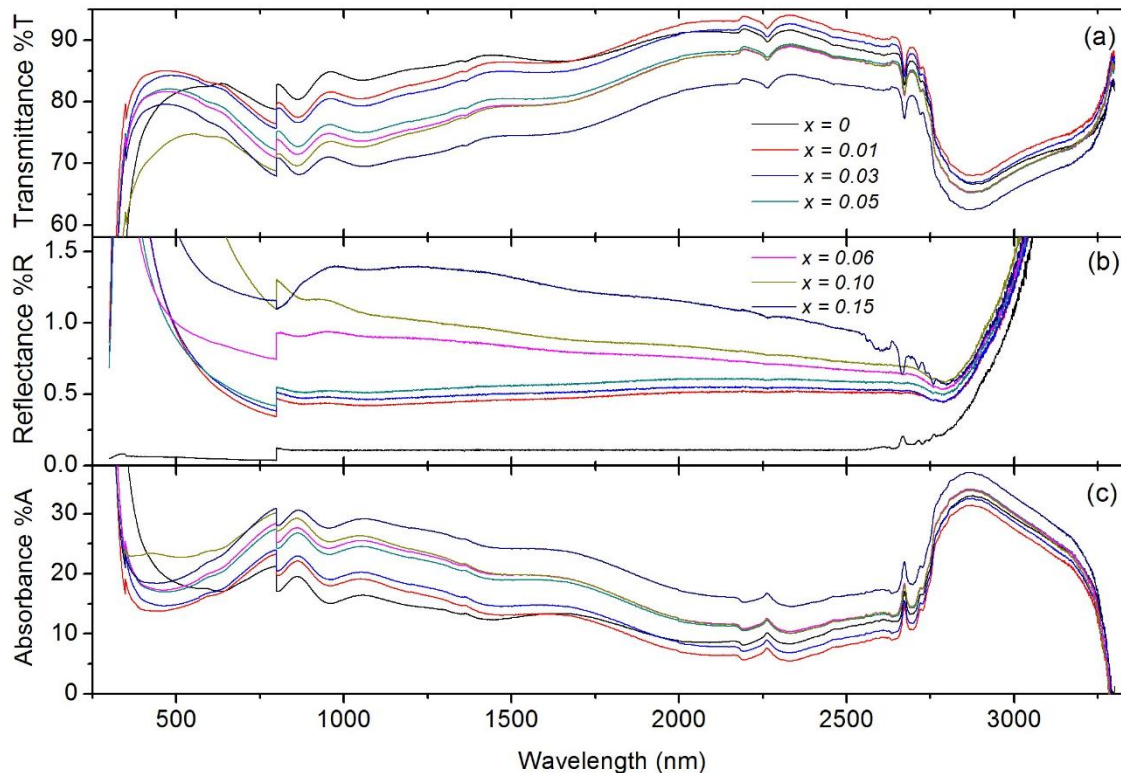


Figure 6.10 Spectra for  $Ti_{1-x}Ir_xO_2$  films with various  $x$ : (a) transmittance, (b) reflectance, and (c) absorbance.

The square root of the optical absorption coefficient ( $\alpha^{1/2}$ ) was derived from the measured transmittance and reflectance using the approximate relation  $T = [(1-R)^2 e^{-\alpha d}] / [1 - R^2 e^{-2\alpha d}]$ , where  $d$  and  $\alpha$  are the film thickness and absorption coefficient, respectively. The optical bandgap ( $E_g$ ) of the films was estimated from the extrapolation method based on the assumption of a direct transition to an empty conduction band for anatase  $TiO_2$  [164]. Computed  $E_g$  values are shown in Table 6.1

TABLE 6.1. Summary of the opto-electrical Properties of  $Ti_{1-x}Ir_xO_2$  at  $T = 300K$ .

Ir (wt. %)	0	1	3	5	6	10	15
$\rho$ ( $\Omega$ cm)	$5.8 \times 10^{-1}$	$1.5 \times 10^{-1}$	$8.3 \times 10^{-2}$	$3.7 \times 10^{-3}$	$1.7 \times 10^{-3}$	$5.2 \times 10^{-4}$	$9.3 \times 10^{-4}$
$n$ ( $cm^{-3} \times 10^{18}$ )	8.9	18	23	66	74	160	770
$\mu$ ( $cm^2$ V <sup>-1</sup> s <sup>-1</sup> )	18.2	20.5	36.3	45.9	41.4	31.9	28.2
$E_g$ (eV)	3.22	3.3	3.32	3.4	3.41	3.41	3.42
$m^*$ ( $m_e$ )	5.01	5.59	7.73	5.94	4.73	4.21	4.90
$\eta$	0	0.13	0.25	0.77	0.87	1.10	0.94

The optical bandgap and carrier concentrations of the undoped films are  $\sim 3.22$  eV and  $\sim 9 \times 10^{18}$   $cm^{-3}$  respectively. This is slightly above intrinsic levels, indicating some presence of inherent defects in the intrinsic films.

Increase in dopant concentrations caused a widening of the bandgap, from  $\sim 3.2$  eV to  $\sim 3.4$  eV, This enlargement of the bandgap can be explained by the conduction band filling with donor electrons causing an up-shift of the Fermi level, Burstein-Moss shift [165]. In this case, the lowest states in the conduction band are blocked and only transitions to energies higher than the Fermi energy are allowed. This behavior is typically observed in degenerately doped n-type semiconductors. Similar bandgap widening has been previously reported in other doped  $TiO_2$  films [166]. Plot of the optical bandgap with respect to  $n^{2/3}$  is shown in Fig. 4 (a). With the exclusion of the higher doping concentrations, i.e.  $x = 0.10 - 0.15$ , a linear relationship between the carrier concentrations and the optical bandgap is observed. This is consistent with the Burstein-Moss shift argument in samples with  $x < 10\%$  [167]. Extrapolating optical gaps values to  $n^{2/3} = 0$  gives  $E_0 = 3.19$  eV, which is in agreement with previously reported values for titanium dioxides [168]. The Fermi level,  $E_f$ , for the undoped samples thus are computed to be

0.03 eV. Small  $E_f$  value coupled with the high carrier concentration results in a large effective mass of the electrons in the films,  $m^* \sim 5m_e$ , computed from equation (1) [167].

$$E_f = \frac{\hbar^2(3\pi^2n)^2}{2m^*} \quad (1)$$

Despite the unusually high  $m^*$  in the studied films, the reported effective masses of electrons in TiO<sub>2</sub> films have been much higher. Previously reported  $m^*$  values ranged from  $\sim 5m_e$  to  $\sim 13m_e$  [169-170]. An existence of a deep impurity band minimum is proposed in order to resolve this inconsistency, shown schematically in Fig. 4 (b). A valley exists in which defect free TiO<sub>2</sub> semiconductors possess effective masses slightly over  $2m_e$ . A deep valley caused by the defects may forms and overlaps with the already existing band minimum. As a result the defect and intrinsic bands blend into one continuous band or separate existence of a densely populated deep valley takes place. In both cases semiconductor exhibits metal-like properties, and depending on defect density would reconcile the variations within the observed effective masses.

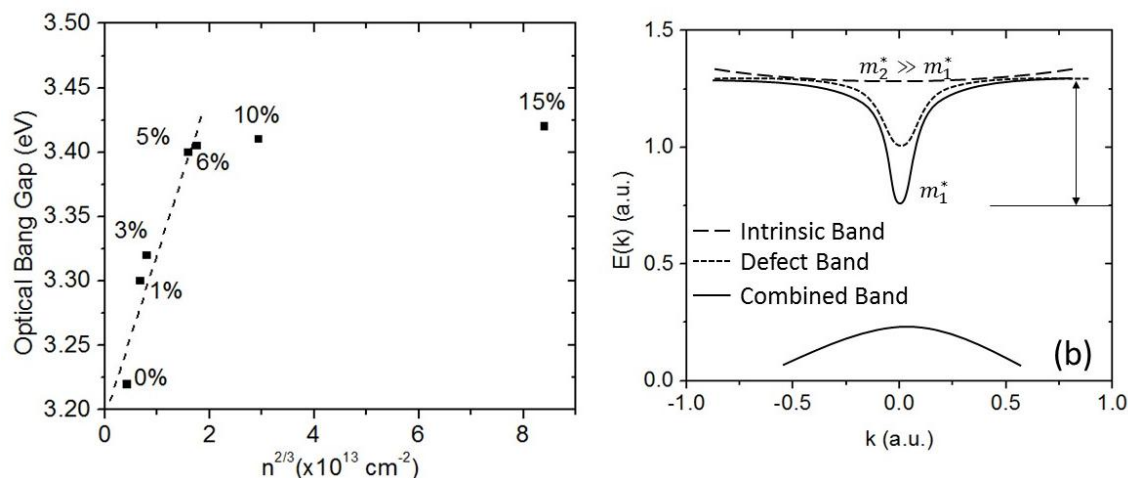


Figure 6.11. (a) Optical bandgap as a function of  $n^{2/3}$  (b) dual-band overlap from the defect states.

Significant increase in the bandgap,  $\sim 0.2$  eV, was observed between  $0 \leq x \leq 0.06$ . Additional doping beyond  $x > 0.06$  had a minor effect on the optical bandgap, totaling  $\sim 0.02$  eV enlargement with nearly tripled dopant concentration by weight. As previously discussed the bandgap increases in the  $0 \leq x \leq 0.06$  region are causing a Burstein-Moss shift. The insignificant increases with additional doping is explained by the bandgap narrowing which is caused by the electron-electron and electron-donor interactions typical of a heavily doped semiconductors [171]. In the case of heavily doped semiconductors these interactions deform density of states by generating significant band tails and forcing them into the forbidden gap [172]. Coupled with the Burstein-Moss effect, these result in minor changes of the bandgap.

### 6.3.5 Iridium doping efficiency

Mean doping efficiency,  $\eta$ , was computed as the number of free-charge carriers per the total number of introduced Ir atoms. Doping efficiency was estimated for the  $T = 300\text{K}$  using

$$\eta = \frac{[n(300\text{K},x) - n(300\text{K},0\%)]}{[\text{Total number of Ir atoms}]} \quad (2)$$

Computed  $\eta$  values for the  $x = 0.01, 0.03, 0.05, 0.06, 0.10, 0.15$  were  $0.13, 0.25, 0.77, 0.87, 1.1, 0.94$  respectively. Doping efficiency results are consistent with the electrical resistivity results, where  $\eta_{0.01} < \eta_{0.03} < \eta_{0.05} < \eta_{0.06} < \eta_{0.10}$  and  $\eta_{0.10} > \eta_{0.15}$ . Maximum doping efficiency was found to be  $\sim 1.1$ , slightly above those reported for the common dopants such as Nb and Ta [173-174]. The lower than expected doping efficiency is partially affected by the localization of nearly all iridium free electrons into the polyoxometalate formations [175]. These formations take place between the interstitial oxygen and substitutional iridium. Formations of the polyoxometalates localize the valence electrons into the structure, not allowing them to be released for use in the films. Another possible effect limiting the doping efficiency can come from the interstitial oxygen atoms themselves. Localization of the charge carrier may take place where oxygen is drawn into the sites near iridium. This way oxygen binds to iridium to act as a charge trap [176]. In this case the oxygen remains neutral or partially charged,  $O^{-(2-\delta)}$ . Releasing  $\delta$  requires usage of two charges from Ir. As a result leading to a reduced doping efficiency, since only  $\delta$  number of free electrons are released, where  $\delta$  at most equals 2 [176]. Interstitial Ti ions may also exist and to some degree contribute to the limiting of the overall doping efficiency [175]. Overall the doping efficiency from Ir is dependent on the location of the dopant ions and their interactions with the host structure. The  $\eta$  limiting mechanisms are inherently complex and difficult to study even under meticulous investigation. At present time no decisive conclusion can be made about the doping efficiency limiting mechanism. However, it is assumed that more than one mechanism plays a role in overall great diminishment of the doping efficiency of Ir.

### 6.4 Conclusion

A novel TCO has been discovered and discussed in this work. The high doping efficiency of Iridium allows for this material to be used as a dopant for various materials. The electrical and optical properties of a promising new class of TCO,  $\text{Ti}_{1-x}\text{Ir}_x\text{O}_2$ , have been investigated. Thin films on the order of 60 nm thick were grown by pulsed laser deposition using high quality sintered  $\text{Ti}_{1-x}\text{Ir}_x\text{O}_2$  targets with Ir concentrations ranging from  $x = 0$  to 0.15. Samples with  $x = 0.10$  had measured resistivities of  $\sim 5 \times 10^{-4} \Omega \text{ cm}$ , comparable to commonly used ITO. Carrier mobilities ranged from  $18.2 \text{ cm}^2 \text{ V}^{-1} \text{ s}^{-1}$  in undoped films to  $45.9 \text{ cm}^2 \text{ V}^{-1} \text{ s}^{-1}$  in films with  $x = 0.05$ . Carrier concentrations increased by  $\sim 2$  orders of magnitude from  $\sim 10^{19} \text{ cm}^{-3}$  to  $\sim 10^{21} \text{ cm}^{-3}$  from  $x = 0$  to  $x = 0.15$ . Carrier concentrations are largely temperature independent, while carrier mobilities increase with decreasing temperature, suggesting that the films are degenerately doped. The transmittance of the films was measured to be  $\sim 95\%$  across a broad portion of the

spectrum, decreasing to ~85% at  $x = 0.10$ . The optical properties measured make the material suitable for use in solar cells, laser, and light emitting diodes operating in both the visible and NIR spectral range. Addition of dopants increased the bandgap in a linear relation to the carrier concentration up to  $x = 0.06$ , signifying Burstein-Moss shift. At doping concentrations above  $0.10$  a noticeable band gap narrowing was observed. Bandgap narrowing coupled with the Burstein-Moss shift for insignificant changes in the bandgap at  $x \geq 0.10$ . Effective mass of the electron was found to range from  $4.2m_e$  to  $7.73m_e$ . A defect generated deep valley model is proposed to reconcile the large range of computed and literature reported effective masses. Doping efficiency was limited to ~1.1, slightly above the conventional dopants such as Nb and Ta. The limit in doping efficiency is attributed to a combination of contributions from interstitial Ti and O ions and localization of free electrons during the interstitial O and substitutional Ir polyoxometalate formations in the film.

## Chapter 7. Glass/Ti<sub>1-x</sub>Ir<sub>x</sub>O<sub>2</sub>/CdS/PbS/Au heterojunction

### 7.1 Introduction

Heterojunctions between two different types of semiconductors are a pivotal part of the semiconducting industry and have been extensively studied for various combinations of semiconductors. Applications for heterojunctions range from photovoltaic cells, to lasers, to light emitting diodes. The formation of heterojunction between CdS and PbS allows for an efficient method to collect the low energy photons by the PbS junction and the high energy photons in the CdS layer. Additionally, the combination of these two materials allows for a possibility of manufacturing the heterojunction at room temperature. Further the heterojunction is resistant to oxidation due to the nanocrystalline structure of the two films. In the course of this work, an efficient heterojunction was achieved, using cost-effective chemical bath deposition method. The resulting junction is shown to have a photovoltaic response in the near infrared spectral region. This is of particular interest for usage in the thermal energy conversion. Barrier heights for the interface layers were analyzed from the capacitance-voltage analyses, and an energy band diagram was constructed from the C-V results. Photovoltaic response to the infrared photons is deduced to be from the photoexcitation of electrons from the conduction band of PbS to the conduction band of CdS. Further, in an effort to achieve highest conversion efficiency, different doping concentrations of donors in CdS and acceptors in PbS were experimented.

Heterojunctions between n-type CdS and p-type PbS were achieved by chemical bath deposition of PbS nanocrystalline thin films on nanocrystalline CdS films. Heterojunctions were completed in methodological depositions. Ti<sub>1-x</sub>Ir<sub>x</sub>O<sub>2</sub> was deposited on glass substrates and found to grow epitaxially. CdS thin films were then deposited on the TCOs in a chemical bath. CdS was found to be in a cubic/hexagonal phase, with interstitially trapped Cd<sup>+2</sup> and S<sup>-2</sup> ions and deviation from stoichiometry. The PbS films were grown in the chemical bath and found to grow epitaxially on CdS crystals. Au was sputtered unto the device to form the back contact and electrode. The heterojunctions showed a marked photovoltaic effect and distinct rectifying characteristics. Photovoltaic effects were measured under irradiation with a tungsten lamp at 1 W/cm<sup>2</sup>, i.e. 1 Sun. The spectral sensitivity of the photovoltaic effect showed a sharp maximum at the absorption edge of Glass/TiO<sub>2</sub>/CdS/PbS/Au heterojunction and a flat region extending toward long wavelengths as far as 1μ. Optimal heterojunction was found to have the open circuit voltage, short circuit current, and fill factor of 0.55 V, 77 μA, 0.28, respectively. From these results it was possible to show that no rectifying contacts existed in the heterojunction, rather Ohmic contacts dominated at both electrodes.

Optimal efficiency of the device was found to be 3.1%. This is mainly attributed to the low fill factors, which could be attributed to numerous sources, e.g, porosity of the chemically deposited films, diffusion of impurities, poor structural contacts, etc. There is definite room for future

improvement of the device, however, it should also be noted that the theoretical efficiency of the device in theory is restricted by the Shockley-Quisser limits to be ~9% [177].

## 7.2 Experimental procedures

### 7.2.1 Junction manufacturing

Detailed device structure was: glass/  $\text{Ti}_{1-x}\text{Ir}_x\text{O}_2$ /CdS/PbS/Au. Initially the glass substrate was cleaned according to the RCA-1 procedures previously described [77]. The samples were then dried with nitrogen gas and placed in lab dishes to be taken to the PLD chamber. At the PLD chamber the slides were rinsed with acetone one additional time, and placed inside the chamber. The chamber was pumped down and  $\text{Ti}_{1-x}\text{Ir}_x\text{O}_2$  thin films were deposited. Films were deposited at several different times in order to achieve various film thicknesses for improved electrical properties at the expense of the optical transmittance however.

Prepared samples were then placed in the prepared chemical bath solution for the CdS deposition. Deposition solution contained 30 mL of cadmium sulfate monohydrate [ $\text{CdSO}_4 \cdot \text{H}_2\text{O}$ ] with a concentration of 0.1 M, mixed with 12 mL of 1 M sodium citrate dihydrate [ $\text{HOC}(\text{COONa})(\text{CH}_2\text{COONa})_2 \cdot \text{H}_2\text{O}$ ], 30 mL of 1 M  $\text{NH}_4\text{OH}$ , and 10 mL of 1 M thiourea [ $\text{CH}_4\text{N}_2\text{S}$ ]. All solutions were added in the sequence as described above, and enough deionized water was added to make the deposition bath a total volume of 100 mL. Solutions were placed into a sealable beaker to prevent escape of the  $\text{H}_2\text{S}$  gases. CdS was deposited in the method described previously. Depositions were done at various doping concentrations in order to achieve optimal doping profile for the highest efficiency, and low CdS resistance without annealing. CdS deposition experiments were achieved at bath deposition temperatures of 95 °C, since this is where the optimal opto-electrical properties were previously discovered. Homogeneous dark yellowish CdS films were acquired in all cases, and no adhesion issues were noticed in the films. Samples were then removed from the deposition bath and rinsed with de-ionized water to wash away any loose particles and dried in air prior to PbS deposition. It was also discovered that glass/  $\text{Ti}_{1-x}\text{Ir}_x\text{O}_2$ /CdS films were less prone to PbS bath effects if they were left to dry for over 24 hours. These results have to be validated and studied in the future work. PbS films were deposited by the chemical bath process previously described.

Seeding was omitted in the PbS deposition on top of the CdS. PbS films were found to bond to the CdS atoms to produce firm heterogeneous adhesive thin films. Initial deposition parameters were 18 mL of NaOH 2.75 M, 10 mL of  $\text{Pb}(\text{NO}_3)_2$  340 mM, 10 mL of  $\text{SC}(\text{NH}_2)_2$  990 mM, 240 mg  $\text{Na}_2\text{SO}_3$ , and 10 mL of  $\text{C}_2\text{H}_6\text{O}$ . These chemicals were mixed in a 50 mL beaker in order. Deposition fluid darkened from the chemical reactions, signifying formation of the PbS. At 25 °C and concentrations stated above, constituent reaction takes place within several minutes, although the rapidity of the reaction was a function of temperature and constituent concentrations. Acidity of the chemical deposition bath was measured to be pH ~12 every time. The glass/ $\text{Ti}_{1-x}\text{Ir}_x\text{O}_2$ /CdS were placed into the beaker at 25°C for 30 minutes. Stir rate was set at

50 RPM and found to produce uniform deposition. Films were extremely dark, signifying PbS deposition. From the glass slide yellowish CdS was still visible. After deposition the films were rinsed with de-iodized water to remove any loose particles prior to the back electrode deposition. This ensured good adhesion of the Au electrode to the device.

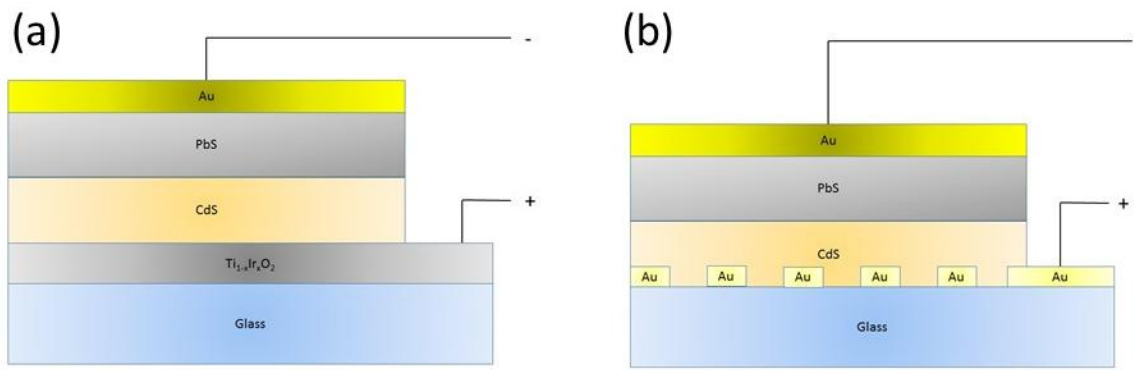


Figure 7.1. (a) Glass/ $Ti_{1-x}Ir_xO_2$ /CdS/PbS/Au (b) glass/Au grid/CdS/PbS/Au device schematic.

Finally to complete the photovoltaic structures Au back contacts were sputtered on the device using Emitech K675 Sputtering Device. Au sputtering was done in range of 5-10 minutes, and it was found that overall sputtering times did not have a profound effect on the performance of the device. Hence sputtering was kept at 5 minutes. Devices were masked at the edges during the Au deposition in order to protect shorts within the device. Au covered the device completely, none of the lower layers were visible through the PbS. Through the glass slide mainly the CdS layer was visible. Resulting glass/ $Ti_{1-x}Ir_xO_2$ /CdS/PbS/Au structure is shown schematically in Figure 7.1 (a).

Another structure of the device which was experimented with was the “classical” gold grid for the bottom electrode, Figure 7.1 (b). Bottom electrodes are connected by a running Au connection at the back of the grid.

The overall device thicknesses were  $\sim 2$  mm. The active layer thicknesses (i.e. CdS/PbS) were  $\sim 1.5$   $\mu\text{m}$  thick. Previous theoretical work has shown that thicknesses of  $\sim 2$   $\mu\text{m}$  are sufficient to absorb all of the solar radiation [178]. In such materials maximum device efficiency was computed to be 4.13%, with the Al and ITO working as the back and front contacts respectively.

The semiconductor films obtained were characterized by X-ray diffraction using the equipment Cu-K $\alpha$  radiation, 40 kV and 30 mA, 1.5406 Å K $\alpha$ 1 source. Optical transmission and reflection spectra were recorded in the wavelength range 300 – 3300 nm using a FTIR Cary 5-E spectrophotometer. Sample thickness was measured by Destak II profilometer. Results were validated using SEM cross sectional imagery. I–V characteristics of the solar cell structures in

the darkness and under 1 Sun ( $1\text{W}/\text{m}^2$ ) illumination. Illumination source was calibrated to the distance and the samples were partially covered to reveal only the  $1\text{ cm}^2$  area during the measurements. I-V curves were acquired and plotted using LabVIEW control software. Junction resistances between each layer were also measured to eliminate the parasitic resistances in efficiency computations.

### 7.2.2 Band structure

Electron affinities and energy band diagrams for nano-crystalline PbS and CdS have been well studied and are presented in Figure 7.2 (a) [180]. Electron affinity is referenced to the vacuum level. In purely intrinsic (ideal) materials the Fermi levels are in the middle of the forbidden gap. Fermi levels are expected to align when two semiconductors are brought together. Hence the Fermi level can be adjusted in such a way as to bring the conduction band of the wide bandgap semiconductor below the conduction band of the lead salt. Such configuration will allow for a built in voltage to be present in the heterojunction, making the device an effective carrier of electrons to the indium tin oxide (ITO) and holes to the opposite electrode.

Several electrodes will make an Ohmic contact with the lead sulfide. Aluminum, silver, and gold are readily available high quality conductors with low resistivity. Silver and gold have been used exclusively in this work due to the ease of deposition and availability of the materials. Gold with its lowest electron affinity is expected to produce lowest junction resistance at the interface, however, at a significant increase in cost of the device.

The Fermi level in the lead sulfide and cadmium sulfide can be adjusted by the crystalline structure of the films. Hence, the built-in potential may be controlled by the deposition parameters of the chemical bath rather than doping of the film. In such a case the built-in potential may be increased without an increase in the doping concentrations of the film. The depletion layer is directly proportional to the built-in potential and doping concentrations. Hence, depletion layer width may be controlled by the deposition parameters of the film rather than doping concentrations. Depletion layer width in turn has a profound effect on the performance of the cell. Hence it is important to create a photovoltaic cell by changing the chemical bath deposition parameters keeping the doping concentrations at a minimum and films as close to intrinsic as possible.

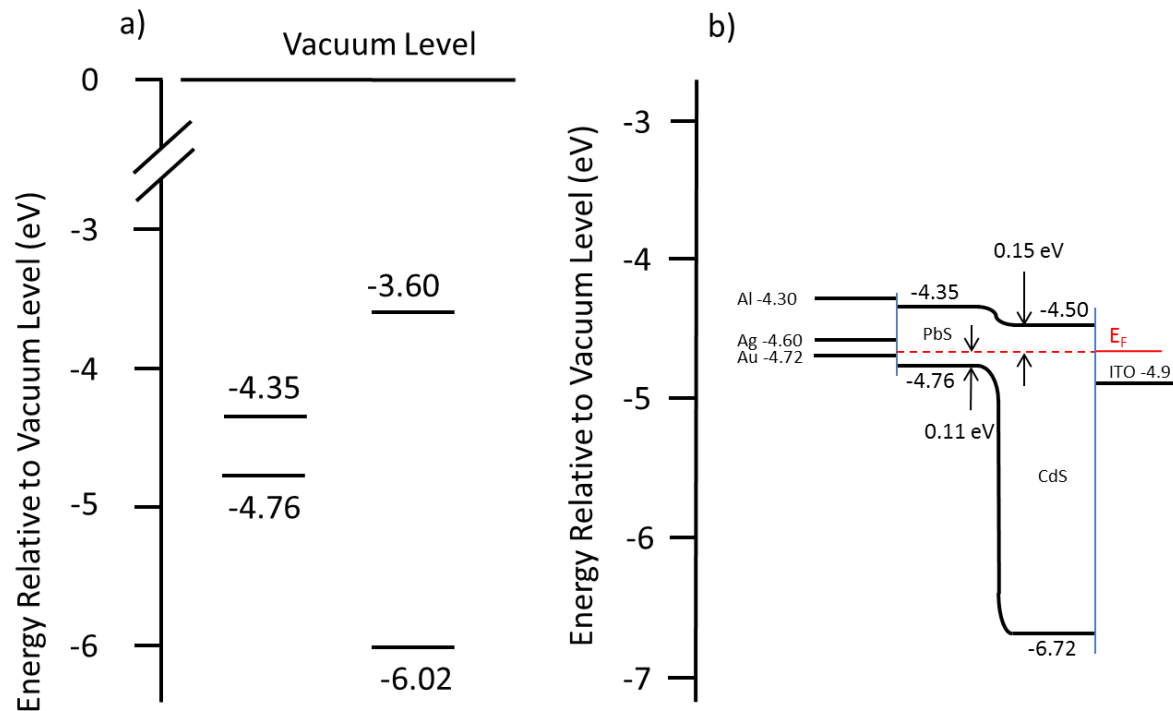


Figure 7.2. Energy band diagram. a) Valence and conduction band edge of nanoparticle CdS and PbS. b) Schematic of a the energy level alignment with  $\text{TiO}_2$  as an electrode on the CdS side and several other possible materials as the electrode on the PbS side.

Heterojunction thicknesses are devised in such a way to ensure that the depletion width extends throughout the entire device. This ensures that any free carrier that is generated will be swept away towards the electrode. Further, in order to increase the electric field within the depletion layer, built-in voltage is maximized to the largest possible extent that allows for a heterojunction.

Device equivalent circuit is shown in Figure 7.3. As can be seen both top and bottom electrodes contribute to the losses within the device. Hence the electrical properties of both need to be taken into account during the device optimization. Top electrode was either Au or Ag, with resistivities ranging from  $1.58 - 2.3 \times 10^{-8} \Omega \text{ m}$ . Geometry of the top electrode was a  $\sim 100 \mu\text{m}$  thick film with  $\sim 1 \text{ cm}^2$  area. Bottom electrode was a topic of intense study and is discussed in greater detail below. Shunt resistance in the CdS/PbS heterojunction has been measured to be  $4.5 \times 10^3 \Omega$  in a typical device with no doping.

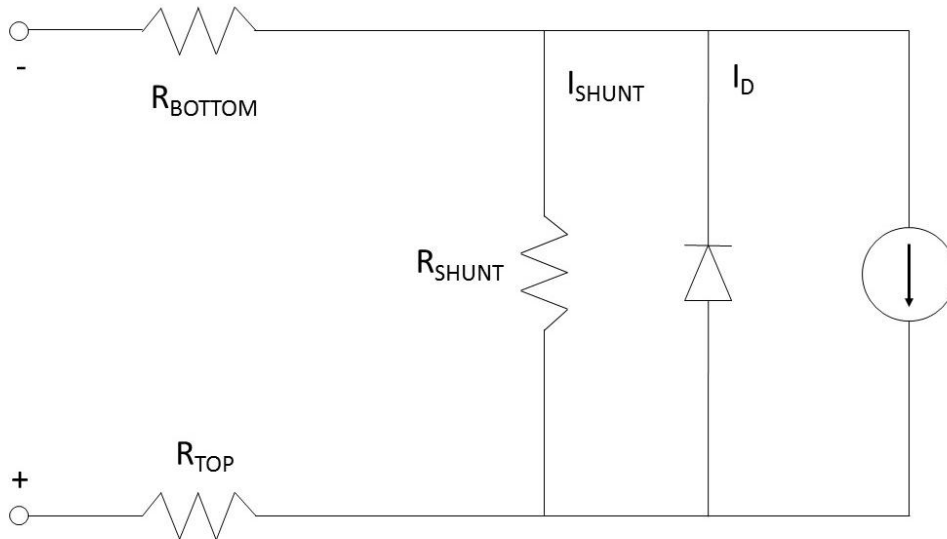


Figure 7.3 Equivalent circuit of the device.

## 7.3 Results

### 7.3.1 CdS/PbS structural analysis

XRD spectra for the CdS and PbS thin films is shown in Figure 7.4. CdS shows strong peaks around 26, 31, 28 degrees, which correlate to the cubic structures in the (111), (220), and (200) planes. PbS shows strong cubic orientation in the (111), and (200) planes. The two strong orientations overlap. PbS also shows a weak cubic orientation in the (220) and (331) planes, whereas CdS shows weak cubic orientation in the (110), and (311) planes. There is some correlation between the weaker peaks as well. Given that the PbS thin film was grown on the CdS, these results indicate that lead sulfide (which is typically found in cubic phase) took on the cubic form and orientation of the CdS. In previous work it was found that CdS tends to form in a cubic-hexagonal mix. During junction deposition, however, CdS took on a predominantly cubic form. This is attributed to the CdS taking the form of the TiO<sub>2</sub> TCO on which CdS was deposited on glass. In the case when CdS is deposited on the glass itself, the growth mechanisms of this material mold the structure of the material into its blended form. This phenomenon, however, is avoided in the case where a cubic structure already exists on the surface of the substrate. Additional observation that can be made is the fact that even in the cluster-by-cluster dominated deposition, the structure of CdS is predominantly cubic on the cubic structured substrate. This is indicative to the overall little influence of the growth mechanism's effect on the structural properties. From here it follows, that a hexagonal structured substrate would induce a hexagonal phase of the CdS, which would result in drastically different performance of the CdS films. Additionally, hexagonal is not a typical PbS phase, hence structural differences (i.e. poor contacts) in CdS/PbS heterojunction would be expected.

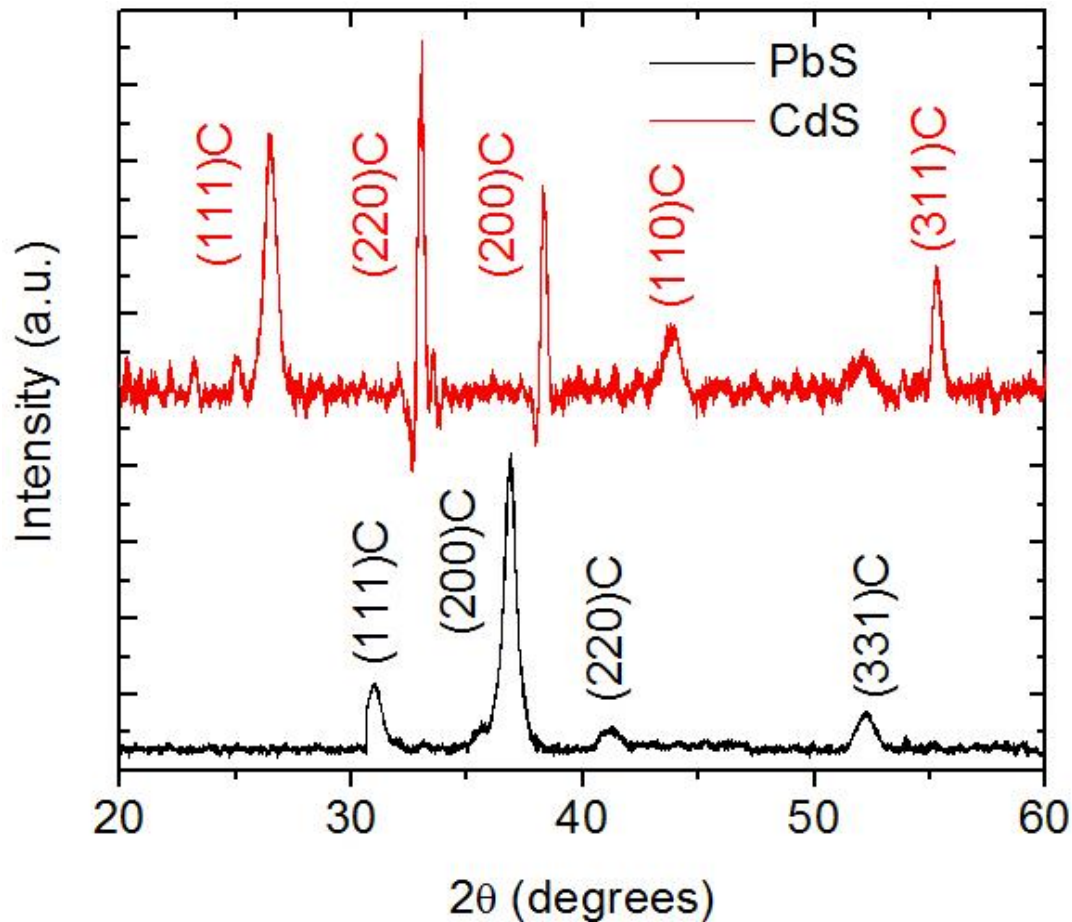


Figure 7.4 XRD data for the CdS and PbS thin films in heterojunction.

### 7.3.2 Glass/AuGrid/CdS/PbS/Au device electrical performance

The goal of this research is to make an efficient way to convert waste mid IR range electromagnetic waves into usable electricity. Doping agents add additional expenses to the overall cost of the device, and is coupled with the cost of the Au grid. Hence in order to increase the overall performance of the cell usage of dopants was avoided to greatest extent. Au grid was used as a preliminary testing ground to show existence of the heterojunction.

Opto-electrical properties of both CdS and PbS were tuned through the chemical bath deposition in order to avoid usage of dopants. During the course of the research it was found that the bandgap of CdS can be minimized by increasing the grain size of the nanocrystals. The smallest achieved bandgap was found to be 2.2 eV. Additionally, interstitial trapped metal and sulfide ions acted as artificial dopants in the films. These interstitially trapped ions would act as electron donors raising the Fermi level closer to the conduction band. The amount of interstitially trapped

ions was found to be greatest at the highest deposition temperatures, hence the materials were deposited at highest permissible temperatures that would not degrade the films.

Completely avoiding doping, however, was not possible; boron and bromine were used as acceptor and donor dopants respectively. The Fermi level in relation to the intrinsic Fermi level is found using equations (7.1) and (7.2)

$$E_F = E_i - kT \ln \frac{N_A}{n_i} \quad (7.1)$$

$$E_F = E_i + kT \ln \frac{N_D}{n_i} \quad (7.2)$$

Where  $E_i$  is the intrinsic Fermi level,  $k$  is the Boltzman constant,  $T$  is temperature,  $N_A$  and  $N_D$  are the acceptor and donor concentrations respectively, and  $n_i$  is the intrinsic carrier concentration. Computations for the donor and acceptor concentrations were done to bring the Fermi level to 0.15 eV from the conduction band in CdS and 0.11 eV from the valence band in PbS respectively.

I-V in this structure show a definite characteristics suggesting a heterojunction with an increasing short circuit current and open circuit voltage as a function of temperature, as shown in Figure 7.4. This behavior suggests that the device can convert a broad range of the IR spectrum and waste heat of various temperatures into electricity. Additionally, measured Mott-Schottky diagrams show a behavior typical of a heterojunction. Mott-Schottky diagrams provide an accurate measurement for the doping concentrations and built-in potential of the heterojunction [180]. Doping efficiency effect on the performance of the cell was is left for the structures utilizing TCOs.

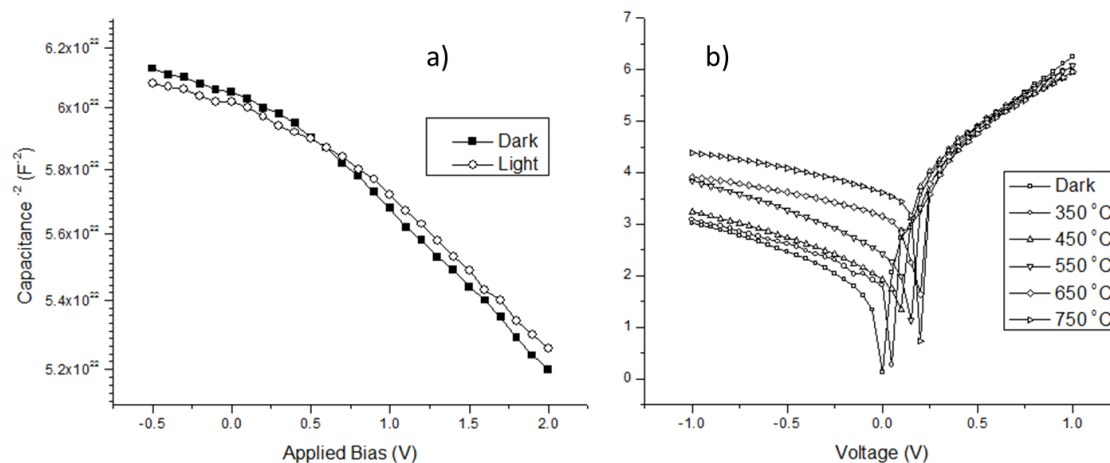


Figure 7.5 Mott-Schottky plot and I-V curves as a function of temperature for a Glass/AuGrid/CdS/PbS/Au structure.

It has been previously reported that proper spacing between the electrodes will have a profound effect on the overall performance of the device [181]. Gold finger spacing was altered in order to achieve highest efficiency. Finger spacing ranged from 1  $\mu\text{m}$  to 150 nm, and I-V measurements were completed under an artificial sun (i.e. 1000  $\text{W}/\text{m}^2$ ). It was found that large spacing between gold fingers (greater than  $\sim 500$  nm) did not produce favorable electrical performance, i.e. efficiencies below 0.5%. Hence gold finger spacing were analyzed meticulously in the range below 500 nm. I-V data for various gold finger spacing are shown in Figure 7.5. 150 nm provides the highest efficiency of 1.96%. Fill factors,  $V_{\text{OC}}$ , and  $I_{\text{SC}}$  are 0.28, 60 mV, and 0.1  $\text{mA}/\text{cm}^2$  respectively. Overall this is a very low efficiency that is due mainly to the low fill factor. The low fill factor is attributed to the shadowing, from the fingers as well as the small cross sectional area of the fingers which causes extremely high series resistances in the bottom electrode. Overall performance of the “classical” grid design are summarized in Table 7.1

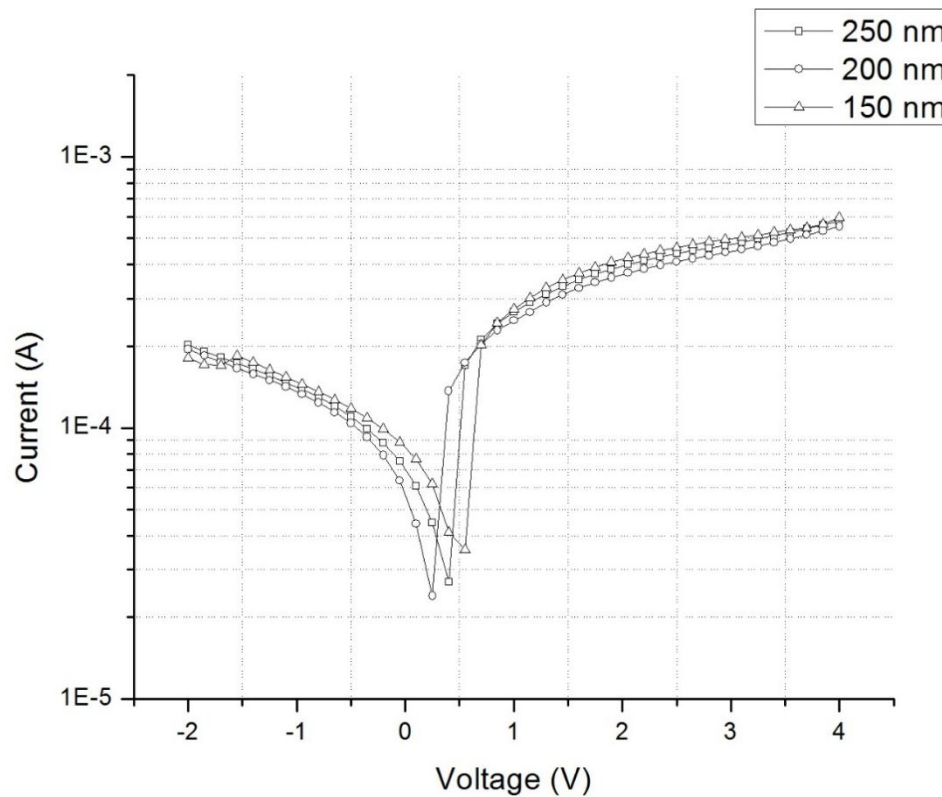


Figure 7.6 I-V data for device with variable gold finger spacing.

Table 7.1 Glass/AuGrid/CdS/PbS/Au electrical performance

Gold Finger Spacing (nm)	$V_{\text{max}}$ (mV)	$I_{\text{max}}$ ( $\text{mA}/\text{cm}^2$ )	$V_{\text{OC}}$ (mV)	$I_{\text{SC}}$ ( $\text{mA}/\text{cm}^2$ )	FF	$\eta$ (%)
500	6	0.40	21	0.8	0.13	0.55
250	9	0.49	26	0.9	0.18	0.60
200	21	0.91	54	1.8	0.20	1.55

---

150	24	1.45	60	2.1	0.28	1.96
-----	----	------	----	-----	------	------

---

Gold finger spacing was limited to the masking procedures used in the manufacturing of the grid. The equipment would generate masks with large deviations which were extremely difficult to handle when the gold finger spacing was decreased below 150 nm. Hence the overall best efficiency of the device was achieved at the 150 nm spaced gold fingers, which turned out to be also the limit of the device efficiency from this classical approach.

### 7.3.3 Glass/Ti<sub>1-x</sub>Ir<sub>x</sub>O<sub>2</sub>/CdS/PbS/Au device electrical performance

A device of a greater interest was the one that eluded usage of the Au grid for a TCO. In the case of the TCO several inherent grid issues were solved. First there was no more a shadowing effect taking place from the non-transparent gold finger. Second, the area of the transparent electrode was much greater than the gold fingers, thus allowing for greater probability of the generated carrier to make it to the electrode. The resistivity of the transparent conducting oxide, however, was ~4 orders of magnitude larger than that of gold, i.e.  $\sim 5 \times 10^{-4} \Omega \text{ cm}$  for the TCO. From the resistance-resistivity relation, in order to have a sufficiently low resistance thus it became necessary to increase the thickness of the electrode.

TCO thicknesses were varied from 70 – 200 nm in thickness, which would give the series resistance at the bottom electrode to range from 700 – 250  $\Omega$ . Percent transmittance at various TCO film thicknesses are shown in Figure 7.7.

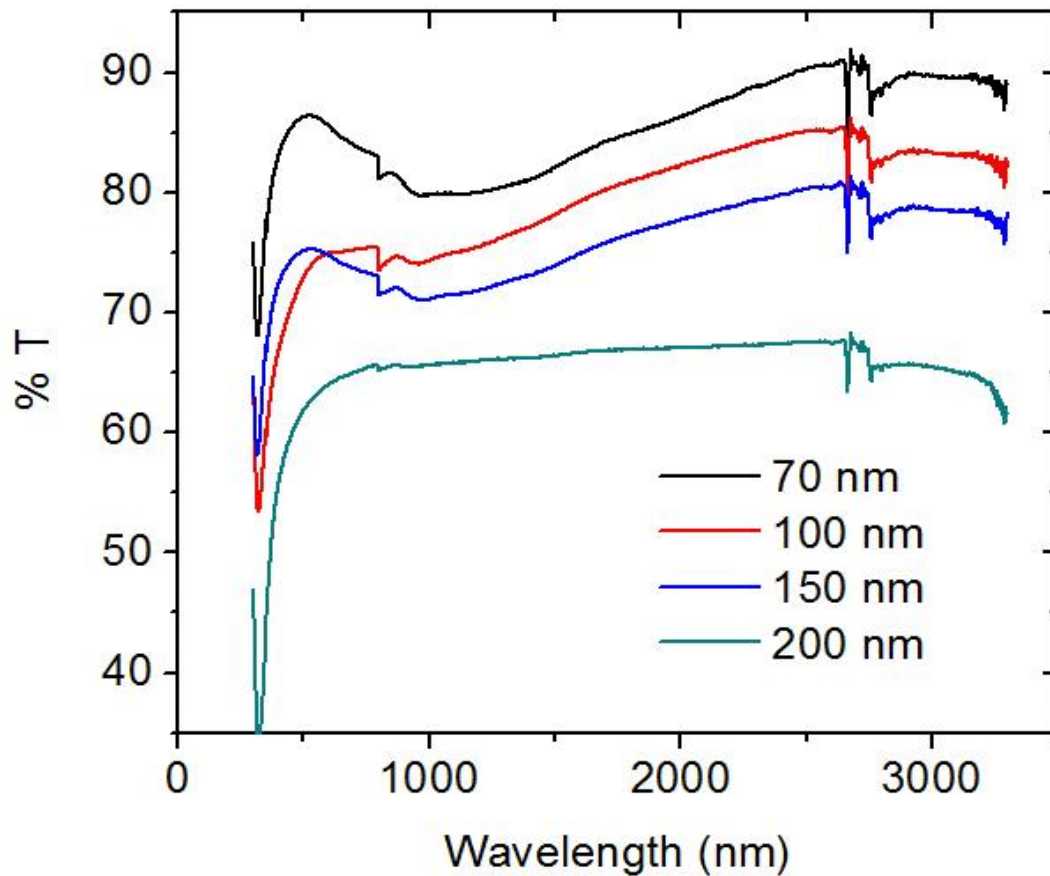


Figure 7.7 %T for various TCO thicknesses.

As the TCO thicknesses were increased the %T decreased proportionally. Disproportionate decrease in the %T was observed at the 150 nm to 200 nm film thickness increases. At these conditions the transmittance decreased  $\sim 10\%$  in the Visible and near infra-red (Vis-NIR) spectral region. This phenomenon was observed visually as well, as shown in Figure 7.8.

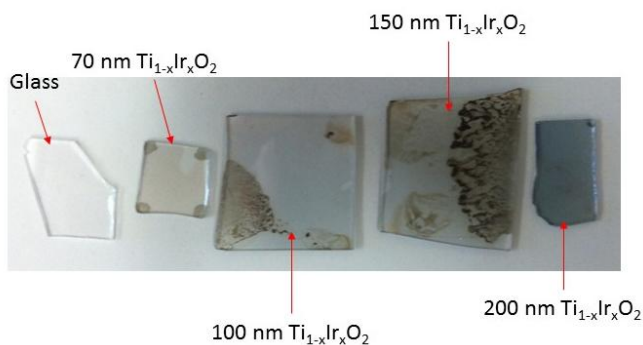


Figure 7.8 Visual observation of the opaqueness of thicker TCOs.

I-V data for the devices with various  $\text{Ti}_{1-x}\text{Ir}_x\text{O}_2$  film thicknesses is shown in Figure 7.9.

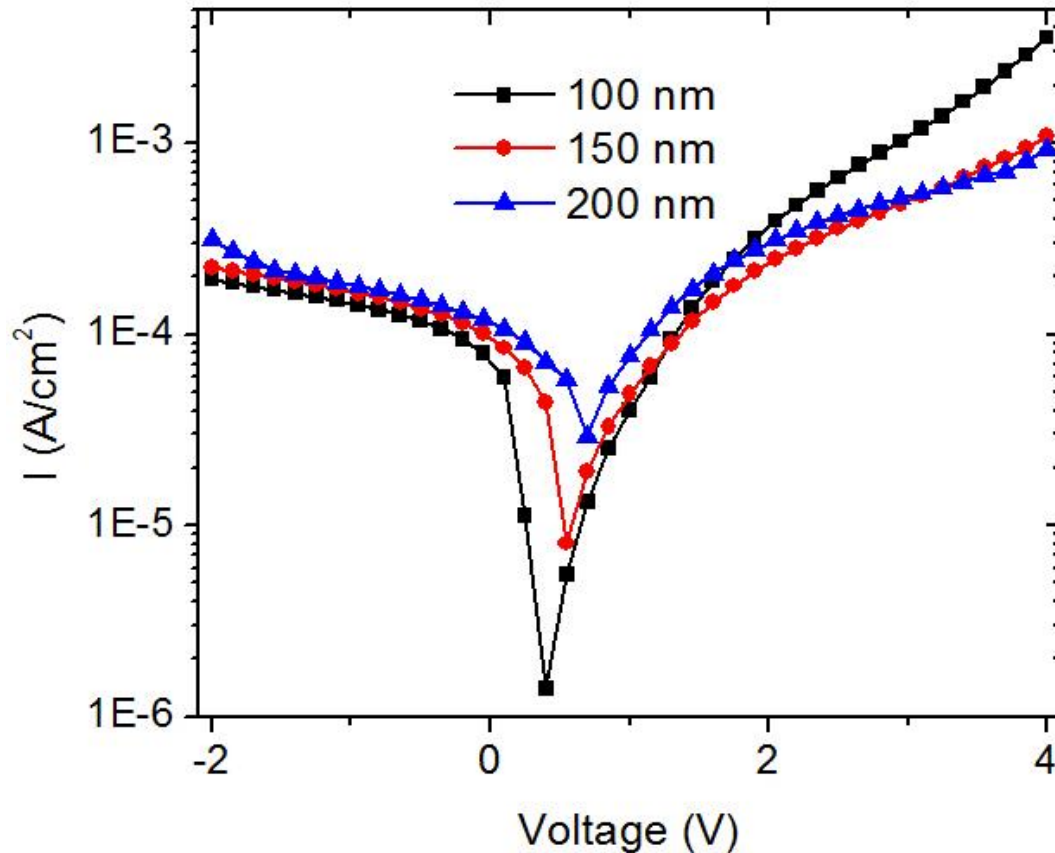


Figure 7.9 I-V data at various TCO thicknesses.

Significant reduction in the series resistance can be observed in the higher thickness samples. Also there is a noticeable increase in the short circuit current and open circuit voltage. This is mainly attributed to the elimination of the shadowing which allows for a higher number of photons to reach the heterojunction. Additionally, the overall increase in the electrode coverage area allows for a higher probability of carrier collection. Films above 200 nm in thickness could potentially decrease the series resistance further, however, the overall transmittance of the films would be diminished close to 50%. TCO thicknesses above 200 nm were not pursued. Summary of the electrical performance of the heterojunction at different TCO thicknesses is summarized in Table 7.2.

Table 7.2 Glass/  $Ti_{1-x}Ir_xO_2$ /CdS/PbS/Au electrical performance

$Ti_{1-x}Ir_xO_2$ thickness (nm)	$V_{OC}$ (mV)	$I_{SC}$ (mA/cm <sup>2</sup> )	FF	$\eta$ (%)
70	19	0.75	0.13	1.84
100	35	0.79	0.26	1.91
150	68	1.92	0.30	2.11
200	92	2.7	0.32	2.15

As previously discussed addition of dopants can induce higher built in voltages, however decrease the depletion width. Doping concentrations were added not to diminish the depletion width to be less than  $\sim 1.5 \mu\text{m}$  (approximate thickness of the CdS/PbS heterojunction). Doping concentrations and built in voltages were extracted from the Mott-Schottky graphs. Data was acquired under 1 MHz frequency under dark conditions. For the purposed of high homogeneity, small area heterojunctions were used in the analysis ( $\sim 1 \text{ mm}^2$ ). Typical Mott-Schottky plots for the heterojunctions are shown in Figure 7.10.

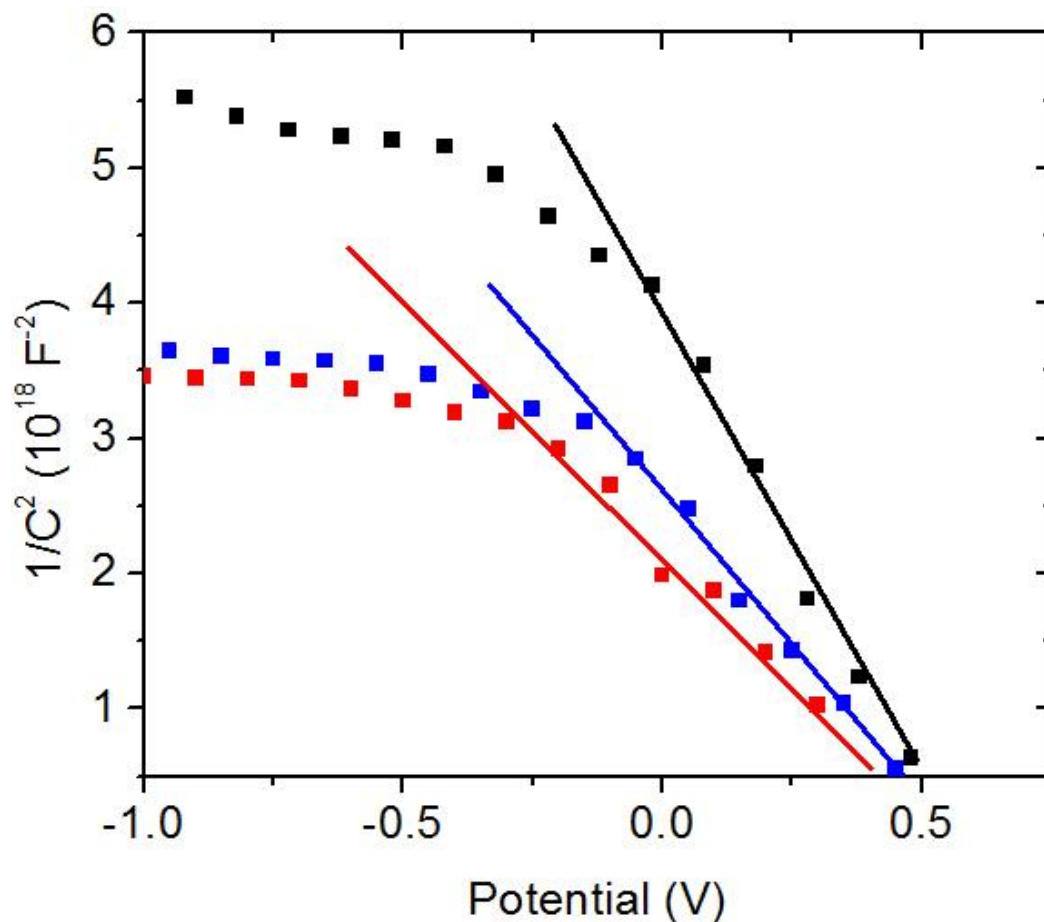


Figure 7.10 Mott-Schottky diagrams for the Glass/ $\text{Ti}_{1-x}\text{Ir}_x\text{O}_2$ /CdS/PbS/Au structure.

Various doping concentrations were used to figure out the concentrations for optimal efficiency. It was computed that the combined donor and acceptor doping concentrations above  $\sim 1 \times 10^{17}$  donors would result in depletion widths below the width of the heterojunction. Hence doping concentrations were kept slightly below the maximum allowable concentration.

Effective carrier concentrations was computed from the slopes of the Mott-Schottky data, and the  $V_{\text{bi}}$  can be extrapolated to the intersection of the potential axis. Data is summarized in Table 7.3.

Table 7.3 Parameters from the Mott-Schottky analysis

Added Dopant Concentrations ( $\times 10^{18}$ )	Computed Dopant Concentrations ( $\times 10^{18}$ )	$V_{bi}$ (mV)	FF	$\eta$ (%)
2.0	1.23	309	0.29	2.11
4.0	3.50	414	0.31	2.17
6.0	4.28	456	0.33	2.24
8.0	6.70	503	0.35	2.25

As can be seen from the data, increase in doping concentrations did not add significant increase in device efficiency. Nevertheless, some efficiency has been increased, this is mainly attributed to the extra carriers that are generated by the donors. Further, it is expected that the excessive donors are deforming the bands of the semiconductors hence causing a change in the band structures of the material, and create barrier heights at the interfaces. This phenomenon has been observed before, and can be addressed by proper electrode design and material selection [182]. Additionally, there is some discrepancy between the added and the computed number of dopants. This discrepancy can be attributed to some of the dopants not being incorporated into the films during film growth. From here it follows that technically doping concentrations slightly above the theoretical maximums can be used in the procedure. This could potentially result in further efficiency increase.

Theoretical computations on the CdS/PbS heterojunctions found the optimal base thickness of the structure to be 2  $\mu\text{m}$  [178]. Hence it was of interest to study base thicknesses and their effect on the overall performance of the cell. For this series of experiments parameters that previously yielded optimal result were held constant: i.e. dopant concentrations and TCO thickness were  $8 \times 10^{18} \text{ cm}^{-3}$  and 200 nm respectively.

PbS layer is the base in the CdS/PbS structure. As previously discussed unfortunately there was a limit on the PbS thicknesses that could be achieved by the chemical deposition method. Reason being is that eventually the acidic and alkaline solutions begin to erode the films at a higher rates than the film growth. Largest film thicknesses obtained in this chemical bath deposition process were  $\sim 1.1 \mu\text{m}$ . Alternate deposition mechanism should be developed to acquire thicker films. Table 7.4 summarizes results of the PbS layer film thicknesses and respective cell performance.

Table 7.4 Base layer thickness (PbS) device performance

PbS thickness (nm)	$V_{OC}$ (mV)	$I_{SC}$ ( $\text{mA}/\text{cm}^2$ )	FF	$\eta$ (%)
800	92	2.7	0.32	2.20
900	98	2.9	0.33	2.22
1000	108	3.2	0.35	2.25
1100	115	3.4	0.37	2.30

There are significant changes in efficiency of the device based on the thickness of the base layer. Device efficiency can be further improved upon by further increasing the base layer thickness. The rather thick films of 2  $\mu\text{m}$  could not be achieved by the present chemical solution methods. Possible non CBD methods would be required to develop film thicknesses further and to improve device efficiency further.

#### 7.3.4 External and internal quantum efficiency of the Glass/ $\text{Ti}_{1-x}\text{Ir}_x\text{O}_2$ /CdS/PbS/Au device

Optimal manufactured devices by the CBD method described in this work have shown efficiencies of 2.30%. Experimentally obtained external (EQE) and the computed internal quantum efficiencies (IQE) for the best performing Glass/ $\text{Ti}_{1-x}\text{Ir}_x\text{O}_2$ /CdS/PbS/Au device is shown in Figure 7.11. Changes in EQE values in the range 1–2.5 eV are minor varying slightly around 20% and is in accordance with the spectral dependence of reflectance from CdS film. From here it follows that the EQE is dependent on the reflection from the CdS. Hence it is favorable to generate highly non-reflecting CdS films. It has been previously demonstrated that reflectivity of the CdS depends on the chemical bath parameters [96]. Further such films could be textured to allow for light trapping. IQE decays sharply above 2.5 eV photon energy, this is near the bandgap of CdS, hence all photons with the energy above the bandgap of CdS are absorbed by the CdS emitter and never make it to the base (PbS), hence limiting the overall performance of the device at high photon energies. Further, efficiency is close to zero at photon energies below  $\sim 0.5$  eV. This is attributed to the low energy photons that pass through the structure without being absorbed. Overall there is significant difference between the EQE and IQE, suggesting that some of the photons are reflected at the electrodes and the glass without ever making it to the junction. This difference could be minimized and addressed in future research.

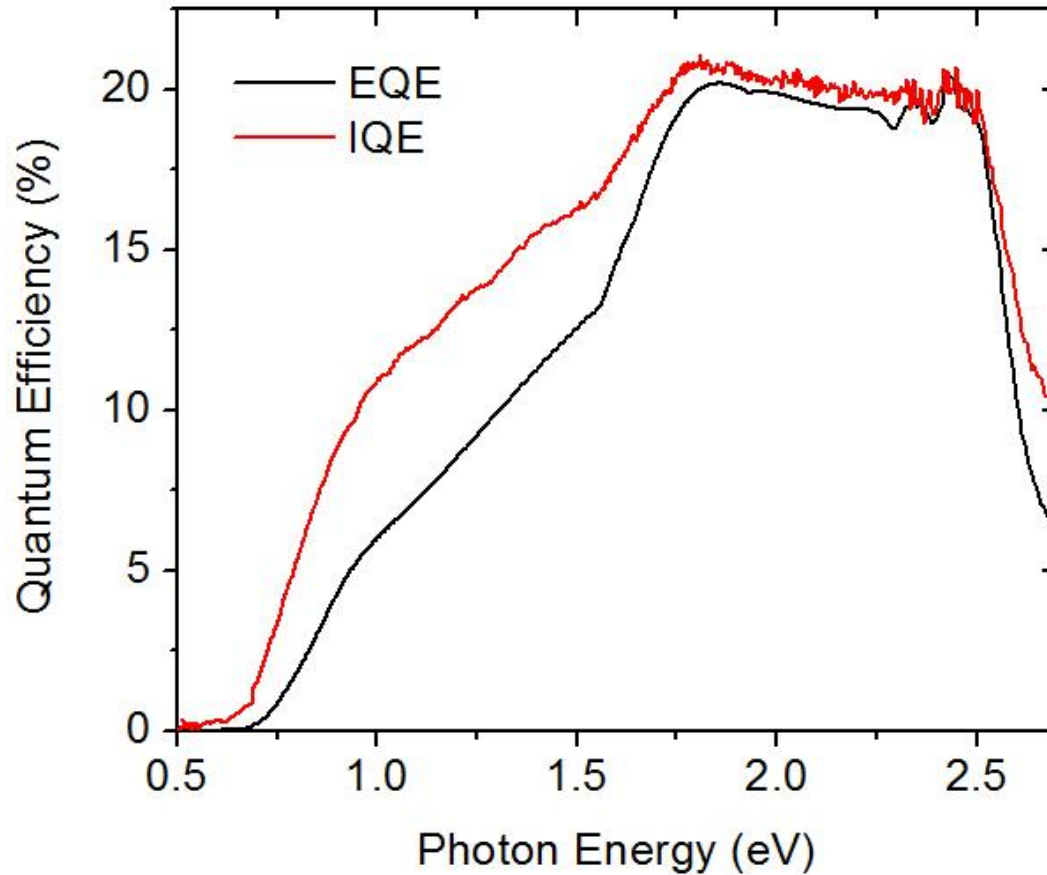


Figure 7.11 External and internal quantum efficiency of the Glass/Ti<sub>1-x</sub>Ir<sub>x</sub>O<sub>2</sub>/CdS/PbS/Au structure.

#### 7.4 Conclusion

Chemical bath deposition technique was used for the preparation of the Glass/Ti<sub>1-x</sub>Ir<sub>x</sub>O<sub>2</sub>/CdS/PbS/Au solar structure with CdS and PbS active layers. Work has shown that there are several ways to increase the efficiency of the device. Most notably high efficiency is achieved through the proper design and structuring of the transparent electrodes, doping profiles, base and emitter thicknesses. Optimal devices were found at the TCO thicknesses of 200 nm,  $8 \times 10^{18} \text{ cm}^{-3}$  doping concentrations, and 1.1  $\mu\text{m}$  base thicknesses. Further increase in efficiency can be achieved through larger base thicknesses, however, such an approach would require additional PbS growth technique. Future work could also address decreasing the grain sizes to achieve even higher built-in voltages for higher efficiencies. Furthermore, grain sizes can be used for optical bandgap tuning. Furthermore, this research has shown that PbS films can be successfully used in multi-junction solar cell devices.



## Chapter 8. Conclusions, summary, and future work

Modern day research is incessantly becoming interdisciplinary in nature, requiring more complex analysis and specialized equipment. Advances in nanotechnology in many aspects are pushing the interdisciplinary research demanded by modern day engineering sciences. The work contained within this research is interdisciplinary in many aspects. It leverages the knowledge of the physics, mechanics, materials, crystallography, electrical engineering all in order to create a cost efficient device for various applications. One of the most promising applications of this technology is the thermal energy conversion. The devices created in this research use nanotechnology, micro- and nano- structures of various semiconductors, interfaces, and thin films. The structural, electrical, and optical properties of these materials have been successfully manipulated to make them suitable for numerous applications. The remarkable opto-electrical properties of these materials make them ideal candidates for future use. This dissertation also addresses numerous other aspects of these materials and technology in general.

The most important results of this research are:

- Development of an improved chemical bath deposition technique for the growth of nanocrystalline semiconducting thin film lead (II) sulfide. Film has also been shown to have tunable opto-electrical properties. Properties have been shown to depend on the growth parameters of the CBD. This method may be applied for growth of various other semiconductors.
- A method was developed to grow high quality single crystal cadmium sulfide in a chemical bath deposition. The growth mechanics of CdS in CBD were analyzed. It was discovered that ion – by – ion growth mechanism is the dominating mechanism in this deposition method. By controlling the deposition parameters largely cubic structure of the CdS can be achieved. Post annealing can achieve phase transitions in the CdS and significantly alter the opto-electrical properties of the film
- Growth mechanisms of CdS and their effects on the opto-electrical performance of the films was analyzed. It was found that ion-by-ion mechanisms produces generally stoichiometric cubic CdS structures. Raising the bath temperatures promotes cluster-by-cluster mechanism and deviation from stoichiometry. Overall this improves the electrical properties of the films, however, at the expense of the optical transparency.
- A novel transparent conducting oxide was developed for the device, Ir doped TiO<sub>2</sub>. The TCO is largely transparent in both the visible and infrared spectrum. The electrical properties of the TiO<sub>2</sub> make the films suitable for the wide variety of devices utilized in both the visible and the infrared spectral regions. Additionally, Iridium allows for an alternative dopant to be used various semiconductors. The electrical properties of the film have been shown to be widely tunable from the nine valence electrons of the Ir. Ir doping had negligible effects on the optical properties of the films.

- A  $\text{Ti}_{1-x}\text{Ir}_x\text{O}_2/\text{CdS}/\text{PbS}/\text{Au}$  device was constructed. Core of the device was the heterojunction between cadmium sulfide and lead sulfide. Efficiency of the heterojunction has been demonstrated to be tunable by the doping profiles of both the donors and acceptors in the materials. Ohmic contacts were demonstrated to be forming at the interface between the TCO and the heterojunction. The barrier heights at the interfaces were shown from the capacitance-voltage profiles.
- Crystalline structure affects the opto-electrical properties of the film. Large grain sizes of PbS increased the mobility of carriers in the thin films. Carrier lifetimes also increased with the increase in grain sizes, due to the decrease of the trap states in the thin films. Additionally, it has been shown that larger grain sizes can be achieved through subsequent film depositions in the chemical bath. Hence the optical and electrical properties of the films can be controlled directly by the chemical bath deposition and its parameters.
- Phase transitions have been demonstrated in CdS. CdS is known to form in either the cubic or the hexagonal structures. The two crystalline structures are close in activation energies. By controlling the bath parameters, largely cubic CdS can be achieved. Addition of the energy to the cubic structure of CdS during post-annealing process converts much of the cubic structure to the hexagonal structure drastically changing the electrical and optical properties of CdS.
- Film adhesion to the substrate was studied as a function of stored energy in the film. If the films were strained, certain amount of energy was stored in the film. If the films were not allowed to relax the stored energy became larger than the adhesive energy, films were found to peel off the substrate. This knowledge allows for a careful planning on the growth of film strain and energy in order to ensure adhesion of the film.
- Burstein-Moss shift was observed in  $\text{TiO}_2$  with Iridium doping. This signifies that iridium is extremely efficient dopant, filling the vacant states in the conduction band, hence shifting the bandgap of the semiconductor. This is significant result telling much about the doping nature of Iridium, and allows for application of Ir as a dopant in various applications and materials.

Presented technology is extremely cost efficient. As the availability of this technology increases and the methods are refined further, vast amount of additional research work can be completed. Few potential future projects on the materials and devices that may be done are provided below:

- Peak of the blackbody radiation is temperature dependent. By computing the location of the blackbody radiation peak, the bandgap of the semiconductors can be tuned in such a way to ensure the maximum conversion efficiency. It has been shown that bandgaps of the materials can be controlled by the deposition parameters. Hence the parameters in the chemical bath can be optimized to ensure highest possible conversion efficiency of the device.

- A monolithic devices have been shown to have high conversion efficiencies. This heterojunction can be used in a monolithic structure to allow for high energy conversion of the device. Bandgaps can be aligned to ensure optimal conversion efficiency. This work will require additional computation for the highest bandgap and optimization of the chemical bath.
- Laser texturing has been found to improve light trapping inside materials. Transparent conducting oxide can be textured to ensure highest light trapping inside the device. Texturing will need to be completed in both ensuring that the light enters the device as well as to ensure the light particles generate a carrier-hole pair.
- Photodetector – the device can be optimized to act as a highly sensitive infrared detector. This would allow for design and analysis of cost efficient infrared sensors of various applications. This technology is not limited to the photovoltaic applications alone. Any device that operates in the infrared spectral region can utilize the technology.
- With further research this technology can be utilized to generate high electric field at relatively low voltages. Coupled with laser texturing technology, which produces the sharp geometry pillars, the technology may be used for field emission displays, electron sources for instruments, sensors, and other synonymous applications.
- Improvement of the bond strength requires further research. This adhesion can be achieved by increasing the contact area on the interface of the materials, and thoughtful construction of the crystals with minimal crystalline strain. Interlocking between the materials can also add additional adhesive strength.
- Surface profile doping of the materials will improve the efficiency of the device further. By heavily doping the interface areas, the band structure may be adjusted in such a way to allow for easier electron transfer, possibly even tunneling at the barrier locations, for improved device performance. This can play an important role in ensuring successful and effective devices.
- By replacing the non-transparent gold electrode with another transparent electrode the device can be used as an optical beam block to block out infrared radiation. Low reflectance and high transmittance will ensure that only specific wavelengths will pass through. Hence the device could become a cost effective and efficient blocking device for infrared radiation.

## References

- [1] Z. Liu. Global Energy Interconnection. Academic Press (2015) 117-118. ISBN: 9780128044056
- [2] M. S. Dresselhaus, G. W. Crabtree, M. V. Buchanan, Addressing Grand Energy Challenges through Advanced Materials. *MRS Bulletin* 30 (2005), 518-524
- [3] J. E. Frisch. Future Stresses for Energy Resources. World Energy Conference – Conservation Commission (1986), 33-37
- [4] U.S. Energy Information Administration EIA, Independent Statistics and Analysis. November 2015.
- [5] S. Perry, J. Klemes, I. Bulatov. Integrating waste and renewable energy to reduce the carbon footprint of locally integrated energy sectors. *Energy* 33 (2008) 1489-1497
- [6] A. Schafer, J. B. Heywood, H. D. Jacoby, I. A. Waitz. Transportation in a climate-constrained world. MIT Press, Cambridge MA (2009) 104-105
- [7] S. K. Agarwal. Water Pollution. APH Publishing (2009) 129-133. ISBN-10: 8176488321
- [8] M. I. Hoffert, K. Caldeira, G. Benford, D. R. Criswell, C. Green, H. Herzog, A. K. Jain, H. S. Kheshgi, K. S. Lackner, J. S. Lewis, H. D. Lightfoot, W. Manheimer, J. C. Mankins, M. E. Mauel, L. J. Perkins, M. E. Schlesinger, T. Volk, T. M. L. Wigley. Advanced Technology Paths to Global Climate Stability: Energy for a Greenhouse Planet. *Science* 298, (2002) 981-987
- [9] G. Chen. Gallium Nitride-based HEMT devices modeling and performance characterization. Dissertation. University of Illinois at Urbana-Champaign (2008) 68-70
- [10] B. Hoefflinger. Chips 2020: A guide to the future of nanoelectronics. Springer-Verlag Berlin Heidelberg (2012) 161-169
- [11] L.E. Bell, Cooling, Heating, Generating Power, and Recovering Waste Heat with Thermoelectric Systems. *Science*. 321(2008) 1457-1461
- [12] R. B. Olsen, D. A. Bruno, J. M. Briscoe. Pyroelectric conversion cycles, *Journal of Applied Physics*. 58 (1985) 4709-4716
- [13] J. Larjola. Electricity from industrial waste heat using high-speed organic Rankine cycle (ORC). *International Journal of Production Economics* 41 (1995) 227-235
- [14] Y. Chen, P. Lundqvista, A. Johansson, P. Platell. A comparative study of the carbon dioxide transcritical power cycle compared with an organic rankine cycle with R123 as working fluid in waste heat recovery. *Applied Thermal Engineering*. 26(2006) 2142-2147
- [15] M. Planck. Distribution of energy in the spectrum. *Annalen der Physik* 4 (1901) 553-563

- [16] A. Einstein. On a Heuristic point of view toward the emission and transformation of light, *Annals of Physics* 17 (1905) 132
- [17] I. Montvay, E. Pietarinen. The Stefan-Boltzmann Law at high temperature for the gluon gas. *Physics Letters B* 110 (1982) 148-154
- [18] D. J. Rowe, G. Thiamova. The many relationships between the IBM and the Bohr model. *Nuclear Physics A* 760 (2005) 59-81
- [19] J. M. Ziman. *Principles of the theory of solids*. Cambridge University Press, London 1964. ISBN: 9781139644075
- [20] T. H. Xu, C. H. Song, Y. Liu, G. R. Han. Band structures of TiO<sub>2</sub> doped with N, C and B. *Journal of Zhejiang University Science B* 7 (2006) 299-303
- [21] C. Kittel. *Quantum theory of solids*. Wiley, New York, 1963
- [22] Q. Zhang. Intensity dependence of the photoelectric effect induced by a circularly polarized laser beam. *Physics Letters A* 216 (1996) 125
- [23] R. Hamer. The limiting frequency of the photo-electric effect. University of California, Dissertation (1922)
- [24] S. M. Sze, K. K. Ng. *Physics of semiconductor devices: 3<sup>rd</sup> edition*. Wiley-Interscience, John\_Wiley and Sons, Inc. (2007)
- [25] R. F. Pierret. *Semiconductor device fundamentals*. Addison-Wesley Publishing Company. (1996)
- [26] R. A. Smith. *Semiconductors, 2<sup>nd</sup> Edition*, Cambridge University Press, London. (1979)
- [27] B. M. Smirnov. *Principles of Statistical Physics: Distributions, Structures, Phenomena, Kinetics of Atomic Sysyems*. Wiley-VCH. (2006)
- [28] P. V. Kamat, N. M. Dimitrijevic, A. J. Nozik. Dynamic Burstein-Moss shift in semiconductor colloids. *Journal of Physical Chemistry* 93 (1989) 2873-2875
- [29] W. B. Joyce, R. W. Dixon. Analytic approximations for the Fermi energy of an ideal Fermi gas. *Applied Physics Letters* 31 (1977) 354
- [30] J. Bardeen, W. Shockley. Deformation potential and mobilities in nonpolar crystals. *Physics Review* 80 (1950) 72
- [31] W. A. Harrison. Scattering of electrons by lattice vibrations in nonpolar crystals. *Physical Review* 104 (1956) 1281-1290
- [32] P. K. Basu, B. R. Nag. Intervalley scattering mechanism in Silicon. *Physics Review B*, 5 (1972) 1633

- [33] B. I. Shklovskii, A. L. Efros. Electronic properties of doped semiconductors. Moscow, Izdatel'stvo Nauka (1979)
- [34] N. Kawasaki, K. Yoshihiro, O. Hideki, F. Akihiko, Y. Minoru. Trap states and transport characteristics in picene thin film field-effect transistor. *Applied Physics Letters* 94 (2009)
- [35] W. K. Peters, B. Cho, R. J. Hill, T. L. Courtney, D. M. Jonas. Band Filling Dynamics and Auger Recombination in Lead Sulfide Nanocrystals. *International Conference on Ultrafast Phenomena* (July, 2010)
- [36] P.J. Drummond, D. Bhatia, A. Kshirsagar, S. Ramani, J. Ruzyllo. Studies of photoconductance decay method for characterization of near-surface electrical properties of semiconductors. *Thin Solid Films* 519 (2011) 7621-7626
- [37] Y. Arafat , F. M. Mohammedy , M. M. S. Hassan. Optical and Other Measurement Techniques of Carrier Lifetime in Semiconductors. *International Journal of Optoelectronic Engineering*. 2 (2012) 5-11
- [38] I.M. de Schepper, M.H. Ernst. Self-diffusion beyond Fick's law. *Physica A: Statistical Mechanics and its Applications*. 98 (1979) 189-214
- [39] Y. Roichman, N. Tessler. Generalized Einstein relation for disordered semiconductors—implications for device performance. *Applied Physics Letters*. 80 (2002) 1948
- [40] K. Funahashi, T. Kashiwa, S. Sakoda, K. Fujii. Exactness in the Wentzel–Kramers–Brillouin approximation for some homogeneous spaces. *Journal of Mathematical Physics*. 36 (1995) 4590
- [41] M. Lenzlinger, E. H. Snow. Fowler-Nordheim Tunneling into Thermally Grown SiO<sub>2</sub>.
- [42] E. F. Schubert. *Light-Emitting Diodes*. Cambridge University Press, (2006)
- [43] B. N. Chapman. Thin-film adhesion. *Journal of Vacuum Science and Technology*. 11, 106 (1974)
- [44] R. People, J. C. Bean. Calculation of critical layer thickness versus lattice mismatch for Ge<sub>x</sub>Si<sub>1-x</sub>/Si strained-layer heterostructures. *Applied Physics Letters* 47, 322 (1985)
- [45] J.W. Matthews, A.E. Blakeslee. Defects in epitaxial multilayers: I. Misfit dislocations. *Journal of Crystal Growth* 27, 118 (1974)
- [46] W. C. Johnson, P. T. Panousis. The influence of Debye length on the C-V measurement of doping profiles. *IEEE Transaction on Electronic Devices*, ED-18 (1971) 965
- [47] W. Shockley. The theory of p-n junctions in semiconductors and p-n junction transistors. *Bel Systems Technology Journal*. 28 (1949) 435

- [48] R. L. Anderson. Experiments on Ge-GaAs heterojunctions. *Solid State Electronics*. 5 (1962) 341
- [49] A. I. Gubanov. Theory of the contact of two semiconductors of the same type of conductivity. *Zhurnal Tekhnicheskoy Fiziki*. 21, 304 (1951)
- [50] H Kroemer. Theory of a wide-gap emitter for transistors. *Proceedings of the IRE*. 45 (1957) 1535-1537
- [51] J.M. Heras, L. Viscido. Work function changes upon water contamination of metal surfaces. *Applications of Surface Science* 4 (1980) 238—241
- [52] H. B. Michaelson. The work function of the elements and its periodicity. *Journal of Applied Physics* 48, 4729 (1977)
- [53] G. I. Roberts, C. R. Crowell. Capacitance effects of Au and Cu impurity levels in Pt n-type Si Schottky barrier. *Solid State Electronics*. 16, 29 (1973)
- [54] C. A. Mead, W. G. Spitzer. Fermi Level Position at Metal-Semiconductor Interfaces. *Physical Review Letters*. 134, A713 (1964)
- [55] J. M. Shannon. Reducing the effective height of a Schottky barrier using low energy ion implantation. *Applied Physics Letters*. 24, 369 (1974)
- [56] C. R. Crowell. W. G. Spitzer, L. E. Howarth, E. Labate. Attenuation length measurements of hot electrons in metal films. *Physics Reviews*. 127, 2006 (1962)
- [57] R. H. Fowler. The analysis of photoelectric sensitivity curves for clean metals at various temperatures. *Physics Review* 38, 45 (1931)
- [58] C. R. Crowell, S. M. Sze, W. G. Spitzer. Equality of the temperature dependence of the gold silicon surface barrier and the silicon energy gap in Au *n*-type Si diodes. *Applied Physics Letters* 4, 91 (1964)
- [59] J. O. Caldin, T. C. McGill, C. A. Mead. Schottky barriers on compound semiconductors: The role of the anion. *Journal of Vacuum Science and Technology* 13, 802 (1976)
- [60] P. O'Brien, J. McAleese. Developing an understanding of the processes controlling the chemical bath deposition of ZnS and CdS. *Journal of Material Chemistry*. 8, 2309 (1998)
- [61] A. D. Uhler. G. R. Helz. Solubility product of galena at 298°K: A possible explanation for apparent supersaturation in nature. *Geochimica et Cosmochimica Acta*. 48, 1155 (1984)
- [62] I. Kaur, D. K. Pandya, K. L. Chopra. Growth Kinetics and Polymorphism of Chemically Deposited CdS Films. *Journal of Electrochemical Society*. 127, 943 (1980)

- [63] A. Al-Borno, M. B. Tomson. The temperature dependence of the solubility product constant of vivianite. *Geochimica et Cosmochimica Acta*. 58, 5373 (1994)
- [64] L. Stradella, M. Argentero. A study of the thermal decomposition of urea, of related compounds and thiourea using DSC and TG-EGA. *Thermochimica Acta*. 219, 315 (1993)
- [65] A. Celikkaya, M. Akinc. Preparation and Mechanism of Formation of Spherical Submicrometer Zinc Sulfide Powders. *Journal of the American Ceramic Society*. 73, 2360 (1990)
- [66] J. M. Hollander, W. L. Jolly. X-Ray Photoelectron Spectroscopy. *Accounts of Chemical Research*. 3, 193 (1970)
- [67] L. Li , J. Hu , W. Yang , A. P. Alivisatos. Bandgap Variation of Size- and Shape-Controlled Colloidal CdSe Quantum Rods. *Nano Letters*. 1, 349 (2001)
- [68] C. C. Hsiu, L. Y. Lang. Chemical bath deposition of CdS quantum dots onto mesoscopic TiO<sub>2</sub> films for application in quantum-dot-sensitized solar cells. *Applied Physics Letters*, 91, 53503 (2007)
- [69] D. Byrne, E. McGlynn, M.O. Henry, K. Kumar, G. Hughes. A novel, substrate independent three-step process for the growth of uniform ZnO nanorod arrays. *Thin Solid Films*. 518, 4489 (2010)
- [70] R.D. Narhe, W. González-Viñas, D.A. Beysens. Water condensation on zinc surfaces treated by chemical bath deposition. *Applied Surface Science*. 256, 4930 (2010)
- [71] R. C. Kainthla, D. K. Pandya, K. L. Chopra. Structural and optical properties of solution grown CdSe<sub>1-x</sub>S<sub>x</sub> films. *The Electrochemical Society*. 129, 99 (1982)
- [72] M. Schubert. *Infrared ellipsometry on semiconductor layer structures: Phonons, plasmons, and polaritons*. Springer, Heidelberg (2004)
- [73] W. Paik, J. O'M. Bockris. Exact ellipsometric measurement of thickness and optical properties of thin light-absorbing film without auxiliary measurements. *Surface Science*. 28, 61 (1971)
- [74] A. Rothen. The ellipsometer, an apparatus to measure thickness of thin surface films. *Review of Scientific Instruments*. 16, 26 (1945)
- [75] R. Rossetti, J. L. Ellison, J. M. Gibson, L. E. Brus. Size effects in the excited electronic states of small colloidal CdS crystallites. *Journal of Chemical Physics*. 80, 4464 (1984)
- [76] W. N. Shafarman, J. Zhu. Effect of substrate temperature and deposition profile on evaporated Cu(InGa)Se<sub>2</sub> films and devices. *Thin Solid Films*. 361, 473 (2000)
- [77] J. C. Meredith, A. P. Smith, A. Karim, E. J. Amis. Combinatorial Materials Science for Polymer Thin-Film Dewetting. *Macromolecules*. 33, 9747 (2000)

- [78] W. Kern, D.A. Poutinen, Cleaning solutions based on hydrogen peroxide for use in silicon semiconductor technology, *RCA Review* 31 (1970) 187
- [79] W. Kern. Radioisotopes in semiconductor science and technology. Part 1. Semiconductor Production Solid State Technologies. 6, 10 (1963)
- [80] W. Kern. Radioisotopes in semiconductor science and technology. Part 2. Semiconductor Production Solid State Technologies. 6, 22 (1963)
- [81] W. Kern. Semiconductor surface contamination investigated by radioactive tracer techniques. Part 1. *Solid State Technology*. 15, 34 (1972)
- [82] W. Kern. Semiconductor surface contamination investigated by radioactive tracer techniques. Part 2. *Solid State Technology*. 15, 39 (1972)
- [83] W. Kern. Radiochemical study of semiconductor surface contamination, I, Adsorption of reagent components. *RCA Review*. 31, 207 (1970)
- [84] H. L. Smith. The formation of films of lead sulphide on glass surfaces. *Journal of Scientific Instruments*. 4, 115 (1927)
- [85] J. M. Doña, J. Herrero. Chemical Bath Deposition of CdS Thin Films: An Approach to the Chemical Mechanism Through Study of the Film Microstructure. *Journal of the Electrochemical Society*. 144, 4081 (1997)
- [86] R. Ortega-Borges, D. Lincot. Mechanism of Chemical Bath Deposition of Cadmium Sulfide Thin Films in the Ammonia-Thiourea System In Situ Kinetic Study and Modelization. *Journal of the Electrochemical Society* 140, 3464 (1993)
- [87] H. Meherzi-Maghraoui, M. Dachraoui, S. Belgacem, K.D. Buhre, R. Kunst, P. Cowache, D. Lincot. Structural, optical and transport properties of Ag<sub>2</sub>S films deposited chemically from aqueous solution. *Thin Solid Films*. 288, 217 (1996)
- [88] B. Haisch, A. Rueda, H. E. Puthoff. Inertia as a zero-point-field Lorentz force. *Physics Review A*. 49, 678 (1994)
- [89] J.L. Machol, F.W. Wise, R.C. Patel, D.B. Tanner. Vibronic quantum beats in PbS microcrystallites. *Physics Review*. 48 (1993) 2819.
- [90] P.R. Norton, Infrared Image Sensors. *Optical Engineering*, 30 (1991) 1649-1663.
- [91] P. C. Findlay, C. R. Pidgeon, R. Kotitschke, A. Hollingworth, B. N. Murdin, C. J. G. M. Langerak, A. F. G. van der Meer, C. M. Ciesla, J. Oswald, A. Homer, G. Springholz, G. Bauer. Auger recombination dynamics of lead salts under picosecond free-electron-laser excitation. *Physical Review B*. 58 (1998) 12908-12915.
- [92] J.A. García-Valenzuela, M.R. Baez-Gaxiola, M. Sotelo-Lerma. Chemical bath deposition of PbS thin films on float glass substrates using a Pb(CH<sub>3</sub>COO)<sub>2</sub>-NaOH-(NH<sub>2</sub>)<sub>2</sub>CS-

$N(CH_2CH_2OH)_3-CH_3CH_2OH$  definite aqueous system and their structural, optical, and electrical/photoelectrical characterization. *Thin Solid Films*. 534, 126 (2013)

[93] C. Puscher. *Polytechnic Journal*. 190, 421 (1868)

[94] R. Cooperstein Method of forming a photosensitive layer of lead sulfide crystals on a glass plate. United States Patent 3030,236. Apr. 17, 1962

[95] A. L. Efros, A. L. Efros, Interband absorption of light in a semiconductor sphere. *Soviet Physics Semiconductors* 16 (1982) 772–775 B. I. Shklovskii, A. L. Efros. *Electronic properties of doped semiconductors*, Springer Series in Solid State Sciences, Springer-Verlag, Berlin, 1984

[96] G. Hodes, N.Y. Chemical Solution Deposition of Semiconductor Films Marcel Dekker Inc New York City, p, V, 2003

[97] E. Pentia, L. Pentilie, I. Matei, T. Botila, E. Ozbay, Chemically prepared nanocrystalline PbS thin films, *Journal of Optoelectronics Advanced Materials* 3 (2001) 525–530

[98] S. Litch *Aqueous Solubilities: Solubility Products and Standard Oxidation Reduction potentials of the Metal Sulfides* *Journal of Electrochemical Society*. 135 (1988) 2971

[99] T. Globus, G. Ganguly, P. Roca i Cabarrocas, Optical characterization of hydrogenated silicon films using interference technique, *Journal of Applied Physics* 88 (2000) 1907

[100] P. Pradyot (2003). *Handbook of Inorganic Chemical Compounds*. McGraw-Hill. ISBN 0–07-049439–8. Retrieved 2009–06-06

[101] E. L. Dereniak, G. D. Boreman, 1996. *Infrared Detectors and Systems* (New York: Wiley)

[102] P.J. Drummond, D. Bhatia, A. Kshirsagar, S. Ramani, J. Ruzyllo. Studies of photoconductance decay method for characterization of near-surface electrical properties of semiconductors. *Thin Solid Films* 519 (2011) 7621–7626

[103] Y. H. Zhang, L. Guo, P. G. Yin, R. Zhang, Q. Zhang, S. H. Yang, A Highly Regular Hexapod Structure of Lead Sulfide: Solution Synthesis and Raman Spectroscopy. *Chemistry - A European Journal* 13, 2903 (2007)

[104] R. Mattis, A.J. Baroody. Carrier lifetime measurement by the photoconductive decay method. *National Bureau of Standards Technical Note* 736 (1972)

[105] R. S. Schoolar, J. R. Dixon. Optical Constants of Lead Sulfide in the Fundamental Absorption Edge Region. *Physical Review* 137(1965) 17

[106] L. M. Batukova, I. A. Karpovich. Carrier lifetime in single-crystal PbS films. *Soviet Physics Journal* 13(1970) 741-743

[107] R. K. Joshia, A. Kanjilalb, H.K Sehgal. Solution grown PbS nanoparticle films. *Applied Surface Science* 221 (2004) 43–47

- [108] N. R. Pavaskar, C. A. Menezes, A. P. B. Sinha. Modification of structural and optoelectronic properties of CdS thin films by Cu doping. *Journal of Electrochemical Society*. 124, 743 (1977)
- [109] F. Boakye, D. Nusenu. The energy bandgap of cadmium sulfide. *Solid State Communications*. 102 (1997) 323-326
- [110] G. Sasikala, P. Thilakan, C. Subramanian. Modification in the chemical bath deposition apparatus, growth and characterization of CdS semiconducting thin films for photovoltaic applications. *Solar Energy Materials and Solar Cells*. 62 (2000) 275-293
- [111] A.G. Stanley. Cadmium sulfide solar cell. *Appl Solid State Sci, Adv in Mater and Device Res*. 5 (1975) 251-366
- [112] G.B. Reddy, V. Dutta, D.K. Pandya, K. L Chopra. Solution grown composite selective surfaces. *Solar Energy Materials*. 15 (1987) 383-390
- [113] P. K. Nair, M T S Nair, A Fernandez, M. Ocampo. Prospects of chemically deposited metal chalcogenide thin films for solar control applications. *Journal of Physics D: Applied Physics*. 22 (1989) 829-836
- [114] R. Naciri, H. Bihri, A. Mzerd, A. Rahioui, M. Abd-Lefdil, C. Messaoudi. The role of the CdS buffer layer in the CuInS<sub>2</sub> Thin film solar cell. *Revue des Energies Renouvelables*. (2007) 165-168
- [115] A. Slonopas, N. Alijabbari, C. Saltonstall, T. Globus, P. Norris. Chemically deposited nanocrystalline lead sulfide thin films with tunable properties for use in photovoltaics. *Electrochimica Acta*. 151 (2015) 140-149
- [116] M. Matsumura, S. Furukawa, Y. Saho, H. Tsubomura. Cadmium Sulfide Photocatalyzed Hydrogen Production from Aqueous Solutions of Sulfite: Effect of Crystal Structure and Preparation Method of the Catalyst. *The Journal of Physical Chemistry*. 89(1985) 1327-1329
- [117] W. Kern and D. A. Poutinen. Cleaning solutions based on hydrogen peroxide for use in silicon semiconductor technology. *RCA Rev*. 31 (1970) 187
- [118] M. T. S. Nair, P. K. Nair, R. A. Zingaro, E. A. Meyers. Conversion of chemically deposited photosensitive CdS thin films to n-type by air annealing and ion exchange reaction. *Journal of Applied Physics*. 75 (1994) 1557-1565
- [119] P. K. Nair, M. T. S. Nair, J. Campos, L. E. Sansores. A critical discussion of the very high photoconductivity in chemical deposited cadmium sulfide thin films: implication for solar cell technology. *Solar Cells*. 22 (1987) 211-227
- [120] I. Kaur, D. K. Pandya, K. L. Chopra. Growth kinetics and polymorphism of chemically deposited CdS films. *Journal of Electrochemical Society*. 127 (1980) 943-948

- [121] A. Mondal, T. K. Chaudhuri, P. Pramanik. Deposition of cadmium chalcogenide thin films by solution growth technique using triethanolamine as complexing agent. *Solar Energy Materials*. 7 (1983) 431-438
- [122] ASTM F76-86. Standard test methods for measuring resistivity and Hall Coefficient and determining Hall mobility in single crystal semiconductors. 1991
- [123] H. Khallaf, I. O. Oladeji, G. Chai, L. Chow. Characterization of CdS thin films grown by chemical bath deposition using four different cadmium sources. *Thin Solid Films* 516 (2008) 7306–7312
- [124] W.D. Park. Optical Constants and Dispersion Parameters of CdS Thin Film Prepared by Chemical Bath Deposition. *Transactions on Electrical and Electronic Materials*. 13 (2012) 196-199
- [125] O. Madelung. *Semiconductors: Data Handbook*. 3<sup>rd</sup> Edition. Springer. 2004
- [126] Joint Committee on Powder Diffraction Standards (JCPDS), Card 10-0454, CdS (cubic), 1999
- [127] Joint Committee on Powder Diffraction Standards (JCPDS), Card 6-0314, CdS (hexagonal), 1999
- [128] D. Lincot, M. Froment, H. Cachet, R.C. Alkire, D.M. Kolb. *Advances in Electrochemical Science and Engineering*. Vol. 6. Wiley-VCH, Weinheim, (1999) 165–235
- [129] Joint Committee on Powder Diffraction Standards (JCPDS), Card 05-0640, CdO, 1999
- [130] O. Vigil, I. Riech, M. Garcia-Rocha, O. Zelaya-Angel. Characterization of defect levels in chemically deposited CdS films in the cubic-to-hexagonal phase transition. *Journal of Vacuum Science & Technology A*. 15 (1997) 2282
- [131] R. Elbaum, S. Vega, G. Hodes. Preparation and surface structure of nanocrystalline cadmium sulfide (sulfoselenide) precipitated from dimethyl sulfoxide solutions. *Chemistry of materials* 13 (2001): 2272-2280
- [132] M. Pentimalli, F. Antolini, E. M. Bauer, D. Capitani, T. Di Luccio, S. Viel. A solid state nuclear magnetic resonance study on the thermolytic synthesis of CdS nanoparticles in a polystyrene matrix. *Materials Letters* 60 (2006) 2657-2661
- [133] K. Wasa, M. Kitabatake, H. Adachi. *Thin film materials technology: sputtering of compound materials*. William Andrew Inc. (2004) 464-491
- [134] M. Imaizumi, T. Ito, M. Yamaguchi, K. Kaneko. Effect of grain size and dislocation density on the performance of thin film polycrystalline silicon solar cells. *Journal of Applied Physics* 81 (1997) 7635

- [135] M.G. Sandoval-Paz, M. Sotelo-Lerma, A. Mendoza-Galván, R. Ramírez-Bon. Optical properties and layer microstructure of CdS films obtained from an ammonia-free chemical bath deposition process. *Thin Solid Films* 515 (2007) 3356–3362.
- [136] S. Ninomiya, S. Adachi. Optical properties of wurtzite CdS. *Journal of Applied Physics* 78 (1995) 1183-1190.
- [137] S. Q. Yuan, P. F. Ji, Y. Li, Y. L. Song, F. Q. Zhou. Unusual Blueshifting of Optical Bandgap of CdS Nanocrystals through a Chemical Bath Deposition Method. *Advances in OptoElectronics*. 2015 (2015).
- [138] L. A. Silva, S. Y. Ryu, J. Choi, W. Choi, M. R. Hoffmann. Photocatalytic Hydrogen Production with Visible Light over Pt-Interlinked Hybrid Composites of Cubic-Phase and Hexagonal-Phase CdS. *Journal of Physical Chemistry C*. 112 (2008) 12069-12073.
- [139] L. I. Berger. *Semiconductor Materials*. CRC Press, Inc. 1997.
- [140] J. L. Roehl, Z. T. Y. Liu, S. V. Khare. Diffusion in CdS of Cd and S vacancies and Cu, Cd, Cl, S and Te interstitials studied with first-principles computations. *Materials Research Express*. 1 (2014).
- [141] R. Mattis, A.J. Baroody, Carrier lifetime measurement by the photoconductive decay method, National Bureau of Standards Technical Note 736 (1972).
- [142] R.K. Ahrenkiel, D.H. Levi, S. Johnston, W. Song, D. Mao, A. Fischer. Photoconductive Lifetime of CdS Used in Thin-Film Solar Cells. 26th IEEE Photovoltaic Specialists Conference, (1997)
- [143] E. Fortunato, D. Ginley, H. Hosono, D. C. Paine. Transparent Conducting Oxides for Photovoltaics. *MRS Bulletin* 32, 242 (2007).
- [144] Da. Jung, K. H. Lee, D. Kim, D. Burk, L. J. Overzet, G. S. Lee. Highly Conductive Flexible Multi-Walled Carbon Nanotube Sheet Films for Transparent Touch Screen. *Japanese Journal of Applied Physics* 52, (2013).
- [145] J. T. Wang, X. L. Shi, W. W. Liu, X. H. Zhong, J. N. Wang, L. Pyrah, K. D. Sanderson, P. M. Ramsey, M. Hirata, K. Tsuru. Influence of Preferred Orientation on the Electrical Conductivity of Fluorine-Doped Tin Oxide Films. *Scientific Reports* 4, 3679 (2014).
- [146] S. S. Lathe, S. Liu, C. Terashima, K. Nakata, A. Fujishima. Transparent, Adherent, and Photocatalytic SiO<sub>2</sub>-TiO<sub>2</sub> Coatings on Polycarbonate for Self-Cleaning Applications. *Coatings* 4, 497 (2014).
- [147] M. S. P. Sarah, M. Z. Musa. Electrical Conductivity Characteristics of TiO<sub>2</sub> Thin Film. *International Conference on Electronic Devices, Systems and Applications (ICEDSA)* (2010).

- [148] Y. Furubayashi, T. Hitosugi, Y. Yamamoto, K. Inaba, G. Kinoda, Y. Hirose, T. Shimada, T. Hasegawa. Novel Transparent Conducting Oxide: Anatase  $\text{Ti}_{1-x}\text{Nb}_x\text{O}_2$ . *Thin Solid Films* 496, 157 (2006).
- [149] T. Hitosugi, Y. Furubayashi, A. Ueda, K. Itabashi, K. Inaba, Y. Hirose, G. Kinoda, Y. Yamamoto, T. Shimada, T. Hasegawa. Ta-doped Anatase  $\text{TiO}_2$  Epitaxial Film as Transparent Conducting Oxide. *Japanese Journal of Applied Physics* 44, L1063 (2005).
- [150] O. Lozano, Q.Y. Chen, P.V. Wadekar, H.W. Seo, P.V. Chinta, L.H. Chu, L.W. Tu, Ikai Lo, S.W. Yeh, N.J. Ho, F.C. Chuang, D.J. Jang, D. Wijesundera, Wei-Kan Chu. Factors Limiting the Doping Efficiency of Transparent Conductors: A Case Study of Nb-doped  $\text{In}_2\text{O}_3$  Epitaxial Thin-films. *Solar Energy Materials and Solar Cells* 113, 171 (2013).
- [151] B. Diouf, W. S. Jeon, R. Pode, J. H. Kwon. Efficiency Control in Iridium Complex-Based Phosphorescent Light-Emitting Diodes. *Advances in Materials Science and Engineering* 2012 (2012)
- [152] M. S. Dabney, M. F.A.M. van Hest, C. W. Teplin, S. P. Arenkiel, J. D. Perkins, D. S. Ginley. Pulsed Laser Deposited Nb Doped  $\text{TiO}_2$  as a Transparent Conducting Oxide. *Thin Solid Films* 516, 4133 (2008)
- [153] H. Tang, K. Prasad, R. Sanjinès, P. E. Schmid, F. Lévy. Electrical and Optical Properties of  $\text{TiO}_2$  Anatase Thin Films. *Journal of Applied Physics*. 75, 2042 (1994)
- [154] M. A. El Khakani, M. Chaker, E. Gat. Pulsed laser deposition of highly conductive iridium oxide thin films. *Applied Physics Letters* 69, 2027 (1996)
- [155] T. Hitosugi, N. Yamada<sup>1</sup>, S. Nakao<sup>1</sup>, Y. Hirose, T. Hasegawa. Properties of  $\text{TiO}_2$ -based Transparent Conducting Oxides. *Physica Status Solidi A* 207, 1529 (2010)
- [156] N. Yamada, T. Hitosugi, N. L. H. Hoang, Y. Furubayashi, Y. Hirose, T. Shimada, T. Hasegawa. Fabrication of Low Resistivity Nb-doped  $\text{TiO}_2$  Transparent Conductive Polycrystalline Films on Glass by Reactive Sputtering. *Japanese Journal of Applied Physics* 46, 5275 (2007)
- [157] M. S. Farhan, E. Zalnezhad, A. R. Bushroa, A. A. D. Sarhan. Electrical and Optical Properties of Indium-tin Oxide (ITO) Films by Ion-assisted Deposition (IAD) at Room Temperature. *International Journal of Precision Engineering and Manufacturing* 14, 1465 (2013)
- [158] B. G. Lewis, D. C. Paine. Applications and Processing of Transparent Conducting Oxides. *MRS Bulletin* 25 (2000)
- [159] R. Eason. Pulsed Laser Deposition of Thin Films: Applications-led Growth of Functional Materials. (A. John Wiley & Sons, Inc., 2007) p. 245
- [160] R.K. Kawar, P.S. Chigare, P.S. Patil. Substrate Temperature Dependent Structural, Optical and Electrical Properties of Spray Deposited Iridium Oxide Thin Films. *Applied Surface Science* 206, 90 (2003)

- [161] E. A. Neifel'd, V. E. Arkhipov, N. A. Ugryumova, A. V. Korolev, Y. M. Mukovskii. Temperature dependence of the activation energy of manganite conductivity in the paramagnetic phase. *Bulletin of the Russian Academy of Sciences: Physics*. 71, 1559 (2007)
- [162] R. J. Mendelsberg, G. Garcia, D. J. Milliron. Extracting Reliable Electronic Properties from Transmission Spectra of Indium Tin Oxide Thin Films and Nanocrystal Films by Careful Application of the Drude Theory. *Journal of Applied Physics* 111, (2012).
- [163] J. P. Niemelä, Y. Hirose, T. Hasegawa, M. Karppinen. Transition in Electron Scattering Mechanism in Atomic Layer Deposited Nb:TiO<sub>2</sub> Thin Films. *Applied Physics Letters* 106, 042101 (2015).
- [164] Y. Sato, Y. Sanno, C. Tasaki, N. Oka, T. Kamiyama, Y. Shigesato. Electrical and Optical Properties of Nb – doped TiO<sub>2</sub> Films Deposited by DC Magnetron Sputtering using Slightly Reduced Nb-doped TiO<sub>2</sub> – x Ceramic Targets. *Journal of Vacuum Science and Technology A* 28, 851 (2010).
- [165] D. Kurita, S. Ohta, K. Sugiura, H. Ohta, K. Koumoto. Carrier Generation and Transport Properties of Heavily Nb-doped Anatase TiO<sub>2</sub> Epitaxial Films at High Temperatures. *Journal of Applied Physics* 100, 096105 (2006).
- [166] D. Kurita, S. Ohta, K. Sugiura, H. Ohta, K. Koumoto. Carrier Generation and Transport Properties of Heavily Nb-doped Anatase TiO<sub>2</sub> Epitaxial Films at High Temperatures. *Journal of Applied Physics* 100, 096105 (2006)
- [167] J. I. Pankove. *Optical Processes in Semiconductors*. 2<sup>nd</sup> Edition. Dover Publishers, New York, 1975. pg. 35
- [168] S. Valencia, J. M. Marín, G. Restrepo. Study of the Bandgap of Synthesized Titanium Dioxide Nanoparticles Using the Sol-Gel Method and a Hydrothermal Treatment. *The Open Materials Science Journal*. 4, 9-14 (2010)
- [169] B. Enright, D. Fitzmaurice. Spectroscopic Determination of Electron and Hole Effective Masses in a Nanocrystalline Semiconductor Film. *Journal of Physical Chemistry*. 100, 1027-1035 (1996)
- [170] C. Kormann, D. Bahnemann, M. Hoffmann. Preparation and characterization of quantum-size titanium dioxide. *Journal of Physical Chemistry*. 92, 5196 (1988)
- [171] S. C. Jain, J. M. McGregor, D. J. Roulston. Band-gap narrowing in novel III-V semiconductors. *Journal of Applied Physics*. 68, 3747 (1990)
- [172] C. E. Kim, P. Moon, S. Kim, Jae-Min Myoung, H. W. Jang, J. Bang, I. Yun. Effect of carrier concentration on optical bandgap shift in ZnO:Ga thin films. *Thin Solid Films*. 518, 6304-6307 (2010)

- [173] X. Feng, K. Shankar, M. Paulose, C. A. Grimes. Tantalum-Doped Titanium Dioxide Nanowire Arrays for Dye-Sensitized Solar Cells with High Open-Circuit Voltage. *Angewandte Chemie International Edition*. 48, 8095 (2009)
- [174] A. R. Siedle, R. A. Newmark, K. A. Brown-Wensley, R. P. Skarjune, L. C. Haddad, K. O. Hodgson, A. L. Roe. Solid-state organometallic chemistry of molecular metal oxide clusters: carbon-hydrogen activation by an iridium polyoxometalate. *Organometallics*. 7, 2078-2079 (1988)
- [175] J. L. Gavartin, D. Muñoz Ramo, A. L. Shluger, G. Bersuker, B. H. Lee. Negative oxygen vacancies in HfO<sub>2</sub>/HfO<sub>2</sub> as charge traps in high-k stacks. *Applied Physics Letters*. 89, 082908 (2006)
- [176] A. Weibel, R. Bouchet, P. Knauth. Electrical properties and defect chemistry of anatase (TiO<sub>2</sub>). *Solid State Ionics*. 177, 229-236 (2006)
- [177] W. Shockley, H. J. Queisser. Detailed Balance Limit of Efficiency of p-n Junction Solar Cells. *Journal of Applied Physics* 32, 510-519 (1961)
- [178] H. A. Mohamed. Theoretical study of the efficiency of CdS/PbS thin film solar cells. *Solar Energy*. 108, 360-369 (2014)
- [179] J. N. Freitas, A. S. Gonçalves, A. F. Nogueira. A comprehensive review of the application of chalcogenide nanoparticles in polymer solar cells. *Nanoscale*. 12(2014) 6371-6397
- [180] M. Mingebach, C. Deibel, V. Dyakonov. Built-in potential and validity of Mott-Schottky analysis in organic bulk heterojunction solar cells. *Physical Review B* (2011)
- [181] D. Pysch, A. Mette, S. Glunz. Series resistance characterization of industrial silicon solar cells with screen-printed contacts using hotmelt paste. *Progress in Photovoltaics: Research and Applications*. 15 (2007) 493-505
- [182] S. Watanabe, Y. Mita. Electrical properties of CdS-PbS heterojunctions. *Solid State Electronics*. 15, 5-10 (1972)